

2007

Effect of pulsed laser process parameters on weld integrity and biocompatibility

Brendan Croom
San Jose State University

Follow this and additional works at: https://scholarworks.sjsu.edu/etd_theses

Recommended Citation

Croom, Brendan, "Effect of pulsed laser process parameters on weld integrity and biocompatibility" (2007). *Master's Theses*. 3477.
DOI: <https://doi.org/10.31979/etd.r96m-b42f>
https://scholarworks.sjsu.edu/etd_theses/3477

This Thesis is brought to you for free and open access by the Master's Theses and Graduate Research at SJSU ScholarWorks. It has been accepted for inclusion in Master's Theses by an authorized administrator of SJSU ScholarWorks. For more information, please contact scholarworks@sjsu.edu.

EFFECT OF PULSED LASER
PROCESS PARAMETERS ON
WELD INTEGRITY AND BIOCOMPATIBILITY

A Thesis

Presented to

The Faculty of the Department of Chemical and Materials Engineering

San Jose State University

In partial fulfillment

of the Requirements for the Degree

Masters of Science

by

Brendan Croom

December 2007

UMI Number: 1452045

INFORMATION TO USERS

The quality of this reproduction is dependent upon the quality of the copy submitted. Broken or indistinct print, colored or poor quality illustrations and photographs, print bleed-through, substandard margins, and improper alignment can adversely affect reproduction.

In the unlikely event that the author did not send a complete manuscript and there are missing pages, these will be noted. Also, if unauthorized copyright material had to be removed, a note will indicate the deletion.

UMI[®]

UMI Microform 1452045

Copyright 2008 by ProQuest LLC.

All rights reserved. This microform edition is protected against unauthorized copying under Title 17, United States Code.

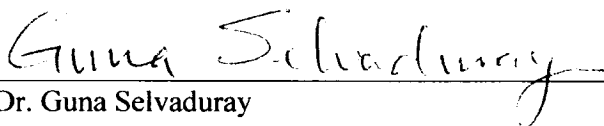
ProQuest LLC
789 E. Eisenhower Parkway
PO Box 1346
Ann Arbor, MI 48106-1346

© 2007

Brendan Patrick Croom

ALL RIGHTS RESERVED

APPROVED FOR THE DEPARTMENT OF
CHEMICAL AND MATERIALS ENGINEERING



Dr. Guna Selvaduray



Dr. Manfred Cantow



Mr. Paren Shah, Conor Medsystems, LLC

APPROVED FOR THE UNIVERSITY



ABSTRACT

EFFECT OF PULSED LASER PROCESS PARAMETERS ON WELD INTEGRITY AND BIOCOMPATIBILITY

by Brendan P. Croom

The effects of pulsed YAG laser welding process parameters on weld integrity and biocompatibility of grade 5 titanium (Ti-6Al-4V) weldments were studied. The laser welds were produced to simulate hermetic seals of titanium packages for biomedical implantable devices. The processing parameters were found to affect the physical characteristics and the fracture strength of the welds. The weld width at half the depth of penetration and the width of the heat affected zone were dependent on the processing parameters, with the total energy input being the most influential factor. With increasing depth of penetration, the fracture strength of the weldments increased. The weld parameters did not influence the microstructure, crystal structure, or chemical composition of the welds. All welds were found to be biocompatible, as determined by cytotoxicity testing.

ACKNOWLEDGMENTS

I would like to begin by thanking my advisor, Dr. Guna Selvaduray. Your guidance throughout this project was invaluable. I finish this thesis believing you could answer any question asked of you. Thank you to my committee members, Dr. Manfred Cantow and Mr. Paren Shah, for taking the time to read my thesis and provide your insight into my research.

I would like to thank everyone at Directed Light Incorporated, especially, Neil Ball, Mark Hardyck, Dan Miller, and Vladimir Solovyev. I appreciate the ability to use your facilities for my laser welding. Your guidance and assistance throughout this endeavor are also greatly appreciated.

A thank you goes out to everyone who assisted me with data collection. Particularly, Angela Craig, John Moskito, and Amy Guo of Evans Analytical Group for the XPS and AES data; Linda Sauer and Ryan Wold of the University of Minnesota for the μ -XRD data; Byron Chun of San Jose State University for the assistance with the cytotoxicity testing; and Ron Sanchez and Octavio Velez of BAE Systems for the assistance with the metallography and tensile testing.

Parts of this work were carried out in the Institute of Technology Characterization Facility, University of Minnesota, which receives partial support from NSF through the NNIN program.

Credit must also be given to the previous researchers that were used as references within this paper. Especially, Argonne National Laboratory, managed and operated by

UChicago Argonne, LLC, for the U.S. Department of Energy under Contract No.

DE-AC02-06CH11357.

Thank you to my parents for your support in all of my education and life. You have helped to get me to where I am and where I am going in the future.

The biggest thank you goes out to my wife. Without your love and support, I would not have finished this thesis. You stood by me and motivated me to finish, more than anything. Thank you for all that you do for me. I love you.

Table of Contents

<u>Section</u>	<u>Page</u>
CHAPTER 1 INTRODUCTION	1
1.1 Laser Welding	1
1.2 Biomaterials	3
1.3 Hermetic Sealing.....	4
1.4 Scope of Research.....	5
CHAPTER 2 LITERATURE REVIEW	7
2.1 Process Development and Welding Techniques.....	7
2.2 Microstructure and Microhardness of the Weldment	13
2.3 Tensile Testing of Weldments	17
2.4 Corrosion.....	19
2.5 Biocompatibility	22
2.6 Summary of Literature Search	24
CHAPTER 3 RESEARCH OBJECTIVES.....	26
CHAPTER 4 EXPERIMENTAL METHODOLOGY.....	28
4.1 Materials	28
4.2 Laser Welding.....	29
4.3. Welding Parameters	30
4.4 Metallography	31
4.5 Microhardness.....	32
4.6 Tensile Test.....	33
4.7 Cytotoxicity Test.....	34
4.8 Surface Analysis	35
CHAPTER 5 RESULTS	37
5.1 Metallography Results	37
5.1.1 Physical Characteristics of the Weld Specimens.....	49
5.1.2 Semi-Quantitative Chemical Analysis of Welds 1 and 6.....	51
5.1.3 Micro X-ray Diffraction Analysis of Weld 6.....	54

Table of Contents (Continued)

<u>Section</u>	<u>Page</u>
5.2 Microhardness Results	55
5.3 Tensile Test Result.....	61
5.4 Microstructural Effects on Microhardness and Tensile Strength	63
5.5 Cytotoxicity Test Results.....	65
5.5.1 Qualitative Cytotoxicity Test Results	65
5.5.2 Quantitative Cytotoxicity Results	72
5.6 Surface Analysis Results.....	75
CHAPTER 6 DISCUSSION OF RESULTS	83
6.1 Calculation of Tensile Strength	83
6.2 Cytotoxicity Testing Interpretation.....	85
CHAPTER 7 CONCLUSIONS	87
CHAPTER 8 RECOMMENDATIONS FOR FUTURE WORK	89
REFERENCES	92
APPENDIX A – CYTOTOXICITY TEST PROCEDURE.....	94
APPENDIX B – GLOSSARY OF BIOLOGICAL TERMS	100
APPENDIX C – XRD RESULTS	101
APPENDIX D – XPS SURVEY SPECTRA RESULTS.....	111
APPENDIX E – SURFACE ANALYSIS RESULTS FOR CONTROL.....	121
APPENDIX F – SURFACE ANALYSIS RESULTS FOR WELD 1	132
APPENDIX G – SURFACE ANALYSIS RESULTS FOR WELD 2	141
APPENDIX H – SURFACE ANALYSIS RESULTS FOR WELD 4	152
APPENDIX I – SURFACE ANALYSIS RESULTS FOR WELD 7	163
APPENDIX J – XPS BONDING STATE COMPARISON SPECTRA RESULTS.....	174

List of Figures

<u>Figure</u>	<u>Page</u>
Figure 1. Example of a hermetic seal produced using laser welding.....	4
Figure 2. A comparison of permeability rates in some common materials	5
Figure 3. Pareto diagram of the parameters that affect the quality of laser welds.....	8
Figure 4. Schematic representation of how a hermetic seal is formed	9
Figure 5. Graph indicating the dependence of weld depth on beam travel speed	10
Figure 6. The effect of laser power and weld speed on the microstructure of the weldment in V-4Cr-4Ti.....	15
Figure 7. Comparison of the hardness variation with distance from the centerline for a) 316L stainless steel and b) V-4Cr-4Ti	16
Figure 8. The comparison of stress-strain curves for the base material, a bead on plate, and a butt weld sample.....	18
Figure 9. a) Comparison of corrosion current as a function of time for unwelded and welded samples. b) Comparison of resting potential as a function of time for unwelded and welded samples.....	20
Figure 10. Potential maps of pitting activity on the surface of 304 stainless steel	21
Figure 11. Surface morphology of 304 stainless steel after pitting corrosion. Note the location of the pits is only on the base metal	22
Figure 12. Comparison of human gingival fibroblast adhesion on control (C), soldered (S) and laser welded (L) samples.....	23
Figure 13. Flow chart of the experimental approach carried out during this research. ...	27
Figure 14. Titanium specimens prior to welding.	28
Figure 15. Laser welding fixture.....	29
Figure 16. Schematic of tensile testing set-up.	33
Figure 17. Weld specimens incubating with HEP-2 cells in titer wells.....	35
Figure 18. Microstructure of the base material	38
Figure 19. Overview of the microstructure of weld 1	39
Figure 20. Microstructure of the fusion zone and heat affected zone of weld 1	40

List of Figures (Continued)

<u>Figure</u>	<u>Page</u>
Figure 21. Overview of the microstructure of weld 2.....	40
Figure 22. Microstructure of the fusion zone and heat affected zone of weld 2.....	41
Figure 23. Overview of the microstructure of weld 3.....	41
Figure 24. Microstructure of the fusion zone and heat affected zone of weld 3.....	42
Figure 25. Overview of the microstructure of weld 4.....	42
Figure 26. Microstructure of the fusion zone and heat affected zone of weld 4.....	43
Figure 27. Overview of the microstructure of weld 5.....	43
Figure 28. Microstructure of the fusion zone and heat affected zone of weld 5.....	44
Figure 29. Overview of the microstructure of weld 6.....	44
Figure 30. Microstructure of the fusion zone and heat affected zone of weld 6.....	45
Figure 31. Overview of the microstructure of weld 7.....	45
Figure 32. Microstructure of the fusion zone and het affected zone of weld 7	46
Figure 33. Overview of the microstructure of weld 8.....	46
Figure 34. Microstructure of the fusion zone and heat affected zone of weld 8.....	47
Figure 35. Overview of the microstructure of weld 9.....	47
Figure 36. Microstructure of the fusion zone and heat affected zone of weld 9.....	48
Figure 37. Schematic of a weld indicating locations of measurements.	49
Figure 38. Physical dimensions of the welds as a function of peak pulse energy.	50
Figure 39. EDX analysis locations and spectra for weld 1.	52
Figure 40. EDX analysis locations and spectra for weld 6.	53
Figure 41. Locations for XRD analysis.	55
Figure 42. Overlay of XRD spectra	55
Figure 43. Microhardness plots for weld 1.	57
Figure 44. Microhardness plots for weld 2.	57
Figure 45. Microhardness plots for weld 3.	58
Figure 46. Microhardness plots for weld 4.	58
Figure 47. Microhardness plots for weld 5.	59

List of Figures (Continued)

<u>Figure</u>	<u>Page</u>
Figure 48. Microhardness plots for weld 6.	59
Figure 49. Microhardness plots for weld 7.	60
Figure 50. Microhardness plots for weld 8.	60
Figure 51. Microhardness plots for weld 9.	61
Figure 52. Comparison of tensile test results.	62
Figure 53. Plot of average tensile strength as a function of depth of penetration.	64
Figure 54. Cytotoxicity test specimen for the positive control.	67
Figure 55. Cytotoxicity test specimen for the negative control.	67
Figure 56. Cytotoxicity test specimen for weld 1.	68
Figure 57. Cytotoxicity test specimen for weld 2.	68
Figure 58. Cytotoxicity test specimen for weld 3.	69
Figure 59. Cytotoxicity test specimen for weld 4.	69
Figure 60. Cytotoxicity test specimen for weld 5.	70
Figure 61. Cytotoxicity test specimen for weld 6.	70
Figure 62. Cytotoxicity test specimen for weld 7.	71
Figure 63. Cytotoxicity test specimen for weld 8.	71
Figure 64. Cytotoxicity test specimen for weld 9.	72
Figure 65. AES depth profile for the control specimen.	79
Figure 66. AES depth profile for the weld 2 specimen.	80
Figure 67. AES depth profile for the weld 4 specimen.	81
Figure 68. AES depth profile for the weld 7 specimen.	82

LIST OF TABLES

<u>Table</u>	<u>Page</u>
Table 1. Advantages and disadvantages of laser welding.....	2
Table 2. Factorial experimental design matrix for the laser welding parameters.	30
Table 3. Parametric values for both levels of interest.....	31
Table 4. Physical dimensions of the welds.	49
Table 5. Semi-quantitative chemical analysis results for welds 1 and 6.	51
Table 6. Lattice parameters for crystal structures within weld 6.	54
Table 7. Average microhardness results.	56
Table 8. Tensile test results.....	62
Table 9. Numeric cytotoxicity scale per ISO-10993-5.	65
Table 10. Summary of qualitative cytotoxicity test results.....	66
Table 11. Quantitative results for the cytotoxicity test	73
Table 12. Mann-Whitney U Test cytotoxicity results.....	75
Table 13. Atomic concentration of the surface of the weld specimens as determined with XPS (in atomic percent).....	78
Table 14. Atomic concentration of the surface of the weld specimens as determined with XPS (in atomic percent).....	78
Table 15. Bonding state of the identified titanium (in percent).	79
Table 16. Bonding state of the identified aluminum (in percent).	79

CHAPTER 1

INTRODUCTION

In 2002, the United States was the world's largest producer of medical devices and medical diagnostics equipment, with a value estimated at \$77 billion. Also during 2002, the United States led the world in exports of medical devices and medical diagnostics equipment, estimated at \$20.3 billion. The United States held 42% of the world's market share in the medical device and diagnostic industry during 2002 [1]. Between 1997 and 2002, the market size for medical devices and diagnostics in the United States increased each year. In the area of medical devices, the number of implanted devices increased between 1997 and 2001 for pacemakers, total knee implants and total hip implants. With the increasing need for more medical devices, the United States has the need to continually develop the technology behind these devices. By being the world's leading producer and exporter in the medical device and diagnostic industry, the United States has the ability to fund research and development in the industry. Of the \$12.2 billion estimated worldwide market for selected cardiovascular devices in 2001, laser welding was used in devices having a value of over \$7.7 billion [1].

1.1 Laser Welding

Welding is a centuries old process that is used to join two solid materials together by the input of heat in order to melt the metal. The heat source is then removed and the molten metal solidifies and fuses the two parts together. One of the latest methods used for welding utilizes lasers. Lasers provide coherent, monochromatic light in a small spot to the objects to be welded, thus providing the heat needed to melt the metals and

facilitate welding. The advantages and disadvantages of laser welding are listed in

Table 1.

Table 1. Advantages and disadvantages of laser welding [2, 3, 4].

Advantages	Disadvantages
A filler material is not necessary	Tendency towards cracking in some materials due to the rapid solidification rate
Able to weld dissimilar metals	Weldment thickness limit for a single pass weld
Faster welding speeds than conventional welding methods	Porosity formation in some alloys
Minimal heat distortion of surrounding material due to low heat input	High capital cost for installation and maintenance
Ability to transmit the laser over long distances with minimal power loss	
Ability to weld in air	
Secondary processes are not required	

Laser welding has the ability to be used for many types of materials and many types of welds. By varying the processing parameters of laser welding, various materials can be welded in a wide range of configurations. Some of the common process parameters include weld speed, pulse power, pulse duration, focal length and intensity-time or pulse wave form [5]. These and other parameters can be altered to tightly control the amount of energy that is imparted to the material, thus controlling the depth of penetration, the breadth of the heat affected zone, weld integrity, and completeness of the weld.

Due to its ability to deliver a high energy-density spot, laser welding is an attractive process for joining materials in many industries. The small spot size keeps the affected area of the material at a minimum, thus keeping the properties of the welded area very close to that of the bulk material [6, 7, 8]. The area that is altered during welding is

called the heat affected zone, the area surrounding the weld that is metallurgically affected but not fully melted by the heat of welding. Since the microstructure of the metal in the heat affected zone is altered, it is possible that the properties of the heat affected zone differ from those of the bulk material. Another advantage to the reduced heat input of laser welding is that any sensitive components that are contained within a laser welded package are not affected by the heat of the laser, thus allowing for the packaging to be minimally larger than the contents.

1.2 Biomaterials

One industry in particular that has adopted the use of laser welding is the biomedical industry. Laser welding is used for a wide range of implantable biomedical devices including pacemakers, stents, cochlear implants, and defibrillators. All of these devices are implanted into the human body where they are subjected to a corrosive environment, and sometimes undergo dynamic loading. In order to function in the human body under these conditions, biomedical implants need to be compatible with the human body, i.e., be biocompatible, which is defined as the inherent ability of a material to elicit an appropriate host response [9].

Metals are a popular type of material used in biomedical applications, providing the structural soundness needed to face the dynamic loads found in the human body. Some metals have been found to be biocompatible in the human body as well. Three alloys frequently used for biomedical implantation fabrication are stainless steels, titanium alloys, and cobalt chromium alloys. Stainless steels and cobalt chromium alloys are highly corrosion resistant due to the amount of chromium present in the alloys and the

resultant formation of a chromium oxide layer on the surface. Titanium alloys form a corrosion resistant oxide layer, titanium dioxide, on the surface, thus making them highly corrosion resistant as well.

1.3 Hermetic Sealing

An important use of laser welding for biomedical devices is to create a hermetically sealed package to enclose the parts of the devices that are not biocompatible or are susceptible to damage by body fluids. Hermetically sealed packages are needed for pacemakers, defibrillators, and several other devices. A hermetic seal keeps the inner contents of the packaging protected from aqueous and gaseous contamination [10].

These seals can be created using many techniques. When implementing laser welding, hermetic seals are created by using a pulsed laser to weld the parts together. The pulses are close enough to cover at least 50% of the previous weld spot, as can be seen in Figure 1. By keeping the weld spots close together, the seal is complete and the inside of the package is kept contamination free and isolated from the human body.

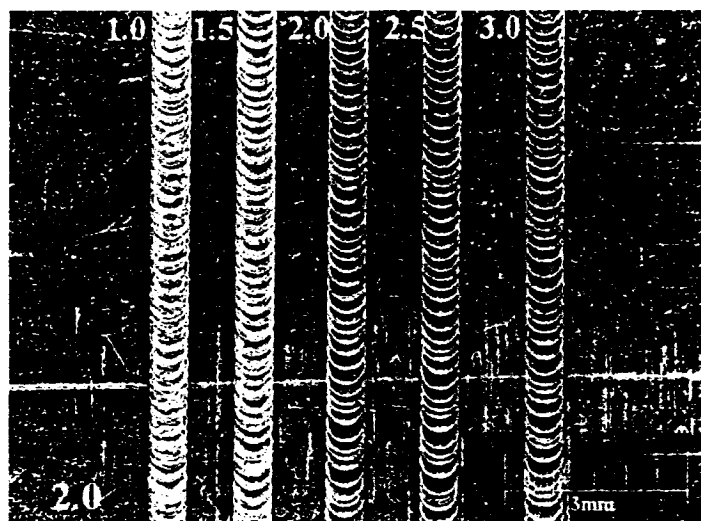


Figure 1. Example of a hermetic seal produced using laser welding [10].

Since all materials are permeable to gases to some extent, hermetic seals are characterized by leakage rates. The leakage of hermetic seals is a combination of bulk leakage through the material and leakage through imperfections in the seam. Most commonly, the package is filled with helium and the amount of helium that escapes from the package over time is monitored. As is shown in Figure 2, metals display lower permeability than most common materials; therefore, bulk leakage is minimized, and, with a good weld, leakage through a seal can be minimized. This provides further justification for the use of metals for hermetically sealed packages.

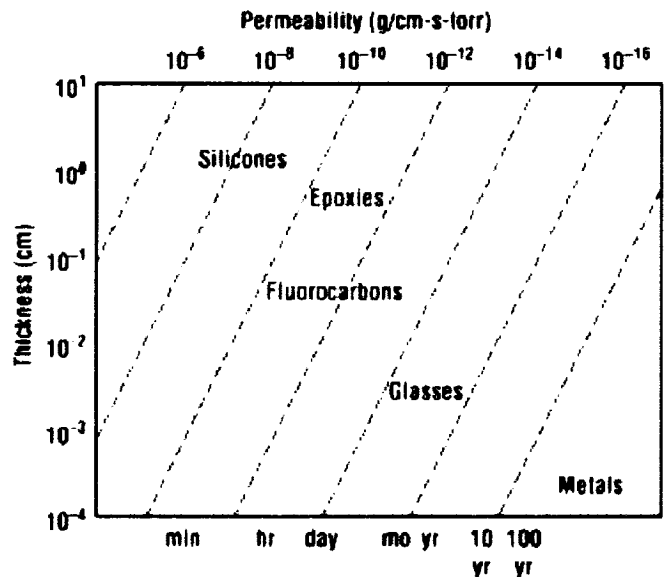


Figure 2. A comparison of permeability rates in some common materials [11].

1.4 Scope of Research

The widespread use of titanium alloys in the medical device industry, because of their proven biocompatibility, and the use of laser welding for hermetic sealing of medical devices contained in titanium packages, coupled with the limited research on the effects of laser welding on the biocompatibility of the welded material, led to this

research effort. The goal of this research, therefore, was to study the effect of pulsed laser welding parameters on the mechanical integrity and biocompatibility of the welds.

Previous studies that have been conducted in the area of laser welding are analyzed and presented in Chapter 2. The studies presented focus on laser welding procedures, microstructural changes due to laser welding, mechanical properties of laser welded specimen, changes to corrosion resistance of laser welded specimens, and effects of laser welding on biocompatibility. The research objectives of this work are described in Chapter 3. The research approach that was taken to reach the research objectives is contained in Chapter 4. The results of the experimentation are presented in Chapter 5, and then followed by a discussion of the results in Chapter 6. The conclusions of this research are in Chapter 7, with recommendations for future work in Chapter 8.

CHAPTER 2

LITERATURE REVIEW

A literature review was conducted in order to assess the research that has been completed in three areas of interest related to this project, namely, process development and welding techniques, microstructure and mechanical properties of the weldment, and corrosion and biocompatibility of laser welded specimens.

2.1 Process Development and Welding Techniques

One aspect of laser welding that makes it more difficult than most welding techniques is the number of process parameters that must be controlled. Each parameter has an effect on the quality of the weld, and equal quality welds can be produced by using different parameters. Many papers [12, 13, 14, 15] describing the parameters of laser welding, welding techniques, and procedures for various alloys, including statistical analyses used for optimization of the processing parameters have been published. Since laser welding is still in its infancy stages relative to other welding techniques, studies on the effect of the processing parameters on various aspects of the weld, including quality, corrosion resistance, strength, toughness, and penetration depth are constantly being reported.

Laser welding requires the control of many parameters to obtain an acceptable weld. By pulsing the laser, even more parameters that have a significant effect on the weld, and introduce further needs for control. Due to the large number of parameters and variables, a full set of experiments to determine the effect of each parameter on the weld can be impractical due to the excessively large number of experimental runs and time

needed. A Pareto diagram of the parameters related to laser welding is shown in Figure 3 [12].

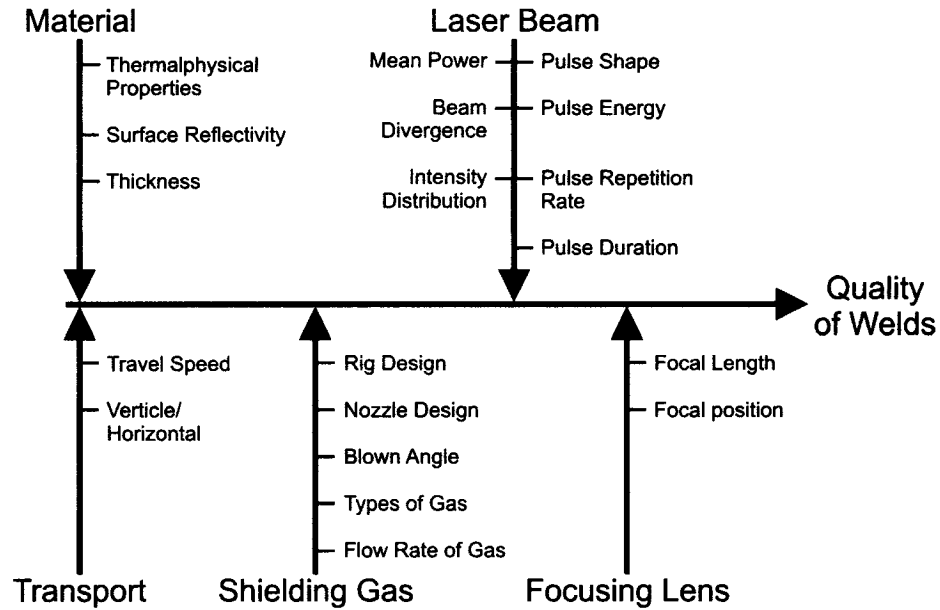


Figure 3. Pareto diagram of the parameters that affect the quality of laser welds [12].

The material parameters help to define the weldability of the material and the part. The thermal-physical properties of interest for the material include melting temperature, thermal conductivity, and thermal diffusivity [4]. Another important material property related to laser welding is reflectivity, which affects the amount of energy transferred to the material [12]. These material parameters help to define the penetration depth that can be obtained on a part, which is determined by Equation 1 [4].

$$T(x,t) = \left(2q\sqrt{\frac{at}{k}} \right) \left[\operatorname{ierfc} \left(\frac{x}{4at} \right) \right] \quad \text{Equation 1}$$

where $T(x,t)$ is the temperature at distance x below the work surface at time t after start of constant heat input, a is the thermal diffusivity, k is the thermal conductivity, x is the desired penetration depth, t is the pulse duration, and q is the absorbed heat input.

The largest list of parameters is associated with the laser itself. Some of these parameters are user-defined, some are inherent to the system, and others are defined by the welding process. The mean power, pulse shape, pulse energy, and pulse duration are more likely to be user-defined parameters. These parameters define the amount of heat and energy that is delivered to the material to facilitate melting. The beam divergence and intensity distribution are system specific parameters that are not easily changed without modifying the system set up. The pulse repetition rate and travel speed are used to determine the amount of overlap for each spot. Their relationship for seam welding can be seen in Figure 4 [12], where T_p is the pulse duration, T_f is the pulse frequency, S is the major pulse diameter, W is the minor pulse diameter, V is the weld speed, and S' is the length of a spot not overlapped by another spot. As the amount of overlap increases, the dimensions of the weld become more uniform due to a more homogeneous melt volume in the weld [12]. The other parameters shown in Figure 4 are usually held constant, or are user-defined to minimize weld defects.

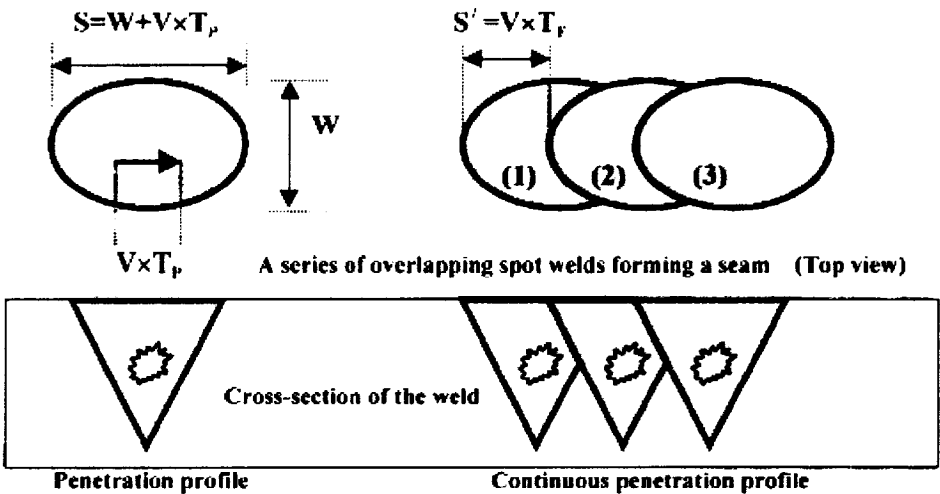


Figure 4. Schematic representation of how a hermetic seal is formed [12].

Since laser welding can be used on a wide range of materials, the methods used for procedural development differ among researchers. A common method used to determine the proper parameters for welding is screen testing, by performing welds at a variety of parameter settings and analyzing the results of these welds. Researchers generally monitor penetration depth and weld defects to determine if the parameters will provide an acceptable weld. Xu et al. [13] performed a procedural analysis of laser welding on V-4Cr-4Ti alloy. They varied the laser power, weld speed, and cover gas control, while they monitored the weld depth, porosity, and oxygen uptake. As their results in Figure 5 indicate, the weld depth is approximately inversely proportional to the travel speed of either the beam or the specimen, depending on the system set up. This study was well documented and presented an effective method that was utilized for procedural development of welding parameters. One important aspect of their results was the demonstration of the high weld speed that can be obtained using laser welding, while still creating high quality welds.

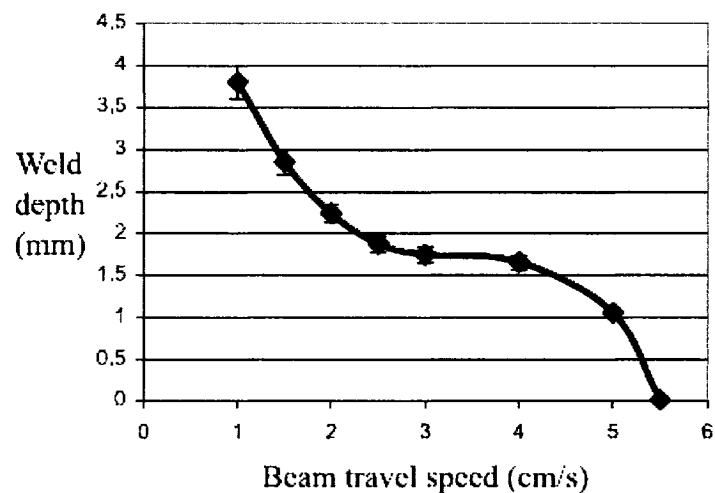


Figure 5. Graph indicating the dependence of weld depth on beam travel speed [13].

Once the parameters of laser welding are understood and a range of settings have been selected, optimization of the laser welding process can proceed. During the optimization process, researchers use statistical analysis to determine which parameter has the greatest effect on the results obtained. One of the most widely used analysis techniques for process optimization is Taguchi analysis, which uses a systematic approach to optimize the experimental design. Inconsistent results can be reduced since the Taguchi analysis also addresses the variance of the experimental results.

Pan et al. [14] utilized the Taguchi method to optimize the laser welding of magnesium alloys. In the research, the authors studied the effects of six welding parameters, which included shield gas, laser energy, weld speed, focal length, pulse frequency, and pulse shape. Each parameter was tested at two or three levels. A full experimental analysis would have needed 486 different combinations of the parameters for statistical confidence. Using the Taguchi method, they were able to achieve the same extent of statistical confidence with just 54 welds. During the study, the integrity of each weld was evaluated by its ultimate tensile strength (UTS). Their results produced a weld that increased the UTS by 2.5 times over previous welding procedures.

Pan et al. demonstrated the effectiveness of using statistical methods like the Taguchi method to efficiently produce statistically relevant results. By studying a large number of parameters, they were able to provide insight into the more influential factors, and their interactions, that control the quality of the welds produced by laser welding. Their study provides a good guide to implementing statistical methods to increase the output of the data from a smaller sample size.

Another useful statistical tool used to optimize laser welding is analysis of the variance (ANOVA), which allows the comparison of groups of data to determine the difference between the means and how significantly different the means are. This process was used by Pan et al. [14] and Casalino et al. [15] to determine the most influential process parameter(s). During their experimentation, Pan et al. varied the shielding gas, laser energy, conveying speed, welding focus position, laser pulse frequency, and laser pulse shape. Through ANOVA, they found that the two most dominant parameters were the pulse shape and laser energy.

Casalino et al. varied the laser power rating, specimen thickness and weld speed. The two measured responses, average width of the melted area and microhardness, were each related to the imperfections of the weld, including porosity, excess weld metal and excessive penetration. Through their experimentation they determined that the weld speed had the greatest effect on the results. This is due to the fact that as the welding speed increases, the coupling of the laser beam with the material decreases. Since the applications and parameters that were varied were different between the two studies, their findings are not contradictory. Through the implementation of ANOVA, the parameters that produce the greatest effect(s) were identified, thus allowing the researcher to monitor these parameters more closely and also better understand the welding process.

Both of these studies demonstrated the validity of using statistical techniques to determine which parameters have more of an effect on the desired outcome of the weld. Pan et al. monitored the mechanical properties of the weld, while Casalino et al. monitored the weld quality. Depending on the application for the weld and the finished

part, either of the two outcomes can be monitored, and sometimes both should be monitored. The Ti-6Al-4V alloy welds that were studied by Casalino et al. were to be used in the aerospace and automotive industries in sensitive parts where the weld quality could have a great influence on the failure of the structure. Casalino et al. presented their findings in a complete manner and interpreted the data to investigate if there were any significant results by way of interactions among the input parameters.

2.2 Microstructure and Microhardness of the Weldment

One aspect of the weldment that is greatly changed during laser welding is the microstructure. Laser welding provides enough energy to melt a small volume of the material, which then quickly solidifies after the laser energy is removed. The rate of solidification for laser welding ranges from 10,000°C to 100,000°C per second [16]. The rapid cooling rate is one factor that limits the use of laser welding on some alloys, due to the increased tendency of hot cracking in the weldment. This rapid cooling rate also leads to the formation of a microstructure that is drastically different in the fusion zone, and the adjacent heat affected zone, than in the base material

During a comparison of electron beam and laser welding of AISI 316L stainless steel, Tjong et al. [16] investigated the microstructural changes and creep behavior of the material. Their investigation discovered cellular or cellular-dendrite formations in the heat affected zone and equiaxed dendrites in the fusion zone. A “parting” was also measured at the central fusion region. The dendritic formation in the fusion zone was attributed to the rapid cooling rate. Tjong et al. noted the microstructural dependence on the ratio of the temperature gradient in the liquid to the solidification rate. When the ratio

is high, planar front growth is preferred. This is seen at the fusion boundary of the weld. The ratio decreases as the liquid-solid interface moves further from the fusion zone, as seen in the heat affected zone, and cellular growth is now preferential [16]. It was also noted that single-phase austenitic solidification was kinetically favored due to dendritic tip undercooling. The laser welding parameters were not reported, nor were the qualification criteria for the welds.

One major factor that influences the microstructure of the weldment is the amount of heat input that the weld area receives. Two process parameters that greatly affect the amount of heat input are laser power, and weld speed. Heo et al. [6] studied the dependence of the microstructure in V-4Cr-4Ti alloy welds on laser power and weld speed. Their study also included the impurity content, impact strength and hardness of the weldment, in addition to determining which set of processing parameters produced full penetration welds. The results of their work are shown in Figure 6. Welding at constant speed while varying the laser power produced the microstructures in Figures 6a, 6b, and 6c. The microstructure shows the same characteristics in all three welds with the only difference appearing to be the volume fraction of each phase present in the fusion zone. The major change that can be noticed in these three figures is the width of the weld. As the laser power increases, the weld width increases due to the larger melt volume from higher heat input. Figures 6b, 6d, and 6e are a comparison of welds using constant laser power and varying weld speeds. It can again be noted that the width of the weld increases with higher heat input. Heo et al. fully documented and explained their results.

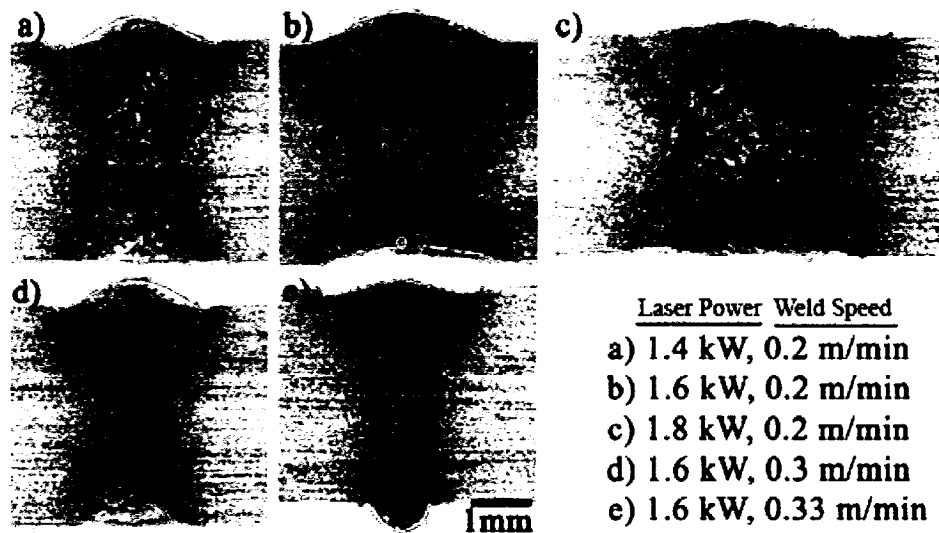


Figure 6. The effect of laser power and weld speed on the microstructure of the weldment in V-4Cr-4Ti [6].

With the change in microstructure of the welded area come changes to the mechanical properties. Two properties of welded parts that are commonly measured are hardness and tensile strength. The hardness of the welded area helps to provide a means to quantitatively evaluate changes to the microstructure by measuring the variation of hardness across the welded region. Heo et al. [6] and Xu et al. [13] measured the microhardness of V-4Cr-4Ti alloy across the welded region. In each of their studies, the lowest hardness was measured within the base metal. The hardness increased as the measurements were taken closer to the centerline of the weld. Tjong et al. [16] measured the microhardness of AISI 316L across the welded region. In their research, the base metal was again the softest region of the weldment. The hardness also increased as the measurements were taken closer to the centerline. The major difference between the findings by Tjong et al. and the findings of other researchers is that a large hardness peak was measured near the fusion line of the weld in 316L stainless steel. Tjong et al.

attribute the hardness peaks to the formation of dendrites and fine grains in the weld metal and heat affected zone, respectively [16]. The hardness variation of the weldment with distance from the centerline for both 316L stainless steel and V-4Cr-4Ti is shown in Figure 7. The hardness within the fusion zone of both 316L and V-4Cr-4Ti is higher than the hardness of the corresponding base material. However, the hardness peaks at the heat affected zone of the 316L weld, while the hardness gradually increases across the heat affected zone of the V-4Cr-4Ti weld. The recorded profile for 316L is attributed to the dendritic formation within the microstructure and the distribution of the residual stresses after welding. For the V-4Cr-4Ti weld, the authors believe the increase in hardness is due to oxygen uptake by the fusion zone.

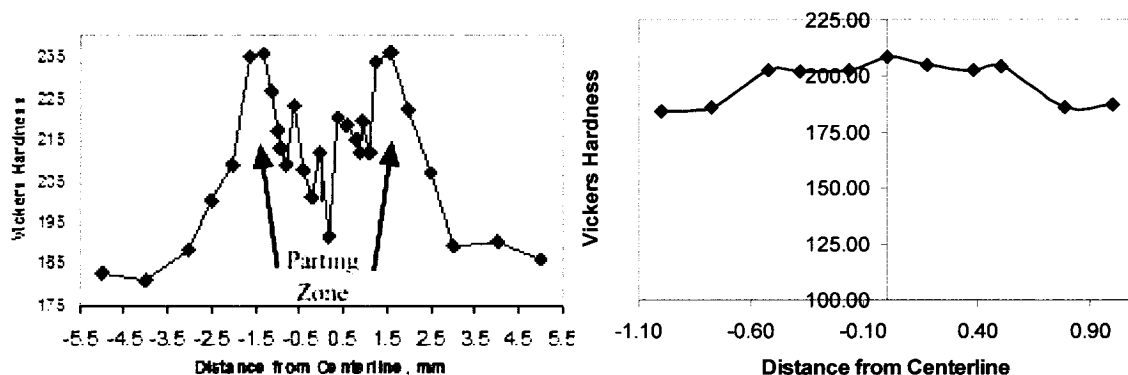


Figure 7. Comparison of the hardness variation with distance from the centerline for a) 316L stainless steel [16] and b) V-4Cr-4Ti [13].

As can be seen in the three studies conducted by Heo et al., Xu et al., and Tjong et al., the Vickers hardness of the heat affected zone and fusion zone is higher than the hardness of the base material. Each alloy was found to have an increase of approximately 20 Vickers hardness units from the base material to the fusion zone. It is difficult to determine the distance between measurements in the study conducted by Heo et al. Xu et al. kept a constant 0.15 mm between measurements, while Tjong et al. measured the

hardness every 0.5 mm. Tjong et al. noted a large increase at a position that they called the “parting” zone. This was not noted in the other two studies, which were conducted on a different alloy.

2.3 Tensile Testing of Weldments

Tensile testing of laser welded parts is a more difficult process than microhardness measurements. There are two orientations that can be tested in tension. One orientation is with the load applied transverse to the weld axis. The other orientation is with the load applied parallel to the weld axis. By performing a tensile test transverse to the weld axis, the integrity of the weld can be measured. This orientation is the more popular method for tensile testing laser welded parts. Caiazzo et al. [7] used multiple sample types in order to discern any influence that was caused by sample preparation. It was found that butt welded samples produced results similar to those of the base material. A comparison of the tension tests of butt welded, bead-on-plate, and base material tension tests performed by Caiazzo et al. is shown in Figure 8. The ultimate tensile strength for the butt welded specimens was approximately 33% lower than the base material, and the butt welded specimens fractured at the onset of plastic deformation. It was also noted that a majority of the butt welded specimens failed either within the weld bead or within the heat affected zone. The authors explain these phenomena as being due to oxidation of the weld root, which would occur at the interface of the heat affected zone and the weld bead, or misalignment of the welded components.

Caiazzo et al. performed a very complete study of the tensile properties of laser welded Ti-6Al-4V. One set of specimens was prepared utilizing a butt weld to determine

the strength of the weld. A second set of specimens was prepared as a bead-on-plate weld that was prepared identical parameters as the first specimen set. The bead-on-plate specimen was used to determine if there was any influence on the data by the edge preparation or coupling conditions of the butt welded specimen. Due to the decreased strength of the butt welded specimen, it was concluded that the preparation of the edge of the specimens influenced the measured strength of the weldment. Therefore, care must be taken in preparing the specimens in order to obtain a weldment with strength similar to the base material.

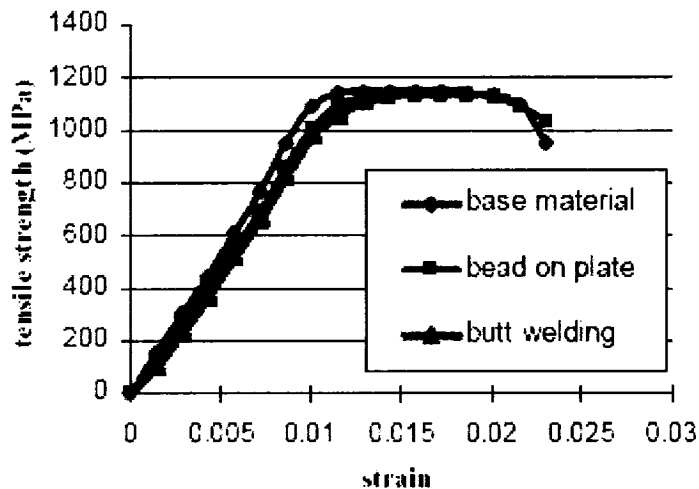


Figure 8. The comparison of stress-strain curves for the base material, a bead on plate, and a butt weld sample [7].

Lui et al. found the tensile properties to be similar for lap welded and non-welded parts. They discovered that there was no statistical difference between the strength of non-welded specimens and specimens lap welded with varying currents. One difference between the two studies is that Lui et al. noted some fractures within the weld while Caiazzo only noted fractures in the base material. Liu et al. performed tensile tests on

laser welded commercially pure titanium. Two cast plates of titanium were weld bonded together, simulating a lap weld, and then subjected to a tensile test. Liu et al. reported the fracture strength of the welded samples, instead of a full stress-strain diagram.

2.4 Corrosion

One of the least reported characteristics of laser welded parts is corrosion resistance. Tzeng [17] studied the effects of welding process parameters on the corrosion rate of laser welded zinc-coated steel. He notes that the use of Nd:YAG laser welding damages the zinc coating of the fusion zone and the heat affected zone due to vaporization of the coating. During the research, the pulse shape, pulse duration, pulse energy and travel speed parameters were varied. A corrosion cell with a standard electrode was used to determine the effect on corrosion resistance of welded specimen. The corrosion current of the welded specimens was found to be larger than the non-welded specimens. The corrosion current is proportional to the corrosion rate, indicating that the welded specimens would corrode faster than non-welded specimens. He noted that the increased corrosion current was due to the increased zinc self corrosion rate of the welded specimens caused by the sacrificial protection of the exposed steel of the weld. It was determined that the zinc coating provides adequate protection of the welded specimens with little variation occurring due to changes to processing parameters. Tzeng also noted that the zinc coating of the welded specimens consisted of zinc and zinc-iron intermetallics. The changes in corrosion current and resting potential over time for welded and unwelded specimens are shown in Figure 9.

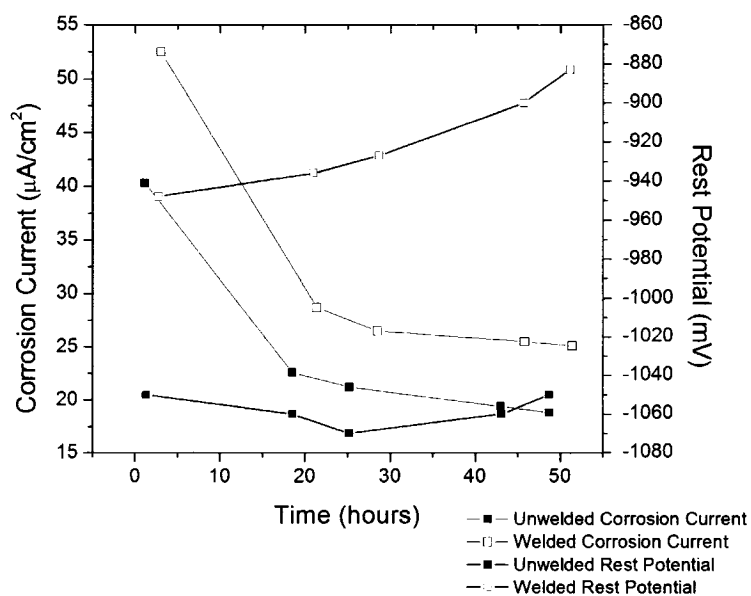


Figure 9. a) Comparison of corrosion current as a function of time for unwelded and welded samples. b) Comparison of resting potential as a function of time for unwelded and welded samples [17].

The purpose of Tzeng's study was to determine if the protective surface layer of zinc remained sufficiently effective to maintain protection of the bulk material after laser welding. After producing acceptable welds, these parts underwent electrochemical characterization. The acceptability criterion for the welds was not stated. It was concluded that the laser welded specimens did not show a significant decrease in corrosion resistance. This conclusion was based on the fact that the corrosion current, which is proportional to the corrosion rate, was approximately 25% higher at the end of testing for the welded specimens than the unwelded specimens.

Austenitic stainless steels have resistance to general corrosion, but are susceptible to pitting corrosion. Lu et al. [18] set out to study the pitting behavior of laser welded 304 stainless steel. Using a three electrode corrosion cell, they monitored the potential map of the 304 stainless steel for pitting in an aqueous solution of 5×10^{-4} M FeCl_3 +

1×10^{-4} M NaNO_3 and a buffer solution of 0.05 M H_3BO_3 + 0.075 M $\text{Na}_2\text{B}_4\text{O}_7 \cdot 10\text{H}_2\text{O}$ containing 3000 ppm of chloride ions. It was found that after only ten minutes, pitting began. Over the first 45 minutes of testing, metastable pits formed on the surface of the base metal. After 120 minutes, stable pits had formed and were growing in the base metal. The potential map and surface morphology of the 304 stainless steel sample can be seen in Figures 10 and 11, respectively. It was noted that the corrosion resistance of the weld material was improved over the base metal due to the fact that pitting occurred only in the base metal. The authors attributed this characteristic to the rapid cooling of the weld material. They stated that the cooling rate was so fast that diffusion was suppressed and the δ -ferrite to γ -austenite phase transformation could not take place [18]. By not allowing the γ -austenite to form, the amount of δ -ferrite was drastically increased within the weld material. The authors also stated that the δ -ferrite and the γ -austenite contained the same chemical composition. Therefore, microsegregation did not take place, and corrosion resistance was not affected. The experiment run by Lu et al. was very well documented.

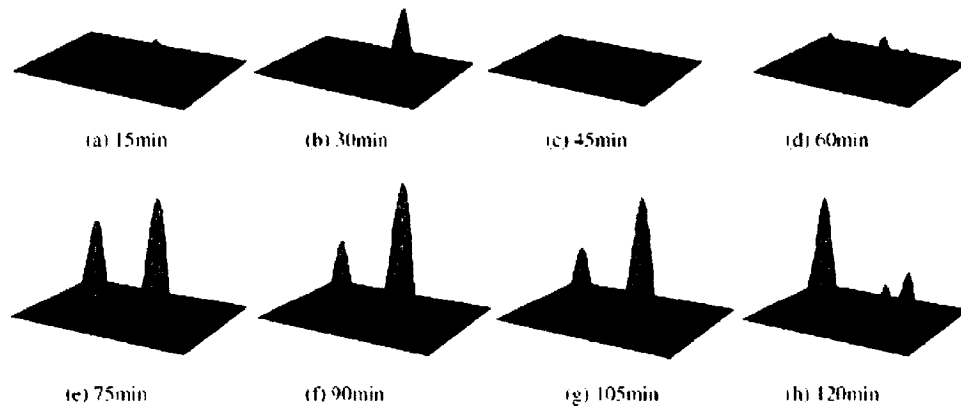


Figure 10. Potential maps of pitting activity on the surface of 304 stainless steel [18].

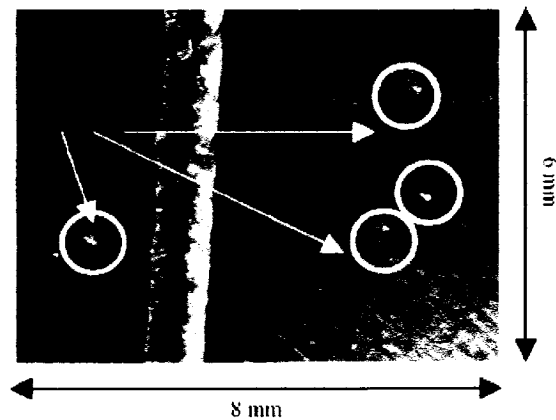


Figure 11. Surface morphology of 304 stainless steel after pitting corrosion. Note the location of the pits is only on the base metal [18].

2.5 Biocompatibility

Laser welding is starting to be widely used by the biomedical industry; yet there is a shortage of data in the open literature supporting its use. Solmi et al. [19] performed a biocompatibility study using human interdental gingival papillae cells on stainless steel molar bands that were laser welded or soldered to stainless steel orthodontic wire. These cells are normally elongated. Round cells indicate unsuccessful adhesion and a flat, non-elongated shape indicates inadequate adhesion to the prosthetics. Cultures were applied to the laser welded prosthetics, soldered prosthetics, and a control, which consisted of a T-30 flask. The morphology of the cells was monitored after 6 hours, 24 hours, 7 days, and 16 days. In order to quantify their results, the authors used phase-contrast light microscopy to image the cells. The authors counted the number of cells present in each image, as well as the number of elongated, round and flat cells. Cell proliferation was determined using semi-quantitative scoring based on the frequency of cell clusters. The morphology of the cells over time for each of the soldered, laser welded and control specimen can be seen in Figure 12.

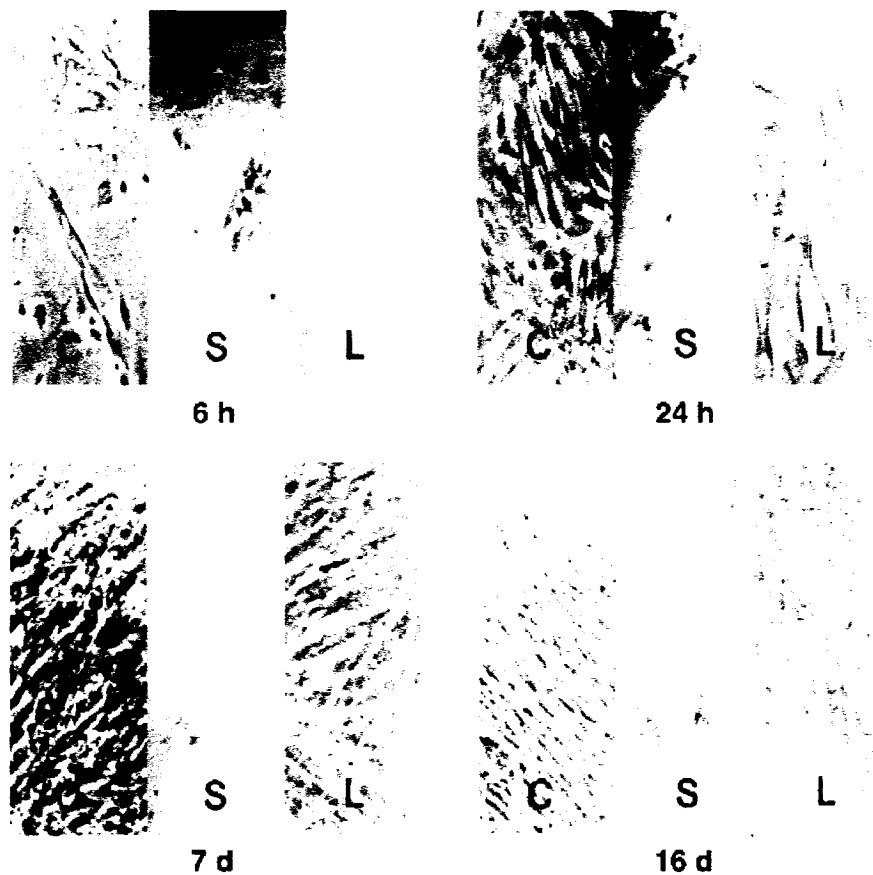


Figure 12. Comparison of human gingival fibroblast adhesion on control (C), soldered (S) and laser welded (L) samples [19].

Their findings indicated that after six and 24 hours there were fewer cells on the laser welded and soldered joints than there were on the control. After seven and 16 days, the laser welded joint showed no difference from the control. Throughout the experiment, fewer elongated cells were present on both the laser welded and soldered joints than were present on the control joint. According to the cell proliferation evaluation, the authors concluded that the cells reacted to the laser welded joint in a manner similar to the reaction with the control joint. This further justifies a hypothesis that laser welding does not have an adverse effect on the biocompatibility of biomedical devices.

The goal of the study conducted by Solmi et al. was to determine the effect of laser welding and soldering of dental prosthesis on interdental gingival papillae. The authors did not intend to measure the effect on the cells by varying the welding or soldering parameters; therefore, the welding and soldering procedure was not discussed in detail. It was also not stated why the welds that were studied were chosen for the experiment. A useful addition to the paper that would complete the study would be a characterization of the weld in order to determine if the weld was acceptable for the application, or if it were merely acceptable for the study.

2.6 Summary of Literature Search

Procedural development and laser welding techniques are two of the more frequently studied areas of laser welding as further knowledge is needed of parameter interactions and parameter effects on the weld dimensions and strength. The studies that were reviewed here provide the methods for process development currently used in research to analyze these interactions. Once a process has been developed for use, it is common to measure the weld strength and microhardness of the microstructure to determine the mechanical properties of the weldment. The least reported topic related to laser welding to date is the biocompatibility of laser welds. The paper detailing the study of the biocompatibility of lingual arches provides a good example of how to perform one type of biocompatibility study. Even though the study was limited to interdental gingival papillae, the procedure is still useful for this study. It also provides a justification for the need for further research. There still has not been a published article that characterizes the weld and the effects on biocompatibility. Since laser welding is quickly becoming a

more accepted process in the biomedical industry, further investigation is needed to determine the effects of laser welding process parameters on biocompatibility for applications in biomedical devices.

CHAPTER 3

RESEARCH OBJECTIVES

With increased application of laser welding within the biomedical industry, there exists a need to understand the effect of laser welding on the biocompatibility of the weldments. Currently, there is a deficiency of reported research, in the open literature, that investigated the changes to the biocompatibility of materials following laser welding. Therefore, the primary objective of this study was to determine the effect of laser welding and the weld parameters on the weldment microstructure, fracture strength, and biocompatibility of Ti-6Al-4V, a material that is widely used in the medical device industry. The biocompatibility of the weldments was assessed by in vitro cytotoxicity testing.

In addition to the primary objective, there were three secondary objectives to this study:

1. Qualitative and quantitative assessments of the changes within the microstructures of the welds,
2. Determination of the strength of the weldments as a function of welding process parameters, and
3. Examination of the changes of the surface chemistry of the welds with respect to the base material.

In order to attain the primary and secondary objectives, the experimental procedures and analyses shown in Figure 13, and described in Chapter 4, were carried out.

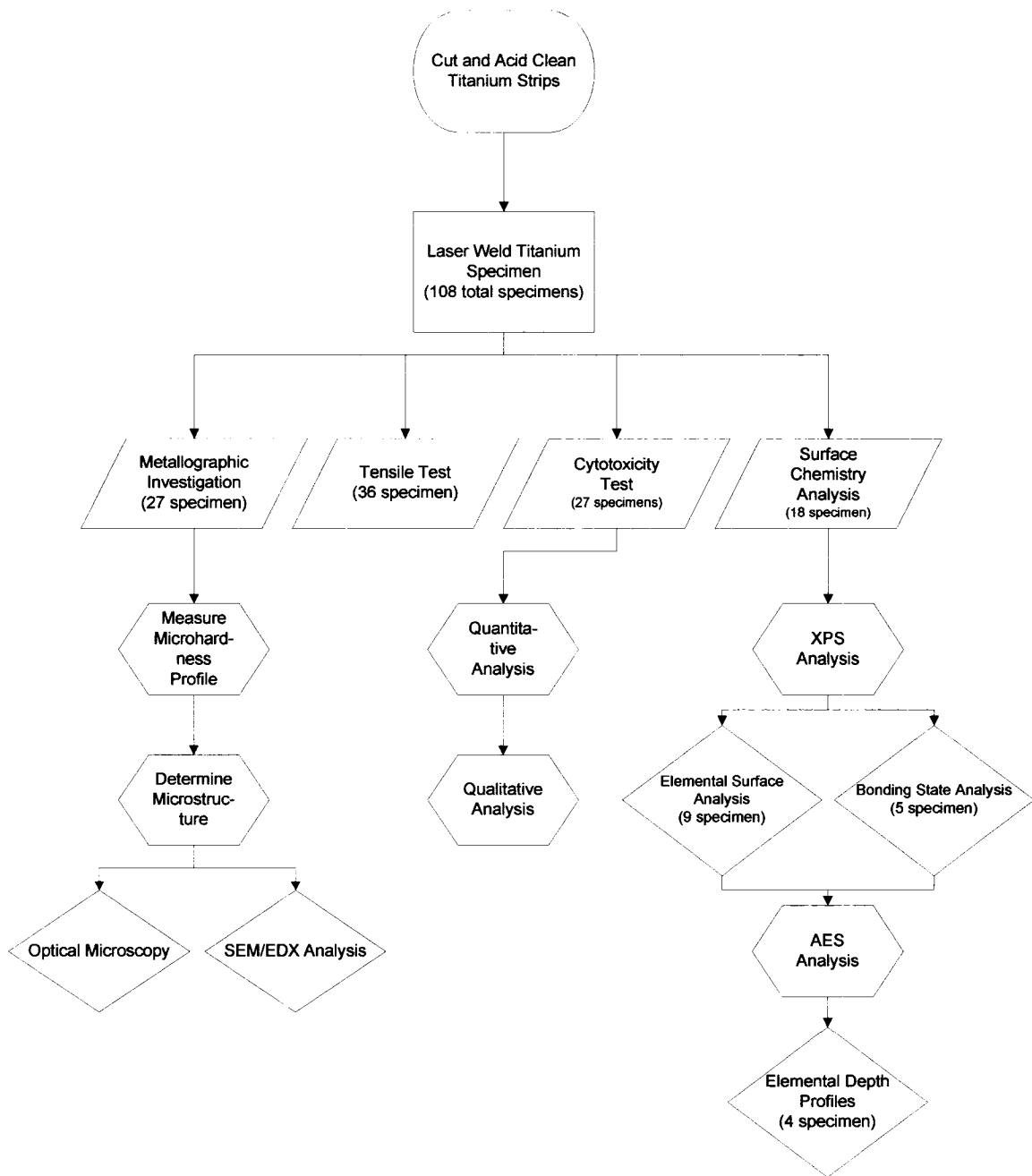


Figure 13. Flow chart of the experimental approach carried out during this research.

CHAPTER 4

EXPERIMENTAL METHODOLOGY

The research approach consisted of experiments and analyses, including laser welding, metallographic investigation, microhardness measurements, tensile testing, x-ray photoelectron spectroscopy (XPS), auger electron spectroscopy (AES), and biocompatibility of the welded and base material.

4.1 Materials

The alloy studied was grade 5 titanium (Ti-6Al-4V). This alloy was selected based on its past and current use in biomedical applications [20]. The alpha-beta titanium alloy contains 6% aluminum and 4% vanadium. The addition of aluminum in the alloy promotes formation of alpha titanium, which consists of a hexagonal close packed crystal structure. Vanadium additions stabilize beta titanium, consisting of a body centered cubic crystal structure. It is reputed to have excellent corrosion resistance and is the most widely used titanium alloy [21]. The material was obtained from Timet in sheet form with a thickness of 0.020-inches. The sheet was cut into specimens that measured 0.5-inches by 1.5-inches, as shown in Figure 14.

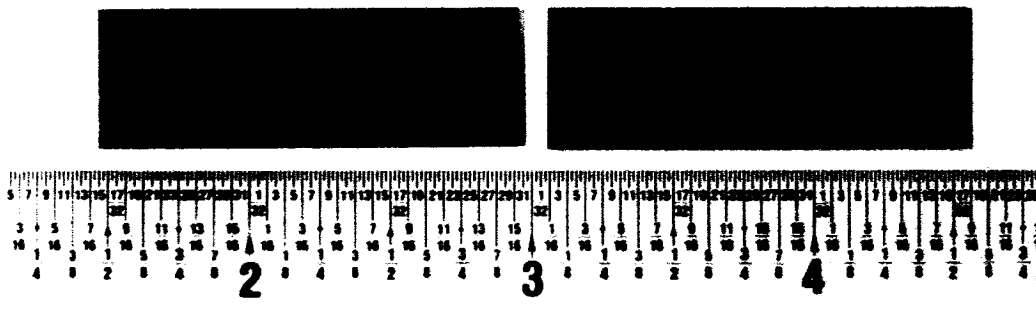


Figure 14. Titanium specimens prior to welding.

4.2 Laser Welding

Two strips were laser welded together to produce homogeneous butt welds. In order to keep the strips well aligned and in intimate contact during welding, the strips were clamped into a fixture during welding. The fixture was fabricated from aluminum 6061-T6, and contained cap screws to ensure intimate contact during welding. A trough was machined into the fixture where the welds were to be created in order to allow for weld clearance and thermal isolation. The fixture with mounted specimens is shown in Figure 15. The fixture was rigidly mounted on a CNC table to provide mobility in both the x-axis and y-axis.



Figure 15. Laser welding fixture.

A pulsed neodymium-yttrium-aluminum-garnet (Nd:YAG) laser was utilized to create a continuous seam weld. The Nd:YAG laser operated at a wavelength of 1064 nanometer. The specimens were enclosed in a glove box that contained an argon

atmosphere during welding. The oxygen level during welding was below 1.0 part per million. The laser beam was delivered to the specimen surface by way of a fiber optic, which provided a 300 to 400 micron diameter beam to the specimen surface.

4.3. Welding Parameters

This study was restricted to the three parameters that were previously determined to have a significant influence on the weld properties [12, 13, 14, 15]. The three welding parameters that were varied were pulse power, pulse duration, and pulse frequency. In order to efficiently examine the effects of varying these parameters, a partial factorial experimental design with three levels for each parameter was utilized. The experimental design and parametric values for each level are shown in Tables 2 and 3, respectively. The values for the high, medium, and low levels were based on exploratory work where the welding parameters were varied, and the depth of penetration of bead-on-plate welds was monitored. The values identified in Table 3 equate to weld penetrations of 0.015-inches for the high values, 0.010-inches for the medium values, and 0.005-inches for the low levels, respectively.

Table 2. Factorial experimental design matrix for the laser welding parameters.

Weld Set	Pulse Power	Pulse Duration	Pulse Frequency
1	–	–	–
2	–	○	○
3	–	+	+
4	○	–	○
5	○	○	+
6	○	+	–
7	+	–	+
8	+	○	–
9	+	+	○

Table 3. Parametric values for both levels of interest.

Material	Level	Pulse Power	Pulse Duration	Pulse Frequency
Ti-6Al-4V	+	52 W	2.0 msec	40 Hz
	○	35 W	1.5 msec	30 Hz
	–	20 W	1.0 msec	20 Hz

4.4 Metallography

Metallographic investigation was conducted on each specimen in the experimental design matrix in accordance with America Society for Testing Materials (ASTM) E3. The welded specimens were cross-sectioned transverse to the weld. The cross sections were mounted in epoxy resin, ground, and polished to create a smooth, flat surface. The grinding and polishing process ranged from 60 grit sandpaper to 0.02 μm colloidal silica. To enhance the features of the microstructure, the polished specimens were etched using Kroll's reagent followed by an alpha etchant to reveal the microstructure and segregation of alpha grains from the beta grains within the microstructure of the weld [22]. The microstructures of three welds were analyzed for each weld set in order to identify any anomalies.

The structure and local chemical composition of the welded specimen was also analyzed. Micro x-ray diffraction ($\mu\text{-XRD}$) was used to determine the crystal structure of the base material, heat affected zone, and fusion zone of the weld. The work was performed using a Bruker AXS microdiffractometer with copper radiation, an incident beam monochromator, and a GADDS multiwire area detector for the wide angle tests. Two detector frames were collected, one at $2\theta = 40$, and one at 70 to cover a range of 25 to 85 degrees two-theta. Each frame was collected for 1800 seconds. The data were then

integrated with a step size of 0.04 degrees two-theta and plotted 2θ as a function of intensity. The data were analyzed using Material Data Incorporated's JADE 7.0 software.

Scanning electron microscopy (SEM) with energy dispersive spectroscopy (EDS) was used to determine the localized elemental chemical composition of the base material, heat affected zone, and fusion zone of the weld. The SEM data were captured using an FEI Quanta 400 SEM with an acceleration voltage of 20 keV. The EDS data were captured using an Oxford Instruments INCA EDS microanalysis system, with a take off angle of 35°.

4.5 Microhardness

Following metallographic investigation, a microhardness profile was developed for the cross section of each weld specimen. The microhardness measurements were conducted using a 25 gram load and Knoop indenter on a Leco DM-400 Hardness Tester with a 12 second hold time. The measurements were recorded in accordance with ASTM E384. A profile was taken from the base material on one side of the weld, across the entire weld, and through to the base material on the other side of the weld. Since the depth of penetration varied between each weld set, the microhardness profiles were conducted at a depth of half the depth of penetration for each weld specimen. The spacing of the microhardness readings was 0.002-inches in order to accurately characterize the change in hardness among the base material, heat affected zone, and fusion zone. A microhardness profile was created on three identical specimens for each

weld set, and combined on a single plot in order to identify any trends in the microhardness across the welds.

4.6 Tensile Test

Tensile testing, conforming to ASTM E8, was conducted in order to determine the strength of the weld, which was determined by applying a tensile load transverse to the weld, as shown in Figure 16. Each tensile specimen was machined into a dogbone shape in order to eliminate potential premature failure due to stress intensity at the edge of an incomplete weld. The tensile load was applied at a strain rate of 0.1 inches per minute until failure. The fracture strength of the welds was calculated by dividing the peak load by the overall thickness of the weldment and by the depth of penetration of the weld. Four specimens were tested to determine the peak load for each parametric set. The test was conducted using an Instron tensile test machine. The data from each replication in the tensile test were averaged. The averages for each specimen were statistically compared to determine if a significant difference existed between the specimens due to the processing parameters.

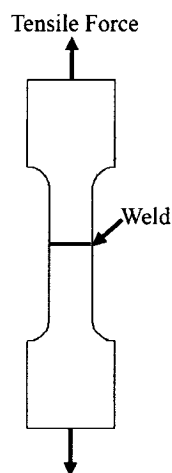


Figure 16. Schematic of tensile testing set-up.

4.7 Cytotoxicity Test

Biocompatibility testing was conducted to determine if laser welding altered the chemistry of the surface of the weld, thus affecting the biocompatibility of the material. In vitro cytotoxicity testing, as defined by ISO 10993-5 [24], was used to determine the toxicity of the welded material to living cells. In order to evaluate the cytotoxicity of each weld, HEP-2 cells were incubated at 37°C with 5% carbon dioxide in titer wells. After the cells reached subconfluency, the specimens were sterilized in an autoclave and introduced into the titer wells with the welds in direct contact with the cells. Weld specimens within titer wells are shown in Figure 17. The cells and specimen were incubated at 37°C with 5% carbon dioxide for 24 hours after the specimens were introduced into the wells. Following the incubation, the cells were evaluated qualitatively using a Nikon Eclipse TS100 inverted microscope at 100 times magnification, and quantitatively using a Coulter Counter. The cytotoxicity testing was performed on three welds from each parametric set. Also included in the cytotoxicity testing were three each of a positive cytotoxicity control consisting of a nickel-coated copper sample, a negative cytotoxicity control consisting of a borosilicate glass slide, and a titanium control that did not contain a weld. For the qualitative analysis, three readings were recorded on each of the three specimens from each sample. The exact protocol used for the cytotoxicity test is contained in Appendix A. Pertinent biological terms are defined in Appendix B.

Due to the distributional nature of the biocompatibility data, a biostatistical analysis was utilized. Mann-Whitney's U test¹, which is a nonparametric test similar to the Student t-test, was used to compare the laser weld data to the control data. Since the controls were selected based on known cytotoxic reactions, the results of the Mann-Whitney U test were used to determine if the welds elicited similar cytotoxic reactions as the control samples to which they were compared.



Figure 17. Weld specimens incubating with HEP-2 cells in titer wells.

4.8 Surface Analysis

X-ray photoelectron spectroscopy (XPS) is a surface sensitive technique that provides chemical compositional data at concentrations on the order of parts per billion. XPS was used to measure the atomic composition of the elements present on the surface of the weld specimens. The bonding states of the titanium, aluminum, vanadium, carbon, and oxygen identified on the surface of the welds were also determined using XPS. One of each weld and one titanium control were analyzed using XPS in order to determine if

¹ The Mann-Whitney U test is used to directly compare the measurements from two samples. Since cell growth does not follow a normal distribution, the nonparametric Mann-Whitney U test must be utilized.

any of the elemental constituents of the microstructure would be measured in higher concentration on the surface of the welds than within the base material. Analysis was conducted on an PHI Quantum 2000 XPS, with a monochromated Al $\kappa\alpha$ source at 1486.6 eV. The acceptance angle was $\pm 23^\circ$, with a take off angle of 45° . The area analyzed was $200\ \mu\text{m}$ in diameter with an analysis depth of approximately 50-100 Å.

Auger electron spectroscopy (AES) is another surface sensitive technique that was utilized during the study. AES was used to perform depth profile analyses on select welds. AES measured the atomic concentration of the elements identified on the surface of the weld specimens with respect to depth into the surface of the specimens. The depth profiles provided confirmation as to whether the elements identified with XPS on the surface of the weld were present within the material, or if they were contaminants from the environment that were deposited on the surface of the weld post welding. The data were captured using an PHI Smart-200 nanoprobe with a cylindrical mirror analyzer, using a 10 keV, 20 nA electron beam. Etching was performed using an Ar^+ ion source at 2 keV and 1 μA at 55° to the sample normal.

CHAPTER 5

RESULTS

Overall, the weld parameters were found to affect the physical characteristics and fracture strength of the welds. However, there was no effect on the biocompatibility of the welds, based on cytotoxicity tests. The physical characteristics of the weld, namely the weld width at half the depth of penetration and the width of the heat affected zone, were found to be affected by the weld parameters, with the primary determinant being the total energy input. The microstructure, chemical composition, and crystal structure of both the heat affected zone and fusion zone, however, were not dependent on the processing parameters. The microhardness was reliant on the welds microstructure, while the fracture strength was influenced by the physical characteristics of the welds. The biocompatibility of the welds, as measured by cytotoxicity testing, was impartial to the processing parameters; all specimens were found to be biocompatible. The chemical composition of the surface of the welds was not related to the processing parameters. These results are described in greater detail in the following sections.

5.1 Metallography Results

The microstructure of the Ti-6Al-4V base material can be seen in Figure 18. The microstructure consists of primary α titanium with dispersed intergranular β titanium. These constituents are labeled within Figure 18. The grains are slightly elongated in the horizontal direction, with some equiaxed grains dispersed throughout.

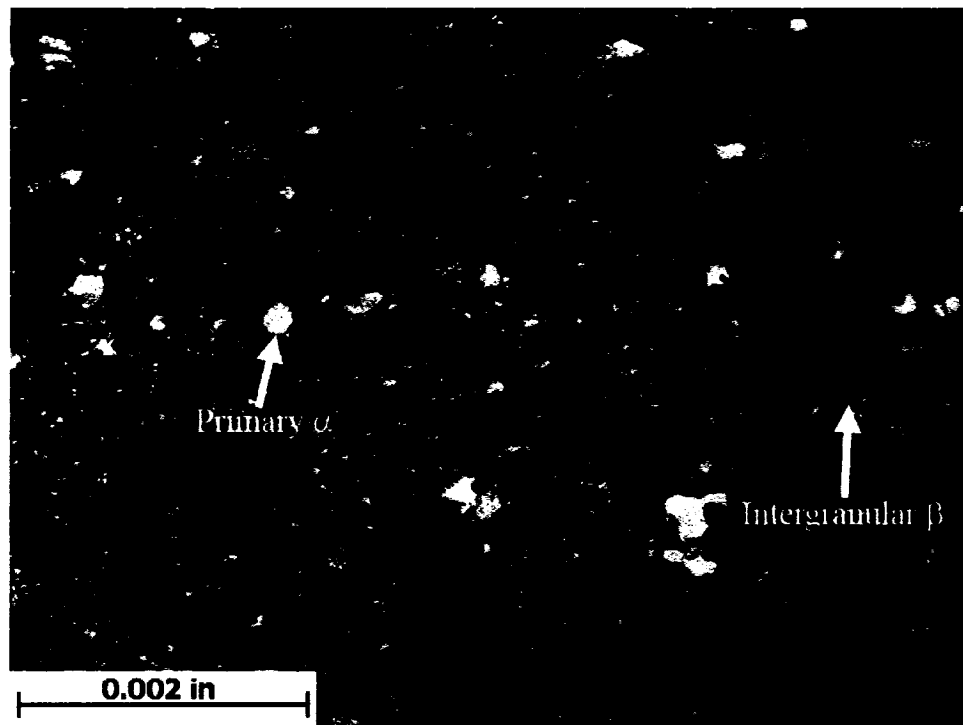


Figure 18. Microstructure of the base material (500X).

The microstructures of the welds are shown in Figures 19 through 36. For each specimen, an overview of the microstructure of the entire weld is first shown at 100X magnification, and then followed by a high magnification view of the microstructure at the boundary of the fusion zone and heat affected zone at 500X magnification. Within the overview of the welds, the heat affected zone is found surrounding the fusion zone.

The overview of the microstructure of the weld 1 specimen is shown in Figure 19. Since the base material of the specimen was unaffected during welding, it is identical to the microstructure of the base material shown in Figure 18, and also consists of primary α titanium with intergranular β titanium. A detailed image of the fusion zone and heat affected zone for the weld 1 specimen is shown in Figure 20. The fusion zone consists of

martensitic α' titanium, while the heat affected zone consists of martensitic α' titanium, primary α titanium, and intergranular β titanium.

The overview and high magnification view of the microstructure for welds 2 through 9 are contained in Figures 21 through 36. Each of the welds contained the same microstructural constituents as were identified in weld 1. The relative amounts of the constituents within the heat affected zone varied from weld to weld, but no correlations could be identified.

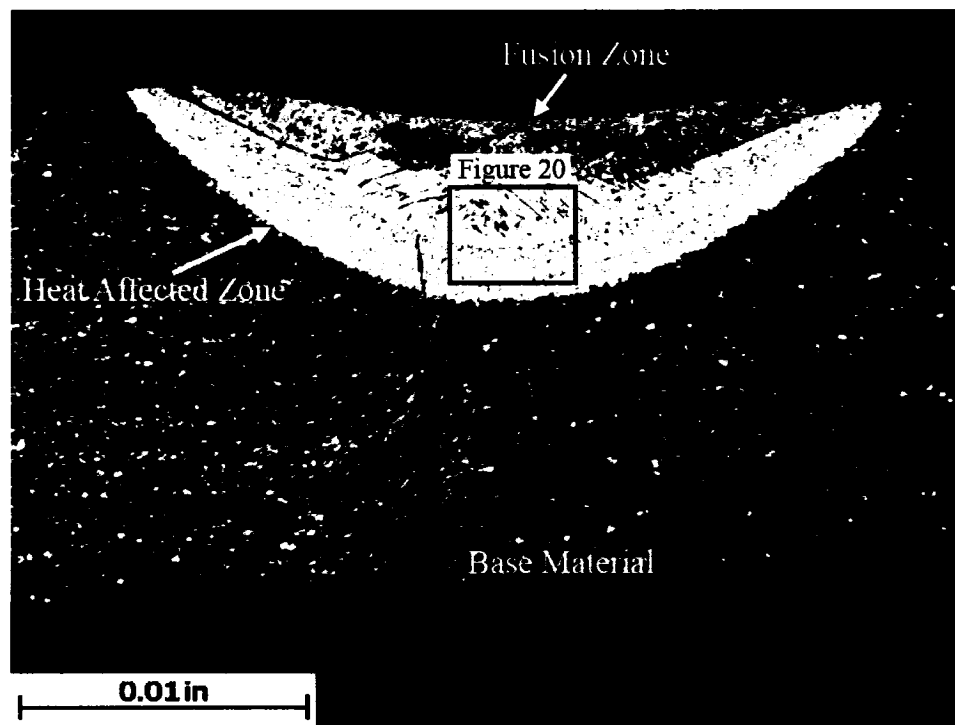


Figure 19. Overview of the microstructure of weld 1 (100X).

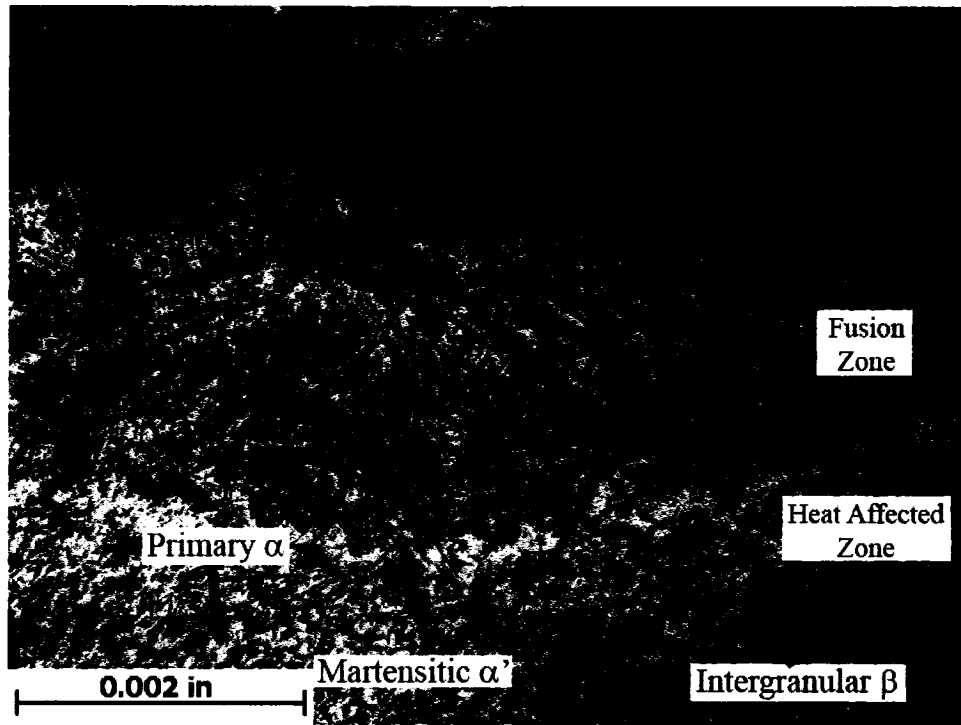


Figure 20. Microstructure of the fusion zone and heat affected zone of weld 1 (500X).

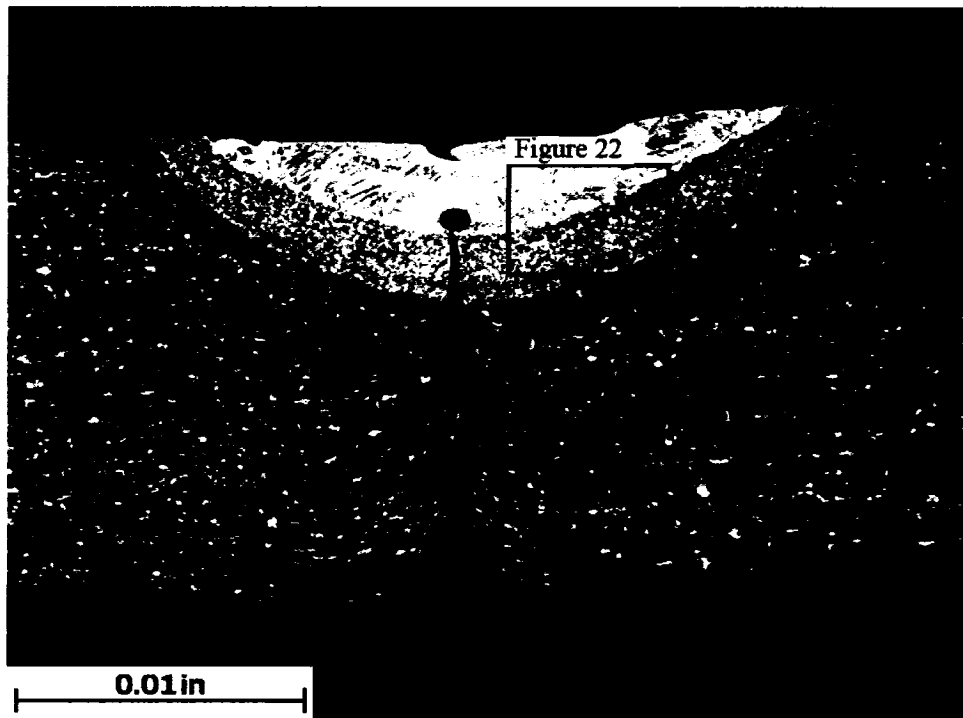


Figure 21. Overview of the microstructure of weld 2 (100X).

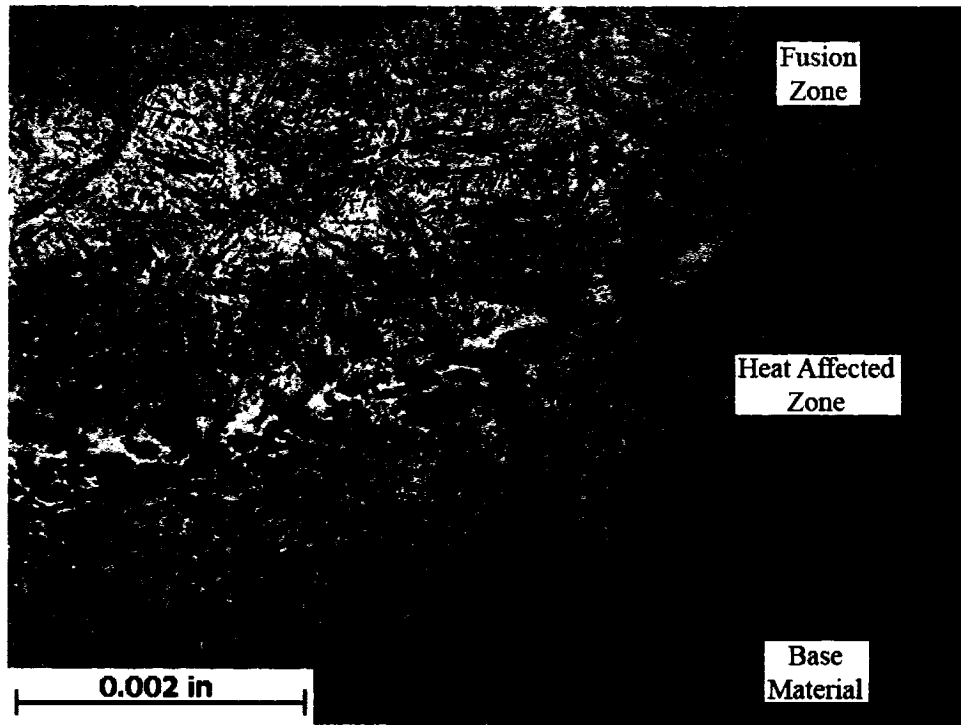


Figure 22. Microstructure of the fusion zone and heat affected zone of weld 2 (500X).

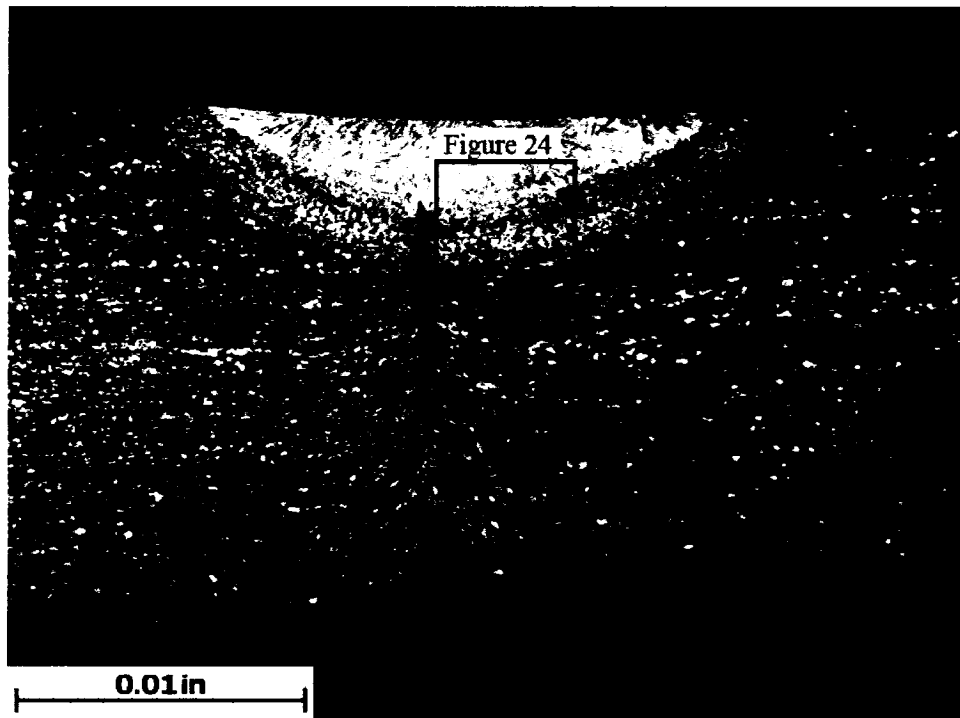


Figure 23. Overview of the microstructure of weld 3 (100X).

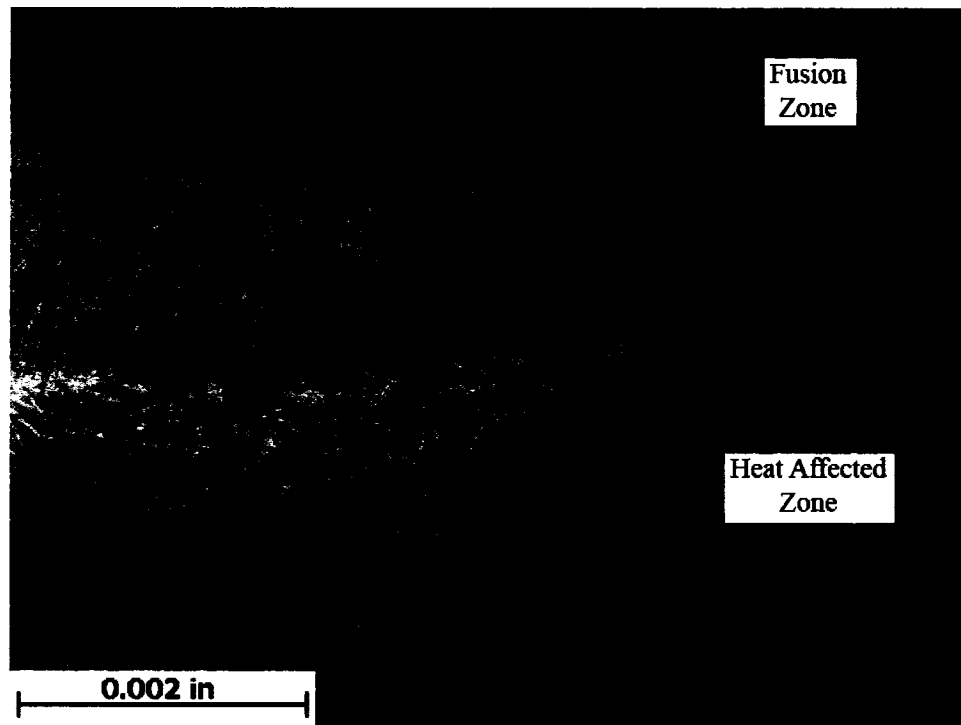


Figure 24. Microstructure of the fusion zone and heat affected zone of weld 3 (500X).

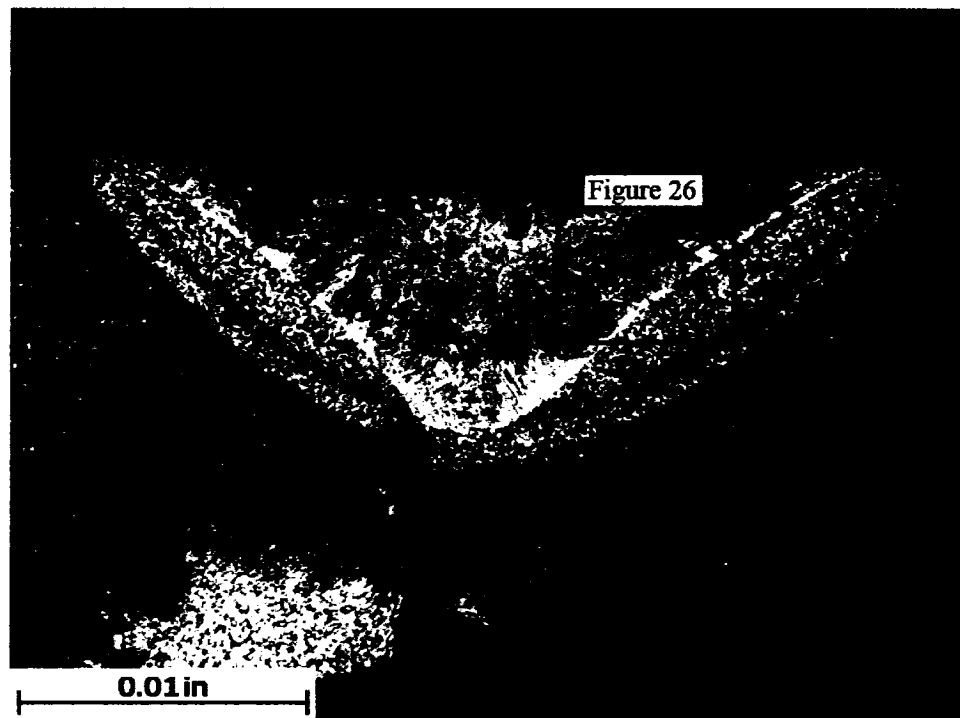


Figure 25. Overview of the microstructure of weld 4 (100X).

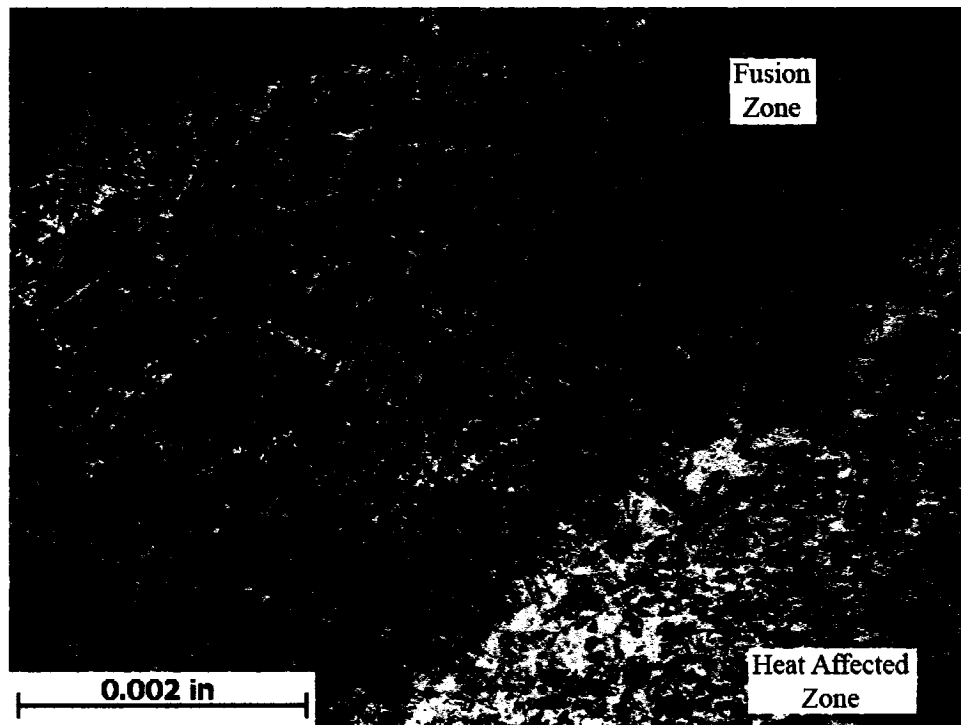


Figure 26. Microstructure of the fusion zone and heat affected zone of weld 4 (500X).

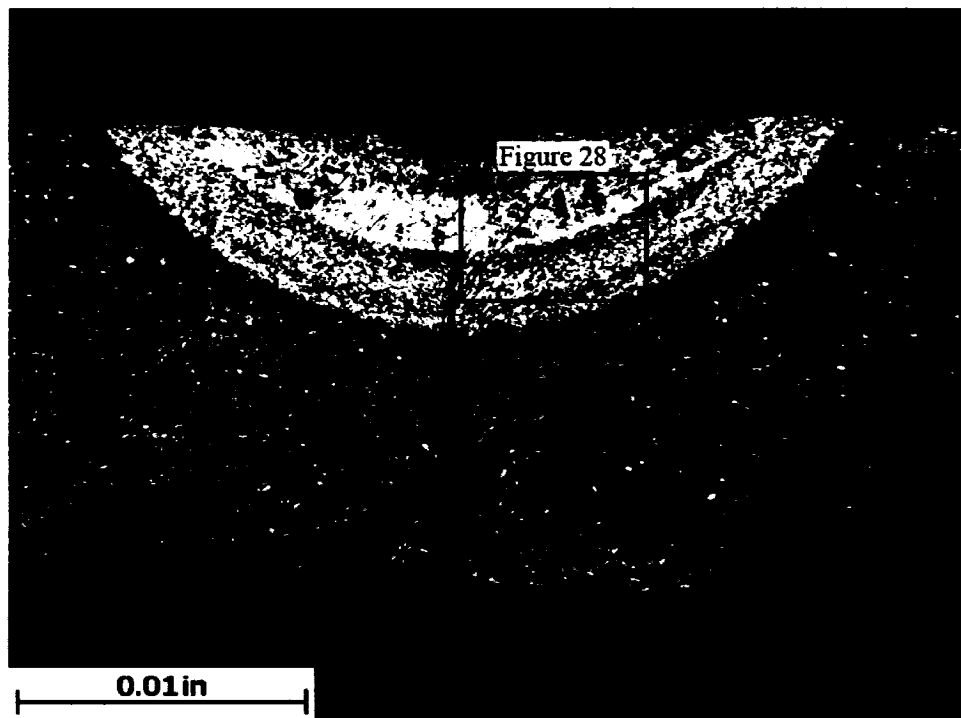


Figure 27. Overview of the microstructure of weld 5 (100X).

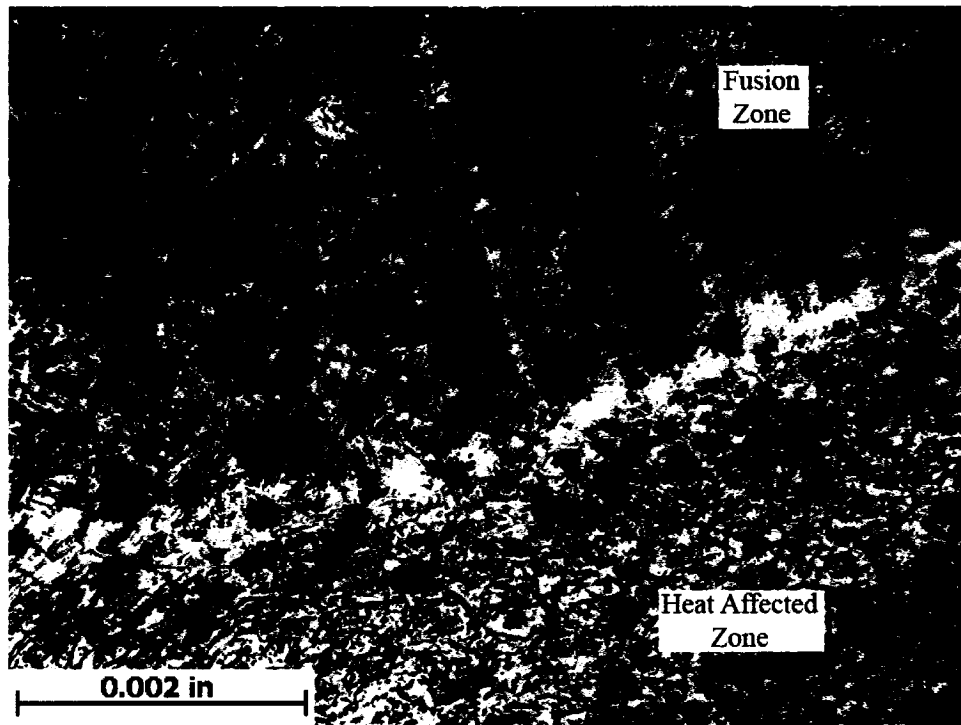


Figure 28. Microstructure of the fusion zone and heat affected zone of weld 5 (500X).

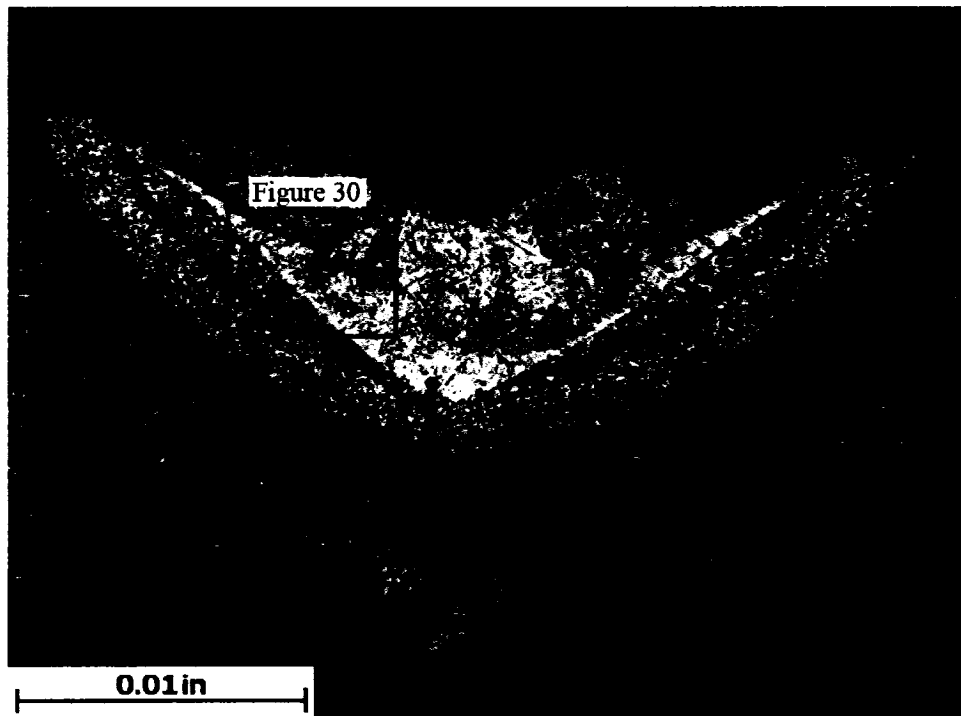


Figure 29. Overview of the microstructure of weld 6 (100X).

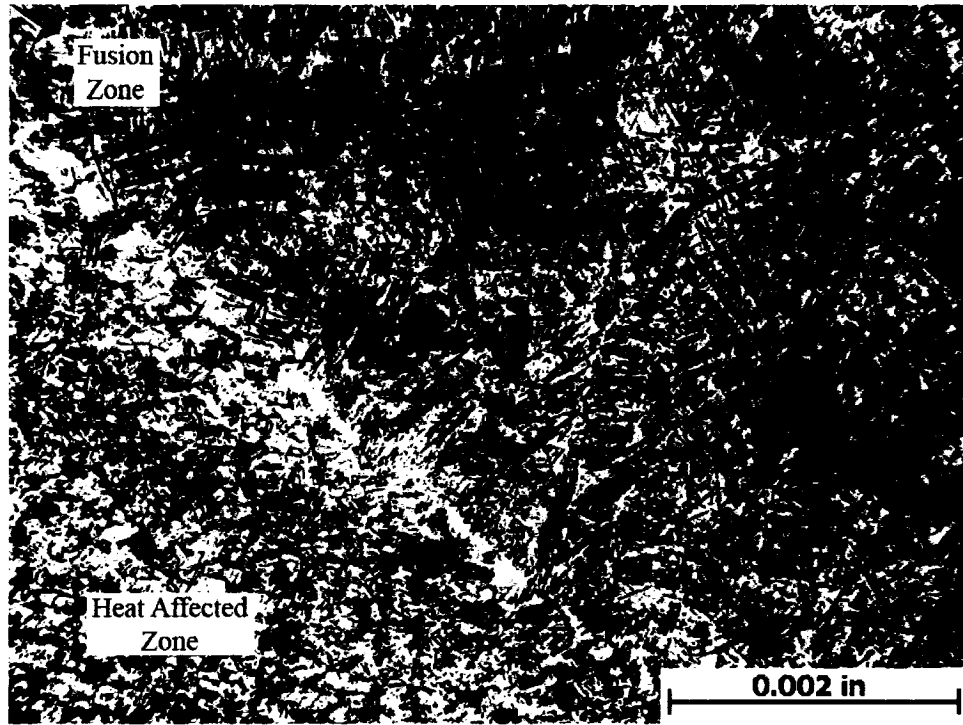


Figure 30. Microstructure of the fusion zone and heat affected zone of weld 6 (500X).

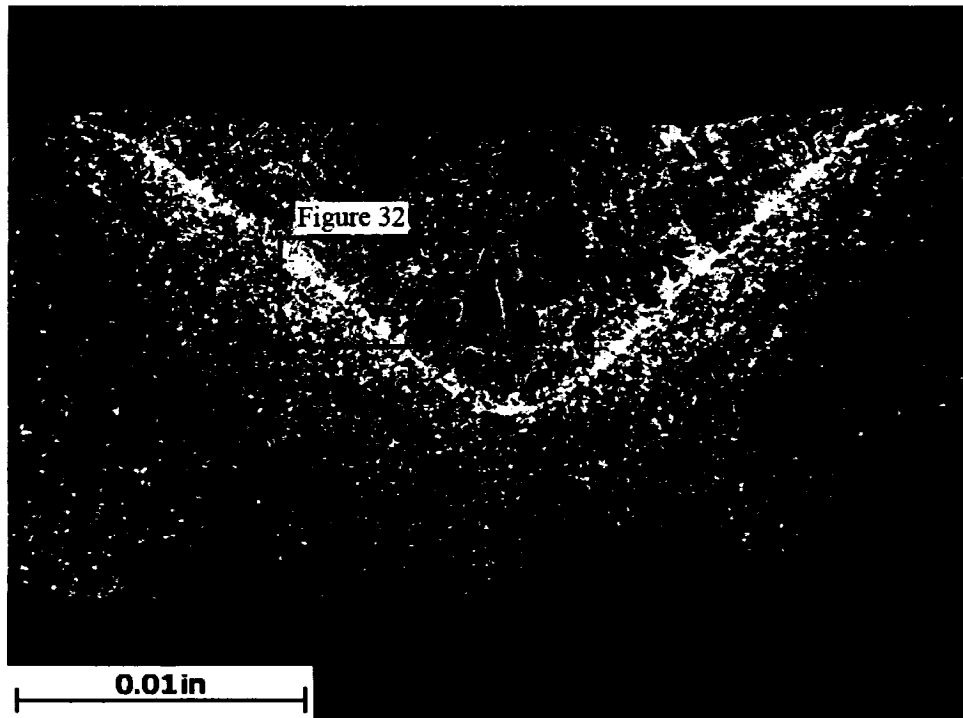


Figure 31. Overview of the microstructure of weld 7 (100X).

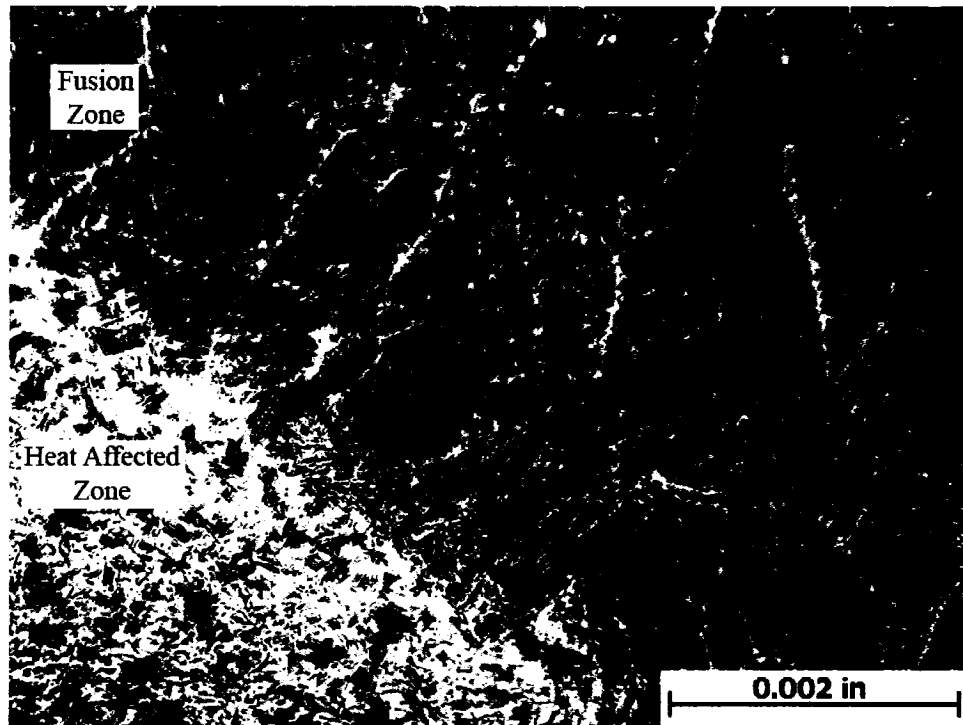


Figure 32. Microstructure of the fusion zone and heat affected zone of weld 7 (500X).

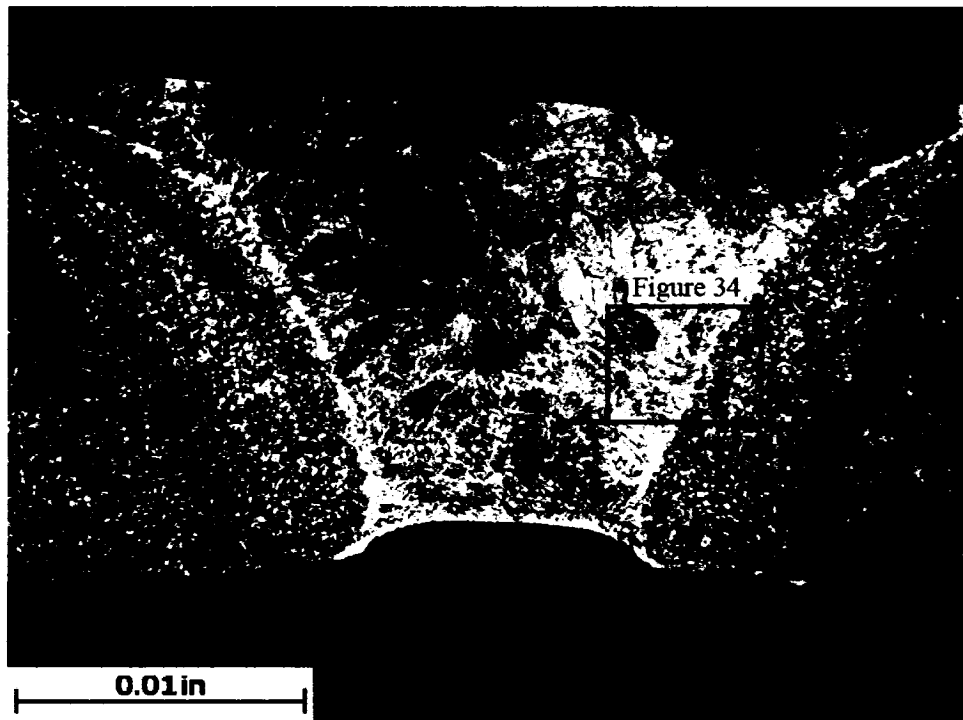


Figure 33. Overview of the microstructure of weld 8 (100X).

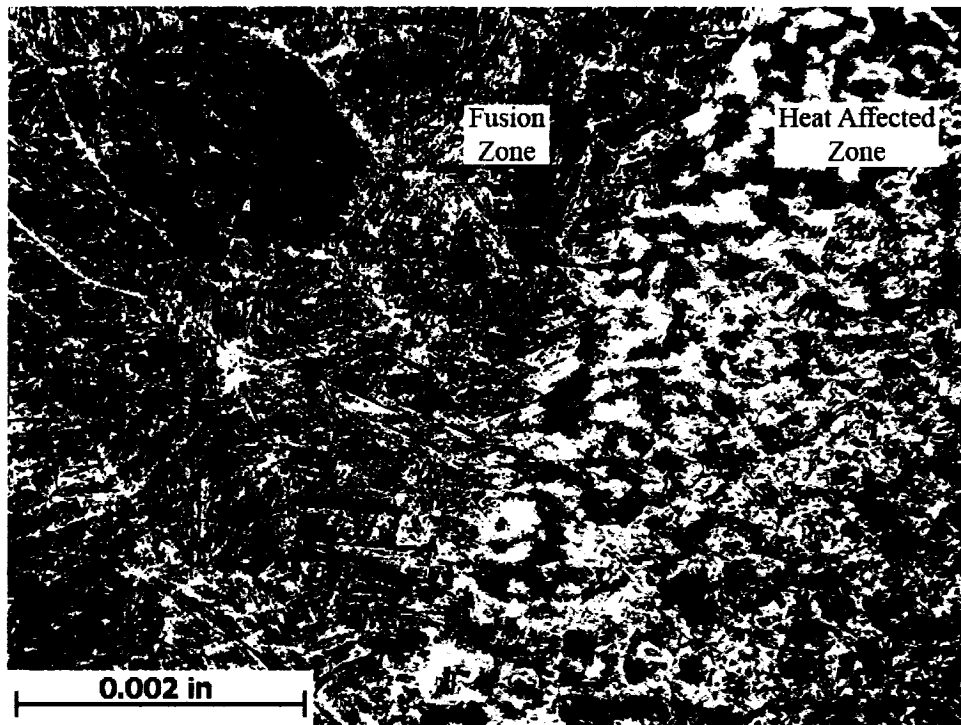


Figure 34. Microstructure of the fusion zone and heat affected zone of weld 8 (500X).



Figure 35. Overview of the microstructure of weld 9 (100X).

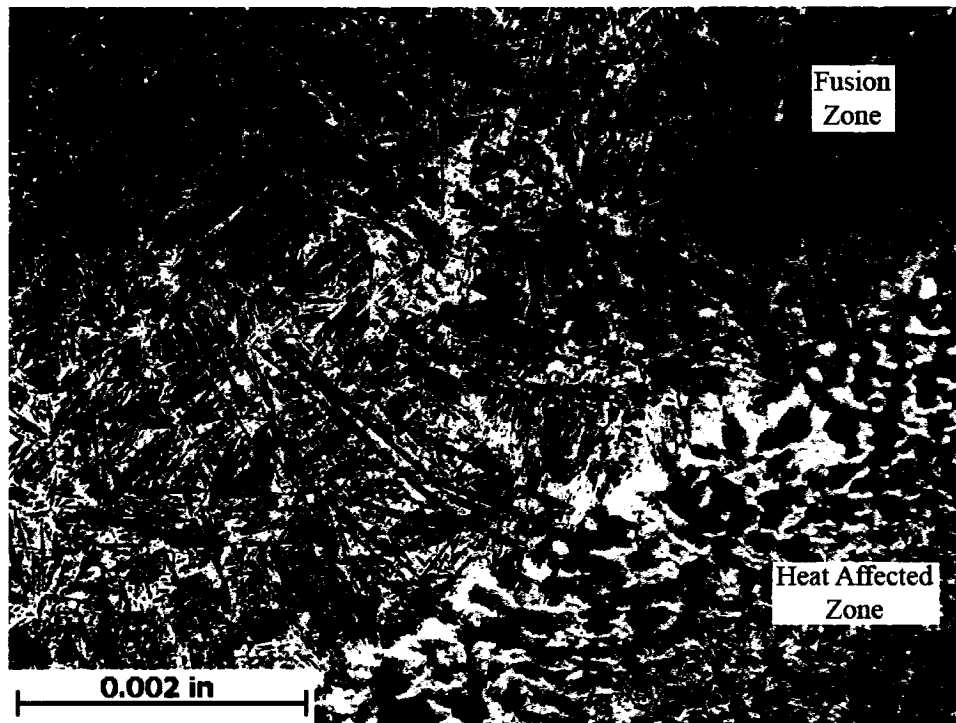


Figure 36. Microstructure of the fusion zone and heat affected zone of weld 9 (500X).

The formation of the microstructures of the welds was dependent on the cooling rate during solidification. When Ti-6Al-4V is cooled from above 966°C, which is the beta transus, the cooling rate through the transus determines the fineness of the transformed microstructure. For Ti-6Al-4V, water quenching provides sufficiently rapid cooling to promote the formation of martensitic α' titanium [23]. The rapid cooling rate of the fusion zone of laser welds, which is significantly higher than the cooling rate of water quenching, promotes the formation of martensitic α' titanium. Therefore, the microstructure of the welds is affected by the cooling rate, which is independent of the processing parameters used during welding.

5.1.1 Physical Characteristics of the Weld Specimens

The physical dimensions of the weld bead in each specimen, for all of the welds, were characterized. They include the depth of penetration, the weld width at the base material surface, the weld width at half penetration, and the width of the heat affected zone at half penetration. These dimensions are shown schematically in Figure 37. The averaged measurements from three specimens for each weld set are tabulated in Table 4. Also included in Table 4 is the peak pulse energy observed by each weld.

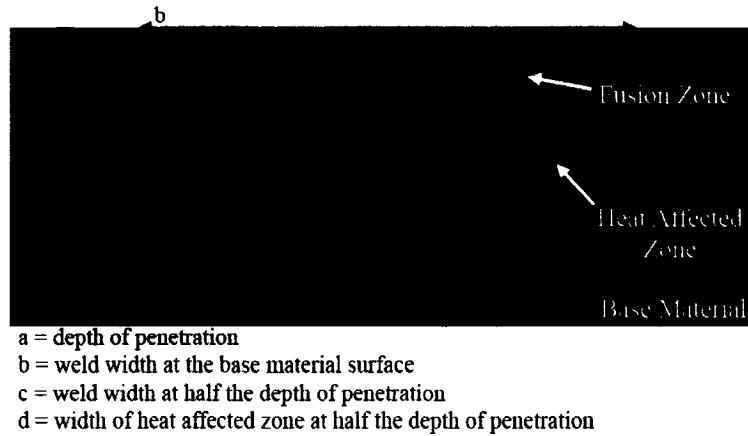


Figure 37. Schematic of a weld indicating locations of measurements.

Table 4. Physical dimensions of the welds.

	Peak Pulse Energy (Joules)	Depth of Penetration (in)	Weld Width at Surface (in)	Weld Width at Half Penetration (in)	Heat Affected Zone Width (in)
Weld 1	0.020	0.005	0.024	0.013	0.002
Weld 2	0.030	0.004	0.020	0.014	0.002
Weld 3	0.040	0.003	0.018	0.013	0.002
Weld 4	0.035	0.010	0.026	0.014	0.003
Weld 5	0.053	0.004	0.022	0.015	0.003
Weld 6	0.070	0.009	0.027	0.015	0.003
Weld 7	0.052	0.011	0.029	0.016	0.003
Weld 8	0.078	0.020	0.035	0.015	0.005
Weld 9	0.104	0.008	0.028	0.018	0.004

The physical characteristics of the welds provides an insight into the amount of energy that was input to the material during welding, as well as an indication of how the parameters interacted to affect the depth of penetration of the weld. The physical dimensions as a function of peak pulse power are plotted in Figure 38. It should be noted that the data from Table 4 were sorted by increasing pulse energy in order to generate the plot in Figure 38. From this plot, it can be seen that the weld width at half the depth of penetration and the width of the heat affected zone were approximately linearly dependent on the peak pulse energy of the laser. The depth of penetration and weld width at the base material surface indicated no relationship to the peak pulse energy of the laser. Therefore, the weld width at half the depth of penetration and the width of the heat affected zone can be approximately calculated using the processing parameters, while the depth of penetration and the weld width at the base materials surface cannot be approximated.

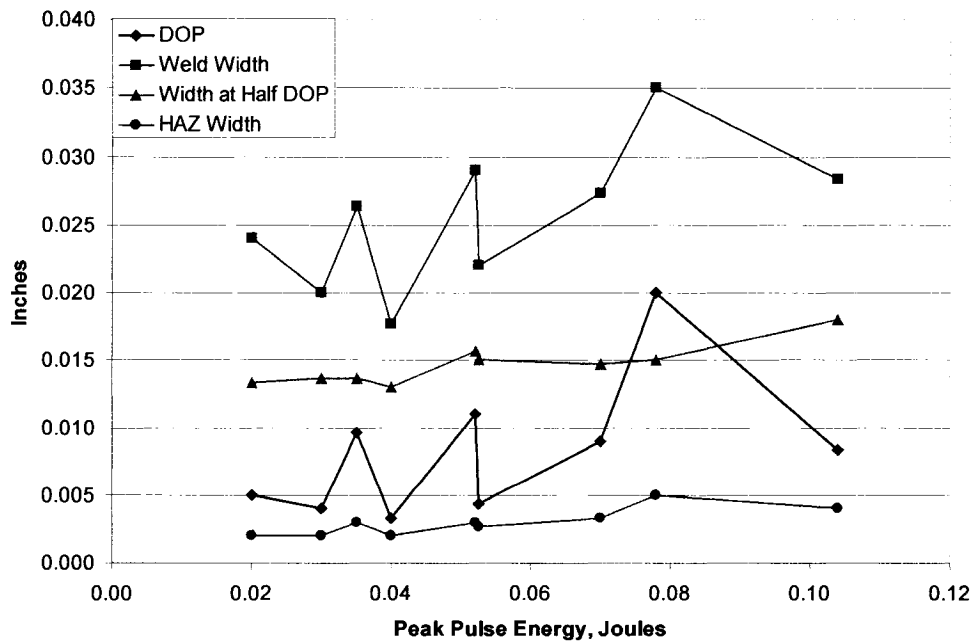


Figure 38. Physical dimensions of the welds as a function of peak pulse energy.

5.1.2 Semi-Quantitative Chemical Analysis of Welds 1 and 6

The base material, heat affected zone, and fusion zone of welds 1 and 6 were analyzed using scanning electron microscopy (SEM) and energy dispersive spectroscopy (EDX). The locations analyzed, along with the related EDX spectra are shown in Figures 39 and 40, respectively. The spectra from the two welds identify only titanium, aluminum, and vanadium within each location of the specimens. The semi-quantitative chemical analysis results from the EDX spectra are shown in Table 5. The data within Table 5 indicate that the chemical composition within the heat affected zone and fusion zone did not change with respect to the chemical composition of the base material. With data from only two welds, the influence of the processing parameters cannot be conclusively determined, however, since the solidification rate for each weld is approximately equal, and since atomic mobility was suppressed during the welding of welds 1 and 6, it is hypothesized that the processing parameters do not affect the chemical composition of the heat affected zone or fusion zone of the welds.

Table 5. Semi-quantitative chemical analysis results for welds 1 and 6.

		Titanium (wt%)	Aluminum (wt%)	Vanadium (wt%)
Literature Values [21]		90.00	6.00	4.00
Weld 1	Base Material	90.16	6.14	3.70
	Heat Affected Zone	89.00	5.95	5.05
	Fusion Zone	90.47	5.00	4.53
Weld 6	Base Material	91.84	5.80	2.36
	Heat Affected Zone	90.22	5.80	3.98
	Fusion Zone	89.99	5.35	4.66

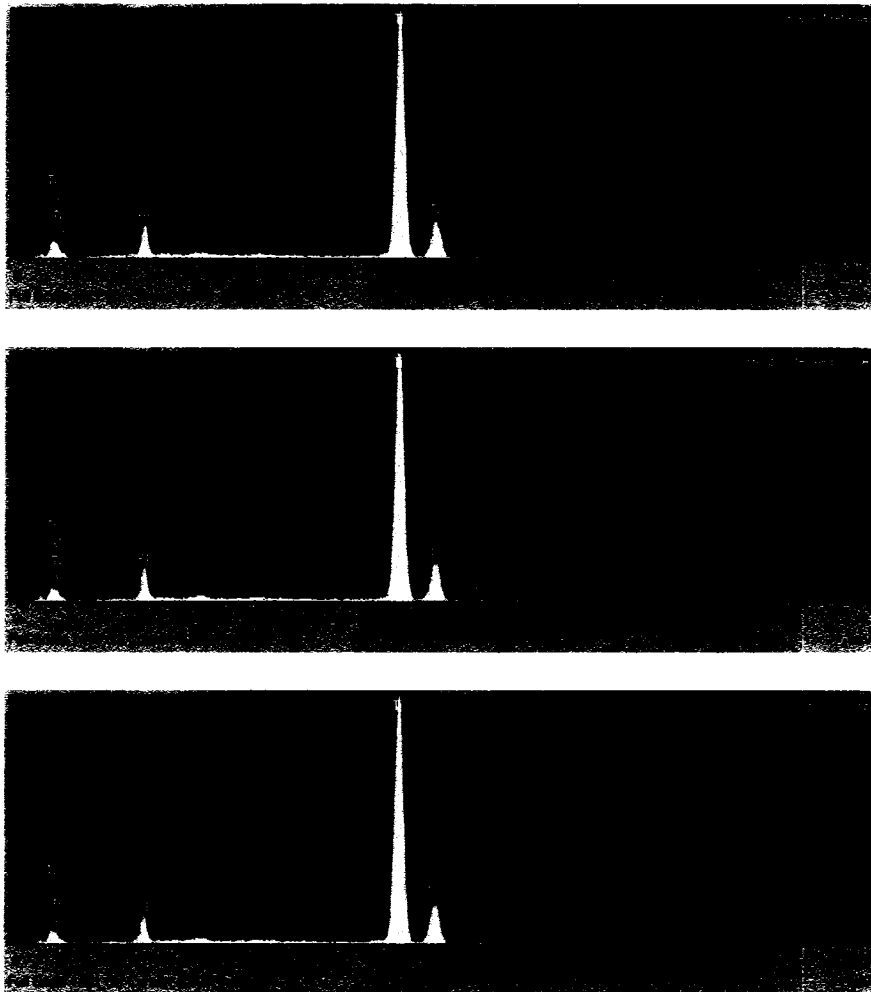


Figure 39. EDX analysis locations and spectra for weld 1.

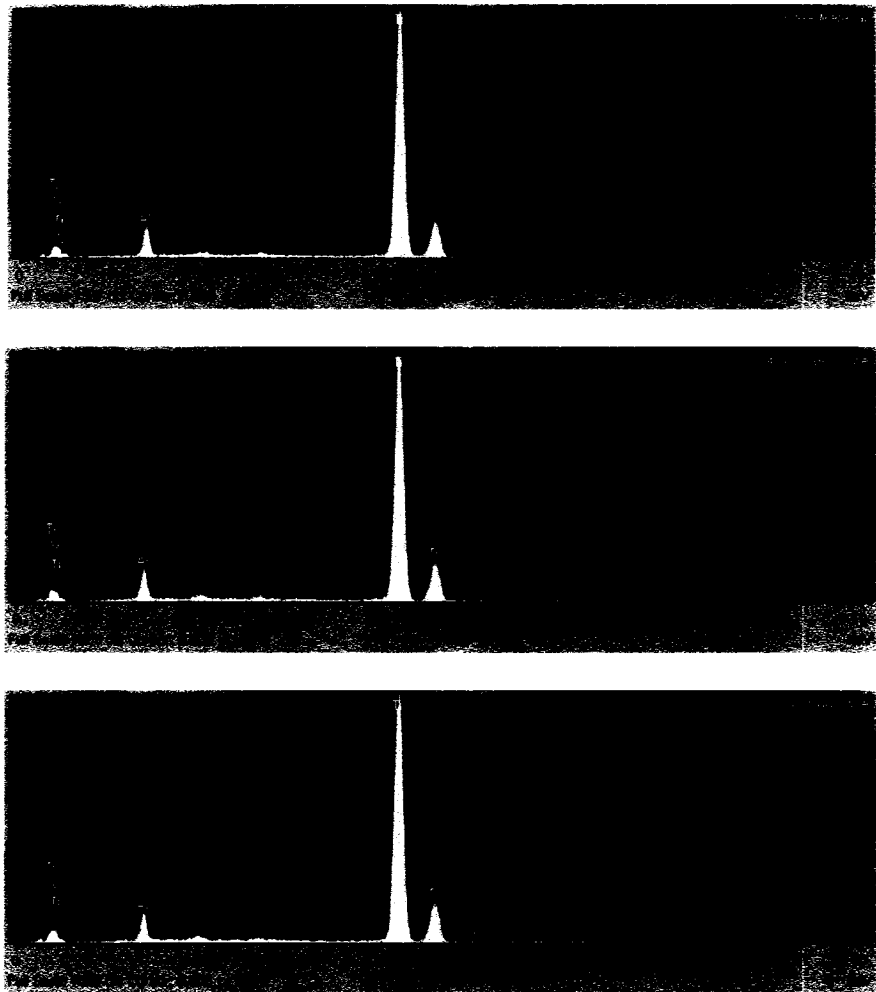
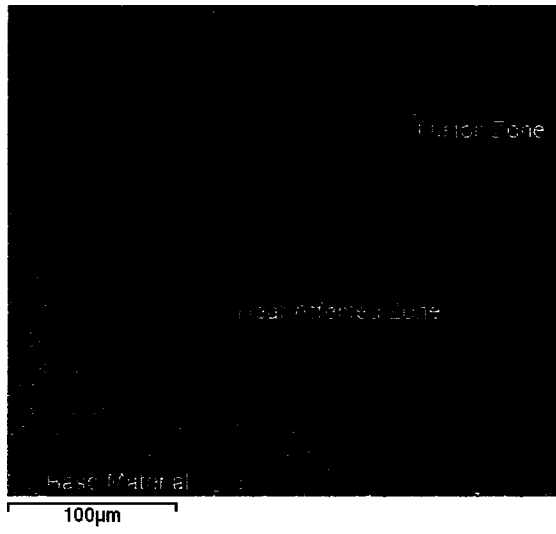


Figure 40. EDX analysis locations and spectra for weld 6.

5.1.3 Micro X-ray Diffraction Analysis of Weld 6

One specimen from weld 6 was submitted for micro x-ray diffraction (μ -XRD) analysis. Three locations were analyzed on the specimen as indicated in Figure 41. Location 1 consisted of the base material, location 2 consisted of the heat affected zone, and location 3 consisted of the fusion zone. The spectra for the three locations are contained in Figure 42, with the detailed results in Appendix C. Within the base material and heat affected zone, two crystal structures were identified. The structures consisted of hexagonal close packed (HCP) crystal structure and body centered cubic (BCC) crystal structure. Within the fusion zone, only the HCP structure was identified. The HCP structure corresponds to α titanium, while the β titanium is composed of the BCC structure. The calculated lattice parameters for each location and structure are presented in Table 6. Within the fusion zone, the formation of β titanium is restricted due to it being unstable below the beta transus and due to the rapid solidification rate during welding. Therefore, as with the microstructure of the welds, the crystal structure is dependent on the cooling rate during weld, and is independent of the processing parameters.

Table 6. Lattice parameters for crystal structures within weld 6.

	HCP Lattice Parameters (Å)		Cubic Lattice Parameter (Å)
	a-Axis	c-Axis	
Location 1	2.9211	4.6809	3.2211
Location 2	2.9193	4.6907	3.2324
Location 3	2.9160	4.6904	-

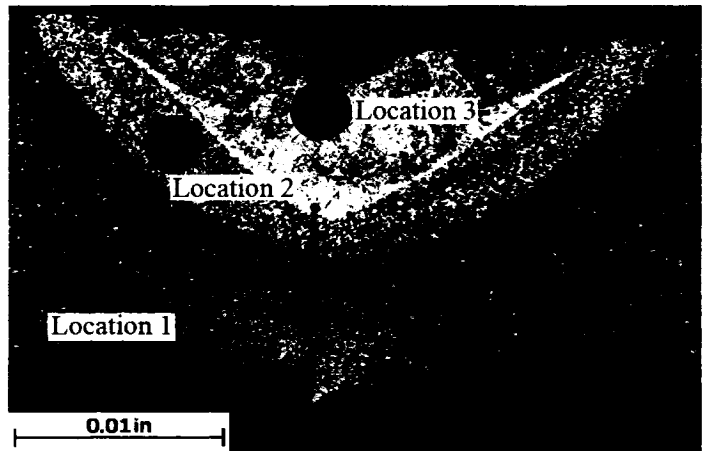


Figure 41. Locations for XRD analysis.

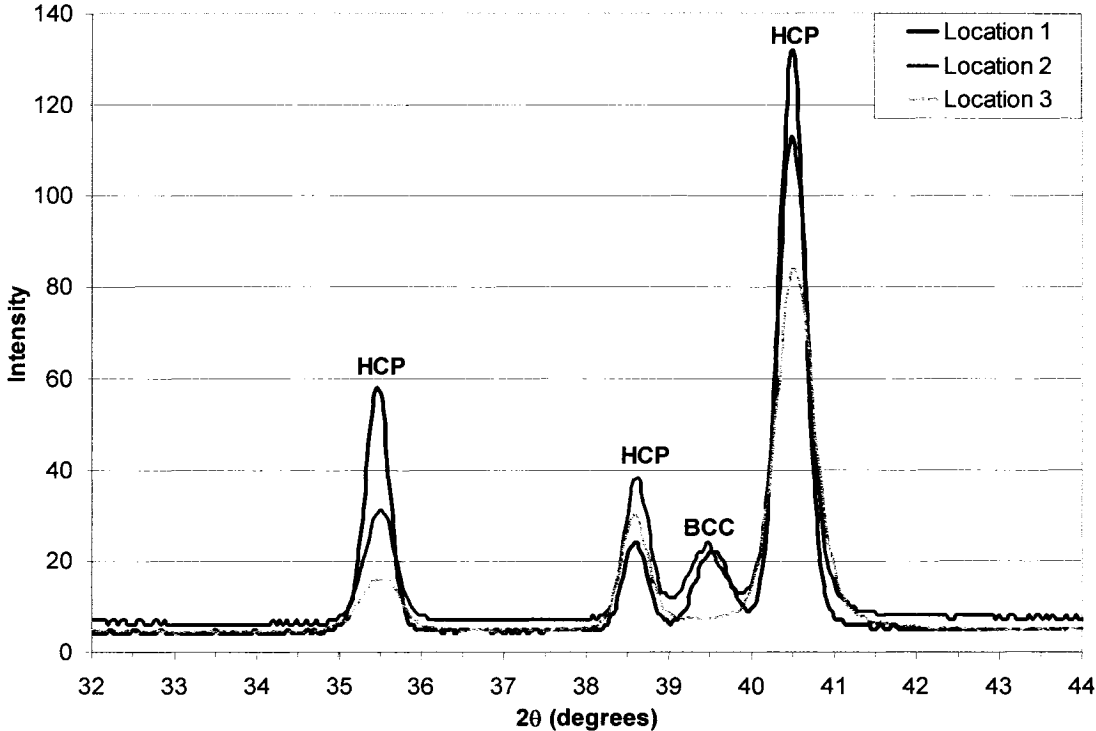


Figure 42. Overlay of XRD spectra. Note the absence of the peak at 39.6° for location 3.

5.2 Microhardness Results

In complement to the qualitative comparison of the microstructure, a profile of the microhardness across the weld provides a quantitative view of the changes in the

microstructure of the material due to welding. The trends obtained from the microhardness analysis for weld sets 1 through 9 are contained in Figures 43 through 51, respectively. The average hardness of the base material, heat affected zone, and fusion zone for each of the nine welds are shown in Table 7. The change in average microhardness from the base material to the heat affected zone, and from the base material to the fusion zone is listed in Table 7 for each weld.

Table 7. Average microhardness results.

Weld	BM (HKN25)	HAZ (HKN25)	FZ (HKN25)	Change from BM to HAZ (HKN25)	Change from BM to FZ (HKN25)
Weld 1	393.3	418.4	383.7	25.1	-9.6
Weld 2	388.7	471.3	454.5	82.6	65.8
Weld 3	392.1	467.7	447.9	75.6	55.8
Weld 4	389.7	491.6	434.2	101.9	44.5
Weld 5	413.7	467.0	478.2	53.3	64.5
Weld 6	371.6	445.3	464.5	73.7	92.9
Weld 7	400.0	434.5	442.8	34.5	42.8
Weld 8	409.4	469.6	491.3	60.2	81.9
Weld 9	400.5	459.6	466.6	59.1	66.1

For all nine of the weld sets, the average microhardness of the heat affected zone was higher than the average microhardness within the base material. For eight of the nine weld sets, an increase in the average microhardness of the fusion zone over the average microhardness within the base material was recorded. The increase in microhardness within both the heat affected zone and the fusion zone can be attributed to the presence of martensitic α' titanium which was formed due to the rapid cooling rate during welding. The microhardness of the weld is not controlled by the welding process parameters used during welding, but rather by the microstructure that is formed, which in turn is controlled by the cooling rate.

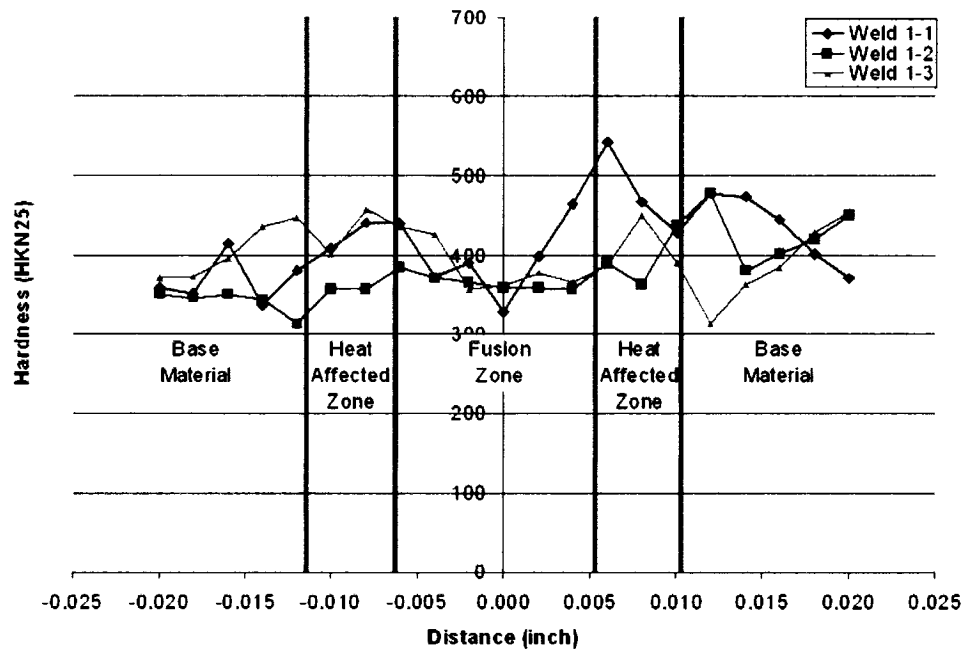


Figure 43. Microhardness plots for weld 1.

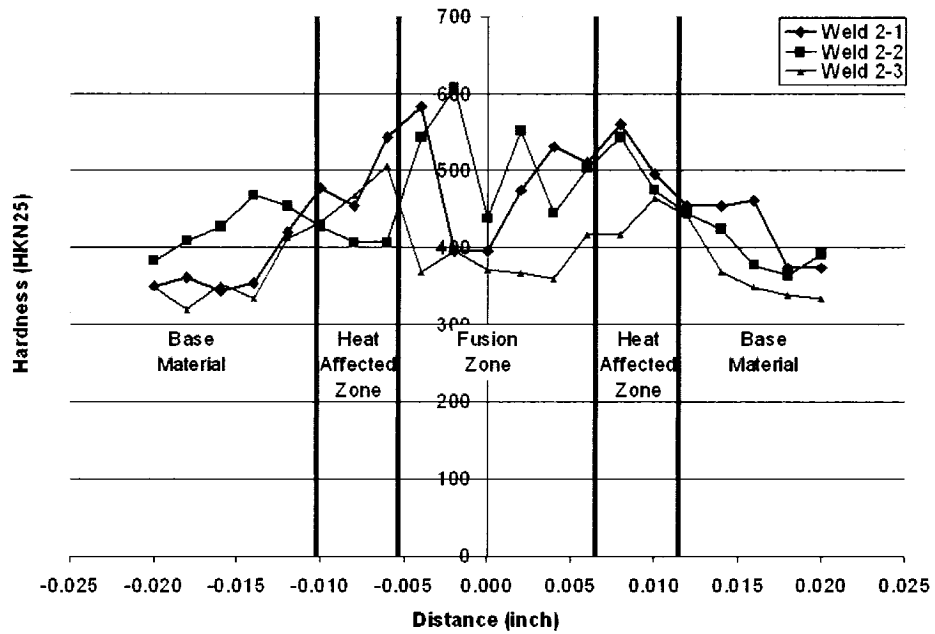


Figure 44. Microhardness plots for weld 2.

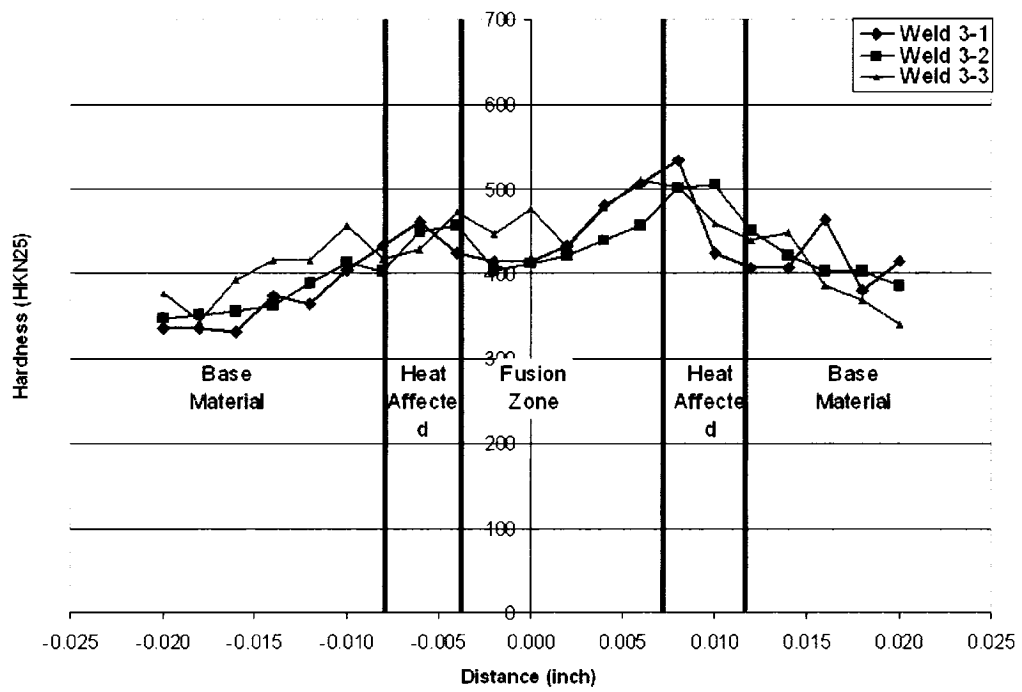


Figure 45. Microhardness plots for weld 3.

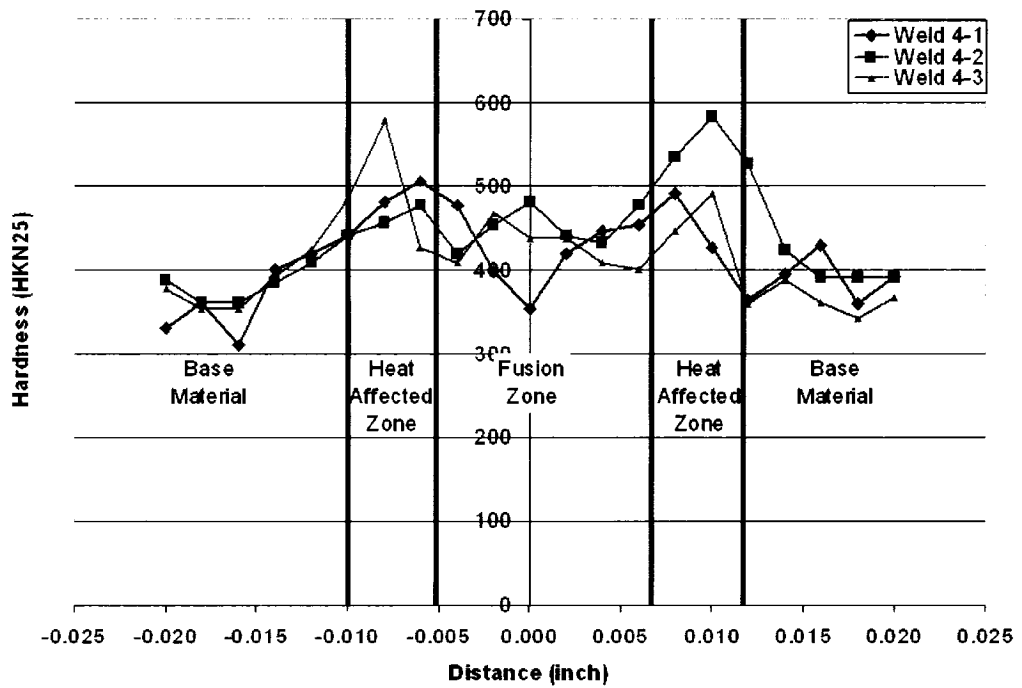


Figure 46. Microhardness plots for weld 4.

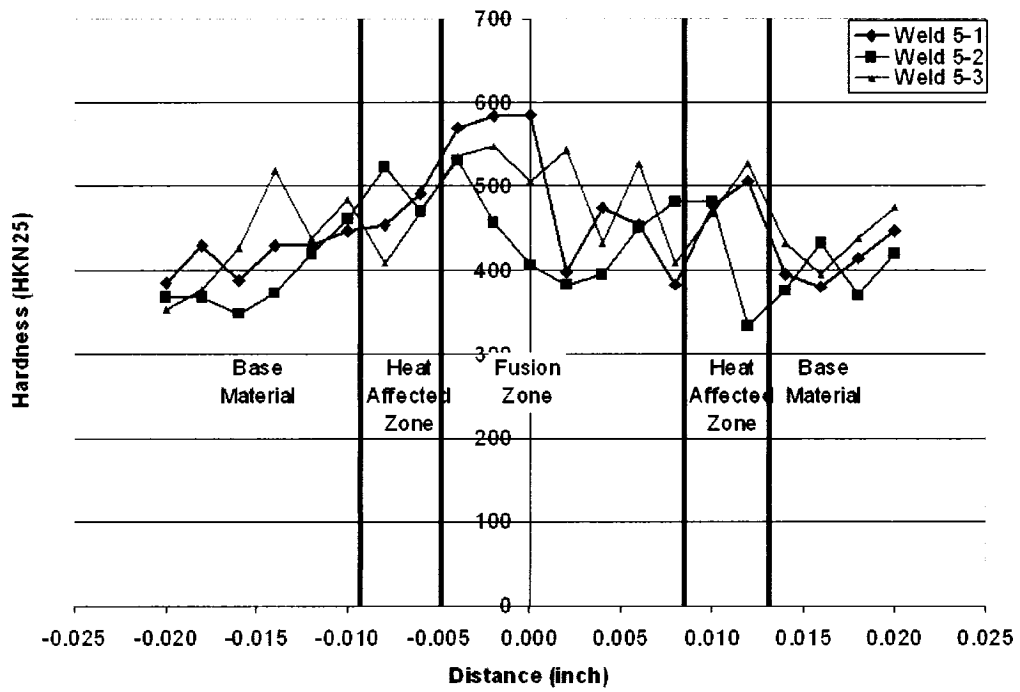


Figure 47. Microhardness plots for weld 5.

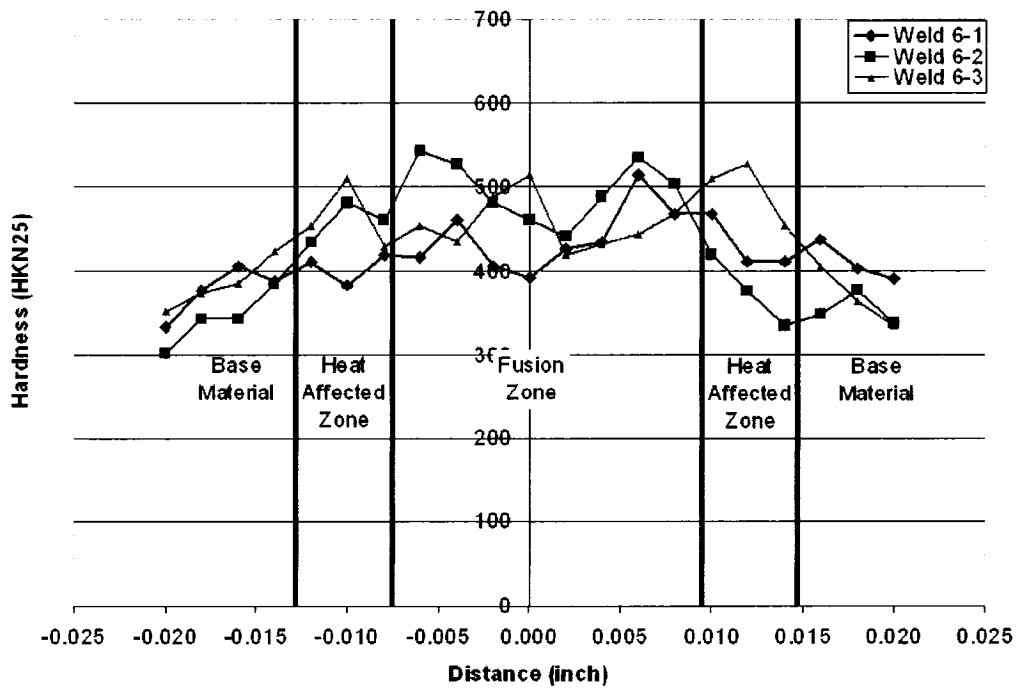


Figure 48. Microhardness plots for weld 6.

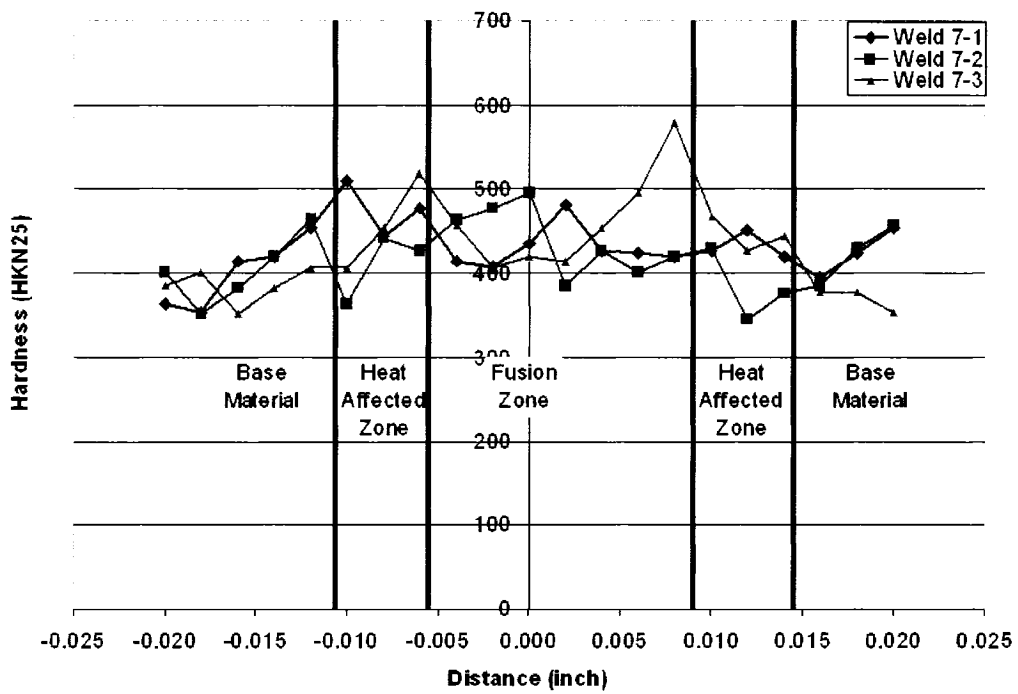


Figure 49. Microhardness plots for weld 7.

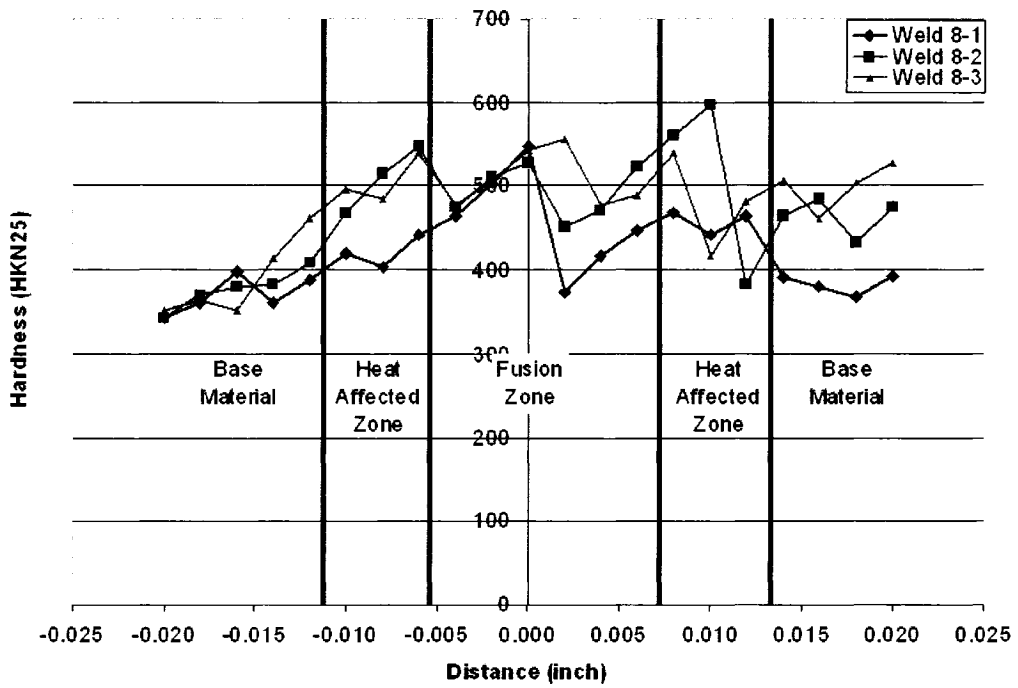


Figure 50. Microhardness plots for weld 8.

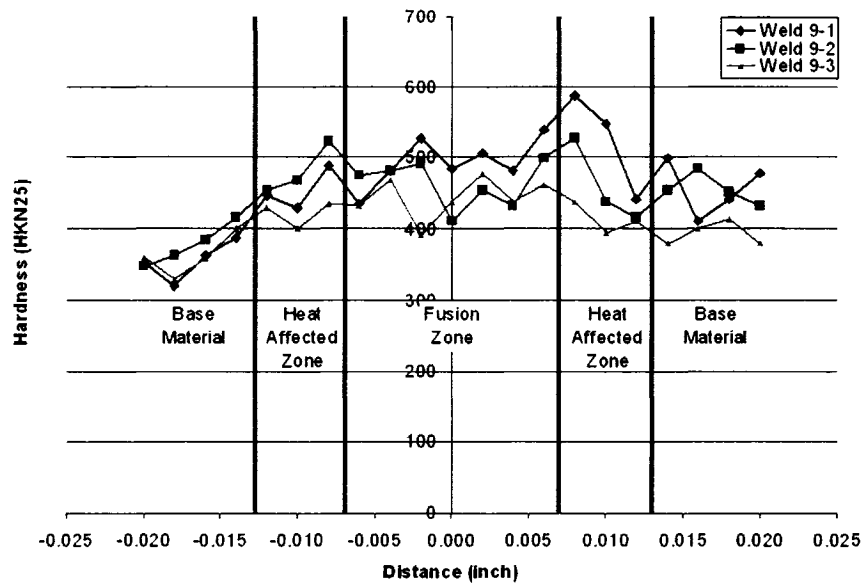


Figure 51. Microhardness plots for weld 9.

5.3 Tensile Test Result

The fracture strengths of the weldments and failure location from the tensile test are presented in Table 8. The tabulated data have been sorted with respect to specimen number. A graphical comparison of the fracture strengths of the weldments and the depth of penetration for each weld is displayed within Figure 52. The data have been sorted by increasing strength with respect to weldment thickness. Nonwelded specimens were used as controls, with the strength also shown in Table 8. The strength of the control specimens was measured at 196 psi, or 0.14 %, greater than the strength of Ti-6Al-4V as reported in the literature [21]. Due to the large variation in the depths of penetration of the welds, the wide range of strengths based on the thickness of the weldments was expected. For all welds that did not achieve full penetration, the failure occurred within the weld, while the weld that did achieve full penetration, weld 8, failed within the base material. The strength with respect to the thickness corresponds well with the depth of

penetration of the welds, with the exception of weld 4. The strength with respect to the depth of penetration does not correlate with the depth of penetration. The variation of the strengths, along with the location of the failures, indicates that stress concentrations at the weld foot influenced the fracture strength of the weldments.

Table 8. Tensile test results.

	Failure Location	Strength w.r.t. Thickness (psi)	Strength w.r.t. Penetration (psi)
Weld 1	Weld	41,628	166,512
Weld 2	Weld	24,050	120,248
Weld 3	Weld	10,554	63,323
Weld 4	Weld	41,757	86,393
Weld 5	Weld	22,967	106,001
Weld 6	Weld	53,589	119,086
Weld 7	Weld	99,007	180,013
Weld 8	Base	138,437	138,437
Weld 9	Weld	53,159	127,581
Control	Base	138,196	---
Literature	Base	138,000	---

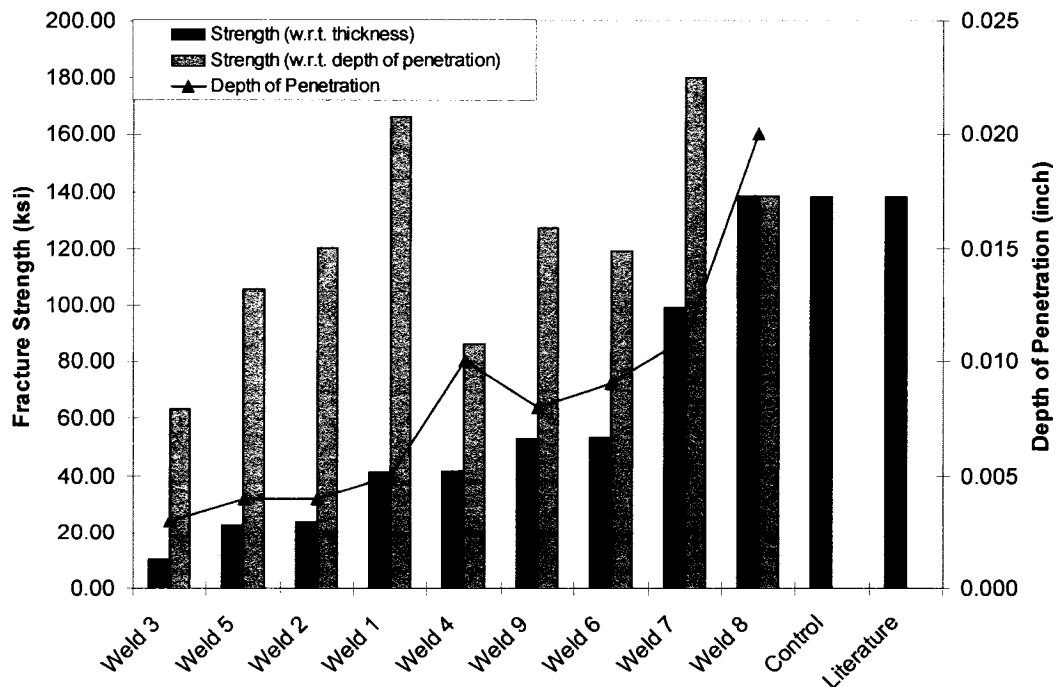


Figure 52. Comparison of tensile test results.

5.4 Microstructural Effects on Microhardness and Tensile Strength

The microstructural evolution of the fusion zone and heat affected zone during welding account for the changes of the mechanical properties in each weld. During the welding process, the laser heats the base material until a certain volume is molten. The melting point of Ti-6Al-4V is 1660°C, which is obviously above the beta transformation temperature of 996°C. When the laser is shut off between pulses, the heat applied by the laser is removed from the molten material, and the fusion zone quickly solidifies. The solidification rate during laser welding is sufficiently fast, obtaining cooling rates as high as 100,000°C per second [16], so that the formation of martensitic α' titanium is promoted. The presence of the martensitic α' titanium within the fusion zone and heat affected zone results in the measured increase, with respect to the base material, in hardness and strength within these zones.

If the strength of the weldment is calculated based on the total thickness, then the depth of penetration of the weld has a significant effect on the strength. As the depth of penetration increases, the strength of the weldment with respect to total thickness increases. With the exception of one data point, this relationship was true of the tensile test data measured during this study, as shown in Figure 53. This relationship results from increased depths of penetration producing a larger cross sectional area that can carry a larger load, thus producing a stronger weldment. When comparing the strengths of welds that contain varying depths of penetration, the highest strength was measured for the weld (welds 8) with full penetration of the weldment thickness.

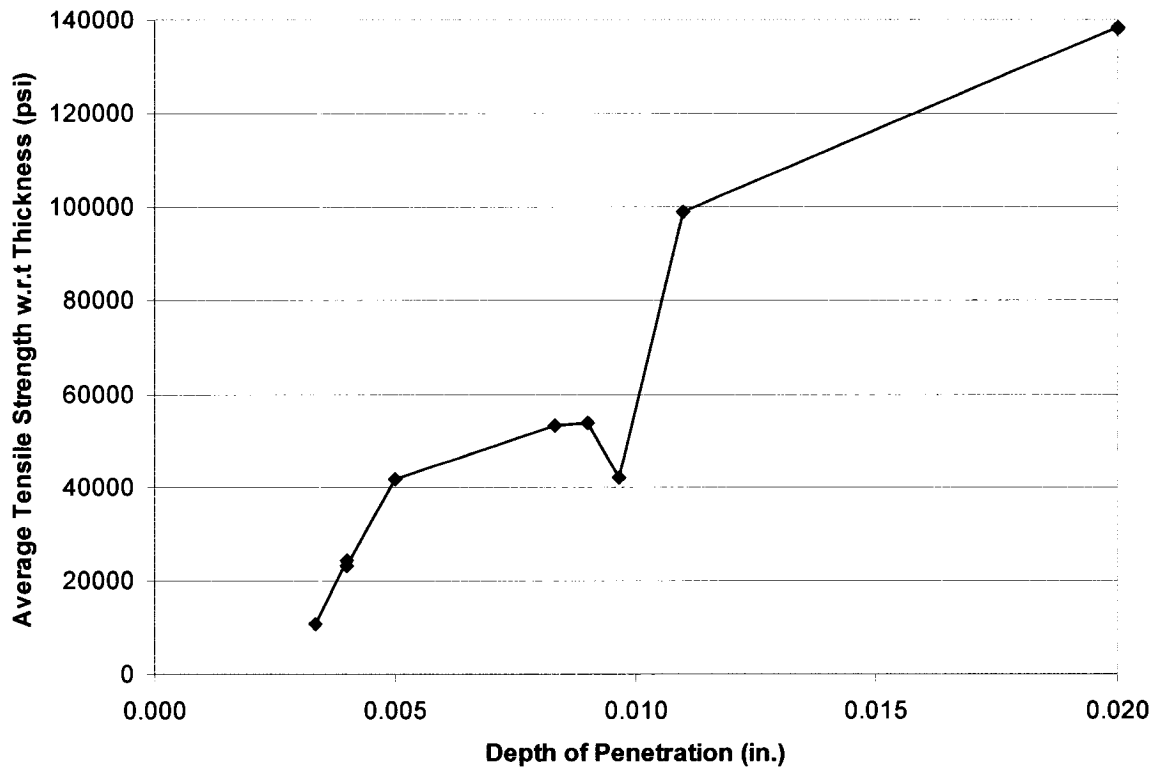


Figure 53. Plot of average tensile strength as a function of depth of penetration.

Increasing the depth of penetration of the weld also aids in increasing the strength of the weldment by decreasing stress concentrations at the weld root. As can be observed in the images of the microstructure of welds 1 through 7 and weld 9, as was shown in Figures 19 through 36, partial penetration welds produce a stress concentration at the root of the weld. The stress concentration at the weld root is not present in weld set 8, as shown in Figure 34. Removing the stress concentration from weld 8 produced a weldment that was as strong as the base material, and failure occurred within the base material during tensile testing. This would allow the strength of a full penetration weld to be predicted as being equal to the base material, and allow designers to use the strength of Ti-6Al-4V during the design of a product.

5.5 Cytotoxicity Test Results

In order to fully measure the biocompatibility of laser welded Ti-6Al-4V, the cytotoxicity test specimens were evaluated qualitatively and quantitatively. Both results are presented separately below.

5.5.1 Qualitative Cytotoxicity Test Results

Following implantation and incubation of the specimens for 24 hours, the cells were qualitatively assessed using an inverted light optical microscope. This was used to monitor the vacuolization, lysis, and general changes in size, shape and configuration of the cells. These observations were used to determine the cytotoxicity scale for each specimen according to Table 9 [25].

Table 9. Numeric cytotoxicity scale per ISO-10993-5.

Cytotoxicity Scale	Interpretation
0	Noncytotoxic
1	Mildly Cytotoxic
2	Moderately Cytotoxic
3	Severely Cytotoxic

The qualitative analysis is summarized in Table 10. Representative images from each specimen are shown in Figures 54 through 64. For the negative control, titanium control, and all nine weld sets, similar recordings were noted for the confluency, interconnectivity, and monitored continual cell growth, however, the opposite was recorded for the positive control. This indicates that the negative control, titanium control, and all nine weld sets have the same effect on the cells. Since the negative control is a known biocompatible material, then the titanium control and all nine welds were concluded to be biocompatible, with no dependence on the welding parameters.

Table 10. Summary of qualitative cytotoxicity test results.

Sample	Confluency	Interconnected Cells	Continued Growth	Vacuolization	Cell Lysis	Surface Roughness (μ -inches)	Cytotoxicity Rating
Positive Control	Non-confluent	Little to No Interconnectivity	Not Observed	Not Observed	Yes	---	3
Negative Control	Full Confluency	Fully Interconnected	Observed	Not Observed	No	---	0
Titanium Control	Full Confluency	Fully Interconnected	Not Observed*	Not Observed	No	0.25	0
Weld 1	Full Confluency	Fully Interconnected	Not Observed*	Not Observed	No	2.36	0
Weld 2	Subconfluency	Fully Interconnected	Observed	Not Observed	No	0.91	0
Weld 3	Full Confluency	Fully Interconnected	Not Observed*	Not Observed	No	0.57	0
Weld 4	Subconfluency	Mostly Interconnected	Observed	Not Observed	No	1.62	0
Weld 5	Full Confluency	Fully Interconnected	Observed	Not Observed	No	0.60	0
Weld 6	Full Confluency	Fully Interconnected	Observed	Not Observed	No	1.35	0
Weld 7	Full Confluency	Fully Interconnected	Not Observed*	Not Observed	No	1.37	0
Weld 8	Full Confluency	Fully Interconnected	Not Observed*	Not Observed	No	2.05	0
Weld 9	Subconfluency	Fully Interconnected	Not Observed*	Not Observed	No	1.10	0

* - Continued growth was suppressed by the high degree of confluency and interconnectivity surrounding the specimen.

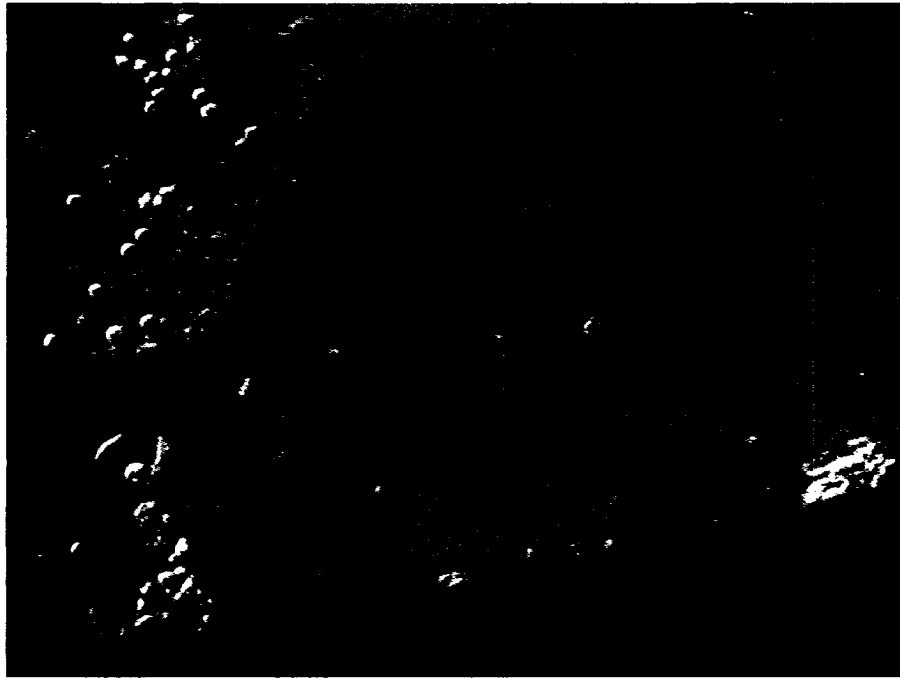


Figure 54. Cytotoxicity test specimen for the positive control (100X).

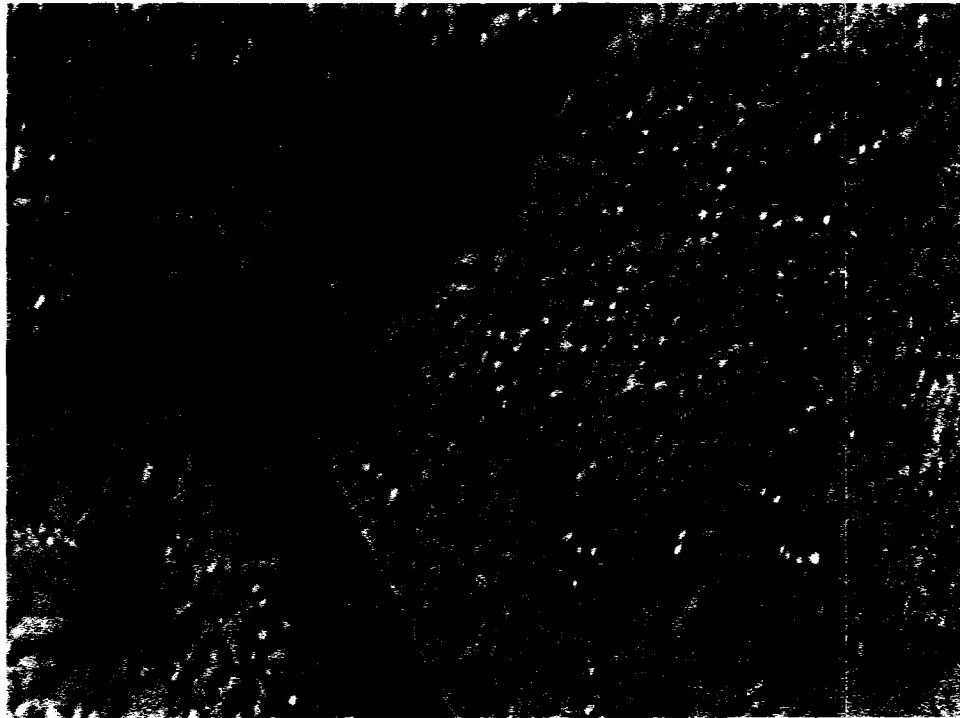


Figure 55. Cytotoxicity test specimen for the negative control (100X).

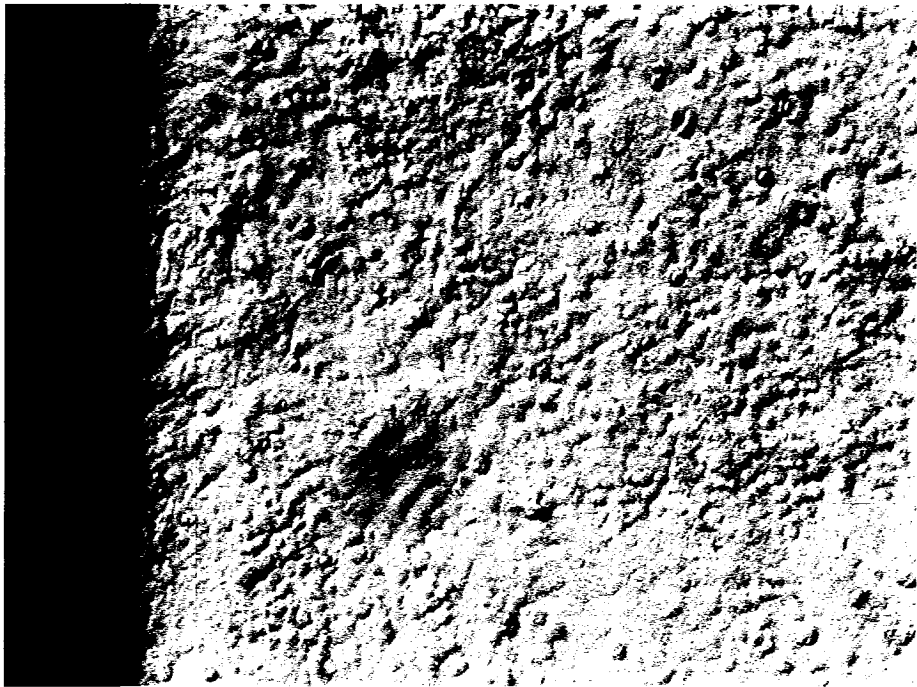


Figure 56. Cytotoxicity test specimen for weld 1 (100X).

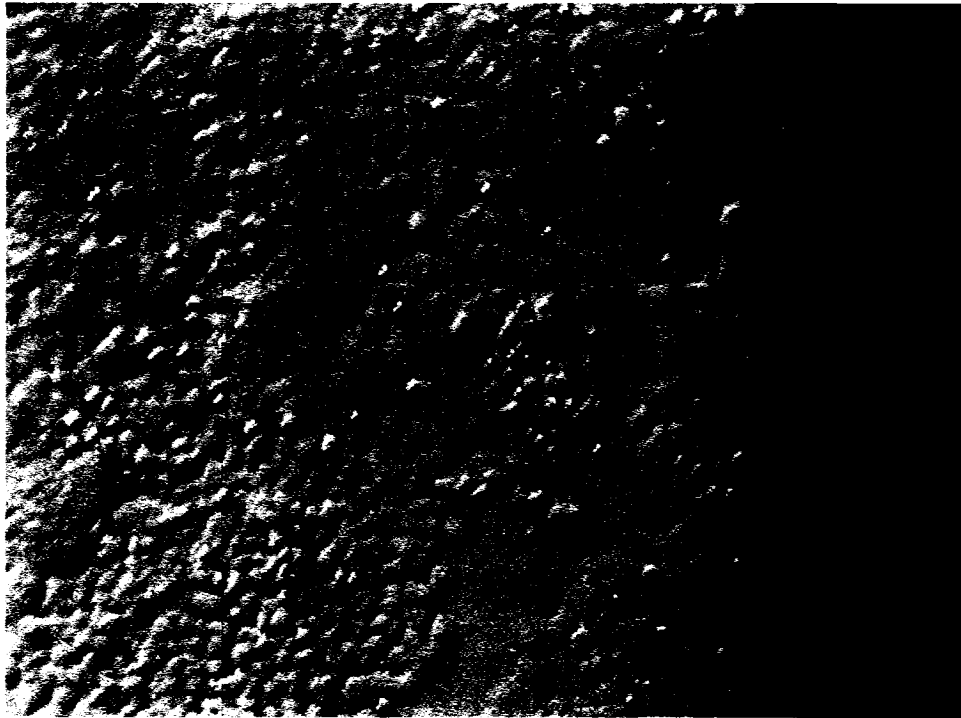


Figure 57. Cytotoxicity test specimen for weld 2 (100X).

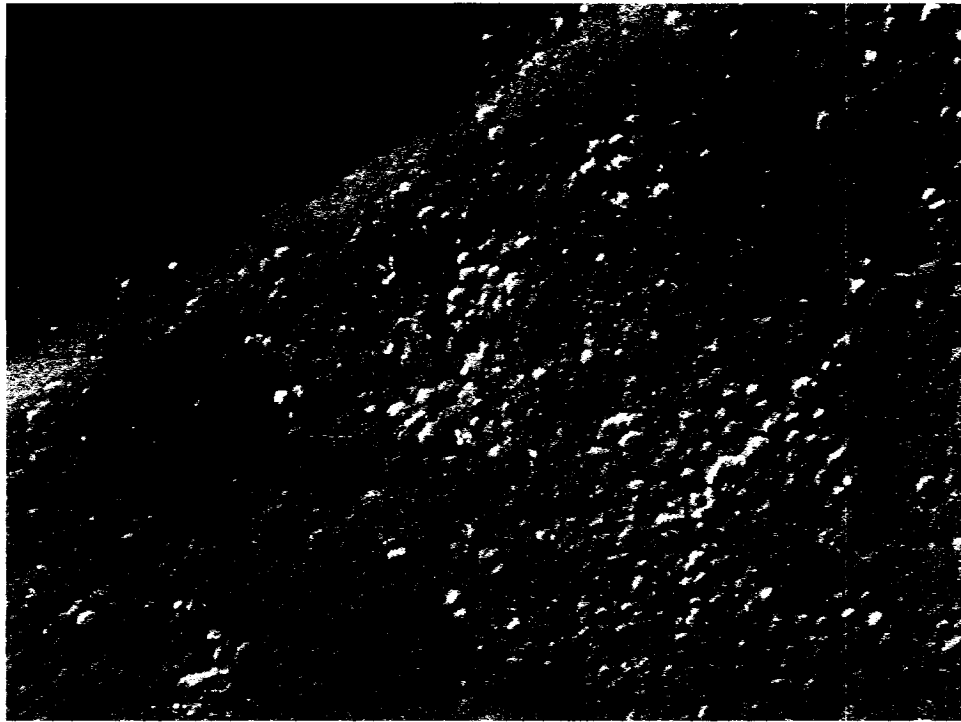


Figure 58. Cytotoxicity test specimen for weld 3 (100X).

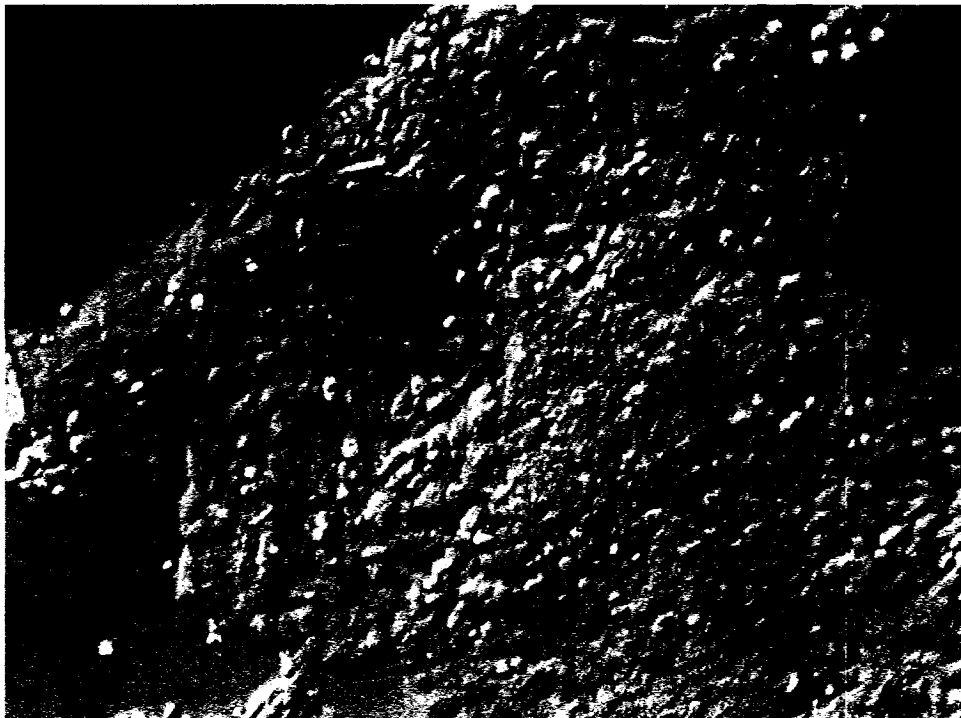


Figure 59. Cytotoxicity test specimen for weld 4 (100X).

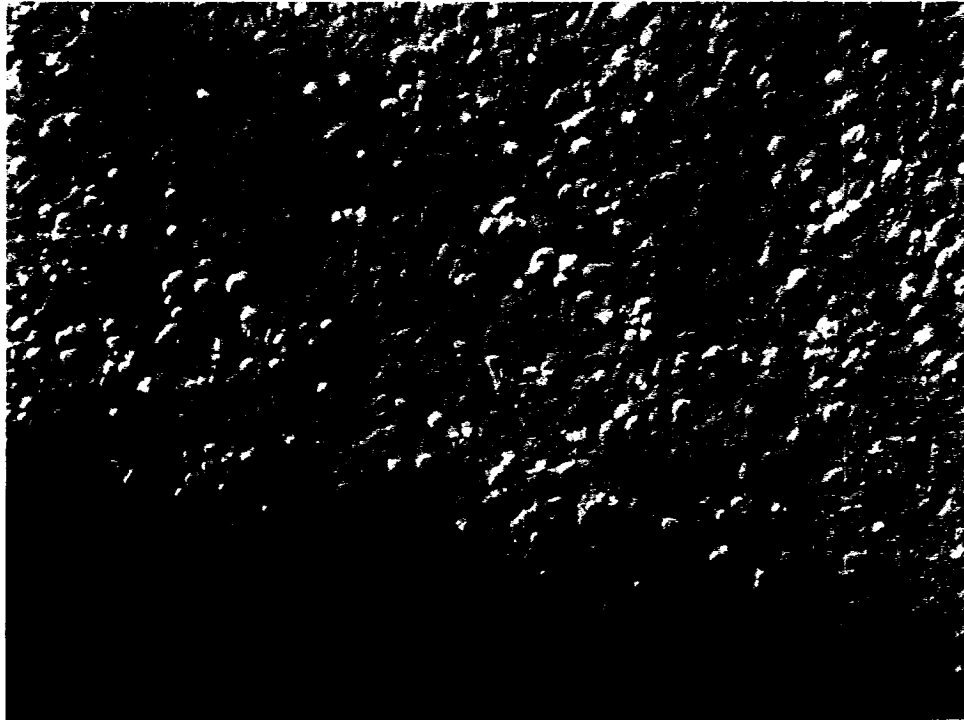


Figure 60. Cytotoxicity test specimen for weld 5 (100X).

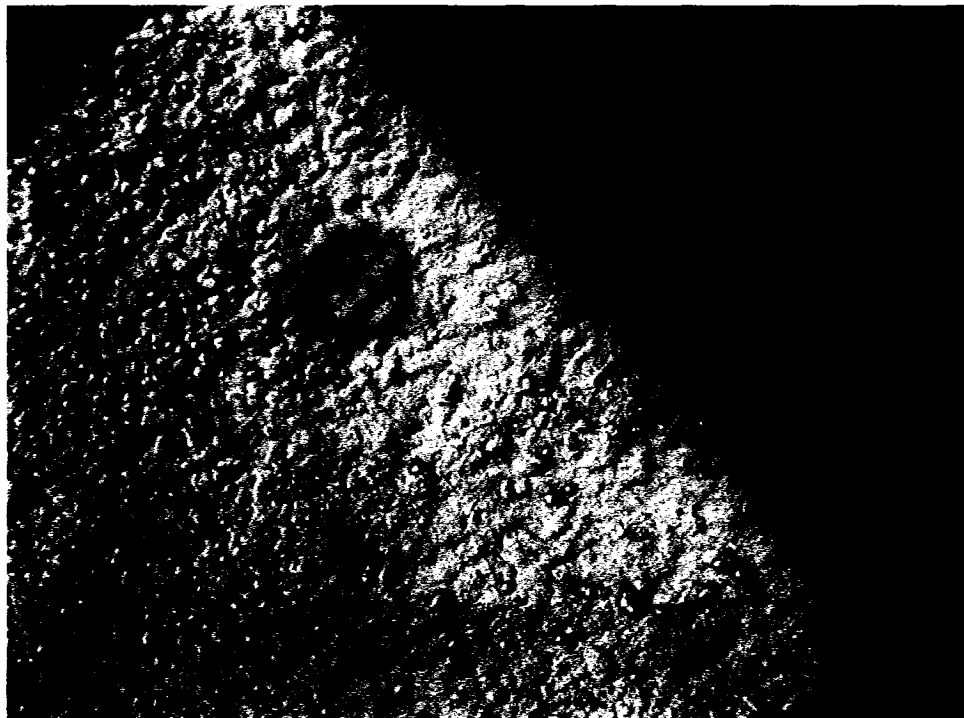


Figure 61. Cytotoxicity test specimen for weld 6 (100X).

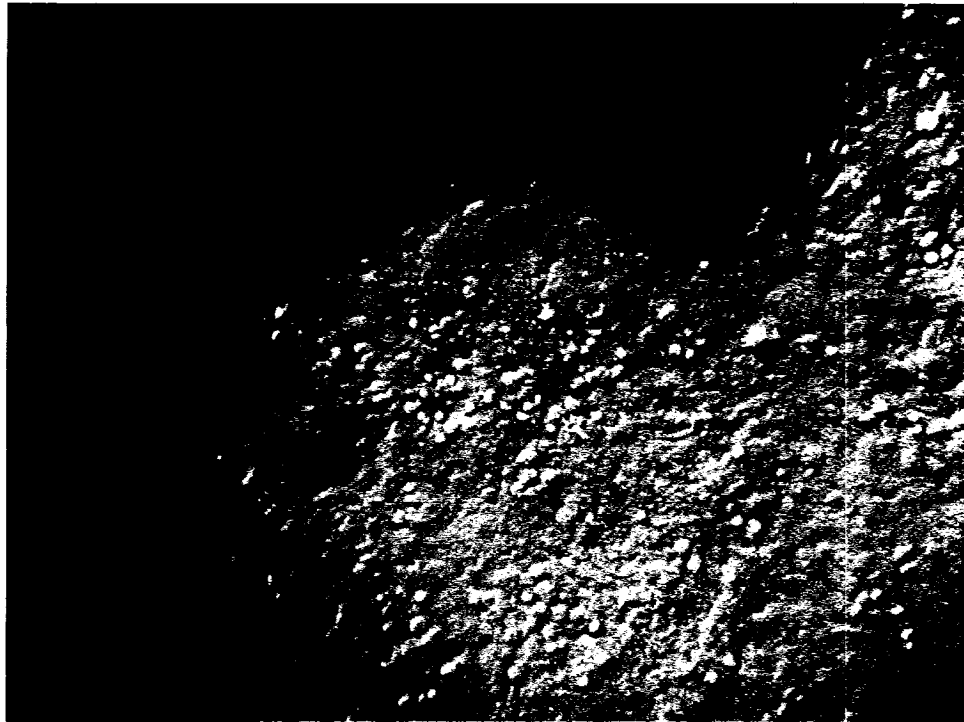


Figure 62. Cytotoxicity test specimen for weld 7 (100X).

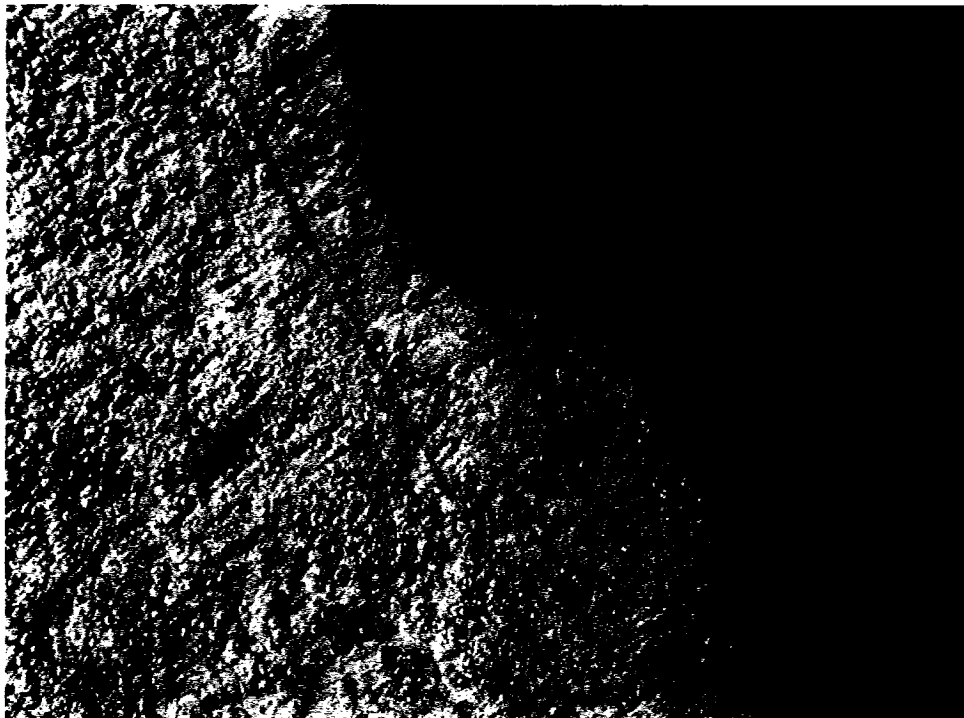


Figure 63. Cytotoxicity test specimen for weld 8 (100X).

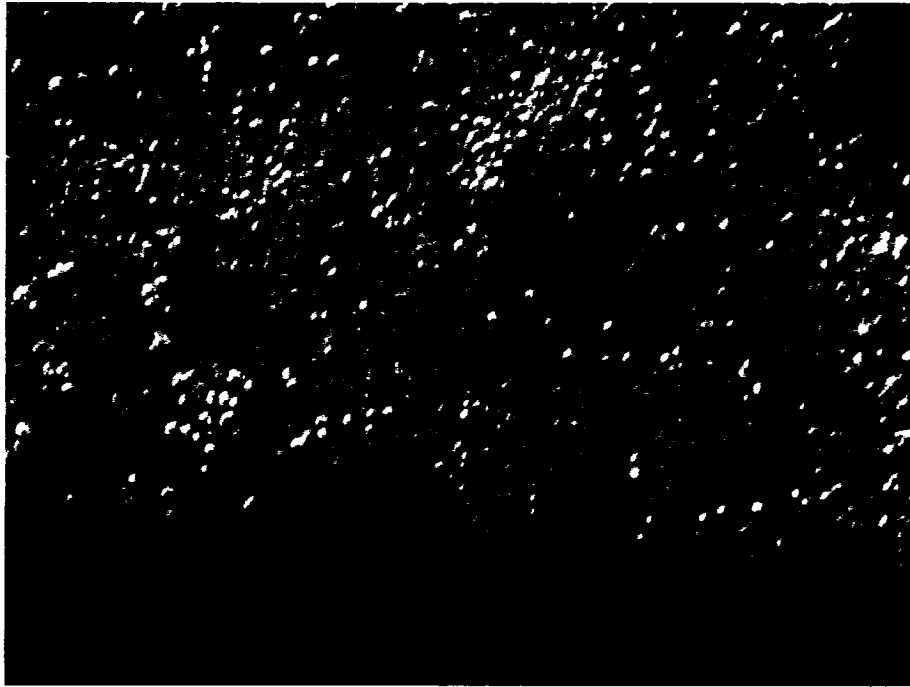


Figure 64. Cytotoxicity test specimen for weld 9 (100X).

5.5.2 Quantitative Cytotoxicity Results

A Coulter Counter was used to count the number of living cells present in one milliliter of media solution from each titer well. These values provide a quantitative view of the cytotoxic effect of each specimen on the cells. The full results are presented in Table 11.

At face value, the measured values seem to correspond to the qualitative cytotoxicity test results. The values seem to indicate that the negative control, titanium control, and all of the welds are biocompatible, while the positive control is bioincompatible. Using the Mann-Whitney U test, the measured cell counts were statistically compared to determine biocompatibility. The nine welds were compared to each of the positive, negative, and titanium controls using a 95% confidence interval.

Table 11. Quantitative results for the cytotoxicity test.

Sample	Specimen	Reading 1	Reading 2	Reading 3
Positive Control	1	49000	36000	41000
	2	31000	33000	18000
	3	31000	32000	20000
Negative Control	1	466000	417000	465000
	2	562000	556000	545000
	3	492000	492000	446000
Titanium Control	1	419000	416000	420000
	2	456000	414000	373000
	3	516000	552000	588000
Weld 1	1	325000	316000	303000
	2	326000	329000	348000
	3	276000	271000	306000
Weld 2	1	356000	332000	301000
	2	374000	447000	458000
	3	477000	446000	452000
Weld 3	1	386000	299000	246000
	2	356000	318000	346000
	3	274000	257000	254000
Weld 4	1	366000	331000	262000
	2	300000	295000	257000
	3	262000	296000	273000
Weld 5	1	390000	359000	343000
	2	240000	247000	226000
	3	339000	322000	325000
Weld 6	1	442000	427000	450000
	2	355000	360000	350000
	3	540000	576000	582000
Weld 7	1	330000	314000	373000
	2	502000	532000	531000
	3	356000	407000	427000
Weld 8	1	454000	441000	456000
	2	482000	480000	489000
	3	293000	306000	316000
Weld 9	1	381000	380000	383000
	2	581000	560000	621000
	3	360000	363000	363000

When comparing the welds to the positive control, the calculated U value for all nine welds was 0.0004. This U value is much less than the α value of 0.05, which corresponds to the 95% confidence interval. Since the positive control was selected based on its bioincompatibility, and the calculated U values are less than the α value, all of the welds are statistically different from the positive control, and therefore biocompatible.

The comparison of the welds to the negative control yielded a mix of results. The calculated U value for weld sets 6, 7, and 9 was greater than 0.05, therefore, these three welds were determined to be statistically similar to the negative control. Since the negative control consisted of biocompatible borosilicate glass, weld sets 6, 7, and 9 are concluded to be biocompatible per the Mann-Whitney U test. Weld sets 1, 2, 3, 4, 5, and 8 provided a U value less than 0.05, which classifies these welds as being bioincompatible.

The Mann-Whitney U test was also utilized to compare the nine welds to the titanium control. Similar to Sgambatoa et al [26], the titanium control was used as a biocompatible control. Welds 2, 6, 7, 8, and 9 yielded a U value greater than 0.05, and are therefore determined to be biocompatible since they are statistically similar to the titanium control, while welds 1, 3, 4, and 5 were found to be bioincompatible. The results from the Mann-Whitney U test are summarized in Table 12. As shown in the table, only welds 6, 7, and 9 yielded consistent non-cytotoxic results when statistically compared to the three controls.

Table 12. Mann-Whitney U Test cytotoxicity results.

	Positive Control		Negative Control		Titanium Control	
	U Value	Conclusion	U Value	Conclusion	U Value	Conclusion
Weld 1	0.0004	Cytotoxic	0.0004	Not Cytotoxic	0.0004	Cytotoxic
Weld 2	0.2893	Not Cytotoxic	0.0004	Not Cytotoxic	0.0118	Cytotoxic
Weld 3	0.0006	Cytotoxic	0.0004	Not Cytotoxic	0.0004	Cytotoxic
Weld 4	0.0004	Cytotoxic	0.0004	Not Cytotoxic	0.0004	Cytotoxic
Weld 5	0.0006	Cytotoxic	0.0004	Not Cytotoxic	0.0004	Cytotoxic
Weld 6	0.8598	Not Cytotoxic	0.0004	Not Cytotoxic	0.2893	Not Cytotoxic
Weld 7	0.2332	Not Cytotoxic	0.0004	Not Cytotoxic	0.0637	Not Cytotoxic
Weld 8	0.5660	Not Cytotoxic	0.0004	Not Cytotoxic	0.0423	Cytotoxic
Weld 9	0.2893	Not Cytotoxic	0.0004	Not Cytotoxic	0.2164	Not Cytotoxic

5.6 Surface Analysis Results

Using x-ray photoelectron spectroscopy (XPS), oxides of titanium, aluminum, and vanadium were identified on the surface of the weld specimens. The concentration of titanium identified as oxide on the surface of the weld specimens decreased with respect to the control specimen. The concentration of aluminum and vanadium identified on the surface of the specimens as oxide remained approximately constant for all specimens analyzed. As a secondary effect, XPS identified a significant amount of contaminants on the surfaces of the welds. Auger electron spectroscopy (AES) was used to measure the concentration of these contaminants with respect to depth into the weld. At a depth of approximately 50 Å into the weld, the concentration of the contaminants identified with XPS decreased to very low or undetectable limits. The data obtained from these two techniques indicate that the weld specimens maintained the ability of Ti-6Al-4V to form the protective oxide layer that is responsible for the alloy's biocompatibility. Also, the contamination on the surface of the welds was determined to be atmospheric contaminants deposited on the surface during storage of the specimens after welding and before analysis, and therefore are easily removable.

The summary of the XPS survey results are presented in Table 13. The data were normalized to 100% of the elements detected. Appendix D contains the survey spectra for each specimen. To complement the elemental composition data, the bonding state of the elements identified in Table 13 were determined via high resolution XPS analysis. High energy resolution spectra, used to determine the bonding states of the control, weld 1, weld 2, weld 4, and weld 7, are presented in Appendices E through I. For each element, the spectra from each specimen are overlaid in the figures in Appendix J.

For the surface of the control specimen, 94% of the titanium was determined to be bound as TiO_2 , with the remainder of the titanium being bound as metallic titanium, TiC , TiO , or TiN . As shown in Table 15, the amount of titanium bound as TiO_2 on the surface of each of the four welds that were analyzed was less than that of the control, which resulted in an increase in the amount of metallic titanium identified. From the XPS analysis, it was also found that 84% of the aluminum detected in the control specimen was identified as Al_2O_3 , with the remainder as metallic aluminum, as seen in Table 16. When vanadium was identified on the surface of the specimens, it was bound as either VO_2 or V_2O_3 .

AES was used to measure the atomic concentration of the elements on the control, weld 2, weld 4, and weld 7. The surface composition of each specimen is presented in Table 14. The atomic concentrations of the elements identified were tracked as a function of depth into the weld, using a sputter rate of $73 \text{ \AA}/\text{min}$ SiO_2 equivalent. The AES depth profiles for the four specimens are presented in Figures 65 through 68. The AES data are contained in Appendices E, G, H and I. For each specimen, the depth

profiles identified titanium, aluminum, vanadium, oxygen, and carbon in significant amounts within the bulk. Since the concentration of the contaminants was greatly reduced within the bulk of the specimens as compared to the surface of the specimens, the contaminants were determined to be atmospheric contaminants that were deposited on the surface of the specimens during storage between welding and analysis.

During the AES depth profiles, the thickness of the oxide layer present on the control, weld 2, weld 4, and weld 7 specimens was estimated. The thickness of the oxide layer was defined as the depth at which the oxygen concentration dropped to half of the maximum concentration obtained for each specimen. The oxide layer for the control specimen was estimated to be 110 Å thick. The weld 2, weld 4, and weld 7 oxide layers were estimated to be 70 Å, 200 Å, and 270 Å thick, respectively. Since the oxide layer of the weld specimens was approximately equal to or greater than the oxide layer thickness of the control specimen, it can be concluded that the welding process did not reduce the tendency of Ti-6Al-4V to form a protective oxide layer.

The XPS data provided insight into the anticipated biocompatibility of the weld specimens by identifying any contaminants that could negatively affect the biocompatibility of the welds and monitoring the bonding states of the elements present. Since a coherent oxide layer of the base material promotes biocompatibility, the oxide formation of titanium, aluminum, and vanadium on the welds identified the cause of the biocompatibility of the weldments. By tracking the concentration of the contaminants as they extend into the weld, the AES data determined the contaminations were due to atmospheric contaminants post welding.

Table 13. Atomic concentration of the surface of the weld specimens as determined with XPS (in atomic percent) ^{a,b}.

Sample	Ti	Al	V	C	O	N	F	Na	Mg	Si	S	Cl	K	Ca	Cu	Zn
Control	10.4	2.9	0.2	0.02	64.9	6.9	2.1	1.9	0.9	6.6	-	-	0.3	2.1	0.3	0.5
Weld 1	7.9	4.8	0.1	0.02	59.0	5.9	1.0	5.0	0.9	7.3	0.7	0.3	3.4	1.5	1.8	0.3
Weld 2	8.1	11.9	-	0.02	62.2	8.1	2.2	2.0	0.7	2.5	0.2	0.2	-	1.3	0.3	0.3
Weld 3	5.1	6.4	-	0.02	68.0	4.0	1.9	0.7	8.8	2.1	0.7	0.1	-	1.0	0.7	0.1
Weld 4	5.2	3.8	-	0.02	53.5	21.6	2.4	4.2	0.8	2.8	1.8	-	0.4	1.8	1.4	0.4
Weld 5	4.0	13.5	-	0.02	61.3	3.6	4.9	4.2	2.0	1.9	1.1	-	-	3.2	0.4	-
Weld 6	5.8	5.1	0.1	0.02	59.1	3.6	5.7	5.1	1.8	6.3	1.2	-	0.5	4.5	0.7	0.4
Weld 7	9.4	8.6	0.1	0.02	56.9	4.9	4.6	4.1	1.8	4.1	1.3	-	-	2.9	0.6	0.7
Weld 8	10.7	7.1	-	0.02	60.2	4.1	3.2	4.1	0.9	5.3	0.6	-	1.4	2.4	0.2	0.2
Weld 9	5.7	7.7	0.2	0.02	59.9	6.2	2.1	4.5	2.4	5.7	1.2	-	0.5	2.8	1.2	-

^a A dash line “-” indicates that the element was not detected.

^b The amount of carbon was corrected to remove atmospheric contamination.

Table 14. Atomic concentration of the surface of the weld specimens as determined with XPS (in atomic percent) ^a.

Specimen	Ti	Al	C	O	N	F	Na	Si	S	Cl	K	Ca	Cu
Control	5	2	19	41	18	-	3	4	-	-	3	5	-
Weld 2	3	13	36	32	10	<1	-	3	<1	<1	-	3	-
Weld 4	1	5	56	15	11	1	4	2	1	<1	-	3	1
Weld 7	3	6	29	30	10	1	4	4	1	<1	4	8	-

^a A dash line “-” indicates the element was not detected.

Table 15. Bonding state of the identified titanium (in percent).

Specimen	Ti Metal, TiC	TiO, TiN	TiO ₂
Control	4	2	94
Weld 1	17	19	64
Weld 2	44	17	39
Weld 4	41	18	40
Weld 7	35	14	51

Table 16. Bonding state of the identified aluminum (in percent).

Specimen	Al Metal	Al ₂ O ₃ , AlN, Al(OH) ₃
Control	16	84
Weld 1	14	86
Weld 2	20	80
Weld 4	15	85
Weld 7	10	90

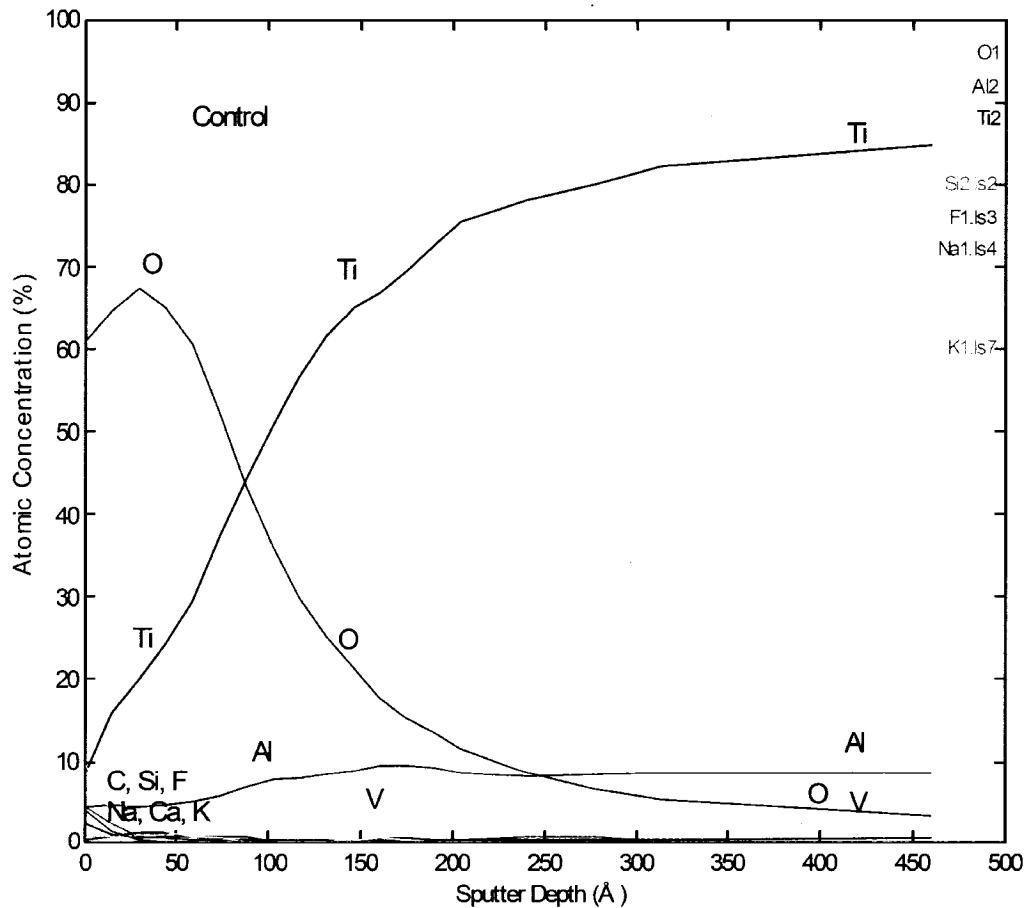


Figure 65. AES depth profile for the control specimen.

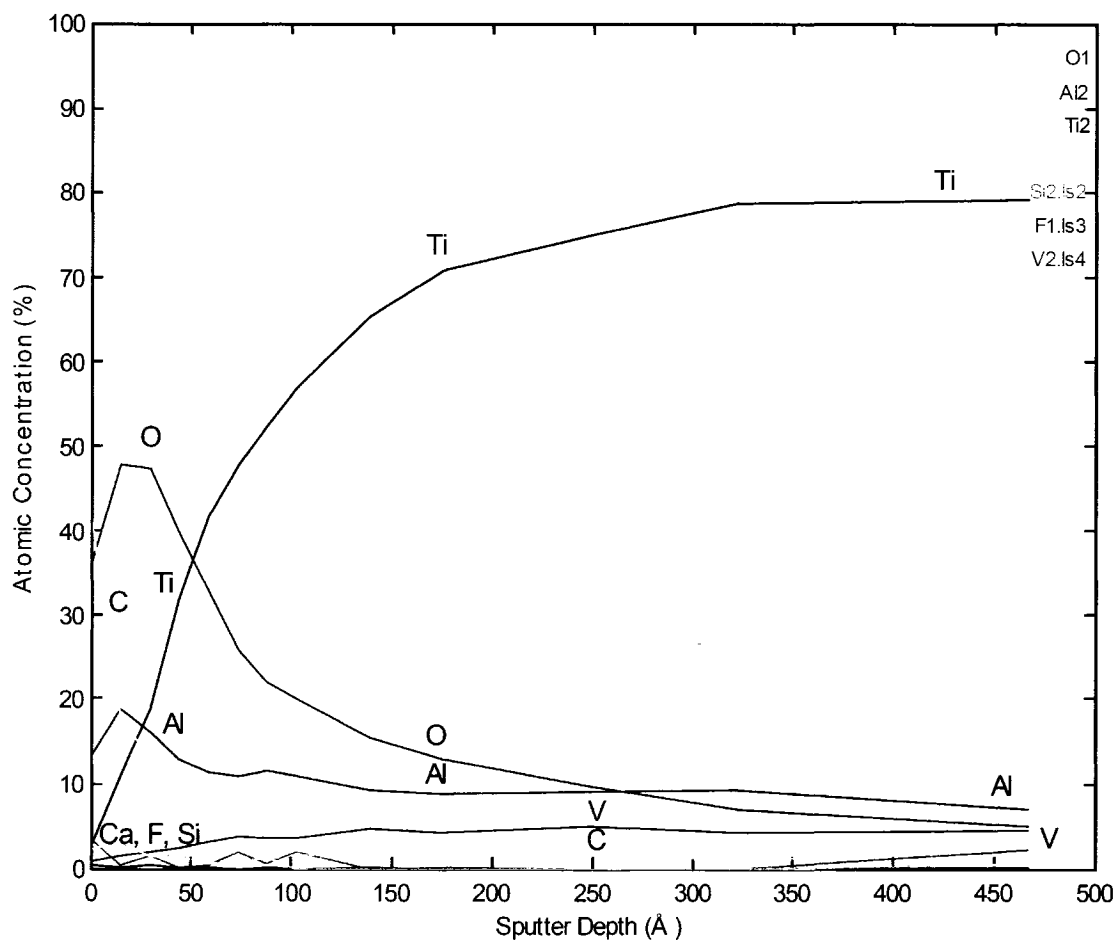


Figure 66. AES depth profile for the weld 2 specimen.

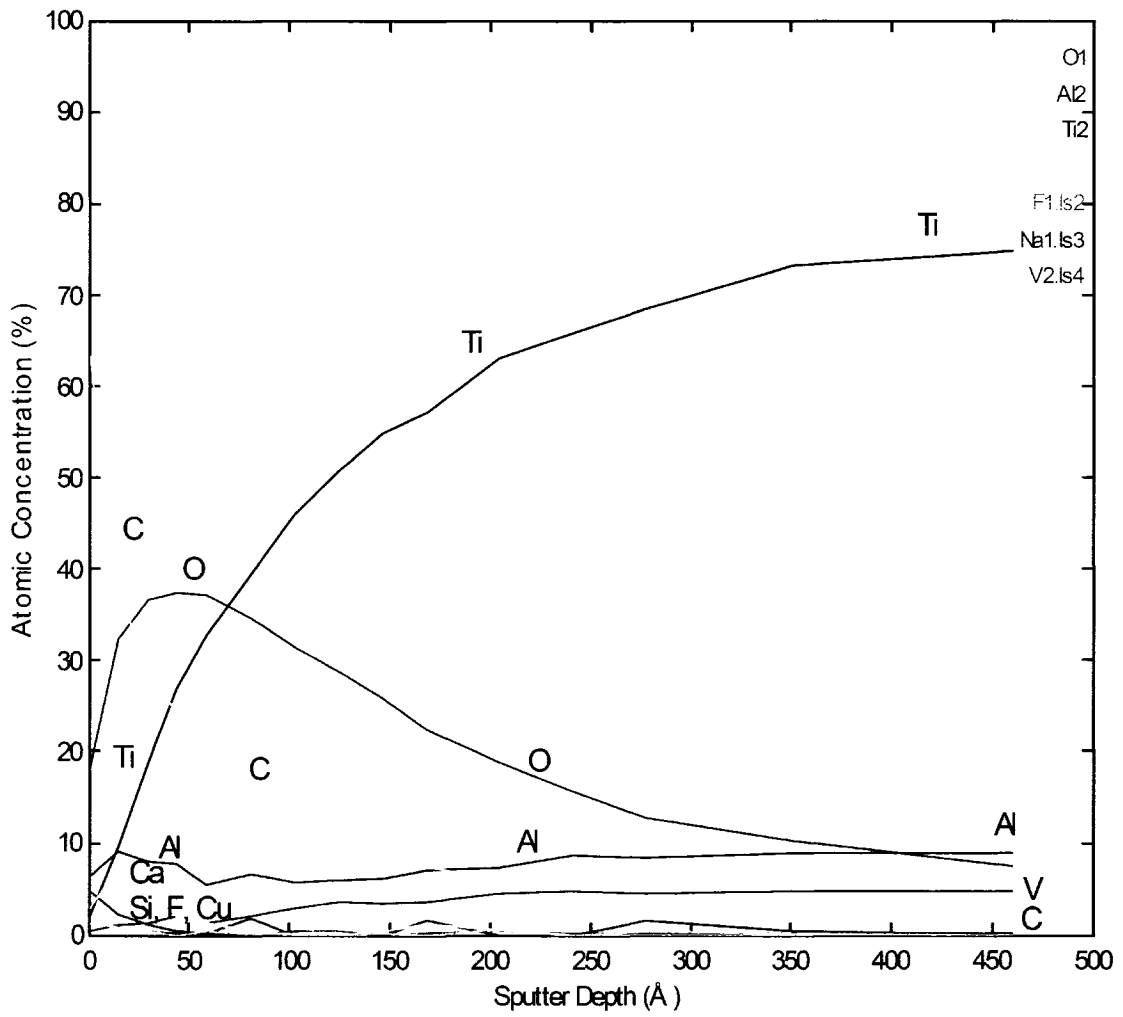


Figure 67. AES depth profile for the weld 4 specimen.

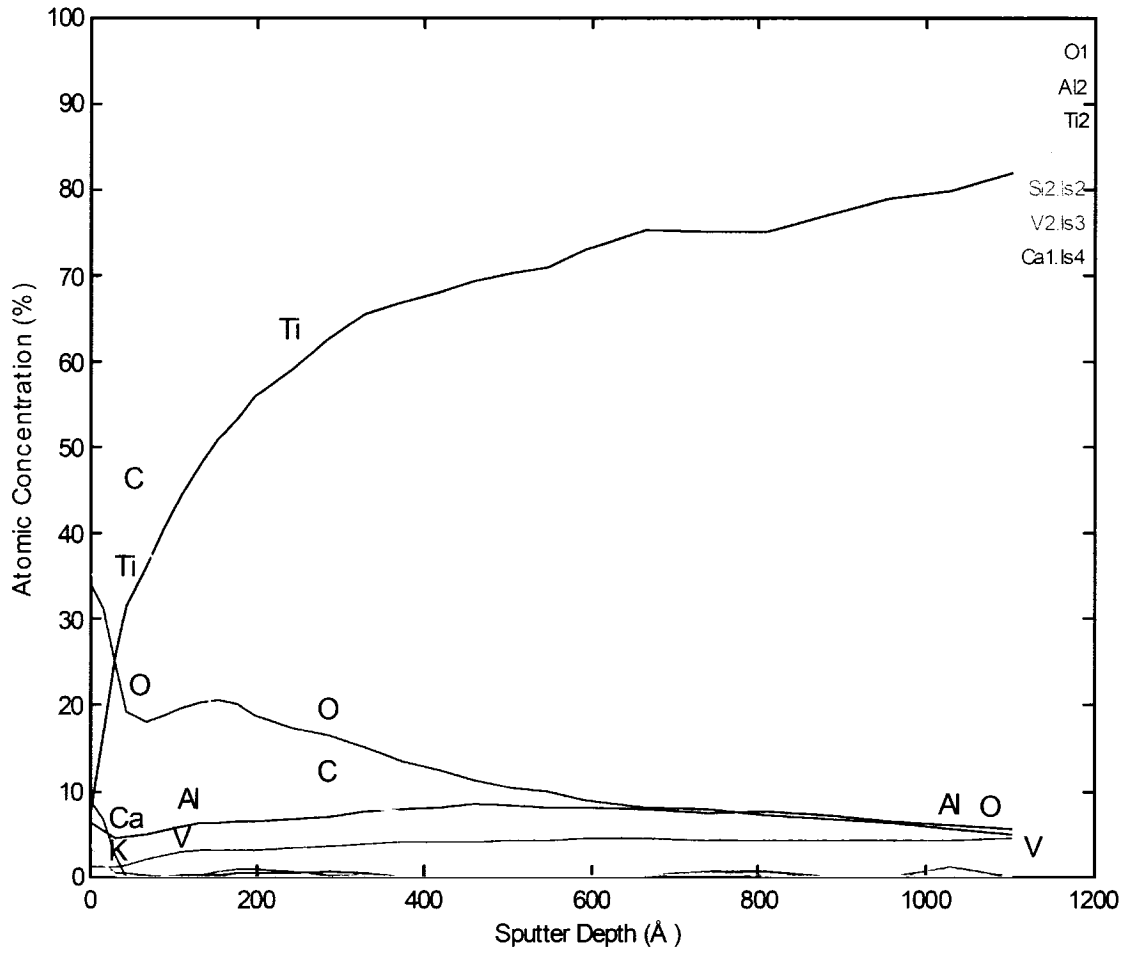


Figure 68. AES depth profile for the weld 7 specimen.

CHAPTER 6

DISCUSSION OF RESULTS

The discussion of the results presents an explanation and justification for the calculation of the fracture strength and for the interpretation of the cytotoxicity test results. The variation in the fracture strength of the weldment is explained and justified. Also, the significance of the two methods of calculating the fracture strength is explained. Limitations to the cytotoxicity testing are also discussed.

6.1 Calculation of Tensile Strength

The ultimate tensile strength of a material is calculated by dividing the peak load recorded during tensile testing by the cross sectional area of the material. It is therefore intrinsically understood that for identical materials of differing cross sectional areas, a different peak load will be measured from specimen to specimen during tensile testing. Likewise, it should also be understood that for different materials of identical cross sectional areas, the measured peak loads will vary during testing. In the case of the tensile testing during this study, materials of similar structure, that contained different cross sectional areas due to the differing depths of penetration during welding, were compared. This resulted in the large variation of the measured nominal fracture strengths of the specimens.

During the tensile testing of the welded specimen, a tensile load was applied transverse to the weld. This created a situation where the specimen reacted as a composite structure due to the presence of three zones of material that are composed of identical chemistry, but drastically different microstructures. The combination of the

composite structure and varying depths of penetration made comparison of the fracture strength of the weldments difficult.

The fracture strength of the weldments was calculated in two fashions. First, the fracture strength was calculated in a traditional manner by using the full thickness of the weldment to determine the cross sectional area. Second, the cross sectional area of the weldment was taken as the depth of penetration of the weld. Since the depth of penetration was not equal to the full thickness of the weldment for most of the welds, a lower peak load was expected.

As shown in Table 8, the two strengths can be drastically different. In the case of weld 1, the strength based on the depth of penetration was four times higher than the strength based on the thickness of the weldment. The formation of martensitic α' titanium, which is composed of a finer grain structure than the base material, justifies the increased hardness within the fusion zone. With the increase in hardness, the increase in strength of the fusion zone is expected, as was measured during the tensile testing.

The two strengths previously described were utilized within this study in order to determine if the changes to the microstructure of Ti-6Al-4V brought about by laser welding had an effect on the mechanical properties of the weldment. The variations measured by both strength calculations were attributed to the differing relative amounts of the constituents of the microstructure, misalignment and poor contact between the strips during welding, and the stress concentration effects due to incomplete penetration.

6.2 Cytotoxicity Testing Interpretation

Cytotoxicity testing is a relatively easy procedure to conduct, however, it is difficult to decipher with absolute certainty. The cytotoxicity test lends itself to both qualitative and quantitative interpretation. The results of the testing do not always correlate and are difficult to reliably reproduce.

Qualitative analysis of cytotoxicity results can be biased based on the observer of the results. The specimens were difficult to grade based on the scale recommended in ISO 10993-5 since no explanation is provided to justify the grading scale. Likewise, determination of any effects to the cells during testing requires prior knowledge of the cellular morphology and integrity prior to implantation of the test material.

Therefore, the quantitative analysis of the cytotoxicity results appears to be a more dependable means of comparison. One difficulty in the quantitative analysis is the determination of cell proliferation or lysis. In order to determine an increase or decrease in cells, the initial number of cells present during implantation of the test specimen must be accurately known. Since cell growth does not follow a normal distribution, it is difficult to accurately predict the number of cells after a given amount of time. Also, cells are sensitive to many factors during growth. Any differences between the local environment or culture media used to grow cells in separate wells could have a drastic effect on the growth of the cell cultures. Finally, an accurate assessment by qualitative analysis requires the use of a control of known cytotoxicity. The specimen of interest must be compared to the control in order to determine if the specimens are more or less cytotoxic than the control. For biological systems, there exist many statistical models for

direct comparison of specimens. However, these models rely on a rank-based evaluation. If the readings for the control specimen are all higher or all lower than the readings for the test specimen, the statistical models determine there to be a statistical difference between the two specimens, regardless of whether the difference between the means of the control specimens and the test specimens is large or small.

These limitations, along with the fact that biocompatibility rating is a spectrum as opposed to being discreet, make cytotoxicity testing difficult to repeat, and leave the results open to scrutiny. It is the author's opinion that a more stringently controlled protocol must be developed for interpreting cytotoxicity test results. The protocol should remain open ended in describing the testing procedure, so as to allow for selection of the cell line of interest to be utilized during testing, but should include clarification as to how to analyze and compare the results of the test.

CHAPTER 7

CONCLUSIONS

Laser welding is currently used within the biomedical industry to produce hermetic seals in implantable medical devices. The goal of this study was to determine the effects of pulsed YAG laser welding parameters on the biocompatibility and weld integrity of laser welded Ti-6Al-4V. Based on the findings of this study, the processing parameters for pulsed YAG laser welding did not affect the biocompatibility of the weldments, while they did have an effect the physical characteristics and mechanical properties of the welds.

The microstructure, chemical composition, and crystal structure within the fusion zone and heat affected zone were not affected by the weld parameters. For each of the welds, the microstructure within the fusion zone was found to consist of martensitic α' titanium, while the heat affected zone was composed of a mixture of martensitic α' titanium, primary α titanium, and intergranular β titanium. The chemical composition of the fusion zone and heat affected zone remained consistent with the base material. The crystal structure of the base material and heat affected zone consisted of both hexagonal close packed and body centered cubic. The rapid cooling rate within the fusion zone retarded the formation of the body centered cubic structure, and only the hexagonal close packed structure was found.

The microhardness within the heat affected zone and the fusion zone increased with respect to the base material. The measured increase was found to be due to the presence of martensitic α' titanium within the heat affected and fusion zones. During

tensile testing, the constituents of the microstructure, the depth of penetration of the welds, and the stress concentration due to incomplete penetration acted to reduce the strength of the weldments. By achieving full penetration of the weld, the fracture strength of the weldment is equal to the strength of the base material, as was measured in weld set 8.

The cytotoxicity testing yielded varying results based on the method of interpretation of the test. For all intents and purposes, all welds were found to be biocompatible. Through qualitative interpretation of the cytotoxicity test, it was determined that processing parameters did not have an effect on the cytotoxicity of laser welded Ti-6Al-4V. The quantitative results depended on the control specimen to which the weld specimens were statistically compared. It is the opinion of the author that these results are due to the statistical models used to interpret the data. Further investigation is required to confidently conclude the effect of processing parameters on the cytotoxicity of laser welded titanium.

X-ray photoelectron spectroscopy identified an oxide layer on the surface of the weld specimens and control specimen. Within the volume analyzed, the amount of aluminum and vanadium bound as an oxide was approximately the same for the control specimen and the weld specimens, while the amount of titanium bound as an oxide was lower on the weld specimens than on the control specimen. The oxide layer on the weld specimens was of similar thickness to the oxide layer on the control specimen. The presence of the oxide layer is responsible for maintaining the biocompatibility of Ti-6Al-4V after laser welding.

CHAPTER 8

RECOMMENDATIONS FOR FUTURE WORK

In the opinion of the author, the mechanical testing, cytotoxicity, and surface analysis warrant future work in order to refine the data obtained within this study. A broader scope is also recommended for future work.

The mechanical testing would benefit from improvements to the welding procedure. One issue with laser welding that affects the reproducibility of welds is the need for tight, intimate contact for the weldment during welding. The fixture used for this study provided adequate contact, but further refinement would increase the reproducibility of welds, which in turn should increase the reproducibility of the mechanical testing data. As an alternative, improvement in edge preparation could be implemented to allow for a tight and flush fit of the parts to be welded.

Refinement in the selection of the processing parameters would allow for more accurate direct comparison of the mechanical properties as well. By selecting a range of weld parameters that result in full penetration welds, the stress concentration effect can be negated. By eliminating the stress concentration, the effect of the processing parameters on fracture strength of the welds can be determined.

As previously stated within this study, biocompatibility is not a discreet classification, but rather is rated on a spectrum. The method of data analysis utilized for the cytotoxicity results limited the comparison of the laser welded specimens to the control specimens. The statistical analysis model used was properly suited for the nonparametric data produced during the cytotoxicity test, however, the model utilized a

rank-based comparison in order to determine statistical differences between the specimens. For weld sets whose recorded cell counts were all lower or higher than the control specimen, the statistical model determined there to be a statistical difference between the two data sets, regardless of the difference between the means of the data sets.

To combat the limitations of the data analysis of the cytotoxicity testing, the test protocol should be further developed. One recommendation the author makes is to apply a constant and known number of cells to each specimen within the titer well for incubation. After allowing the specimens to incubate for a specific and defined amount of time, the number of cells present within the titer wells should be counted. From these raw data, the viability of the cells in the presence of the specimen can be determined by the percent of cellular reproduction. The viability can then be directly compared using a non-ranking, nonparametric statistical model.

The surface analysis should be repeated for specimens that have received surface treatments that are currently employed in the biomedical industry. This would help to provide a direct comparison to the surface chemistry of the medical implant. The specimens should also be maintained in a controlled environment between welding and analysis in order to eliminate any environmental contaminants.

Future work should consider studying the effects of laser welding other metals and alloys. Medical implants are commonly composed of stainless steel alloys, cobalt-chromium alloys, and titanium alloys, to name a few alternate materials. New materials are constantly being developed and researched for future application. Studying

alternative materials would broaden the amount of biocompatibility data in the open literature.

Laser welding is not the only joining method that can be used to produce hermetic seals. Alternative joining methods should be studied in order to determine the effect of joining on biocompatibility. Some examples of joining techniques that can be used to produce hermetic seals include brazing, resistance welding, and friction stir welding. As with the materials, new joining techniques are constantly being researched and invented. The novel joining methods would provide a new topic for research and publication.

This list of future work should not be taken as all inclusive. These points of future work are the opinion of the author. Even the best of work, when viewed from another set of eyes, can use some refinement or future consideration to obtain more thorough results.

REFERENCES

1. Advanced Medical Technology Associates, The Medical Technology Industry at a Glance 2004, (The Lewin Group, Falls Church, VA).
2. M. Kocak and J.F. dos Santos, "*Trends in industrial applications and quality assessment*," *Revue de la Soudure*, **55**, pp. 26-35 (1999).
3. J.C. Lippold, "*Solidification behavior and cracking susceptibility of pulsed-laser welds in austenitic stainless steels*," *Welding Research Supplement*, **73**, pp. 129s-139s (1994).
4. M.M. Schwartz, Source Book on Electron Beam and Laser Welding, (American Society for Metals, Metals Park, OH), pp. 317.
5. Laservall S.p.A., JLK1 Use and Maintenance Handbook, (Laservall S.p.A. North America Division, Pawtucket, RI).
6. N.J. Heo, T. Nagasaka, T. Muroga, A. Nishimura, K. Shinozaki, and N. Takeshita, "*Metallurgical and mechanical properties of laser weldment for low activation V-4Cr-4Ti alloy*," *Fusion Engineering and Design*, **61**, pp. 749-755 (2002).
7. F. Caiazzo, F. Curcio, G. Daurelio, and F.M.C. Minutolo, "*Ti-6Al-4V sheets lap and butt joints carried out by CO₂ laser: mechanical and morphological characterization*," *Journal of Materials Processing Technology*, **149**, pp. 546-552 (2004).
8. J. Liu, I. Watanabe, K. Yoshida, and M. Atsuta, "*Joint strength of laser-welded titanium*," *Dental Materials*, **18**, pp. 143-148 (2002).
9. D.F. Williams, *The Williams' Dictionary of Biomaterials*, (Liverpool University Press, United Kingdom).
10. K.J. Ely, "*Welding thin-sheet stainless steels for medical applications*," *Proceedings from the Materials & Processes for Medical Devices Conference*, pp. 37-42 (2004).
11. K.J. Ely, "*Issues in hermetic sealing of medical products*," *Medical Device and Diagnostic Industry*, pp. 186-195 (January 2000).
12. Y. Tzeng, "*Parametric analysis of the pulsed Nd:YAG laser seam-welding process*," *Journal of Materials Processing Technology*, **102**, pp. 40-47 (2000).
13. Z. Xu, K. Natesan, C.B. Reed, and D.L. Smith, "*Procedure development of laser welding of V-4Cr-4Ti alloy*," *International Journal of Refractory Metals and Hard Materials*, **18**, pp. 231-236 (2000).
14. L.K. Pan, C.C. Wang, Y.C. Hsiao, and K.C. Ho, "*Optimization of Nd:YAG laser welding onto magnesium alloy via Taguchi analysis*," *Optics and Laser Technology*, **37**, pp. 33-42 (2004).

15. G. Casalino, F. Curcio, and F.M.C. Minutolo, "*Investigation on Ti-6Al-4V laser welding using statistical and Taguchi approaches,*" Journal of Materials Processing Technology, **167**, pp. 422-428 (2005).
16. S.C. Tjong, S.M. Zhu, N.J. Ho, and J.S. Ku, "*Microstructural characteristics and creep rupture behavior of electron beam and laser welded AISI 316L stainless steel,*" Journal of Nuclear Materials, **227**, pp. 24-31 (1995).
17. Y. Tzeng, "*Effects of process parameters on the corrosion rate of pulsed Nd:YAG laser-welded zinc-coated steel,*" Journal of Materials Processing Technology, **124**, pp. 1-7 (2002).
18. B.T. Lu, Z.K. Chen, J.L. Luo, M.B. Patchett, and Z.H. Xu, "*Pitting and stress corrosion cracking behavior in welded austenitic stainless steel,*" Electrochimica Acta, **50**, pp. 1391-1403 (2005).
19. R. Solmi, D. Martini, M. Zanarini, S.I. Penco, L. Rimondini, P. Carinci, G. Borea, and A. Ruggeri, "*Interactions of fibroblasts with soldered and laser-welded joints,*" Biomaterials, **25**, pp. 735-740 (2004).
20. S. Fariabi, Edwards Lifesciences, *private communication*, (October 2005).
21. Engineering Alloy Digest Inc., "*Ti-6Al-4V,*" Alloy Digest, (June 1972).
22. American Society for Testing and Materials, ASTM E407: Standard Practice for Microetching Metals and Alloys, (ASTM International, West Conshohocken, PA).
23. American Society of Materials International, Materials Properties Handbook: Titanium Alloys, (ASM International, Materials Park, OH).
24. ISO Standards Technical Committee 194, Biological Evaluation of Medical Devices – Part 5: Tests for In Vitro Cytotoxicity, (International Organization for Standardization, Geneva, Switzerland).
25. P. Kjellstrand, P. Okmark, R. Odselius, H. Thysell, G. Riede, B. Holmquist, "*Adherence of blood cells to dialyzer membranes as a measure of biocompatibility,*" International Journal of Artificial Organs, **14**, pp. 698-702 (1991).
26. A. Sgambato, A. Cittadinia, R. Arditoa, A. Dardelia, A. Facchinib, P. Dalla Priab, A. Colombo, "*Osteoblast behavior on nanostructured titanium alloys,*" Materials Science and Engineering C, **23**, pp. 419–423 (2003).

APPENDIX A – CYTOTOXICITY TEST PROCEDURE

This lab will be separated into five primary stages. As illustrated in the procedures below, these stages consist of media preparation, initial culturing, sub-culturing, replating the cells and material specimen exposure, and evaluation of the cells.

The cell lines and culture medium that are used for Cytotoxicity testing are selected based on reproducibility, accuracy, storage conditions, and the presence of mycoplasma. Once the cell lines and culture media have been selected they should be maintained in proper storage conditions and maintained at proper pH, sterility and temperature levels. During the preparation of the cell stock culture a given number of cells will be incubated with the culture medium to form a cell culture. Once this culture reaches near confluency cells from this culture will then be sub-cultured into smaller vessels (titer wells) and incubated as well. Once these cells grow to a point of subconfluency, a material specimen will then be placed on the surface of this culture. These cells will then be exposed to the material for a given amount of time and evaluated for cytotoxic reactions accordingly.

I. Culture Media Preparation

- A. Mixing powder media (autoclavable) DMEM without glutamine and sodium bicarbonate
 1. Have the following glassware ready:
 - a. 1 two-liter volumetric flask that has been cleaned and thoroughly rinsed with distilled and deionized water
 - b. 4 500 ml glass media bottles cleaned and sterilized
 2. Empty two bottles/packets of powdered media (each is enough for 1 liter) into a 2-liter volumetric flasks, fill half with deionized water, and place on stirring plate and stir with a magnetic stirring rod until the powder is dissolved.
 3. Add water to the two-liter mark on the flask, making sure the stirring rod is not in the flask as it will displace some volume.

4. Fill the media bottles with 500 ml of the dissolved powder media and sterilize in the autoclave on the 6th floor of Duncan hall.
- B. Making complete media**
- i. From autoclaved stock media. Mix the media above with the following reagents to make media with 8% fetal calf serum (FCS) or newborn calf serum (NCS). This is mixed in the tissue culture hood using sterile technique.
 1. Thaw the newborn calf serum (NCS), glutamine, and penicillin-Streptomycin solution in a 37° C water bath.
 2. Add the following volumes to 500 mL of cooled media:
 - a. 5 ml glutamine
 - b. 1 ml Pen-Strep
 - c. 45 ml NCS or FCS
 - d. 8 ml 7.5% sodium bicarbonate solution (sterile)
 - ii. From sterile premixed/prepackaged stock DMEM solution with sodium bicarbonate and without glutamine.
 1. Add the following to the media bottle
 - a. 5 ml glutamine
 - b. 1 ml Pen-Strep
 - c. 44 ml NCS or FCS

II. Initial Culturing Procedure

1. Obtain HEP-2 cells frozen in liquid nitrogen
2. Thaw the cells in 37° C water bath for approximately 5-10 minutes
3. Obtain a 75cm² flask
4. Pipette 10-15 ml media solution into flask
5. Pipette the cells into the flask
6. Swirl the flask gently
7. Incubate in 37° C incubator for 3-4 days

III. Subculture Procedure

1. Pre-warm the culture media and thaw in a tube of trypsin (trypsin/EDTA) in the warm water bath at 37° C.
2. Obtain a flask of sub-confluent cells, about 3-4 days since the last passage. Inspect the cells with the inverted microscope to make sure they are healthy and there is no contamination.
3. Using a vacuum or a pipette, thoroughly remove the medium from the flask and rinse the cells with Hanks Solution (without Calcium and Magnesium) twice.
4. Using a vacuum or a pipette, remove the Hanks Solution.
5. Add 1-1.5 ml of trypsin to each 25-cm² flask or 2 ml to each 75-cm² flask.
6. Incubate the cells at 37° C for 5-10 minutes. Inspect the cells periodically on the inverted microscope to make sure they are being dispersed.
7. During the time the cells are trypsinizing in the incubator; prepare new flasks with the appropriate label (Cell type, number of cells, your initials, date) on the top of the flask.

- a. For 25-cm² flasks, add 5 ml of media to each flask.
 - b. For 75-cm² flasks, add 10 ml of media to each flask.
 - c. If you are preparing to transfer the cells to 2-cm² titer well dishes, have the appropriate number of wells ready. DO NOT place media into the wells. Take note the number of wells that will be needed during this test. This amount will be used in step 10.c.
 - i. Note: Each material specimen and control specimen should be given its own well. A minimum of three replicates for each test sample and control sample is required.
8. After the incubation period, remove the flask from the incubator. In the fume hood, strike the sides of the flask to jar the cells loose. Inspect the flask to make sure the cells are coming off. The cells will detach from the flask in large aggregates.
 9. After the cells have detached from the flask surface, add 2-5 ml of fresh media to the cell suspension to inhibit the action of the trypsin.
 10. Break up the aggregate cells by pipetting them repeatedly (about 10-20 times) against the sides of the flask using a sterile cotton plugged Pasteur pipette. Be careful not to draw the cells up into the cotton of the pipette; that can result in the loss of cells and introduce contamination.
 11. At this stage the cells can be counted using the hemocytometer or the Coulter Counter.
 - a. If you use the hemocytometer count 4 large corner squares, take the average, and multiply by 10⁴ to determine the number of cells per ml in your cell suspension.
 - b. If you use the Coulter Counter, dilute the cell suspension 1:100 by taking 100 µl (0.1 ml) of cell suspension diluted with 9.9 ml of counting saline solution and count 100 µl or 500 µl on the Coulter Counter. Take an average of 3 or 4 counts and multiply the average by 1000 if your count 100 µl or 200 if you count 500 µl.
 12. From the cell concentration (cells/ml) that you determine in step 9, you will now make a dilution.
 - a. If you are using a 25 cm² flasks, make a dilution to give you 10⁵ cells/ml and put one ml in each flask.
 - b. If you are using a 75 cm² flasks, make a dilution to give you 3x10⁵ cells/ml and put one ml in each flask
 - c. If you are using a 2 cm² wells, make a dilution to give you 3x10⁴ cells/ml. Prepare enough solution to fill all required wells as each well requires 1ml of the cell solution. Using a 1mL serological pipette and a propipettor, transfer 1 ml of the cell solution into each titer well vessels.
 13. Incubate the sub-culture at 37 ±2° C in air with or without 5% carbon dioxide as appropriate for the buffer system chosen for the culture medium. Each flask/well should be incubated for 3-4 days.

14. Return all reagents to the refrigerator or freezer and clean up the work area with alcohol. Make sure there are no glass pipettes in the wastebaskets. They should be disposed of in the appropriate glass waste receptacle.

IV. Implantation of Test Specimens

1. Obtain 2-cm² titer well dishes with sub-confluent cells that have completed the initial incubation period.
2. Verify the subconfluency and morphology of the cell culture with a microscope before starting the test.
3. Remove and discard culture medium.
4. Carefully place individual specimens of the test sample on the cell layer in the center of each titer well. Use precaution to prevent unnecessary movement of the specimens, as this could possibly dislodge or cause physical trauma to the cells.
 - a. Note: Verify that each specimen lies flat on the bottom of each well to help ensure proper contact with the cells, and does not float on top of the media. For larger specimens, prepare a small well of media separate from those of the cell cultures. Dip the specimens in the media before implanting the specimen into the well with the cell culture. This will help break the surface tension of the material and help ensure proper exposure/contact with the cells.
5. Add 1ml of fresh culture medium to each vessel.
6. Prepare replicate vessels for both the positive and negative control specimens.
7. Incubate the sub-culture with the material specimens at 37 ±2° C in air with or without 5% carbon dioxide as appropriate to for the buffer system chosen for the culture medium. The wells should be incubated for 1-2 days.
8. Clean laboratory space and discard of any waste properly.
9. Once the cells have been exposed to the specimens for the desired amount of time, discard the supernatant culture medium and determine the cytotoxic effects as outlined below.

V. Evaluation of Cells

- A. Qualitative Evaluation: Inverted Light Microscope
 1. Obtain 2-cm² titer well dishes with cells that have completed the appropriate specimen expose period.
 2. Place the titer plate onto an inverted light microscope and look for lysed cells. If the content of the well is very cloudy, this is a sign that the cells have lysed. Some dead cells may also look shriveled. Also note spacing of cells and general morphology as compared that of the controls.
 3. Record findings.
- B. Quantitative Evaluation: Coulter Counter Cell Counting
 1. Obtain 2-cm² titer well dishes with cells that have completed the appropriate specimen expose period.
 2. Remove media from titer wells that are to be examined.
 3. Wash cells with .5 ml of Hank's solution and remove hanks solution.
 4. Repeat Hanks wash.

5. Add 0.15 ml of trypsin to each well.
6. Incubate the cells at 37° C for 10 minutes. Inspect the cells periodically on the inverted microscope to make sure they are being dispersed.
7. Pipette 9.9 ml of counting saline solution into provided capped vials. Prepare one vial per-well being tested.
8. After the incubation period remove the cells from the incubator and add 0.7 ml of media to each well.
9. Break up the aggregate cells by pipetting them repeatedly (about 10-20 times) against the sides of the flask using a sterile cotton plugged Pasteur pipette. Be careful not to draw the cells up into the cotton of the pipette; that can result in the loss of cells and introduce contamination.
10. Carefully remove the test specimen from the titer well and dispose of appropriately.
11. Dilute the cell suspension by pipetting 0.1 ml (100 µl) of the cell suspension into the 9.9 ml saline solution vial.
12. Place the vial into the Coulter Counter and take 3 to 4 counts per vial.
13. Record the data and take an average of the counts. Multiply that average by 1000 (dilution factor) to determine the average number of cells per ml.
 1. Repeat for next specimen.

Note:

- If there are evident differences in the test result for replicate culture vessels, then the test is either inappropriate or invalid
- If the negative, positive or any other controls do not have the expected responses in the test system then repeat the assay.
- If results are inconsistent among replicates or invalid, the tests shall be repeated. ⁽¹⁰⁾

Data Collection Sheet:

Specimen Type: _____

1. Qualitative Evaluation

- a. General observations of general morphology, vacuolization, detachment, cell lysis, membrane integrity, and general changes in size, shape and configuration of these cells:

- b. Estimated Cytotoxic value based on Cytotoxicity Scale (Table 1).

2. Quantitative Analysis

- a. Hemocytometer Results

	Square 1	Square 2	Square 3	Square 4	Average Value for Sample
Sample 1					
Sample 2					
Sample 3					
Sample 4					
Sample 5					
Overall Average Value of Specimen Type					

- b. Coulter Counter Results

	Coulter Counter Value
Sample 1	
Sample 2	
Sample 3	
Sample 4	
Sample 5	
Overall Average Value	

APPENDIX B – GLOSSARY OF BIOLOGICAL TERMS

1. biocompatibility – the inherent ability of a material to elicit an appropriate host response.
2. cytotoxicity – the measure of the toxic reaction of cells to a material.
3. titer well – small incubation vessel for cytotoxicity testing.
4. confluency – the state when 100% of the surface area of the incubation vessel is covered in cells.
5. subconfluency – the state when between 80% to 99% of the surface area of the incubation vessel is covered in cells.
6. positive cytotoxicity control – a specimen that elicits a known toxic response from cells.
7. negative cytotoxicity control – a specimen that elicits a known non-toxic response from cells.
8. Coulter counter – a device that utilizes the Coulter principle to count particles and cells.
9. vacuolization – the state when cellular cytoplasm fills with small cavities.
10. lysis – the dissolution or destruction of cells.
11. nonconfluency – the state when less than 80% of the surface area of the incubation vessel is covered in cells.
12. interconnectivity – the state of cell membranes being in intimate contact.

APPENDIX C – XRD RESULTS

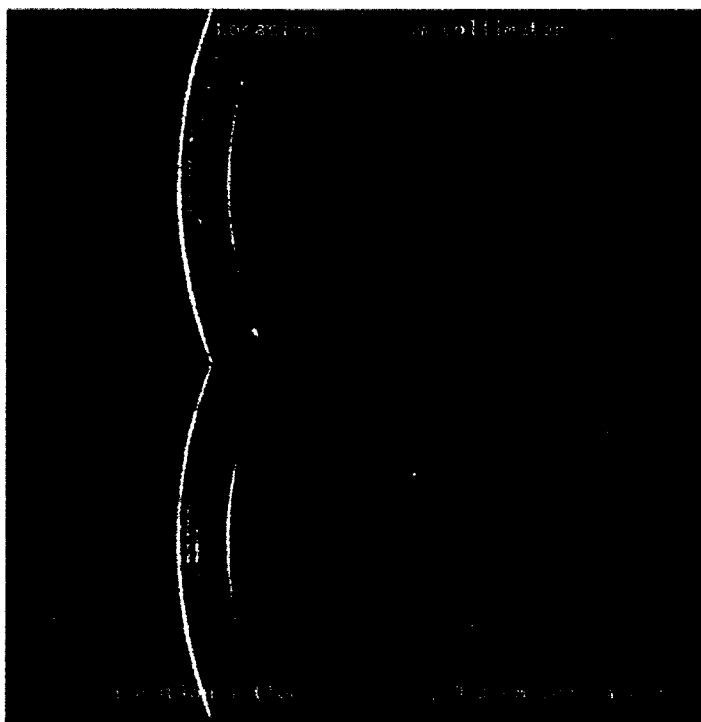


Figure 69. Two Dimensional Detector Frames from the base material.

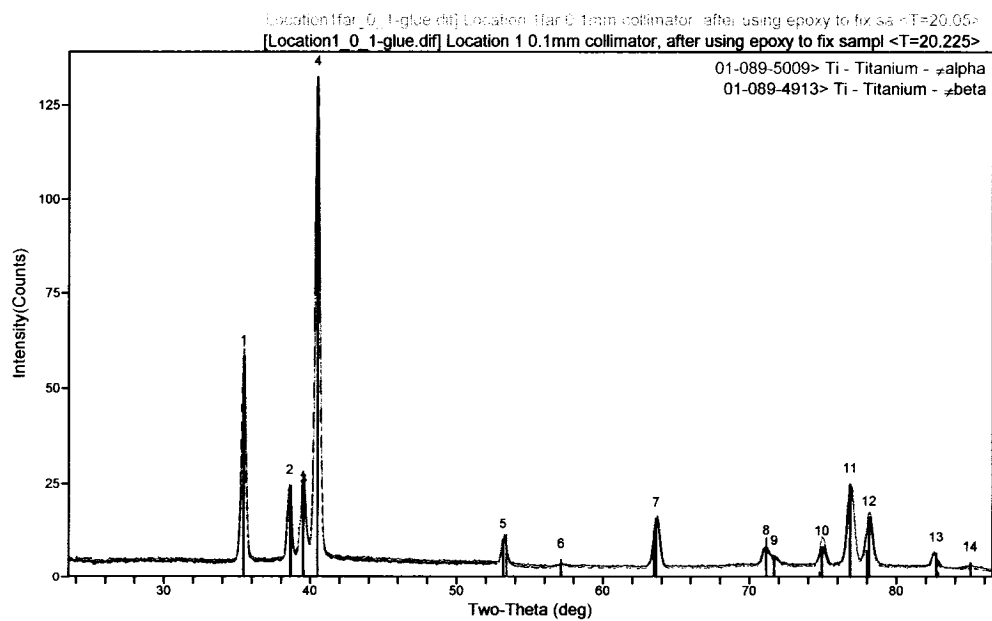


Figure 70. Spectrum for the base material.

Peak ID Extended Report (14 Peaks, Max P/N = 5.4)

[Location1_0_1-glue.dif] Location 1 0.1mm collimator, after using epoxy to fix sample
<T=20.225>

PEAK: 15-pts/Parabolic Filter, Threshold=1.0, Cutoff=0.1%, BG=3/1.0, Peak-
Top=Summit

2-Theta	d(θ)	Height	Height%	Phase ID	d(θ)	I%	(h k l)	2-Theta	Delta
35.461	2.5294	53.9	43.6	Ti	2.5326	26.1	(1 0 0)	35.414	-0.046
38.615	2.3297	18.3	14.8	Ti	2.3241	25.9	(0 0 2)	38.712	0.097
39.539	2.2774	13.3	10.7	Ti	2.279	100	(1 1 0)	39.51	-0.029
40.499	2.2256	123.6	100	Ti	2.2247	100	(1 0 1)	40.515	0.016
53.187	1.7207	6.5	5.2	Ti	1.7141	12	(1 0 2)	53.407	0.22
57.14	1.6107	1.8	1.4	Ti	1.6115	12.7	(2 0 0)	57.11	-0.03
63.624	1.4613	12.9	10.4	Ti	1.4645	11.9	(1 1 0)	63.467	-0.157
71.14	1.3242	4.6	3.7	Ti	1.3238	11.1	(1 0 3)	71.166	0.026
71.7	1.3152	1.9	1.6	Ti	1.3158	20.2	(2 1 1)	71.667	-0.033
74.943	1.2662	4.7	3.8	Ti	1.2687	1.5	(2 0 0)	74.766	-0.176
76.862	1.2393	20.4	16.5	Ti	1.2399	10.8	(1 1 2)	76.812	-0.05
78.143	1.2221	11.8	9.6	Ti	1.2242	7.7	(2 0 1)	77.987	-0.155
82.737	1.1655	3.6	2.9	Ti	1.1641	1.4	(0 0 4)	82.857	0.119
85.057	1.1396	1.6	1.3	Ti	1.1395	5.2	(2 2 0)	85.063	0

Peak Search Report (14 Peaks, Max P/N = 5.4)

[Location1_0_1-glue.dif] Location 1 0.1mm collimator, after using epoxy to fix sample
<T=20.225>

PEAK: 15-pts/Parabolic Filter, Threshold=1.0, Cutoff=0.1%, BG=3/1.0, Peak-
Top=Summit

2-Theta	d(θ)	BG	Height	H%	Area	A%	FWHM	XS(Å)
35.461	2.5294	4.5	53.9	43.6	507.2	42.3	0.32	>5000
38.615	2.3297	6.2	18.3	14.8	155.5	13	0.289	>5000
39.539	2.2774	8.9	13.3	10.7	134.6	11.2	0.345	1331
40.499	2.2256	8.8	123.6	100	1197.8	100	0.33	2403
53.187	1.7207	3.7	6.5	5.2	76.1	6.4	0.4	693
57.14	1.6107	3.1	1.8	1.4	3.5	0.3	0.335	>5000
63.624	1.4613	3	12.9	10.4	170.4	14.2	0.45	562
71.14	1.3242	3.8	4.6	3.7	77.2	6.4	0.57	338
71.7	1.3152	3.7	1.9	1.6	3.9	0.3	0.38	>5000
74.943	1.2662	3.5	4.7	3.8	63.2	5.3	0.458	819
76.862	1.2393	4.5	20.4	16.5	276.2	23.1	0.461	889
78.143	1.2221	4.4	11.8	9.6	156.3	13.1	0.45	1162
82.737	1.1655	3	3.6	2.9	39.5	3.3	0.37	>5000
85.057	1.1396	2.5	1.6	1.3	3.2	0.3	0.442	>5000

Calculate Lattice Constants from Peak Locations and Miller Indices [Hexagonal]

2-Theta	d(θ)	h	k	l	a-Axis	c-Axis
35.461	2.5294	1	0	0	2.9207	
38.615	2.3297	0	0	2		4.6594
40.499	2.2256	1	0	1	2.9207	4.6836
53.187	1.7207	1	0	2	2.9207	4.6954
63.624	1.4613	1	1	0	2.9226	
76.862	1.2393	1	1	2	2.9207	4.6852

Average Lattice Constants = 2.9211 4.6809

Calculate Lattice Constants from Peak Locations and Miller Indices [Cubic]

2-Theta	d(θ)	h	k	l	a-Axis
39.539	2.2774	1	1	0	3.2207
57.14	1.6107	2	0	0	3.2214

Average Lattice Constants = 3.2211

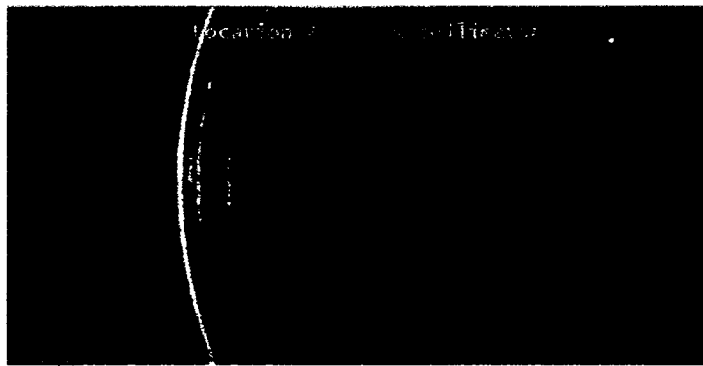


Figure 71. Two Dimensional Detector Frames from the heat affected zone.

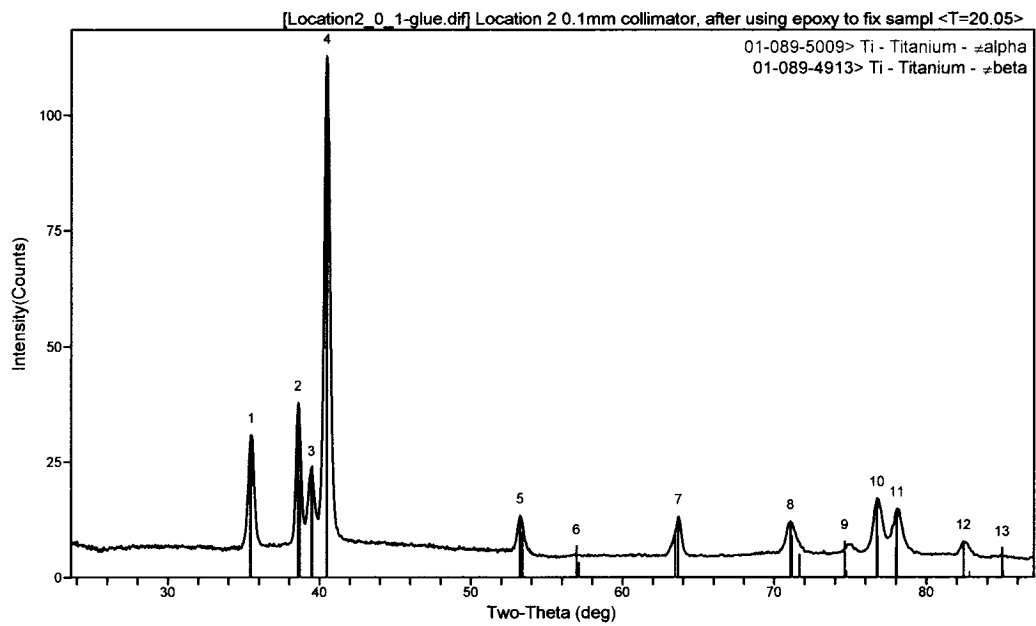


Figure 72. Spectrum for the heat affected zone.

Peak ID Extended Report (13 Peaks, Max P/N = 4.7)

[Location2_0_1-glue.dif] Location 2 0.1mm collimator, after using epoxy to fix sample <T=20.05>

PEAK: 17-pts/Parabolic Filter, Threshold=1.0, Cutoff=0.1%, BG=3/1.0, Peak-Top=Summit

2-Theta	d(θ)	Height	Height%	Phase ID	d(θ)	I%	(h k l)	2-Theta	Delta
35.482	2.5279	24.3	24.1	Ti	2.5326	26.1	(1 0 0)	35.414	-0.067
38.6	2.3306	27.4	27.2	Ti	2.3241	25.9	(0 0 2)	38.712	0.112
39.477	2.2808	10.4	10.4	Ti	2.279	100	(1 1 0)	39.51	0.033
40.481	2.2265	100.8	100	Ti	2.2247	100	(1 0 1)	40.515	0.034
53.241	1.7191	8.1	8	Ti	1.7141	12	(1 0 2)	53.407	0.166
56.972	1.6151	2.1	2.1	Ti	1.6115	12.7	(2 0 0)	57.11	0.138
63.682	1.4601	8.5	8.4	Ti	1.4645	11.9	(1 1 0)	63.467	-0.215
71.08	1.3252	6.6	6.6	Ti	1.3238	11.1	(1 0 3)	71.166	0.086
74.636	1.2706	2.3	2.3	Ti	1.2687	1.5	(2 0 0)	74.766	0.131
76.762	1.2406	9.8	9.7	Ti	1.2399	10.8	(1 1 2)	76.812	0.051
78.082	1.2229	7.3	7.3	Ti	1.2242	7.7	(2 0 1)	77.987	-0.095
82.442	1.1689	2.9	2.9						
84.987	1.1403	2.1	2	Ti	1.1395	5.2	(2 2 0)	85.063	0.076

Peak Search Report (13 Peaks, Max P/N = 4.7)

[Location2_0_1-glue.dif] Location 2 0.1mm collimator, after using epoxy to fix sample <T=20.05>

PEAK: 17-pts/Parabolic Filter, Threshold=1.0, Cutoff=0.1%, BG=3/1.0, Peak-Top=Summit

2-Theta	d(θ)	BG	Height	H%	Area	A%	FWHM	XS(Å)
35.482	2.5279	6.6	24.3	24.1	292.7	25.5	0.41	531
38.6	2.3306	10.5	27.4	27.2	232.1	20.2	0.288	>5000
39.477	2.2808	13.3	10.4	10.4	87.1	7.6	0.283	>5000
40.481	2.2265	12.1	100.8	100	1149.9	100	0.388	664
53.241	1.7191	5.3	8.1	8	109.9	9.6	0.461	425
56.972	1.6151	4.6	2.1	2.1	4.3	0.4	0.334	>5000
63.682	1.4601	4.8	8.5	8.4	115.9	10.1	0.466	499
71.08	1.3252	5.5	6.6	6.6	126.7	11	0.649	254
74.636	1.2706	5.4	2.3	2.3	4.7	0.4	0.393	>5000
76.762	1.2406	7.3	9.8	9.7	146.5	12.7	0.509	553
78.082	1.2229	7.5	7.3	7.3	115.5	10	0.535	486
82.442	1.1689	4.8	2.9	2.9	48.7	4.2	0.563	476
84.987	1.1403	4.2	2.1	2	4.1	0.4	0.442	>5000

Calculate Lattice Constants from Peak Locations and Miller Indices [Hexagonal]

2-Theta	d(θ)	h	k	l	a-Axis	c-Axis
35.482	2.5279	1	0	0	2.919	
38.6	2.3306	0	0	2		4.6611
40.481	2.2265	1	0	1	2.919	4.7017
53.241	1.7191	1	0	2	2.919	4.6894
63.682	1.4601	1	1	0	2.9202	
76.762	1.2406	1	1	2	2.919	4.7107

Average Lattice Constants = 2.9193 4.6907

Calculate Lattice Constants from Peak Locations and Miller Indices [Cubic]

2-Theta	d(θ)	h	k	l	a-Axis
39.477	2.2808	1	1	0	3.2256
56.799	1.6196	2	0	0	3.2391

Average Lattice Constants = 3.2324

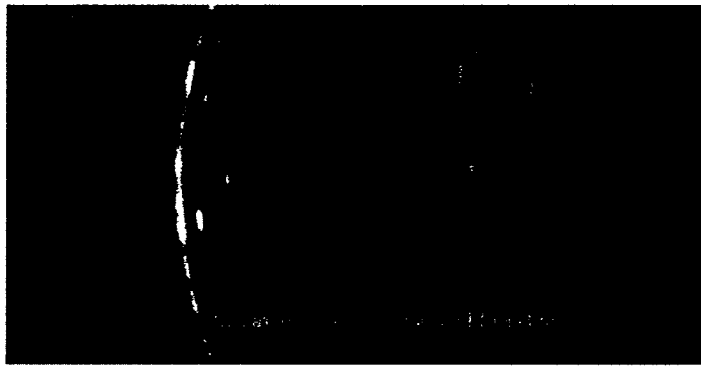


Figure 73. Two Dimensional Detector Frames from the fusion zone.

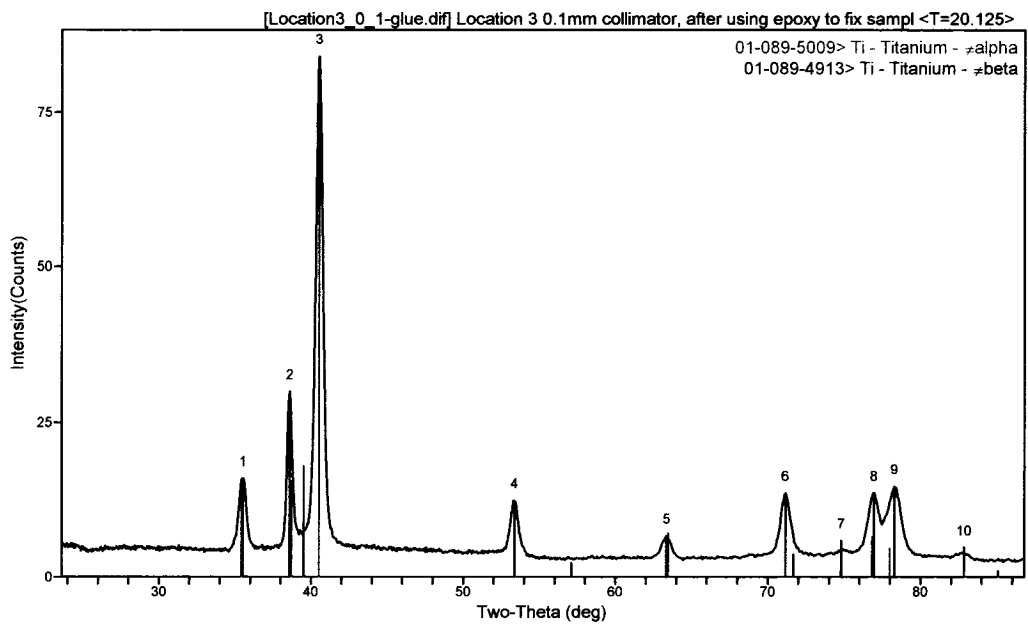


Figure 74. Spectrum for the fusion zone.

Peak ID Extended Report (10 Peaks, Max P/N = 4.2)

[Location3_0_1-glue.dif] Location 3 0.1mm collimator, after using epoxy to fix sample
<T=20.125>

PEAK: 21-pts/Parabolic Filter, Threshold=1.0, Cutoff=0.1%, BG=3/1.0, Peak-
Top=Summit

2-Theta	d(θ)	Height	Height%	Phase ID	d(θ)	I%	(h k l)	2-Theta	Delta
35.52	2.5253	11.4	14.8	Ti	2.5326	26.1	(1 0 0)	35.414	-0.105
38.598	2.3307	23.9	31	Ti	2.3241	25.9	(0 0 2)	38.712	0.114
40.52	2.2245	77.1	100	Ti	2.2247	100	(1 0 1)	40.515	-0.005
53.359	1.7156	8.5	11	Ti	1.7141	12	(1 0 2)	53.407	0.048
63.36	1.4667	3.7	4.8	Ti	1.4645	11.9	(1 1 0)	63.467	0.107
71.16	1.3239	9.5	12.3	Ti	1.3238	11.1	(1 0 3)	71.166	0.006
74.8	1.2682	2	2.6	Ti	1.2687	1.5	(2 0 0)	74.766	-0.034
76.957	1.238	6.2	8	Ti	1.2399	10.8	(1 1 2)	76.812	-0.145
78.283	1.2203	7.7	10	Ti	1.2242	7.7	(2 0 1)	77.987	-0.295
82.84	1.1643	1.8	2.3	Ti	1.1641	1.4	(0 0 4)	82.857	0.017

Peak Search Report (10 Peaks, Max P/N = 4.2)

[Location3_0_1-glue.dif] Location 3 0.1mm collimator, after using epoxy to fix sample
<T=20.125>

PEAK: 21-pts/Parabolic Filter, Threshold=1.0, Cutoff=0.1%, BG=3/1.0, Peak-
Top=Summit

2-Theta	d(θ)	BG	Height	H%	Area	A%	FWHM	XS(Å)
35.52	2.5253	4.6	11.4	14.8	176.2	15.6	0.525	278
38.598	2.3307	6.1	23.9	31	249.4	22.1	0.355	1064
40.52	2.2245	6.9	77.1	100	1130.9	100	0.499	315
53.359	1.7156	3.9	8.5	11	138	12.2	0.551	279
63.36	1.4667	3.1	3.7	4.8	70.8	6.3	0.657	223
71.16	1.3239	4.1	9.5	12.3	178.8	15.8	0.64	262
74.8	1.2682	4	2	2.6	4	0.4	0.393	>5000
76.957	1.238	7.4	6.2	8	100	8.8	0.548	434
78.283	1.2203	7	7.7	10	160.2	14.2	0.707	243
82.84	1.1643	3.1	1.8	2.3	3.5	0.3	0.431	>5000

Calculate Lattice Constants from Peak Locations and Miller Indices [Hexagonal]

2-Theta	d(θ)	h	k	l	a-Axis	c-Axis
35.52	2.5253	1	0	0	2.916	
38.598	2.3307	0	0	2		4.6614
40.52	2.2245	1	0	1	2.916	4.6995
53.359	1.7156	1	0	2	2.916	4.6758
71.16	1.3239	1	0	3	2.916	4.664
78.283	1.2203	2	0	1	2.916	4.7511

Average Lattice Constants = 2.9160 4.6904

PDF#01-089-4913: QM=Calculated(C); d=Calculated; I=Calculated

Titanium - β -Ti

Ti

Radiation=CuK α 1

Lambda=1.54060

Filter=

Calibration=

2 θ =38.758-83.155

I/Ic(RIR)=9.61

Ref: Calculated from ICSD using POWD-12++

Cubic - Powder Diffraction, Im-3m (229)

Z=2

mp=

CELL: 3.283 x 3.283 x 3.283 <90.0 x 90.0 x 90.0>

P.S=cI2 (\$GB) (?)

Density(c)=4.495

Density(m)=4.49A

Mwt=47.90

Vol=35.38

F(4)=999.9(.0000,4/0)

Ref: Levinger, B.W.

J. Met., v5 p195 (1953)

Strong Lines: 2.32/X 1.34/2 1.64/1 1.16/1

FIZ=076165: TEM 298.

M Cell at 1173 K: 3.312.

M Stable above 1155 K.

M PDF 00-044-1288.

No R value given.

At least one TF missing.

Lattice parameters of beta titanium at room temperature Cell from Z.

Kristallogr., Kristallogeom., Kristallphys., Kristallchem., 94 299-300 (1936): 3.32 at 1173 K.

a (IM3-M) N

2-Theta	d(θ)	I(f)	(hkl)	Theta	1/(2d)	2 π /d	n ²
38.758	2.3214	100	(110)	19.379	0.2154	2.7066	2
55.973	1.6415	12.7	(200)	27.986	0.3046	3.8277	4
70.161	1.3403	20.2	(211)	35.081	0.3731	4.688	6
83.155	1.1607	5.2	(220)	41.578	0.4308	5.4132	8

PDF#01-089-5009: QM=Calculated(C); d=Calculated; I=Calculated

Titanium - α

Ti

Radiation=CuK α 1

Lambda=1.54060

Filter=

Calibration=

2 θ =35.171-86.971

I/I_c(RIR)=6.43

Ref: Calculated from ICSD using POWD-12++

Hexagonal - (Unknown), P63/mmc (194)

Z=2

mp=

CELL: 2.944 x 2.944 x 4.678 <90.0 x 90.0 x 120.0>

P.S=hP2 (\$GA) (?)

Density(c)=4.530

Density(m)=4.49A

Mwt=47.90

Vol=35.11

F(11)=999.9(.0000,11/0)

Ref: Rostoker, W.

J. Met., v4 p981 (1952)

Strong Lines: 2.24/X 2.55/3 2.34/3 1.72/1 1.47/1 1.33/1 1.25/1 1.23/1

FIZ=076265: M PDF 00-044-1294.

M Cell with 17.9% O: 2.953, 4.760, with 34% O: 2.955, 4.

No R value given.

At least one TF missing.

See PDF 01-089-2762.

Observations on the lattice parameters of the α and Ti O phases in the titanium-oxygen system Cell from Z.

Phys.

Chem.

(B), 11 433-455 (1930): 2.953, 4.729.

c (P63/MMC) N

2-Theta	d(0)	I(f)	(h k l)	Theta	1/(2d)	2 π /d	n ²
35.171	2.5496	26.1	(1 0 0)	17.585	0.1961	2.4644	
38.456	2.339	25.9	(0 0 2)	19.228	0.2138	2.6863	
40.252	2.2387	100	(1 0 1)	20.126	0.2233	2.8066	
53.092	1.7236	12	(1 0 2)	26.546	0.2901	3.6454	
63.108	1.472	11.9	(1 1 0)	31.554	0.3397	4.2685	
70.768	1.3303	11.1	(1 0 3)	35.384	0.3759	4.7233	
74.35	1.2748	1.5	(2 0 0)	37.175	0.3922	4.9288	
76.385	1.2458	10.8	(1 1 2)	38.192	0.4013	5.0434	
77.553	1.2299	7.7	(2 0 1)	38.777	0.4065	5.1085	
82.394	1.1695	1.4	(0 0 4)	41.197	0.4275	5.3725	
86.971	1.1193	1.7	(2 0 2)	43.485	0.4467	5.6133	

APPENDIX D – XPS SURVEY SPECTRA RESULTS

C07N7289_10.spe: SJSU-Croom: SJSU-Croom			EAG
2007 May 7	Al mono	101.4 W 100.0 μ 45.0° 187.85 eV	1.0445e+005 max 39.44 min
Su 1s/Area3: Control/1			

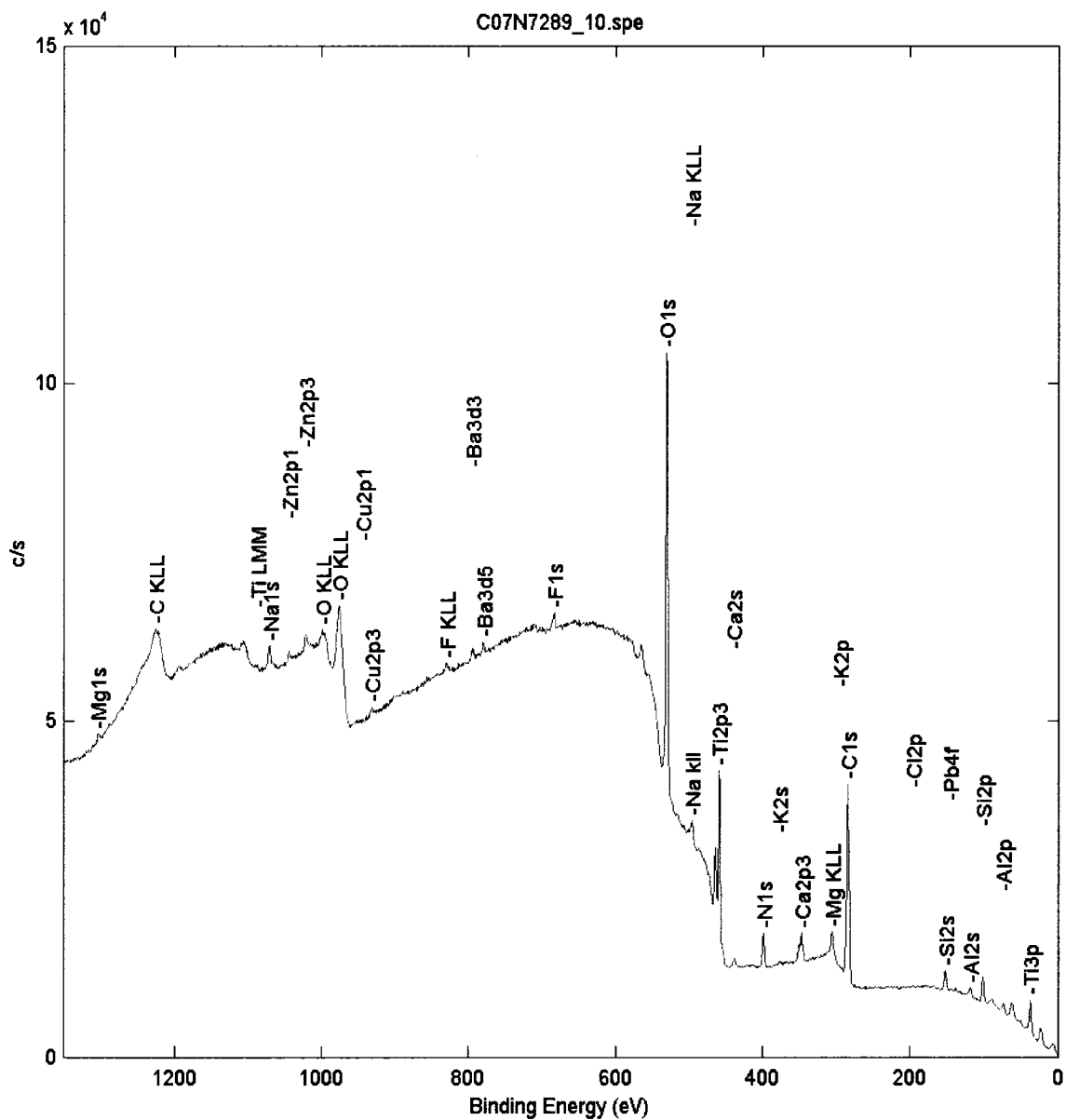


Figure 75. XPS chemical composition survey spectrum for the control.

C07N7289_11.spe: SJSU-Croom: SJSU-Croom EAG
 2007 May 7 Al mono 101.4 W 100.0 μ 45.0° 187.85 eV 1.1176e+005 max 39.44 min
 Su 1s/Area2: #1/1

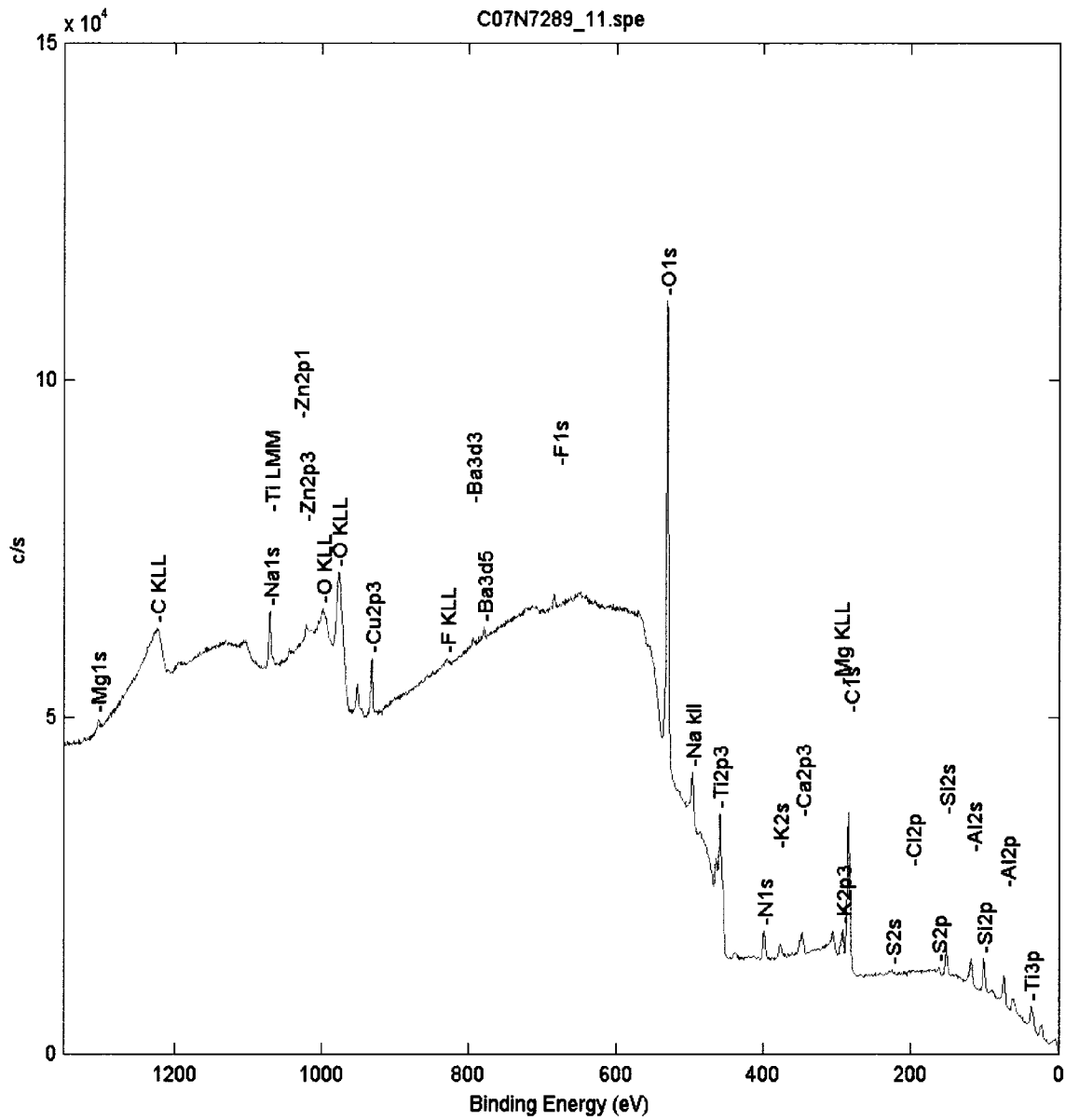


Figure 76. XPS chemical composition survey spectrum for weld 1.

C07N7289_12.spe: SJSU-Croom: SJSU-Croom EAG
 2007 May 7 Al mono 101.4 W 100.0 μ 45.0° 187.85 eV 1.0800e+005 max 39.44 min
 Su 1s/Area4: #2/1

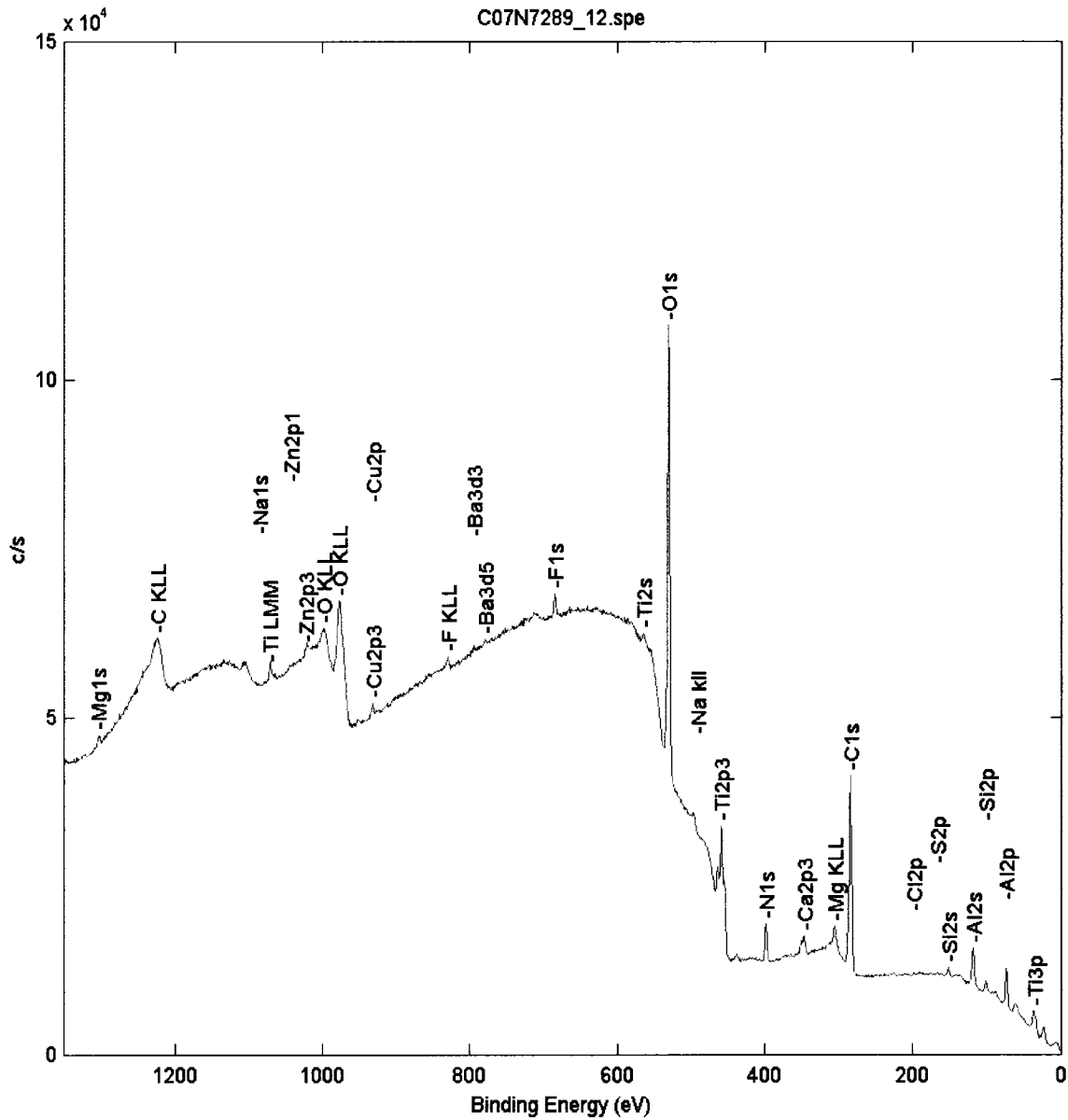


Figure 77. XPS chemical composition survey spectrum for weld 2.

C07N7289_13.spe: SJSU-Croom: SJSU-Croom EAG
 2007 May 7 Al mono 101.4 W 100.0 μ 45.0° 187.85 eV 9.5334e+004 max 39.44 min
 Su 1s/Area5: #3/1

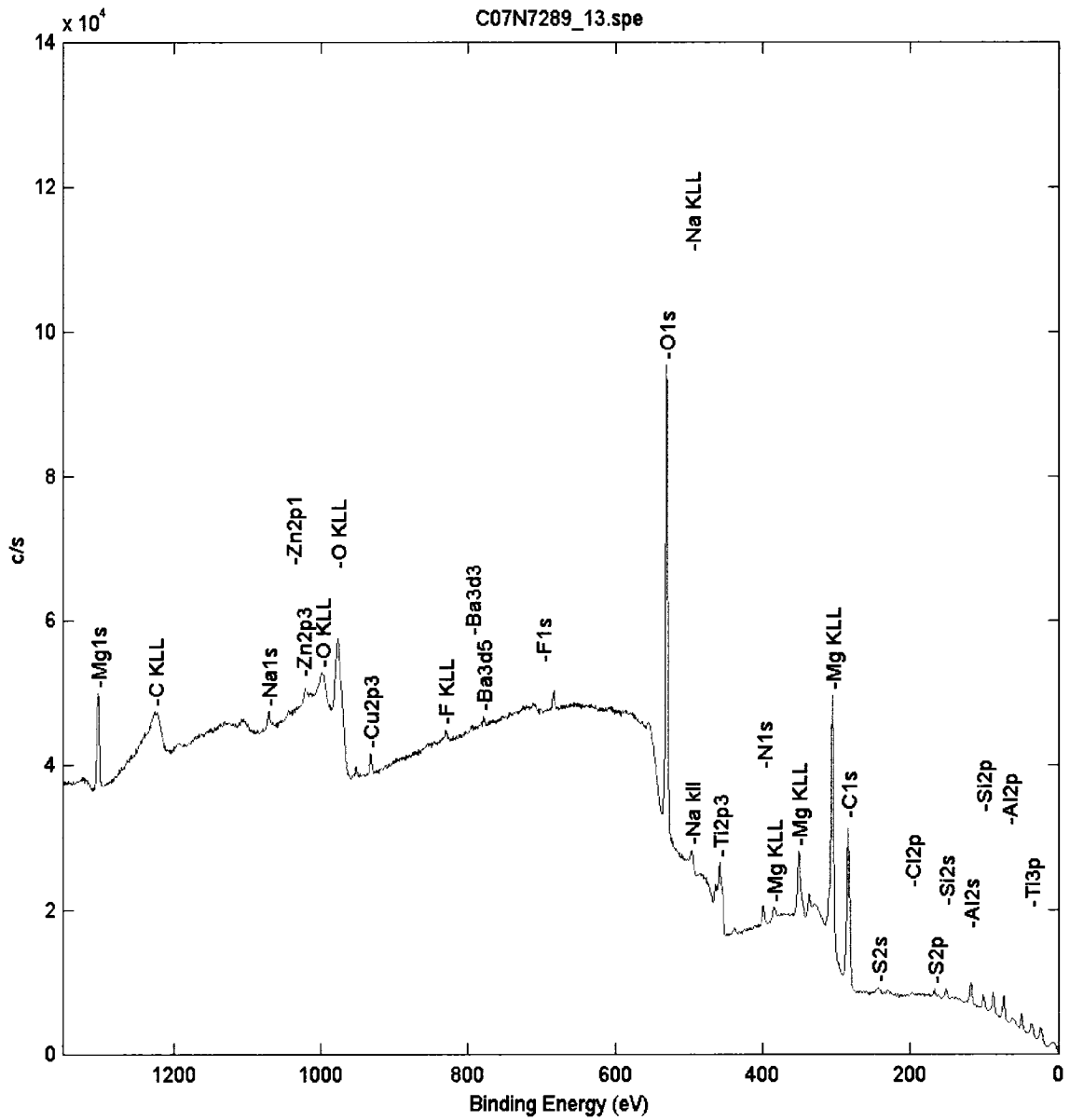


Figure 78. XPS chemical composition survey spectrum for weld 3.

C07N7289_14.spe: SJSU-Croom: SJSU-Croom EAG
 2007 May 7 Al mono 101.4 W 100.0 μ 45.0° 187.85 eV 1.0259e+005 max 39.44 min
 Su 1s/Area6: #4/1

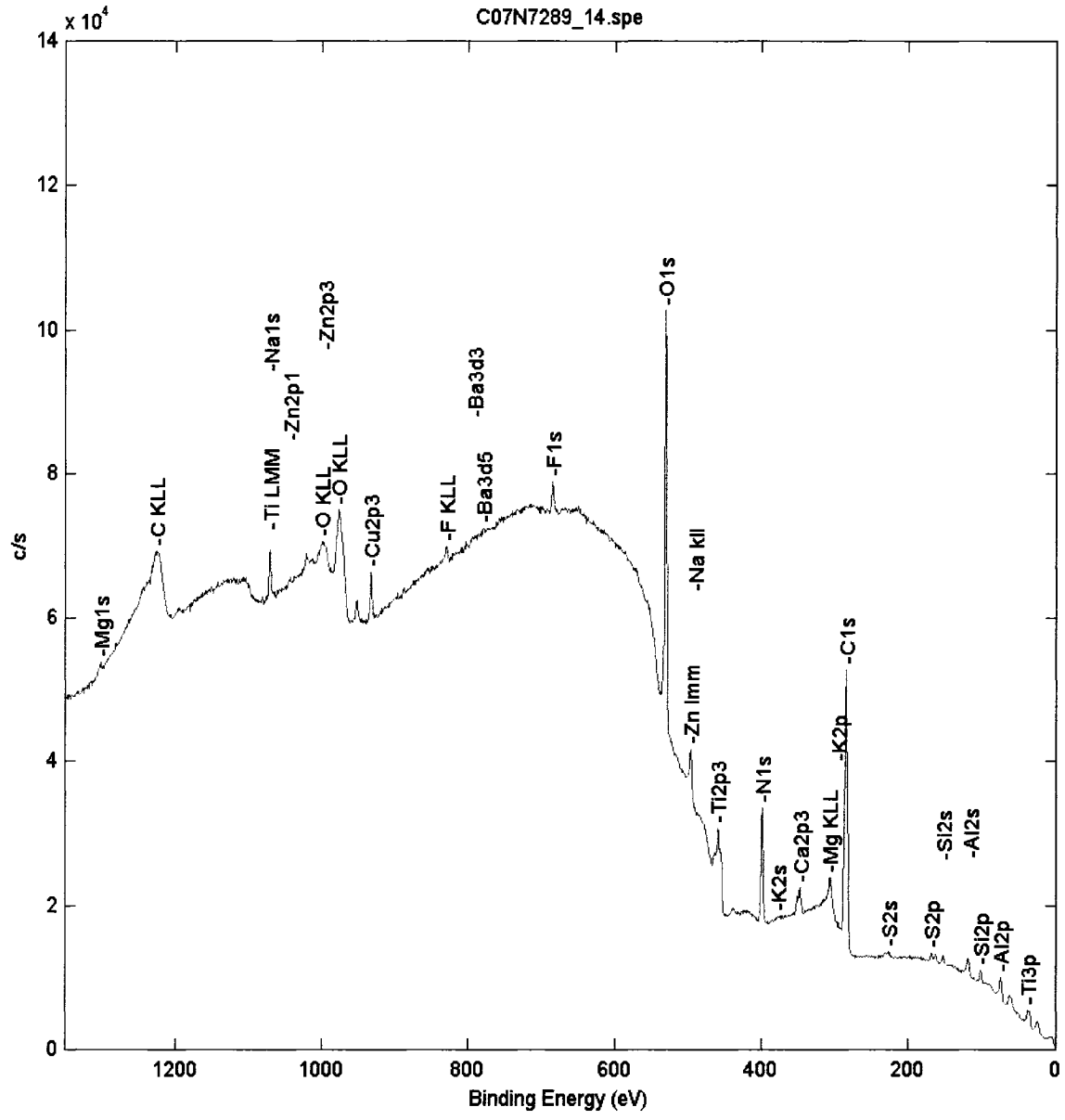


Figure 79. XPS chemical composition survey spectrum for weld 4.

C07N7289_15.spe: SJSU-Croom: SJSU-Croom EAG
 2007 May 8 Al mono 101.4 W 100.0 μ 45.0° 187.85 eV 1.2959e+005 max 39.44 min
 Su 1s/Area7: #5/1

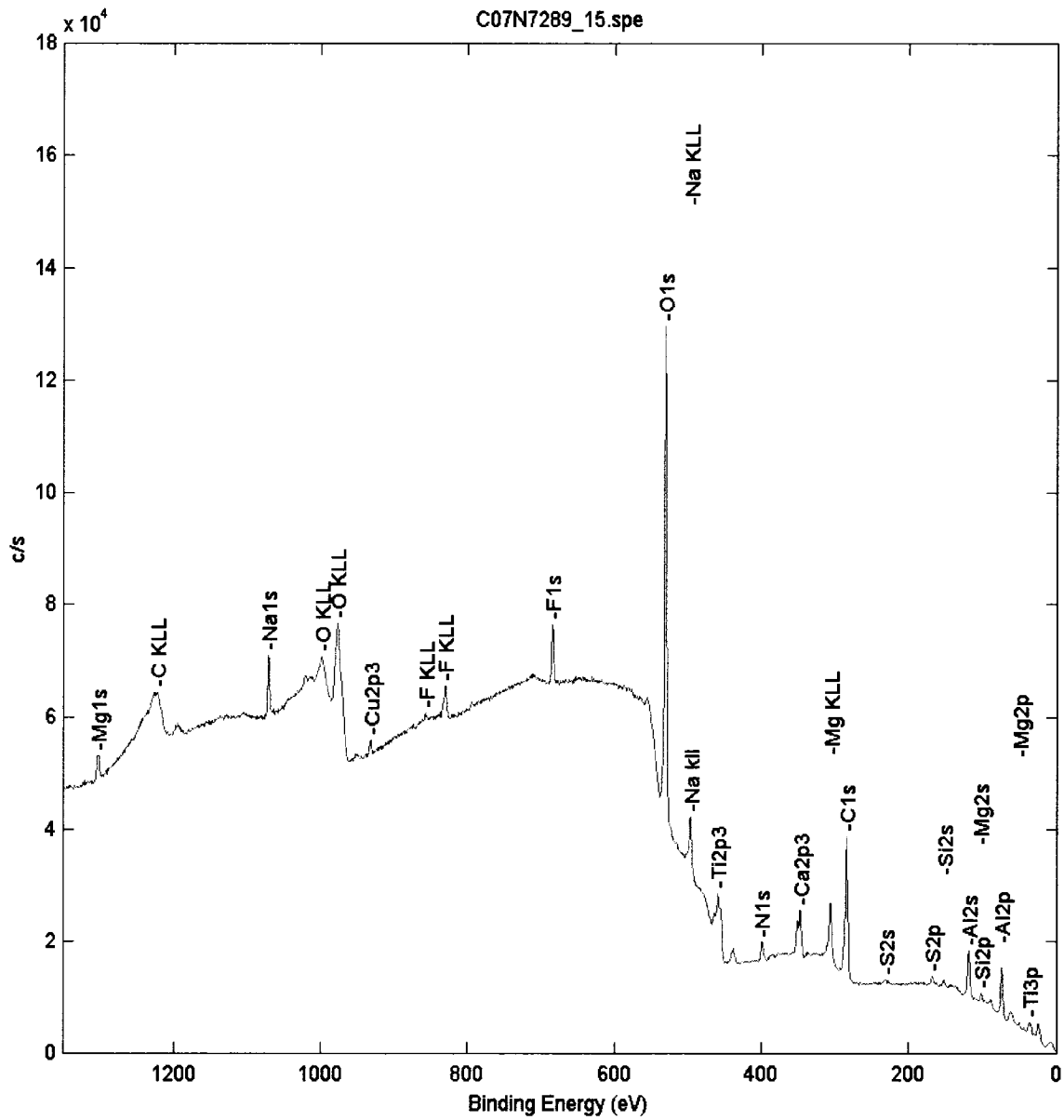


Figure 80. XPS chemical composition survey spectrum for weld 5.

C07N7289_16.spe: SJSU-Croom: SJSU-Croom EAG
 2007 May 8 Al mono 101.4 W 100.0 μ 45.0° 187.85 eV 1.4307e+005 max 39.44 min
 Su 1s/Area8: #6/1

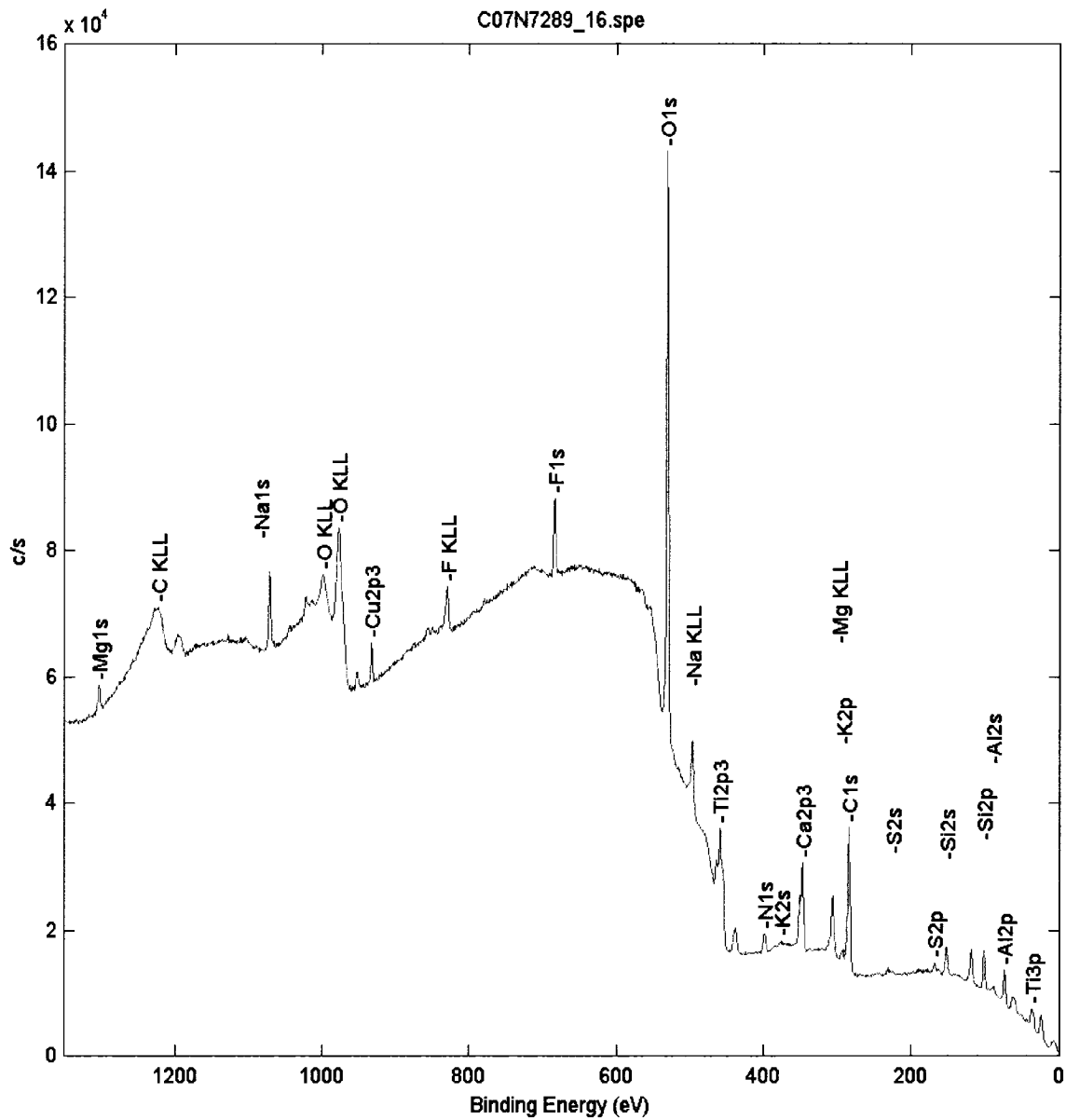


Figure 81. XPS chemical composition survey spectrum for weld 6.

C07N7289_17.spe: SJSU-Croom: SJSU-Croom EAG
 2007 May 8 Al mono 101.4 W 100.0 μ 45.0° 187.85 eV 1.4942e+005 max 39.44 min
 Su 1s/Area9: #7/1

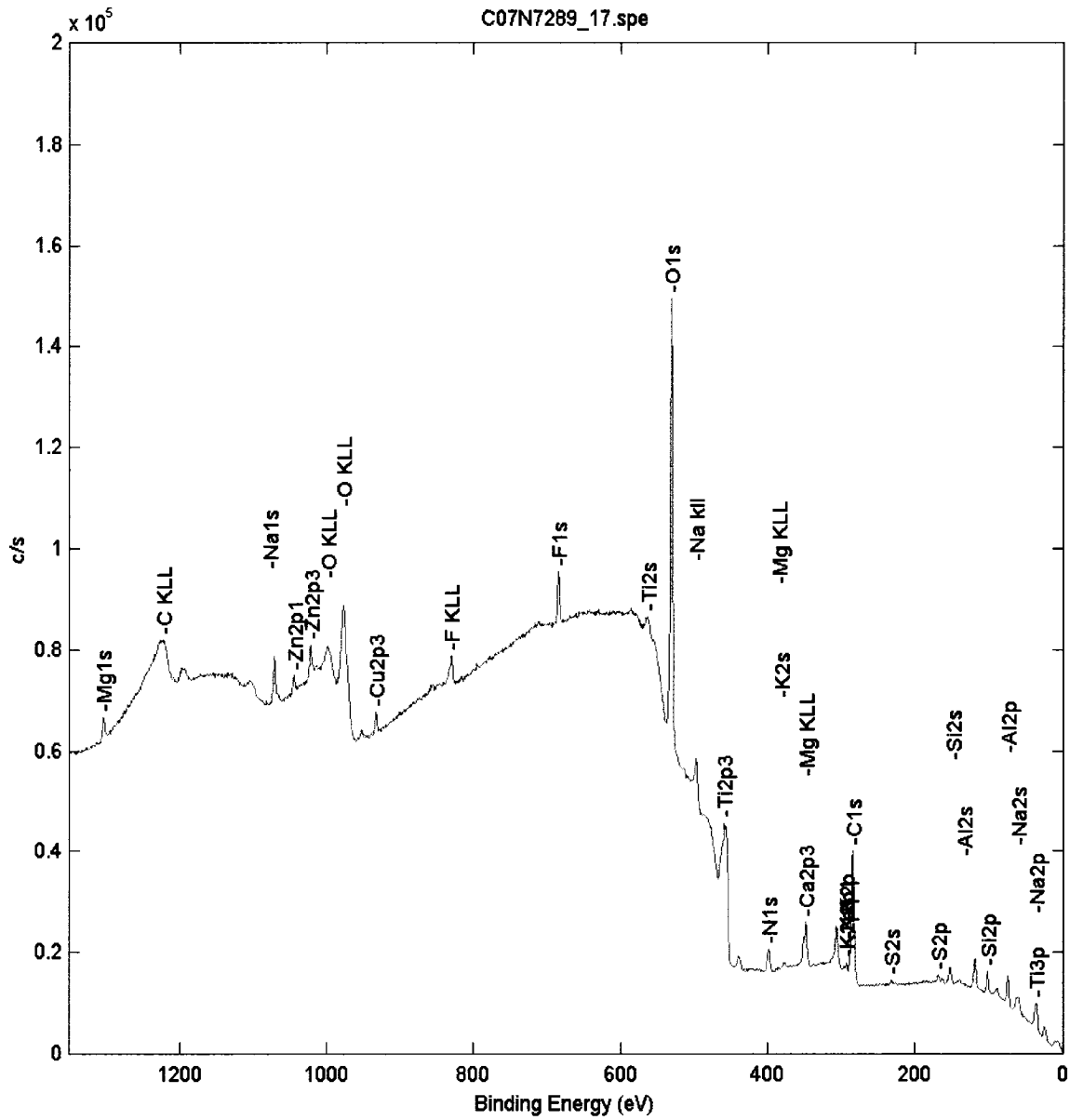


Figure 82. XPS chemical composition survey spectrum for weld 7.

C07N7289_18.spe: SJSU-Croom: SJSU-Croom EAG
 2007 May 8 Al mono 101.4 W 100.0 μ 45.0° 187.85 eV 1.2581e+005 max 39.44 min
 Su 1s/Area10: #8/1

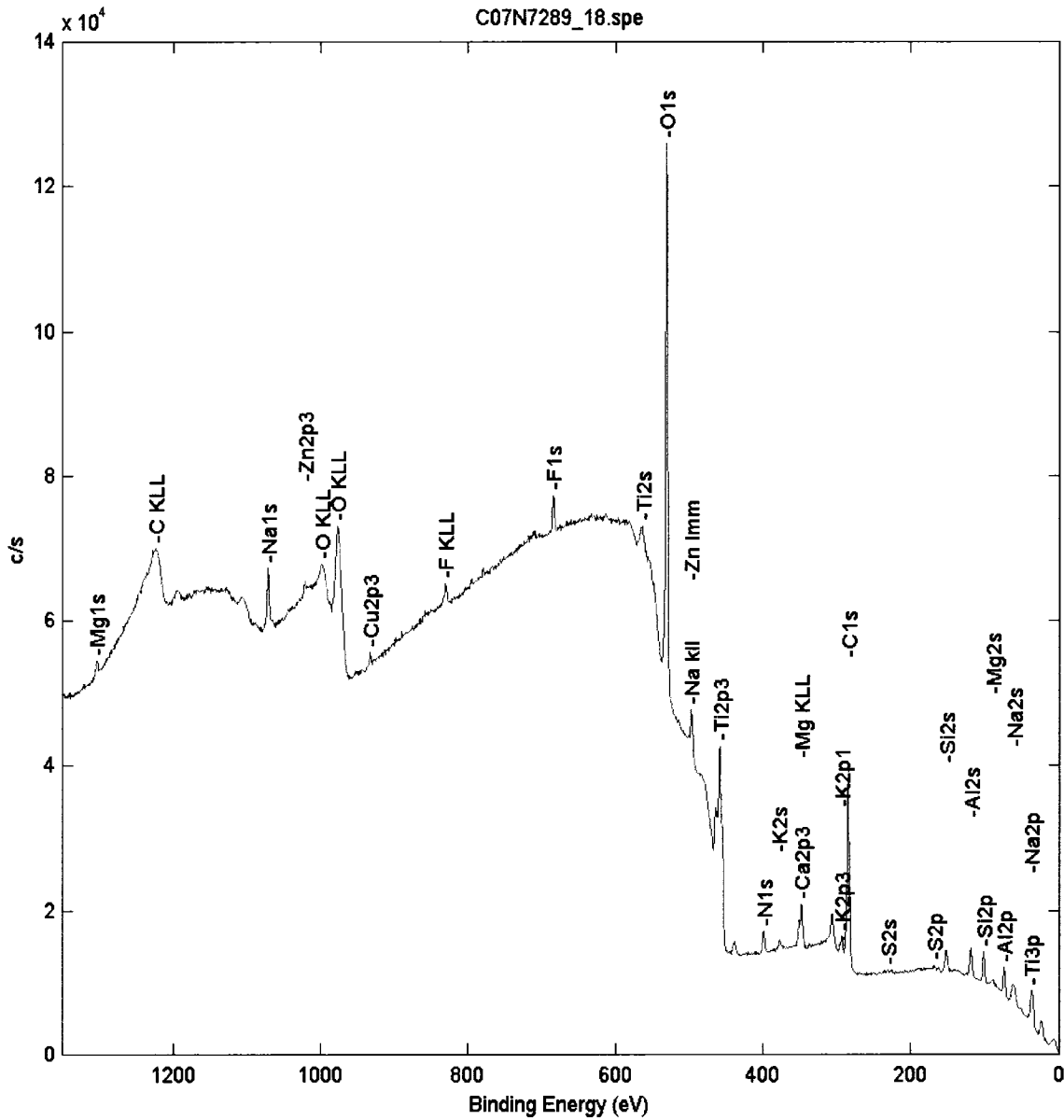


Figure 83. XPS chemical composition survey spectrum for weld 8.

C07N7289_19.spe: SJSU-Croom: SJSU-Croom EAG
 2007 May 8 Al mono 101.4 W 100.0 μ 45.0° 187.85 eV 9.3463e+004 max 39.44 min
 Su 1s/Area11: #9/1

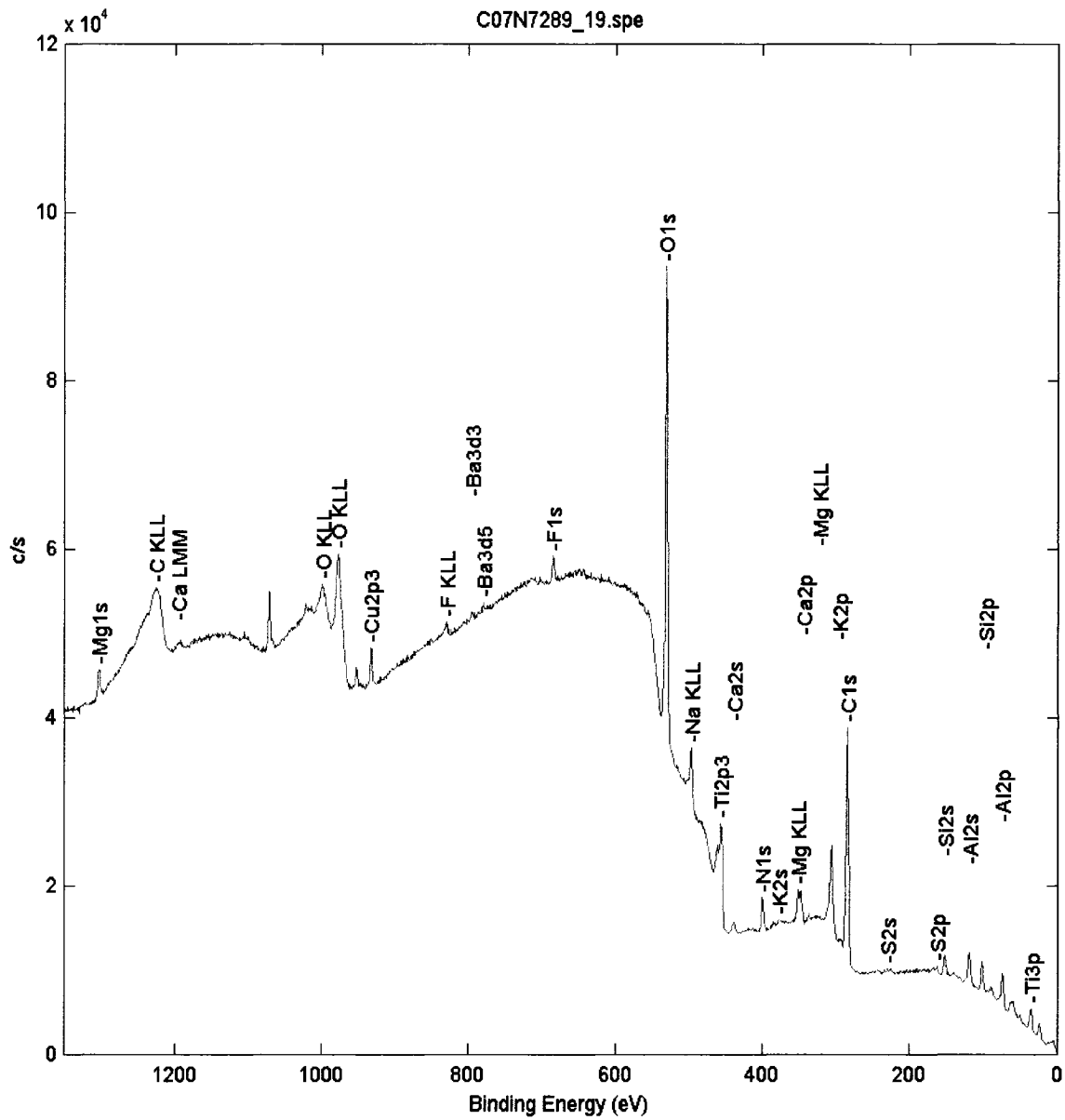


Figure 84. XPS chemical composition survey spectrum for weld 9.

APPENDIX E – SURFACE ANALYSIS RESULTS FOR CONTROL

C07N7289_34.spe: Croom: Welds EAG
 2007 May 14 Al mono 39.7 W 200.0 μ 45.0° 58.70 eV 1.1001e+004 max 4.71 min
 Ti2p/Point1: Control/1 (Shft)

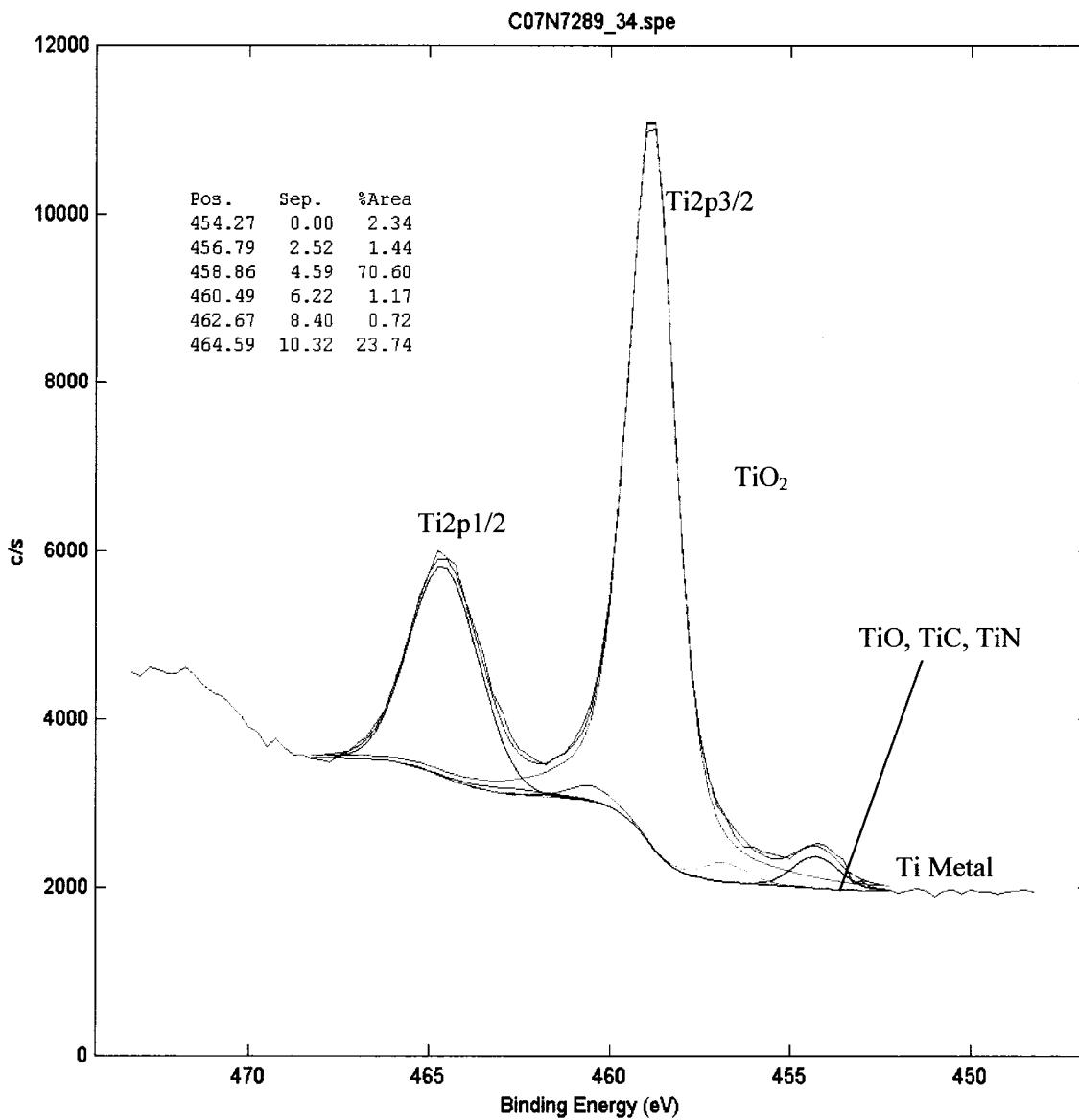


Figure 85. Titanium bonding state spectrum for the control.

C07N7289_34.spe: Croom: Welds EAG
 2007 May 14 Al mono 39.7 W 200.0 μ 45.0° 58.70 eV 1.4458e+003 max 4.33 min
 Al2p/Point1: Control/1 (Shft)

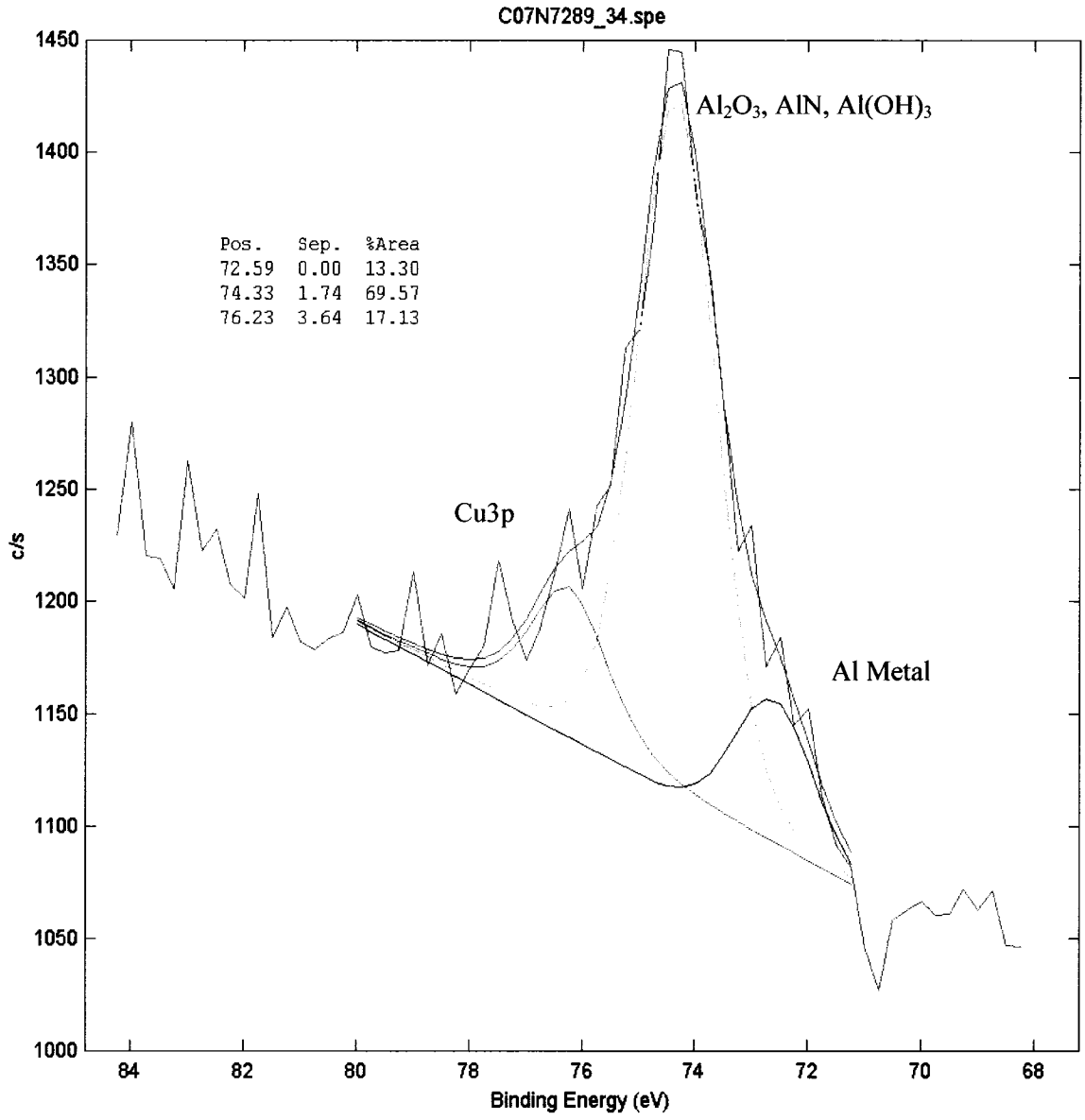


Figure 86. Aluminum bonding state spectrum for the control.

C07N7289_34.spe: Croom: Welds EAG
 2007 May 14 Al mono 39.7 W 200.0 μ 45.0° 23.50 eV 7.5150e+003 max 2.12 min
 O1s/Point1: Control/1 (Shf)

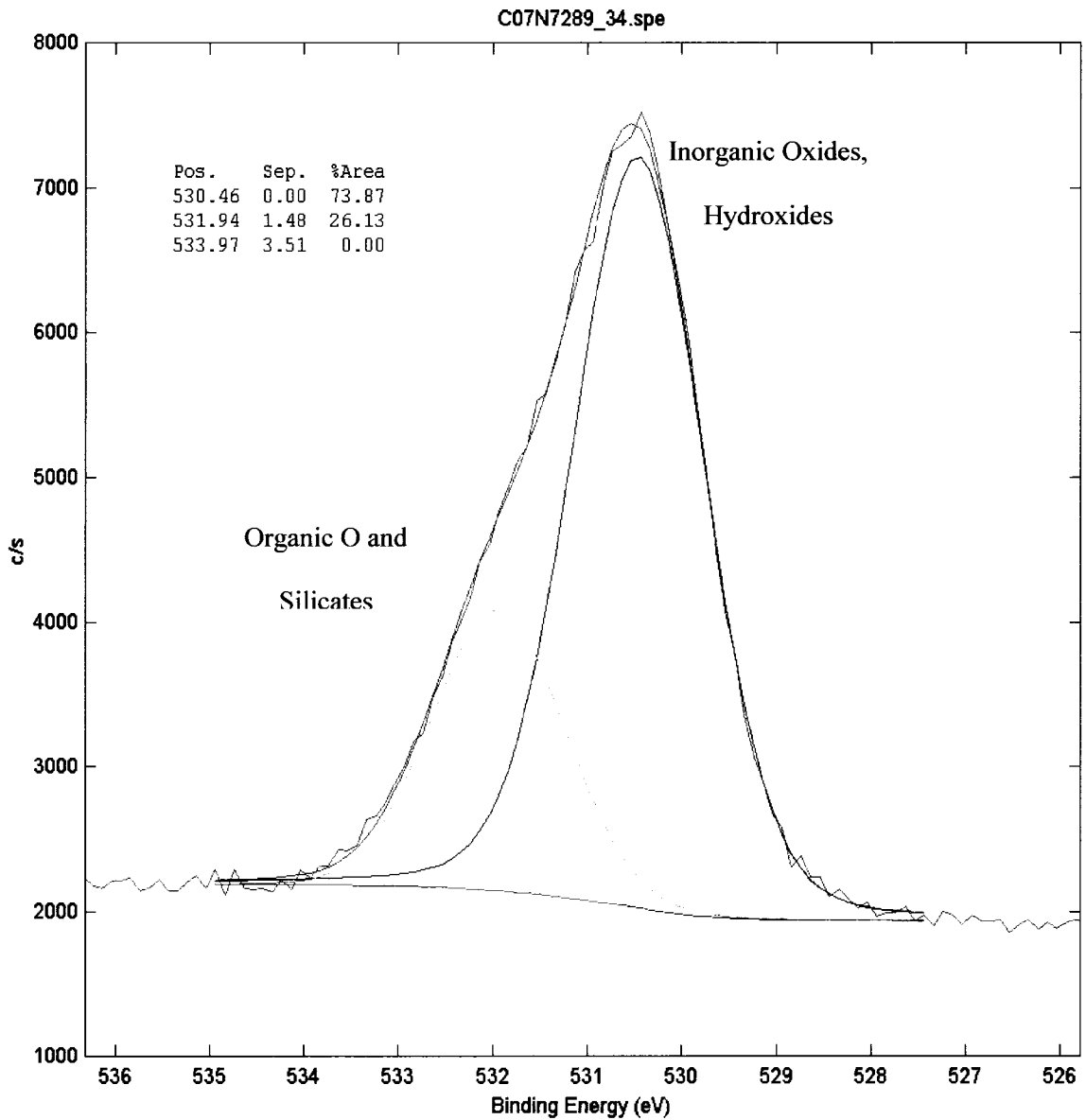


Figure 87. Oxygen bonding state spectrum for the control.

C07N7289_34.spe: Croom: Welds EAG
 2007 May 14 Al mono 39.7 W 200.0 μ 45.0° 23.50 eV 2.3452e+003 max 2.78 min
 C1s/Point1: Control/1 (SG3 Shift)

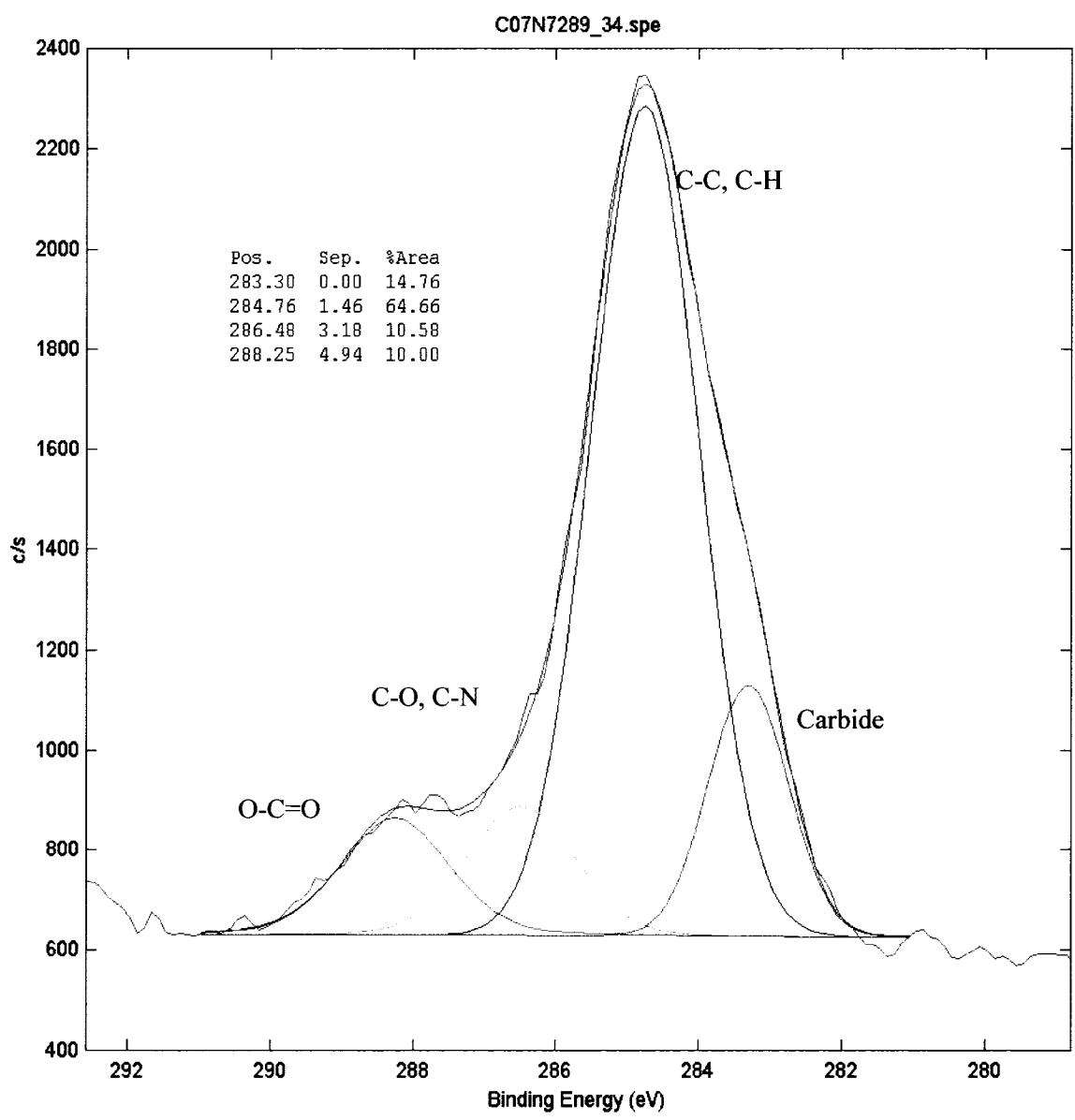


Figure 88. Carbon bonding state spectrum for the control.

C07N7289_34.spe: Croom: Welds EAG
 2007 May 14 Al mono 39.7 W 200.0 μ 45.0° 58.70 eV 2.7457e+003 max 2.47 min
 N1s/Point1: Control/1 (Shft)

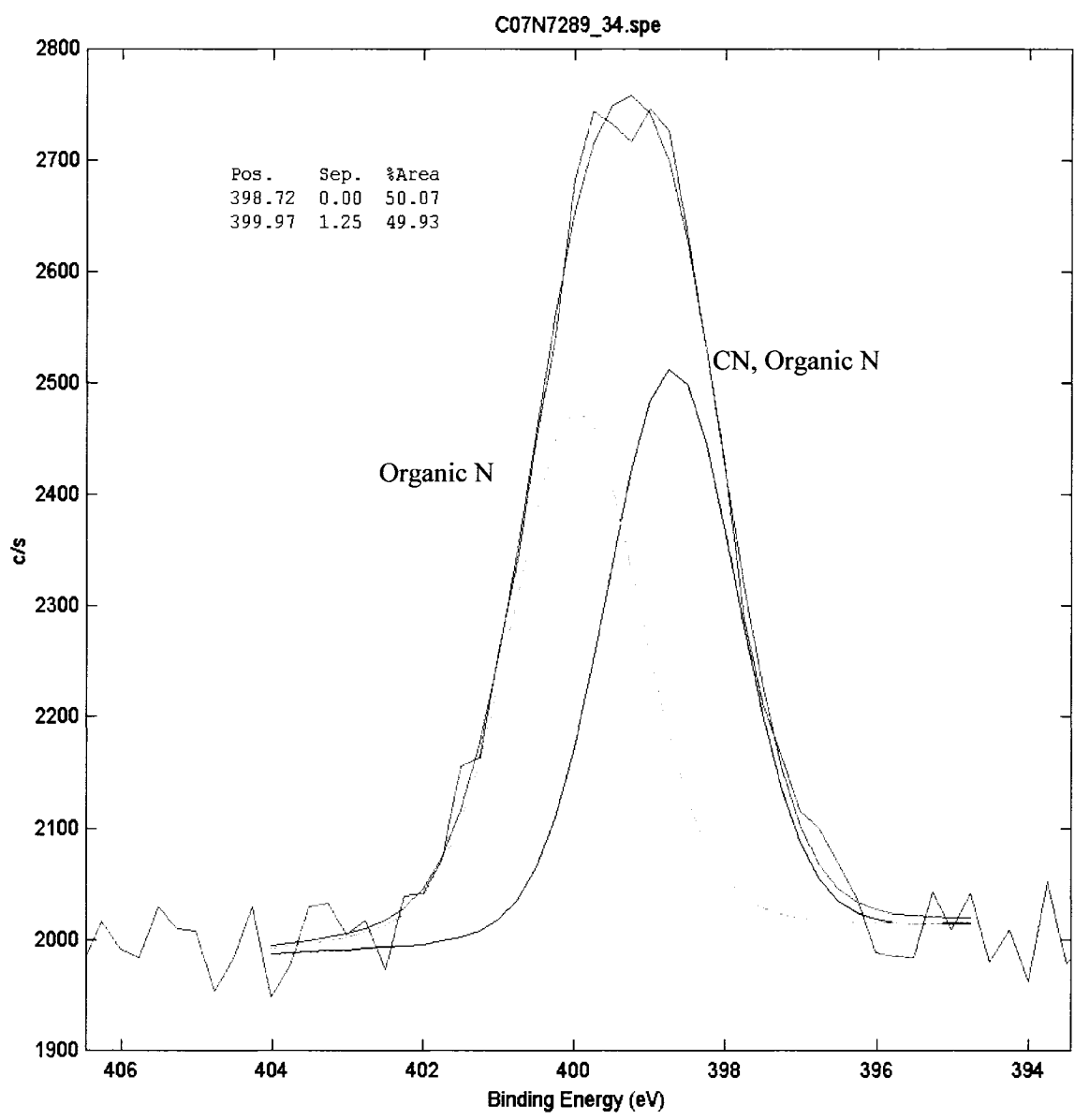


Figure 89. Nitrogen bonding state spectrum for the control.

C07N7289_34.spe: Croom: Welds			EAG
2007 May 14	Al mono 39.7 W 200.0 μ 45.0°	23.50 eV	7.5150e+003 max 3.02 min
O1s/Point1: Control/1 (Shft)			

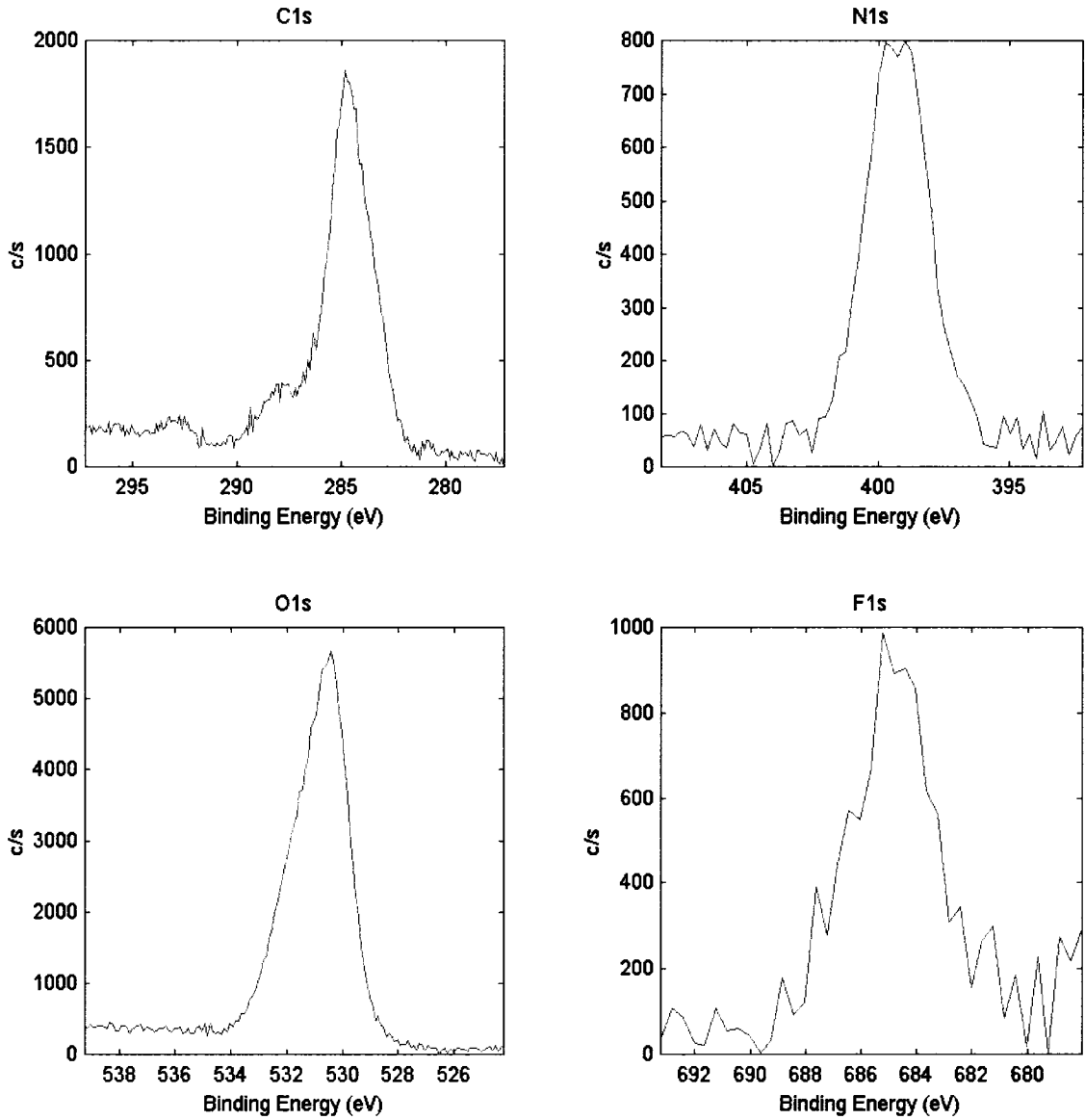


Figure 90. Bonding state spectra for carbon, nitrogen, oxygen, and fluorine for the control.

C07N7289_34.spe: Croom: Welds EAG
2007 May 14 Al mono 39.7 W 200.0 μ 45.0° 23.50 eV 7.5150e+003 max 3.02 min
O1s/Point1: Control/1 (Shft)

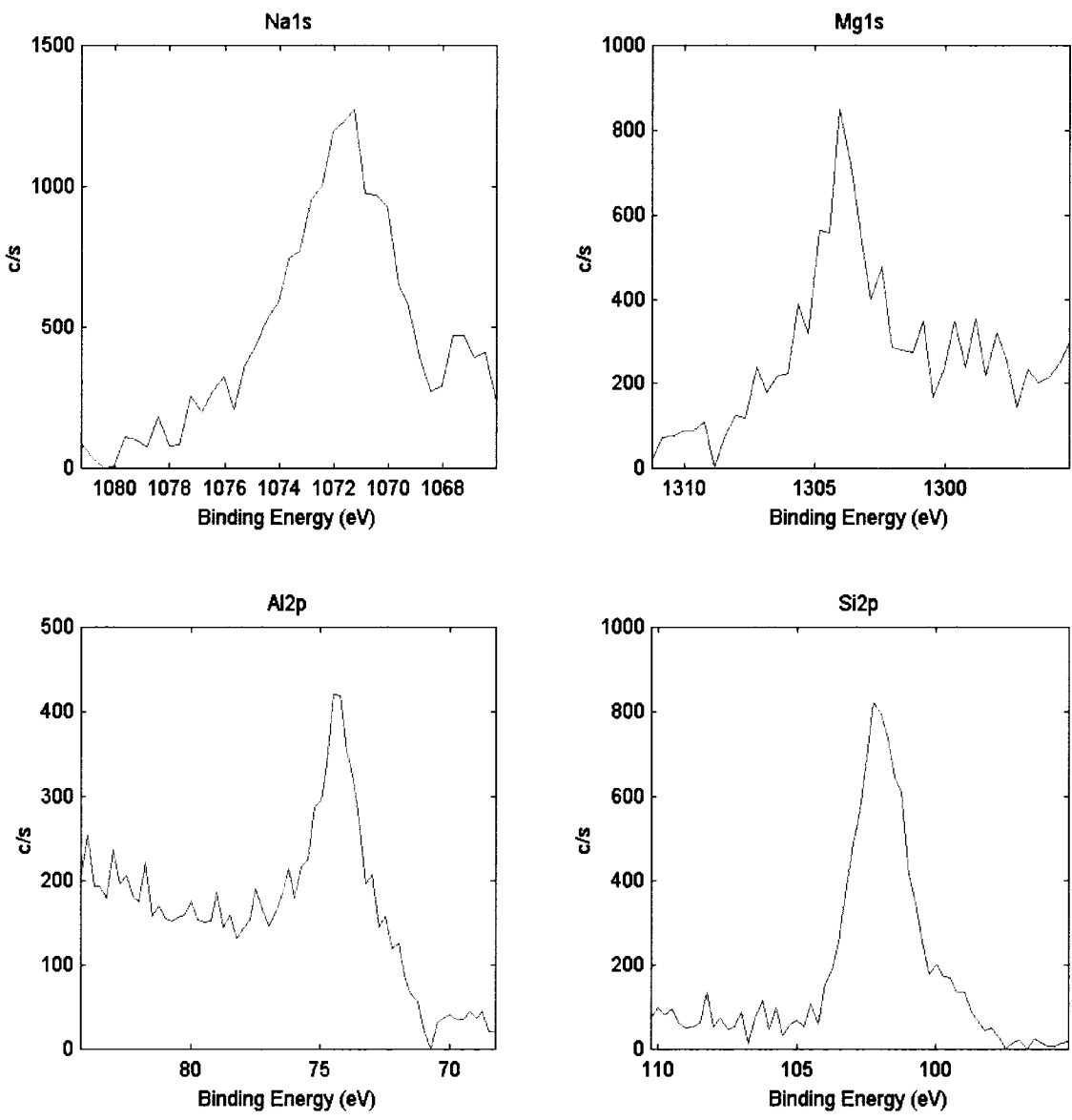


Figure 91. Bonding state spectra for sodium, magnesium, aluminum, and silicon for the control.

C07N7289_34.spe: Croom: Welds			EAG
2007 May 14	Al mono 39.7 W 200.0 μ 45.0°	23.50 eV	7.5150e+003 max 3.02 min
O1s/Point1: Control/1 (Shft)			

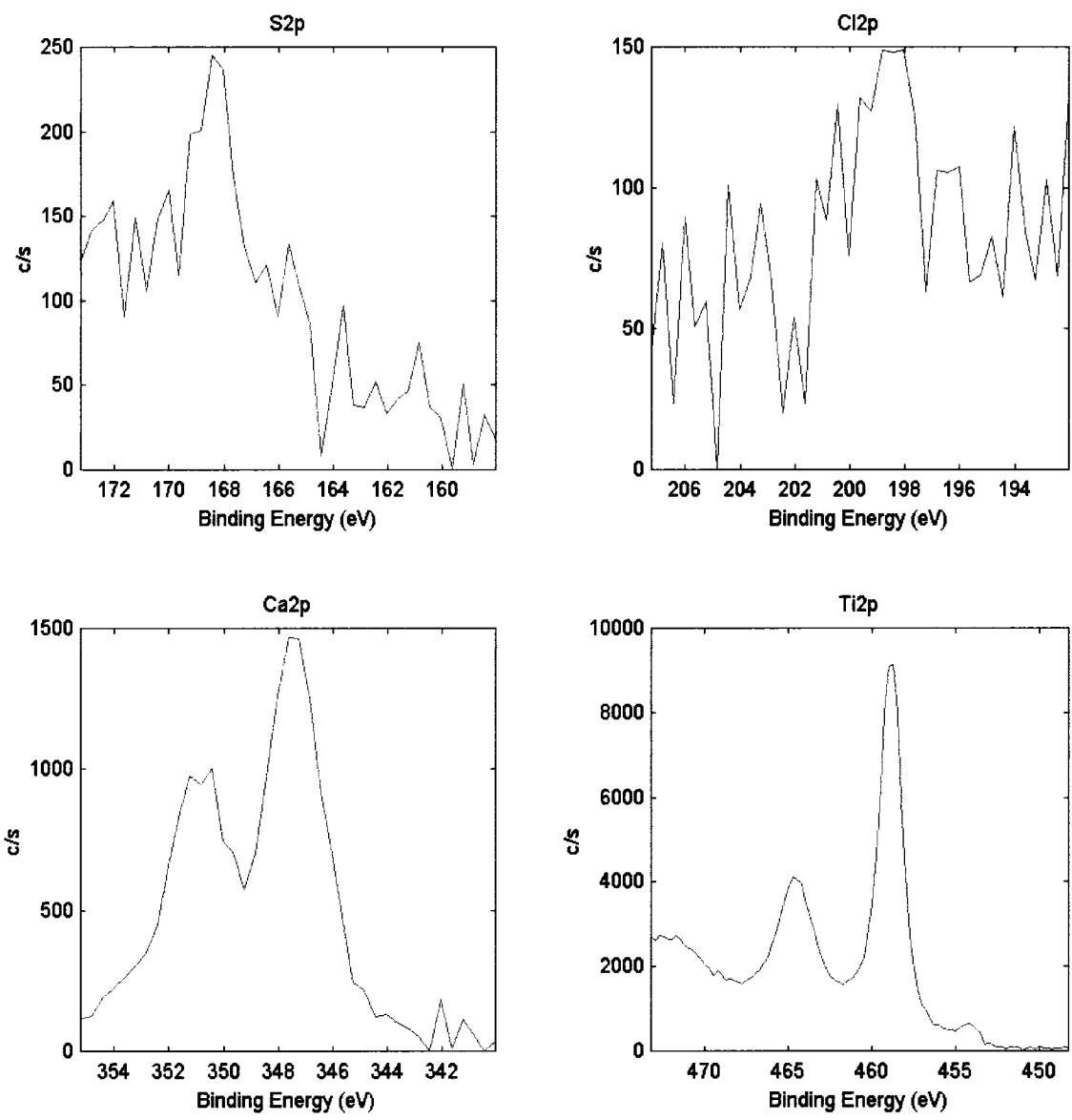


Figure 92. Bonding state spectra for sulfur, chlorine, calcium, and titanium for the control.

C07N7289_34.spe: Croom: Welds			EAG
2007 May 14	Al mono 39.7 W 200.0 μ 45.0° 23.50 eV	7.5150e+003 max	3.02 min
O1s/Point1: Control/1 (Shft)			

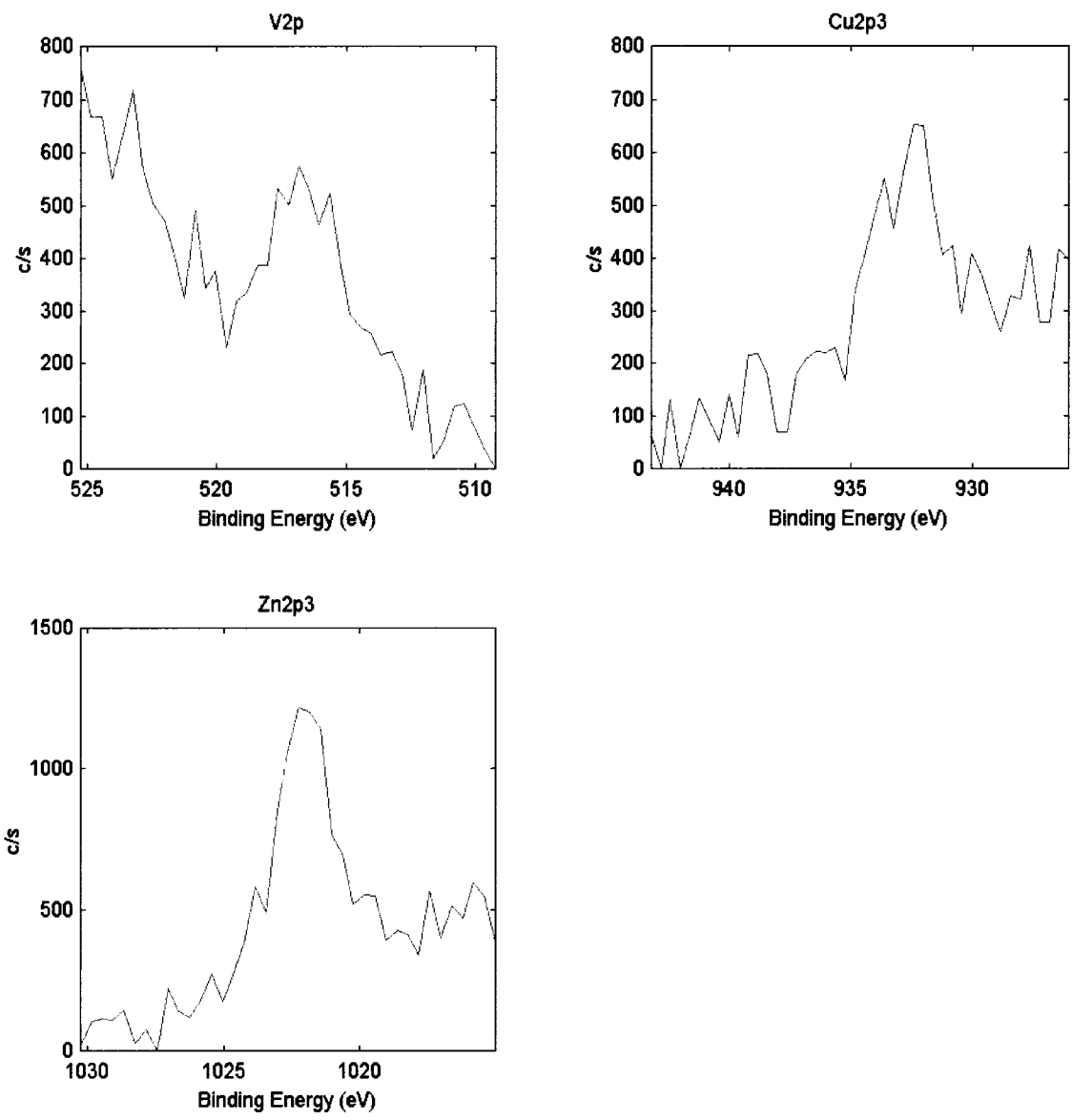


Figure 93. Bonding state spectra for vanadium, copper, and zinc for the control.

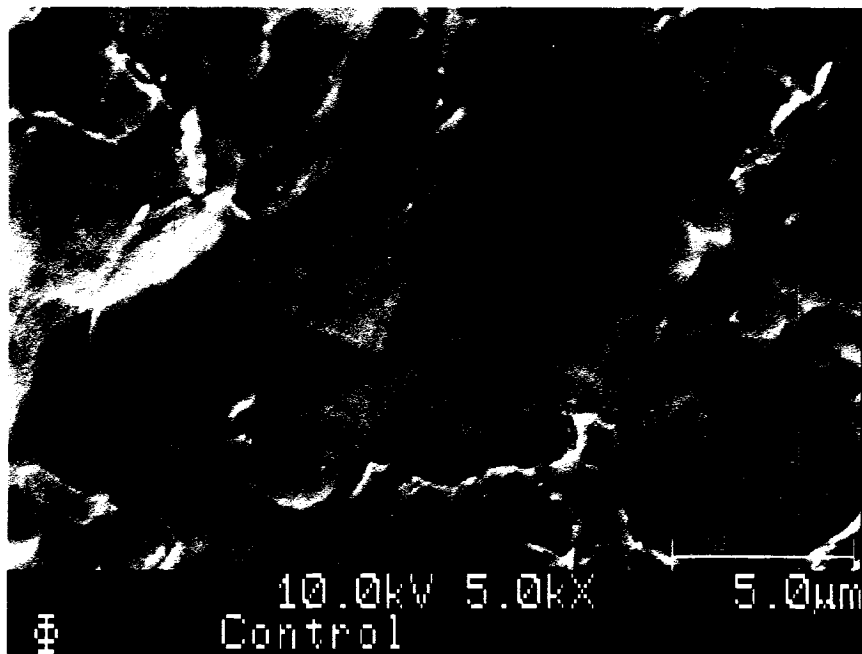
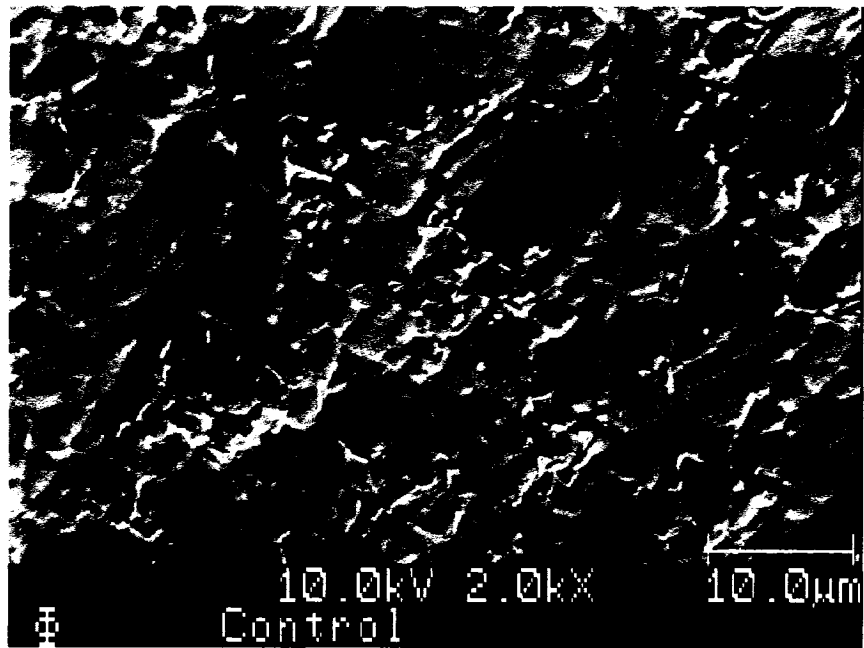


Figure 94. SEM images of the surface of control specimen.

C07N728910.spe: Control
 2007 May 29 10.0 keV 0 FRR
 Sur1/Full/1 (S9D9) EAG-CA
 4.0936e+004 max
 10.85 min

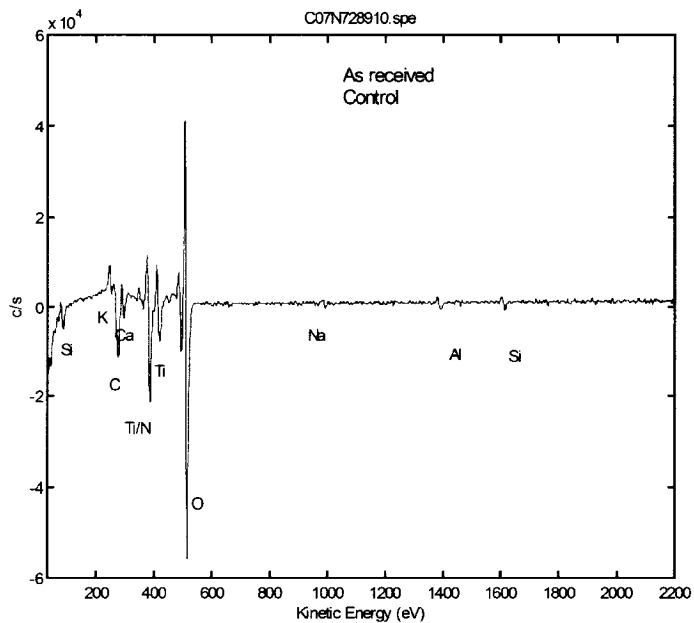


Figure 95. As received auger survey spectrum for the control specimen.

C07N728912.spe: Control
 2007 May 29 10.0 keV 0 FRR
 Sur1/Full/1 (S9D9) EAG-CA
 4.0584e+004 max
 6.51 min

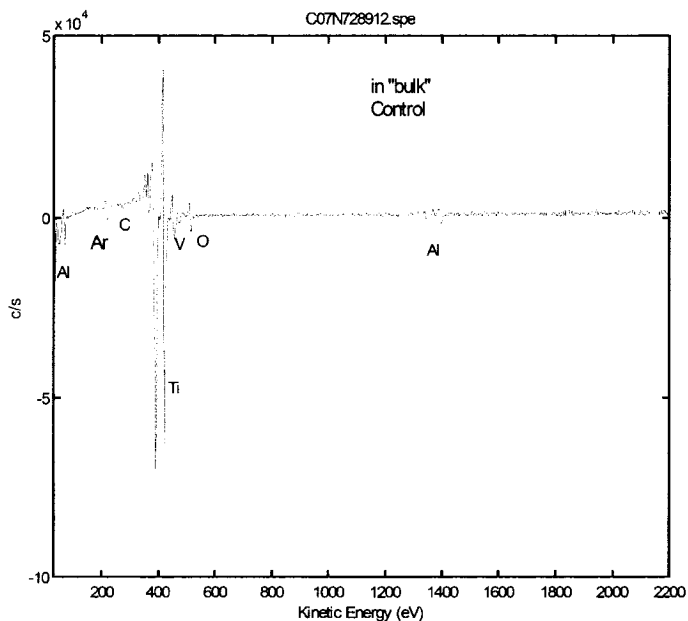


Figure 96. After Sputtered auger survey spectrum for the control specimen.

APPENDIX F – SURFACE ANALYSIS RESULTS FOR WELD 1

C07N7289_35.spe: Croom: Welds	EAG
2007 May 14 Al mono 39.7 W 200.0 μ 45.0° 58.70 eV	7.3807e+003 max 3.87 min
Ti2p/Point2: s1/1 (Shft)	

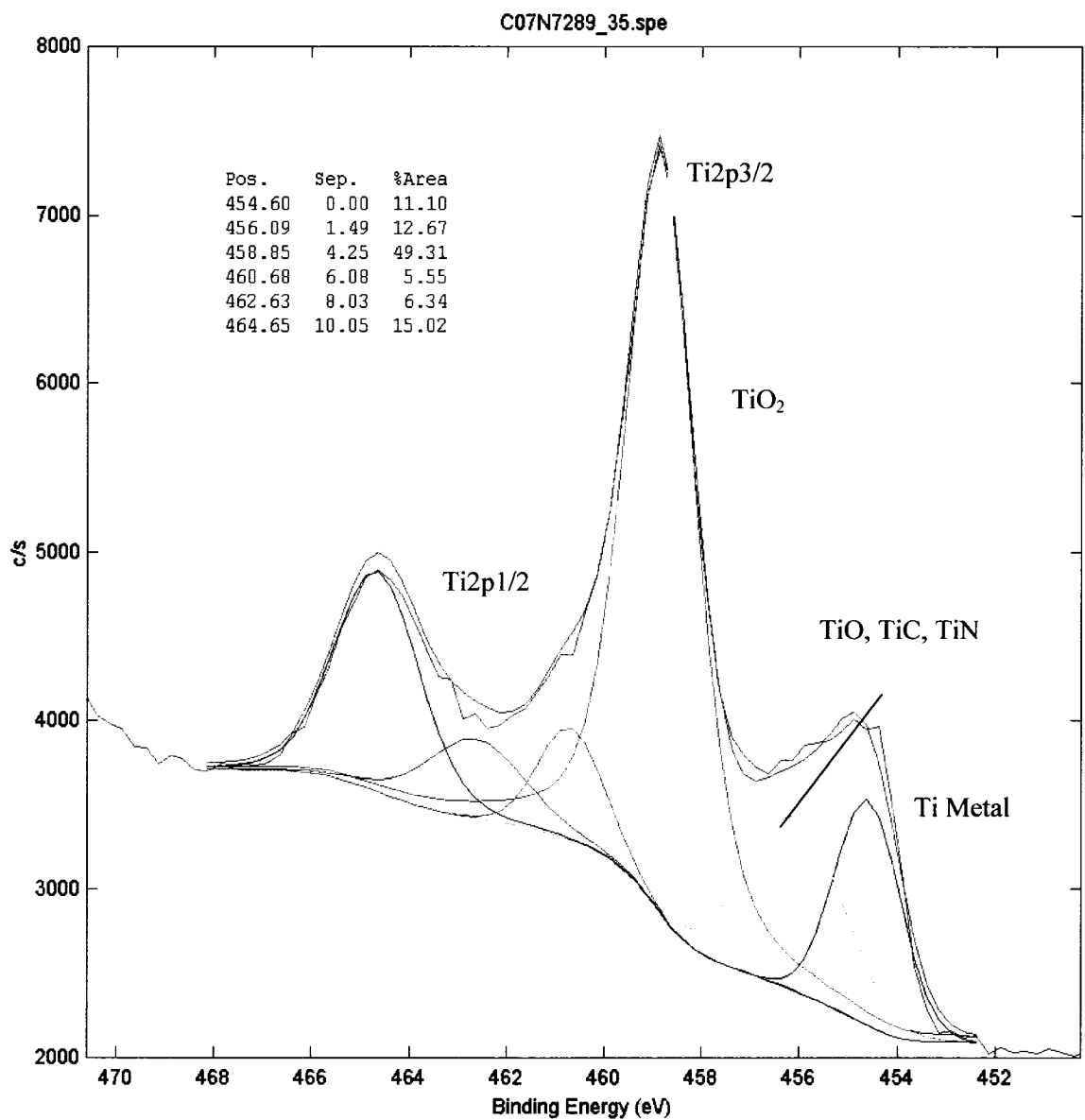


Figure 97. Titanium bonding state spectra for weld 1.

C07N7289_35.spe: Croom: Welds EAG
 2007 May 14 Al mono 39.7 W 200.0 μ 45.0° 58.70 eV 2.1018e+003 max 4.33 min
 Al2p/Point2: s1/1 (Shft)

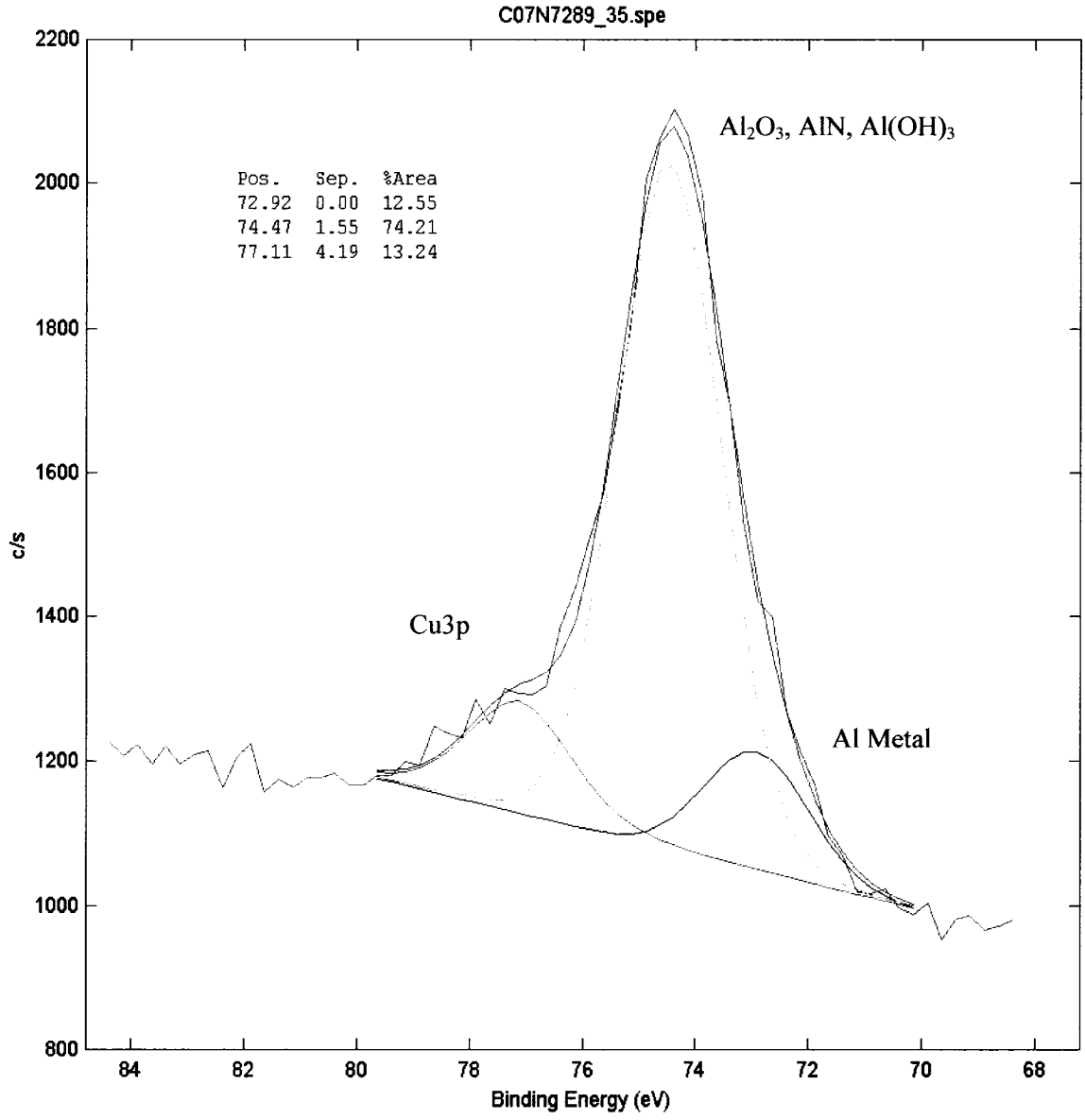


Figure 98. Aluminum bonding state spectra for weld 1.

C07N7289_35.spe: Croom: Welds EAG
 2007 May 14 Al mono 39.7 W 200.0 μ 45.0° 23.50 eV 6.9650e+003 max 2.46 min
 O1s/Point2: s1/1 (Shft)

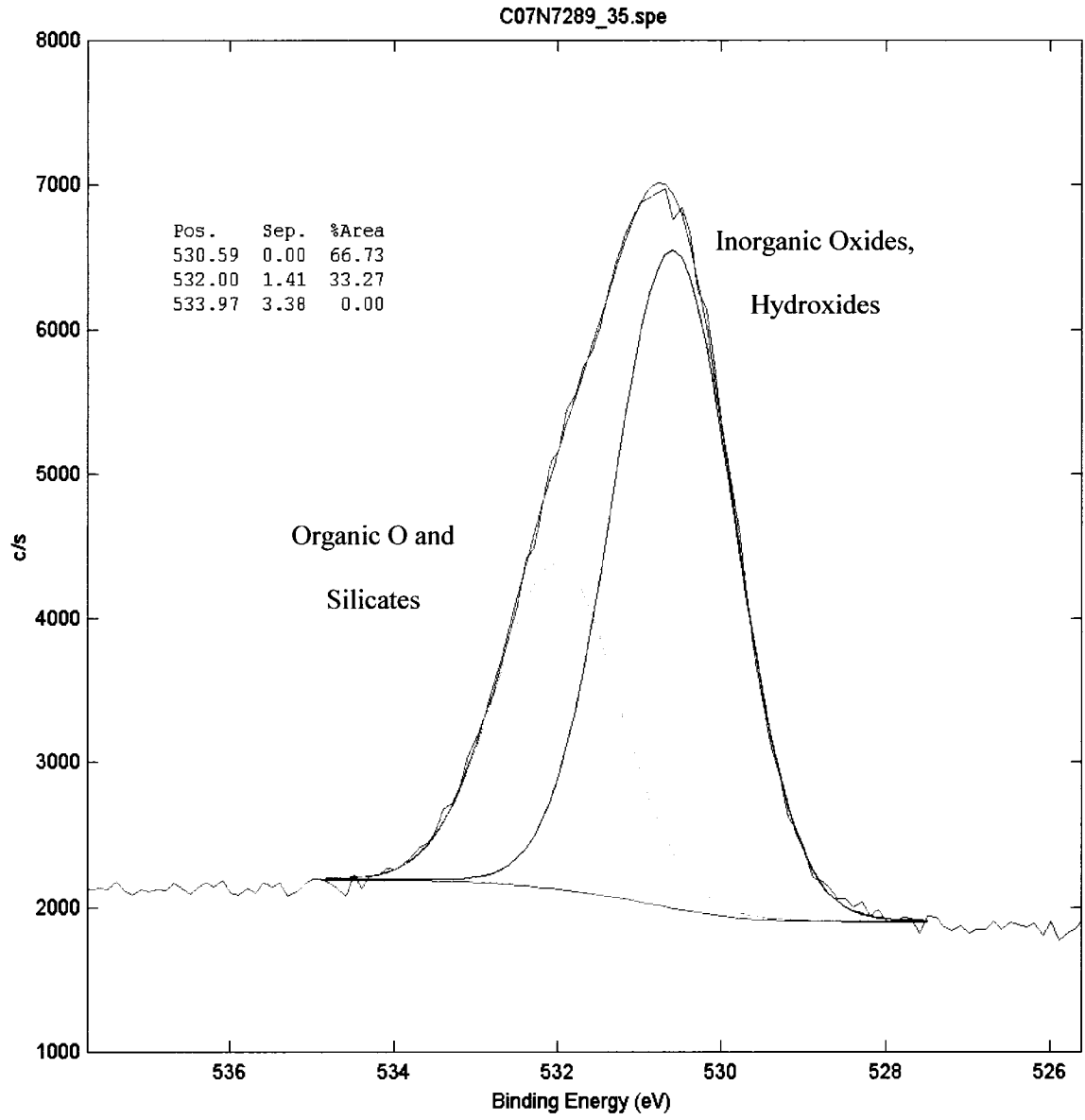


Figure 99. Oxygen bonding state spectra for weld 1.

C07N7289_35.spe: Croom: Welds EAG
 2007 May 14 Al mono 39.7 W 200.0 μ 45.0° 23.50 eV 1.8477e+003 max 8.16 min
 C1s/Point2: s1/1 (SG3 Shift)

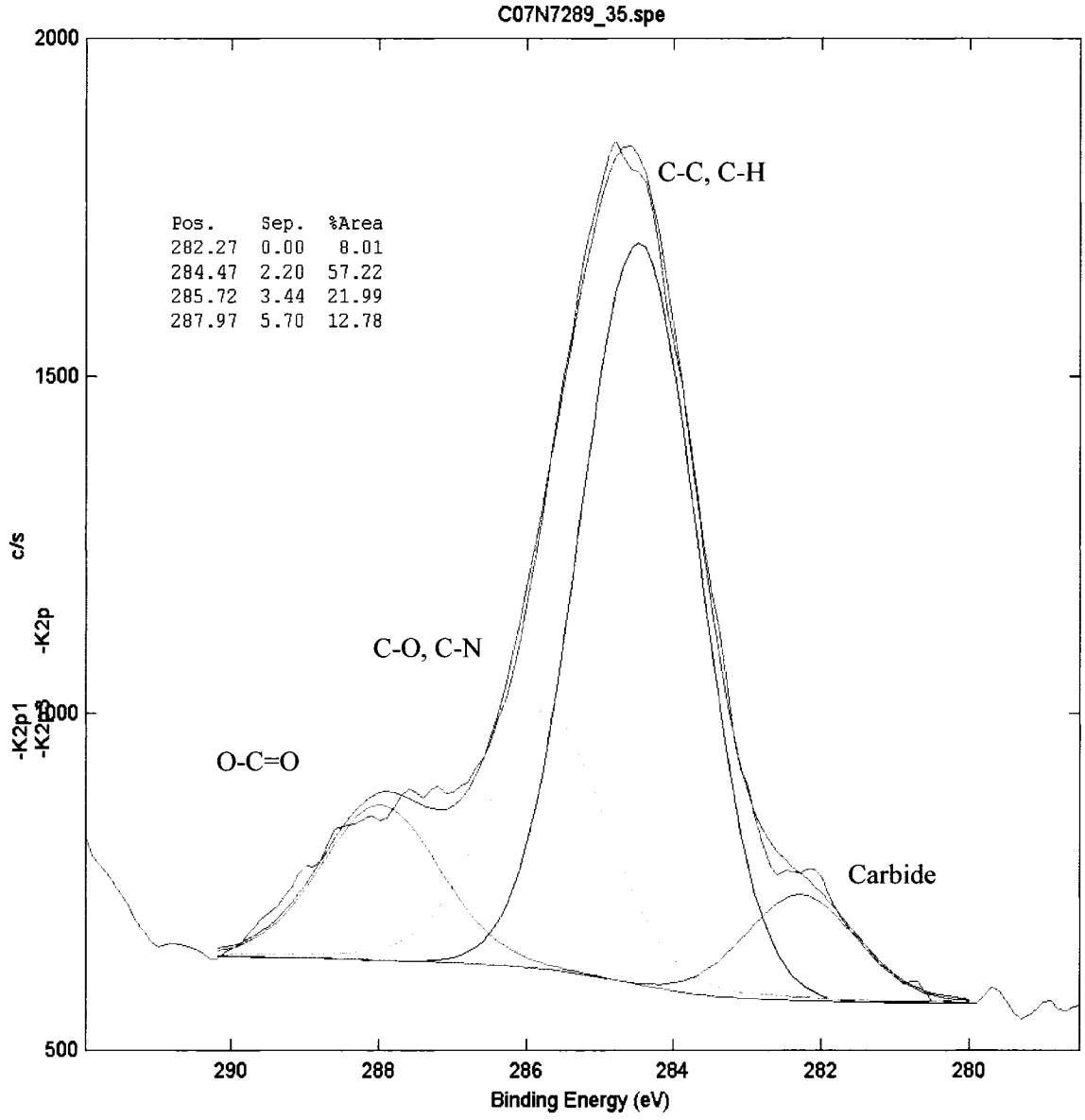


Figure 100. Carbon bonding state spectra for weld 1.

C07N7289_35.spe: Croom: Welds EAG
 2007 May 14 Al mono 39.7 W 200.0 μ 45.0° 58.70 eV 2.6559e+003 max 2.33 min
 N1s/Point2: s1/1 (Shift SG3)

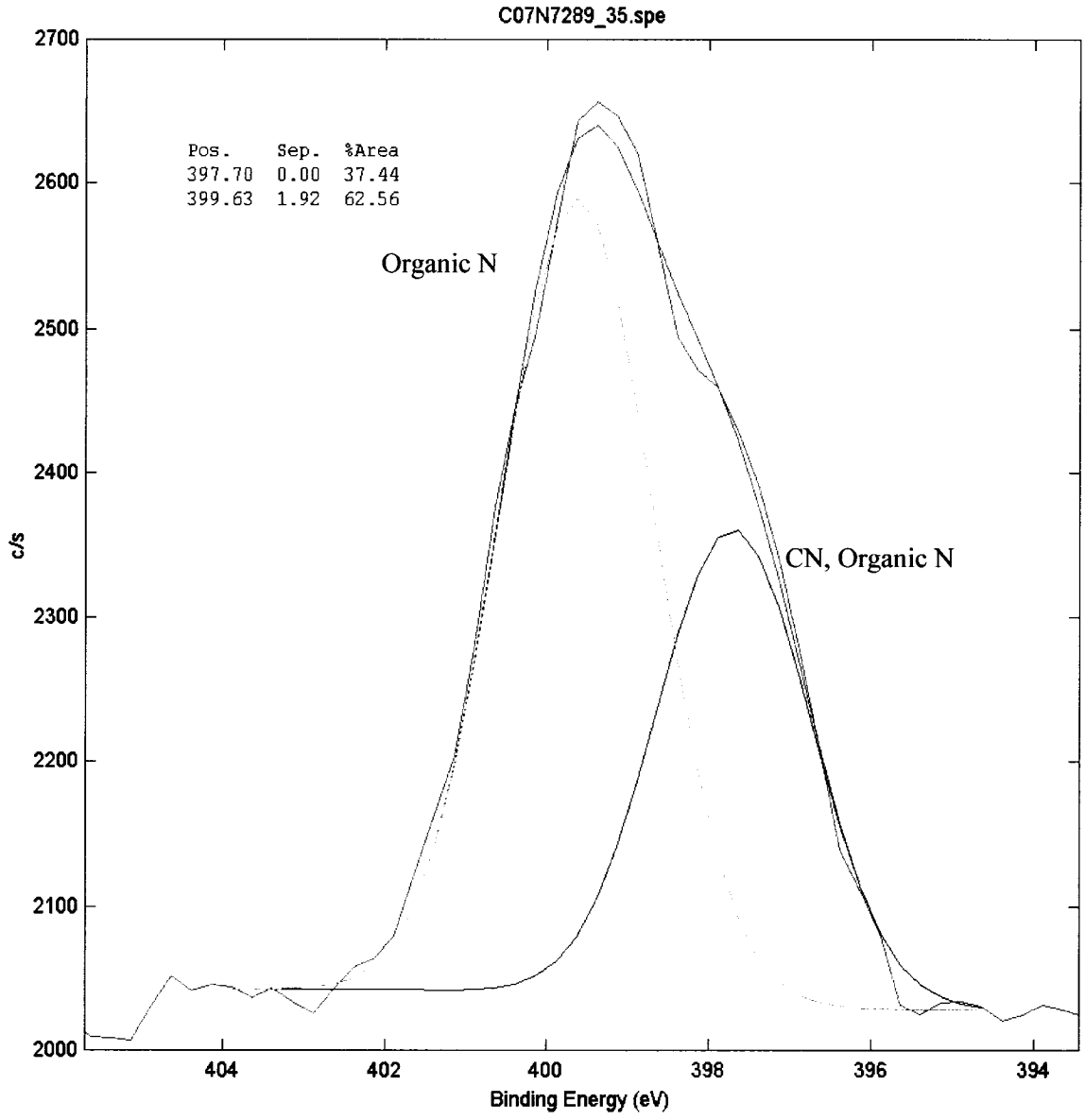


Figure 101. Nitrogen bonding state spectra for weld 1.

C07N7289_35.spe: Croom: Welds			EAG
2007 May 14	Al mono 39.7 W 200.0 μ 45.0°	23.50 eV	6.9650e+003 max 3.02 min
O1s/Point2: s1/1 (Shift)			

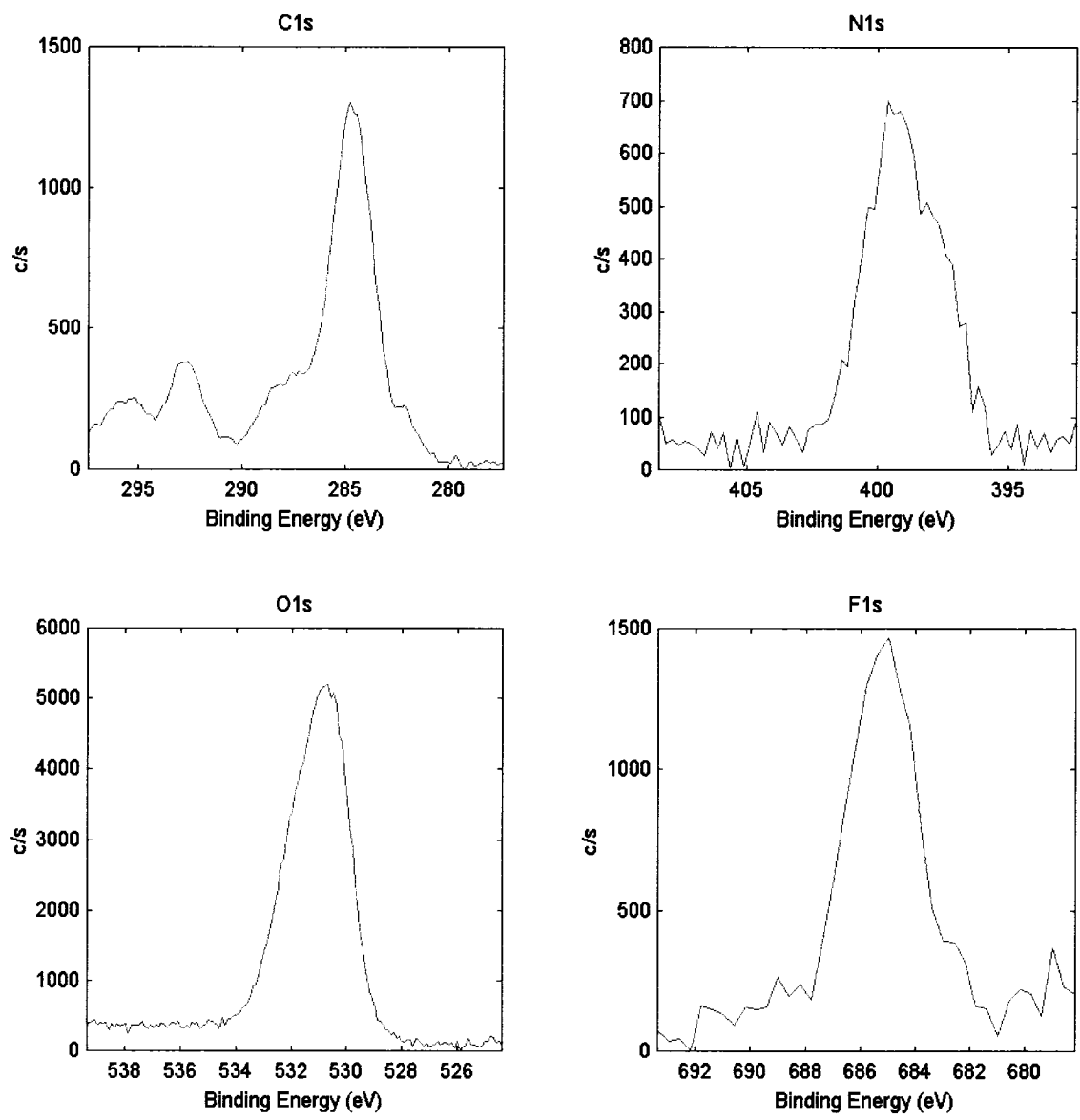


Figure 102. Bonding state spectra for carbon, nitrogen, oxygen, and fluorine for weld 1.

C07N7289_35.spe: Croom: Welds EAG
 2007 May 14 Al mono 39.7 W 200.0 μ 45.0° 23.50 eV 6.9650e+003 max 3.02 min
 O1s/Point2: s1/1 (Shft)

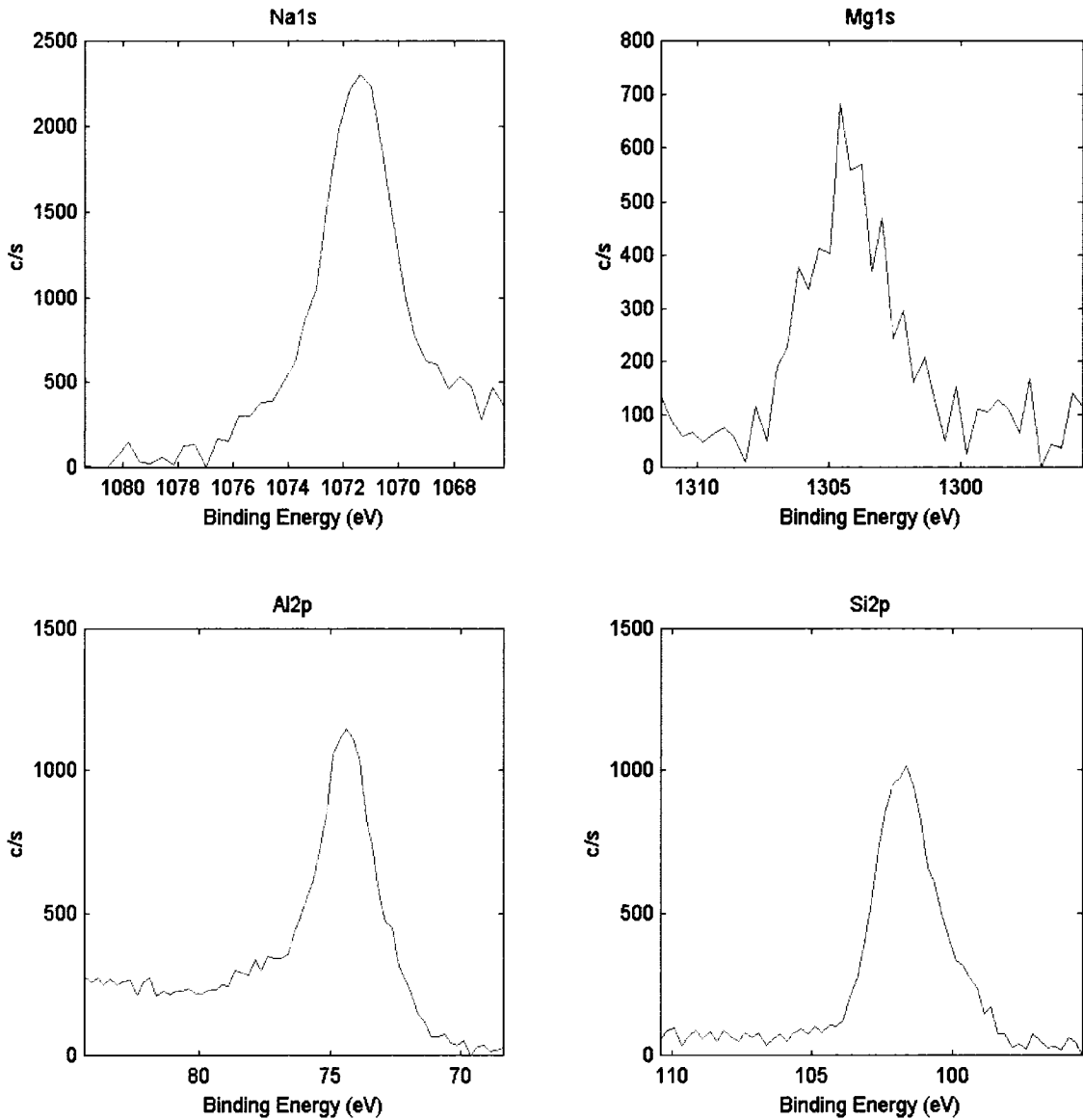


Figure 103. Bonding state spectra for sodium, magnesium, aluminum, and silicon for weld 1.

C07N7289_35.spe: Croom: Welds			EAG
2007 May 14	Al mono 39.7 W 200.0 μ 45.0°	23.50 eV	6.9650e+003 max 3.02 min
O1s/Point2: s1/1 (Shft)			

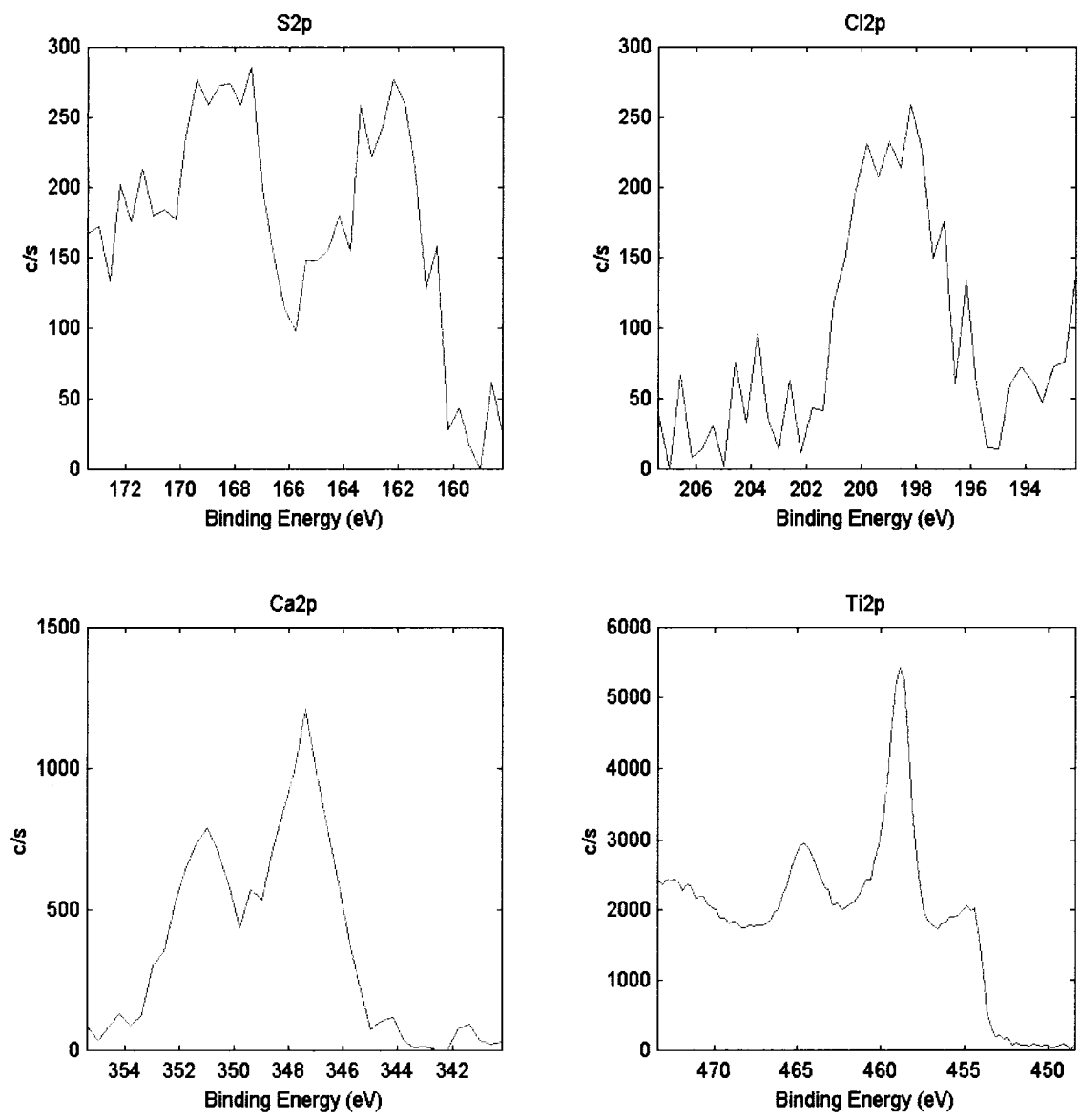


Figure 104. Bonding state spectra for sulfur, chlorine, calcium, and titanium for weld 1.

C07N7289_35.spe: Croom: Welds EAG
2007 May 14 Al mono 39.7 W 200.0 μ 45.0° 23.50 eV 6.9650e+003 max 3.02 min
O1s/Point2: s1/1 (Shft)

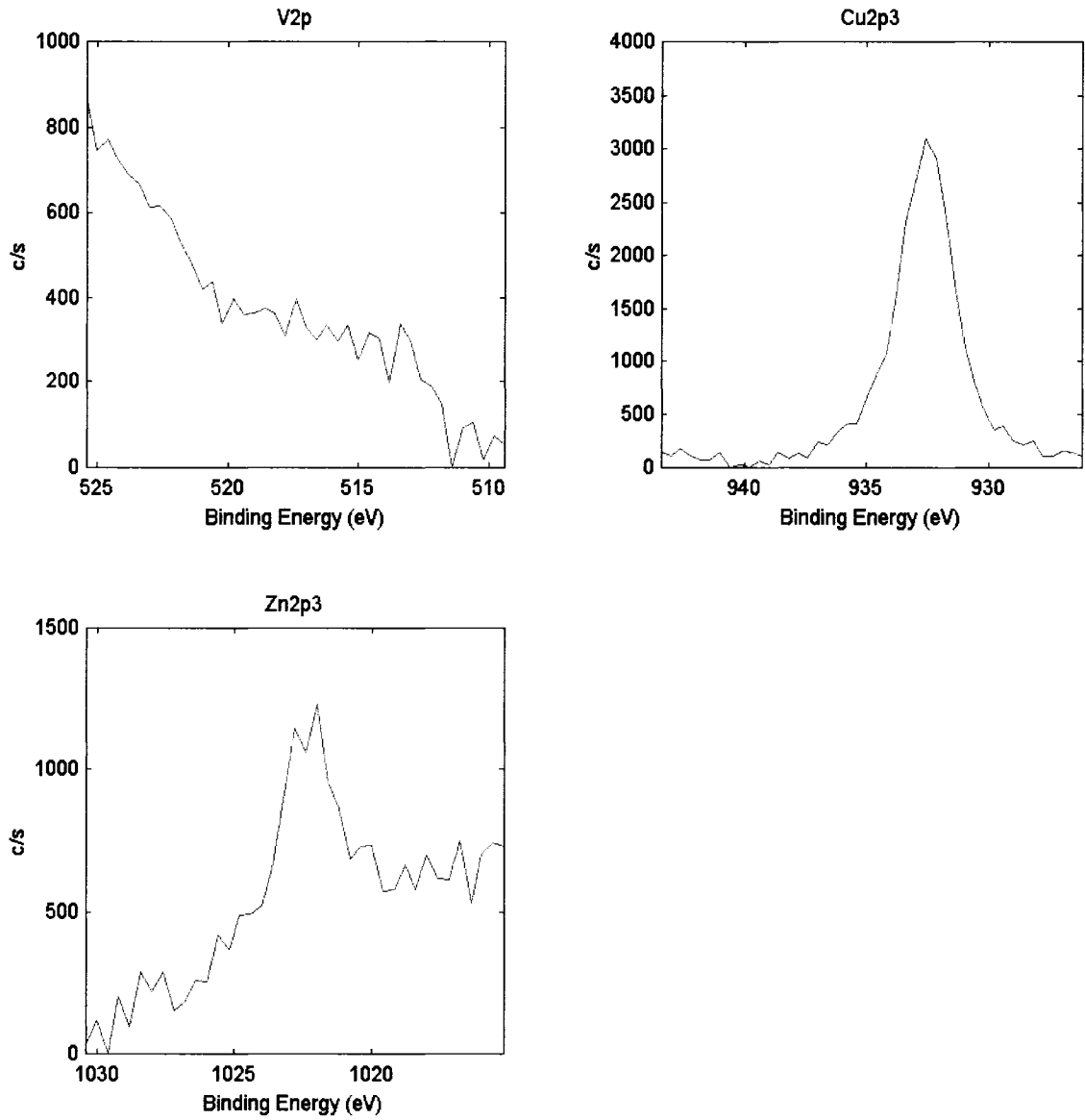


Figure 105. Bonding state spectra for vanadium, copper, and zinc for weld 1.

APPENDIX G – SURFACE ANALYSIS RESULTS FOR WELD 2

C07N7289_37.spe: Croom: Welds	EAG
2007 May 14 Al mono 39.7 W 200.0 μ 45.0° 58.70 eV	4.7707e+003 max 4.71 min
Ti2p/Point3: s2/1 (Shft)	

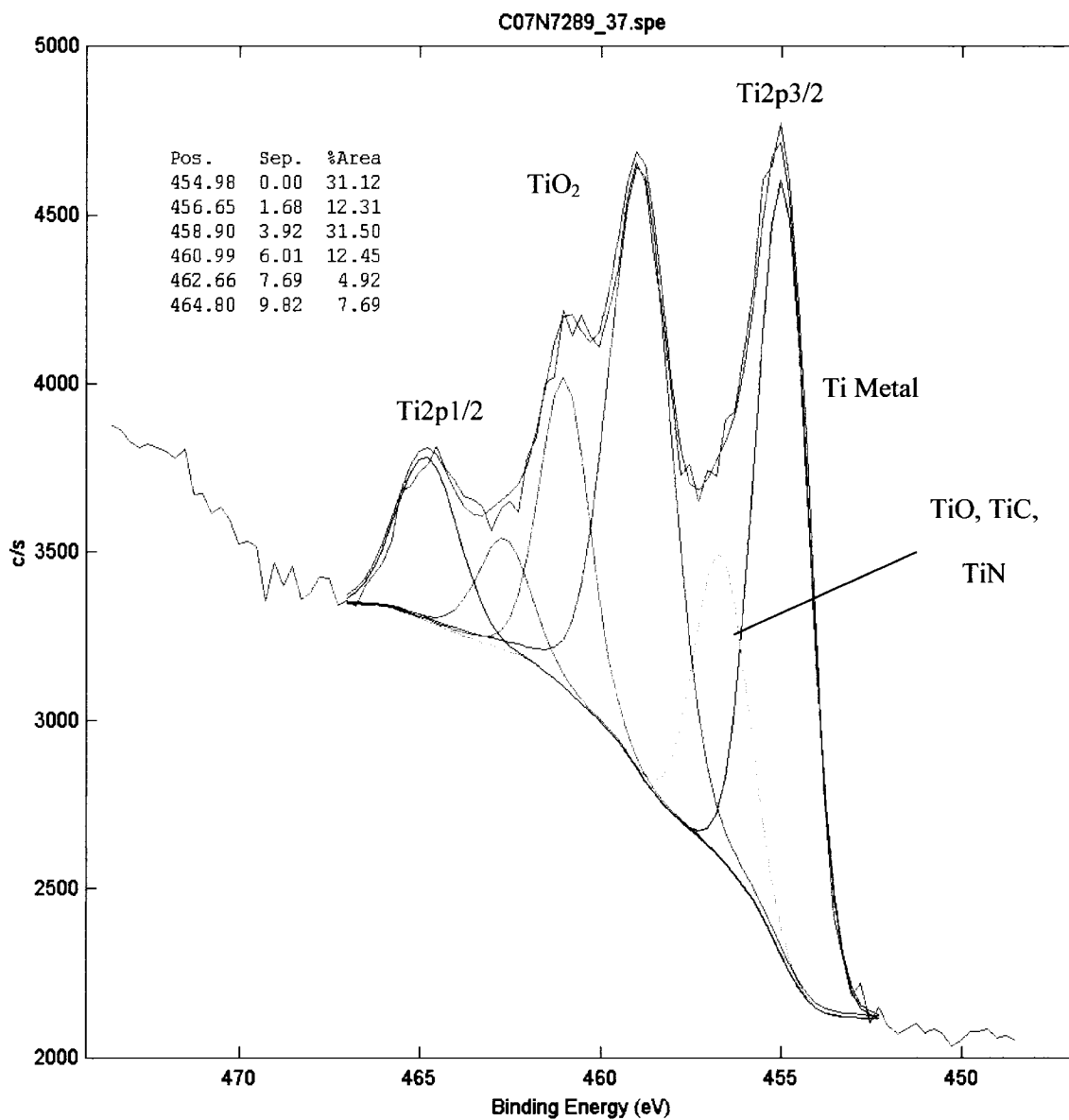


Figure 106. Titanium bonding state spectrum for weld 2.

C07N7289_37.spe: Croom: Welds EAG
 2007 May 14 Al mono 39.7 W 200.0 μ 45.0° 58.70 eV 2.1850e+003 max 3.40 min
 Al2p/Point3: s2/1 (Shft)

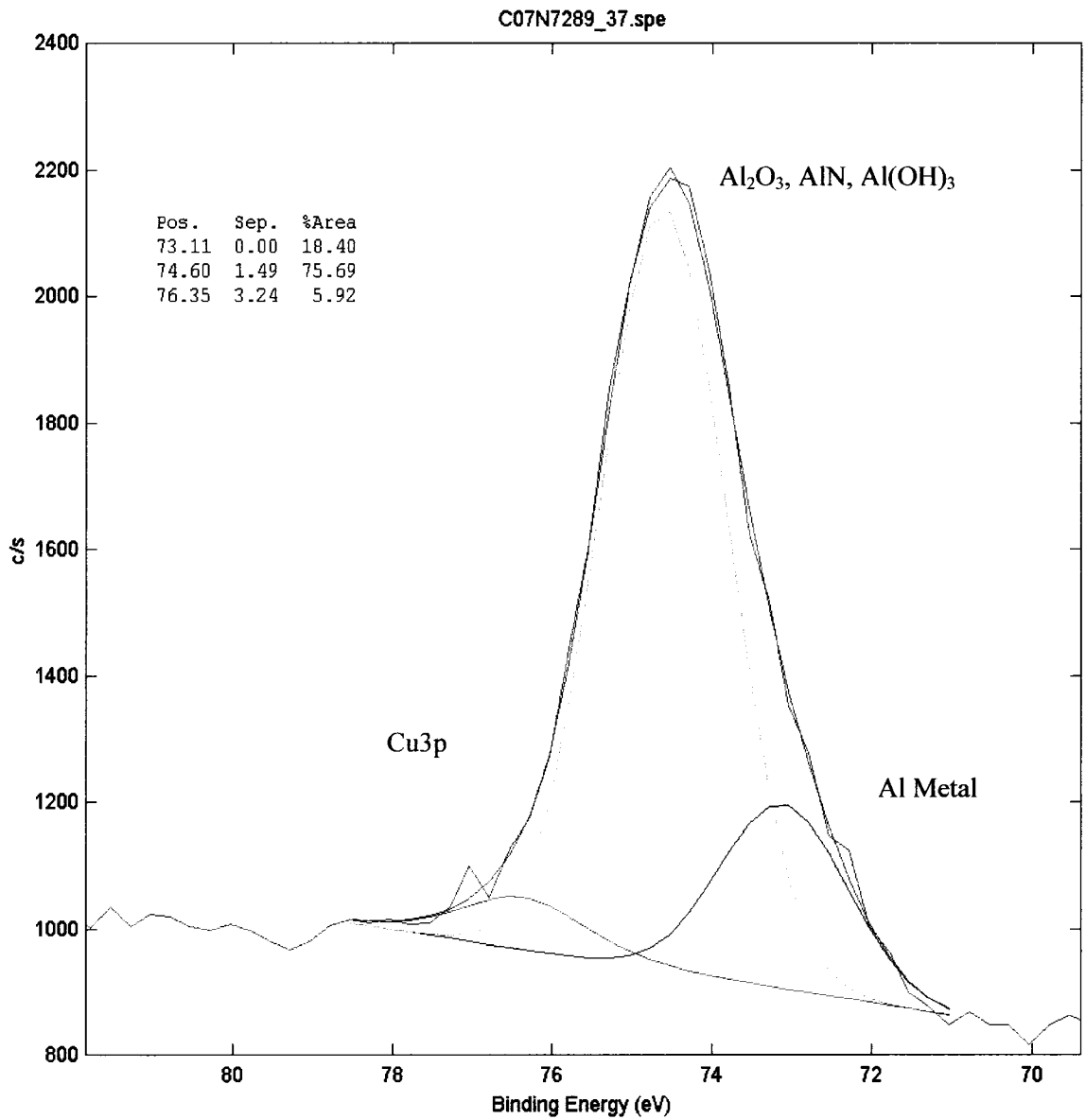


Figure 107. Aluminum bonding state spectrum for weld 2.

C07N7289_37.spe: Croom: Welds EAG
 2007 May 14 Al mono 39.7 W 200.0 μ 45.0° 23.50 eV 5.7077e+003 max 2.38 min
 O1s/Point3: s2/1 (Shift SG3)

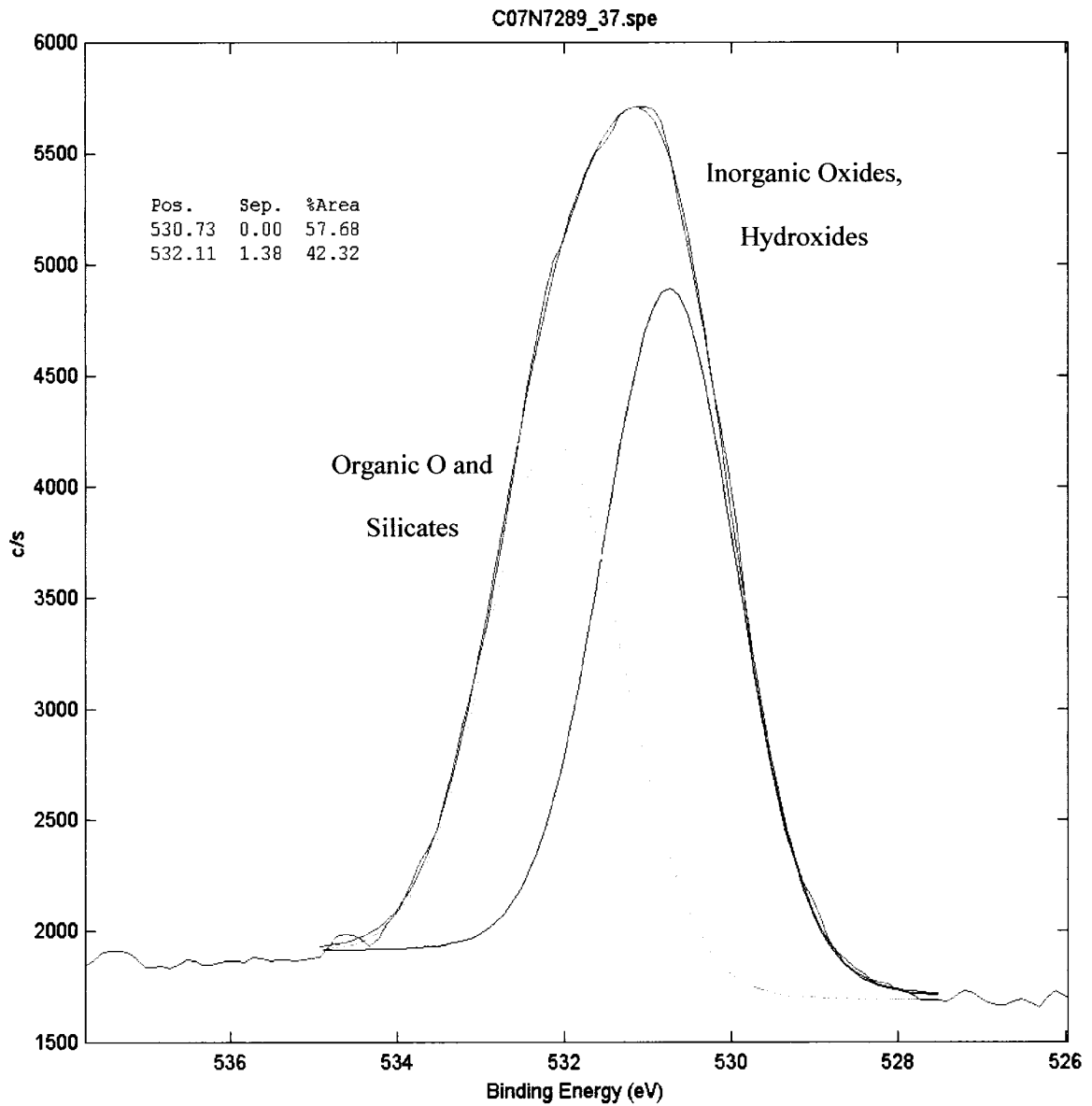


Figure 108. Oxygen bonding state spectrum for weld 2.

C07N7289_37.spe: Croom: Welds EAG
 2007 May 14 Al mono 39.7 W 200.0 μ 45.0° 23.50 eV 2.1694e+003 max 9.66 min
 C1s/Point3: s2/1 (Shft)

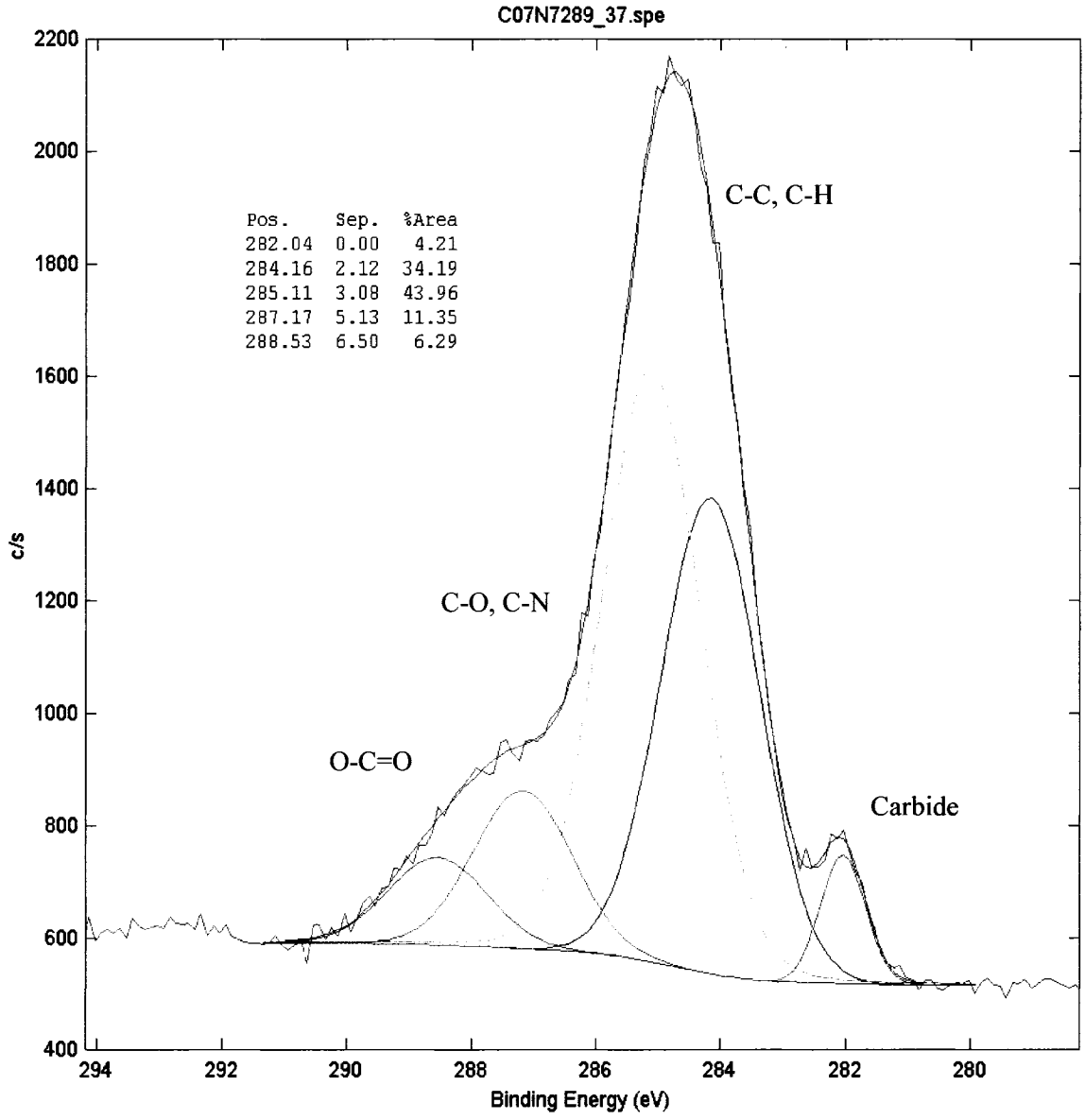


Figure 109. Carbon bonding state spectrum for weld 2.

C07N7289_37.spe: Croom: Welds EAG
 2007 May 14 Al mono 39.7 W 200.0 μ 45.0° 58.70 eV 3.2432e+003 max 2.38 min
 N1s/Point3: s2/1 (Shift)

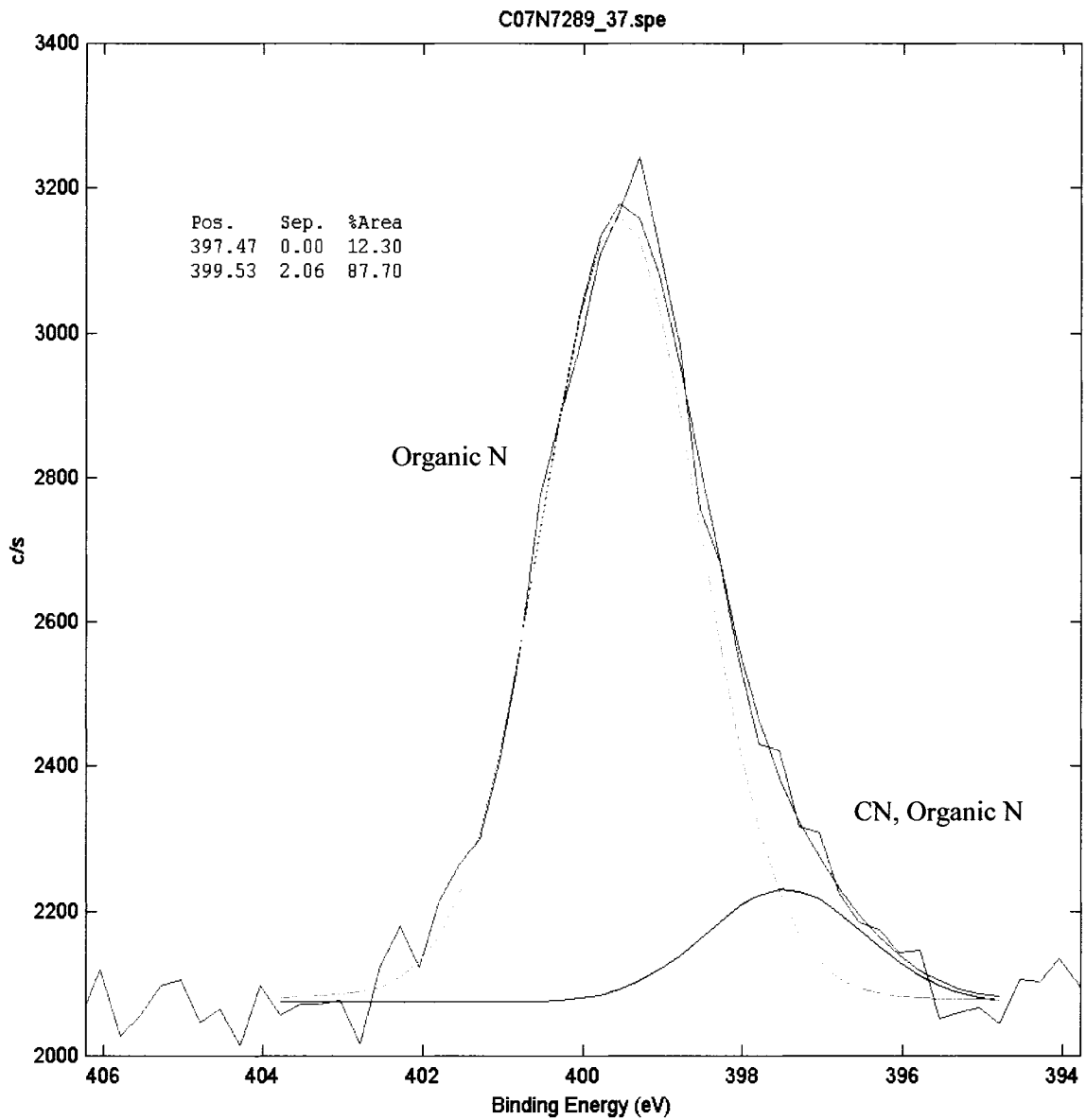


Figure 110. Nitrogen bonding state spectrum for weld 2.

C07N7289_37.spe: Croom: Welds EAG
2007 May 14 Al mono 39.7 W 200.0 μ 45.0° 23.50 eV 5.7077e+003 max 3.02 min
O1s/Point3: s2/1 (Shft SG3)

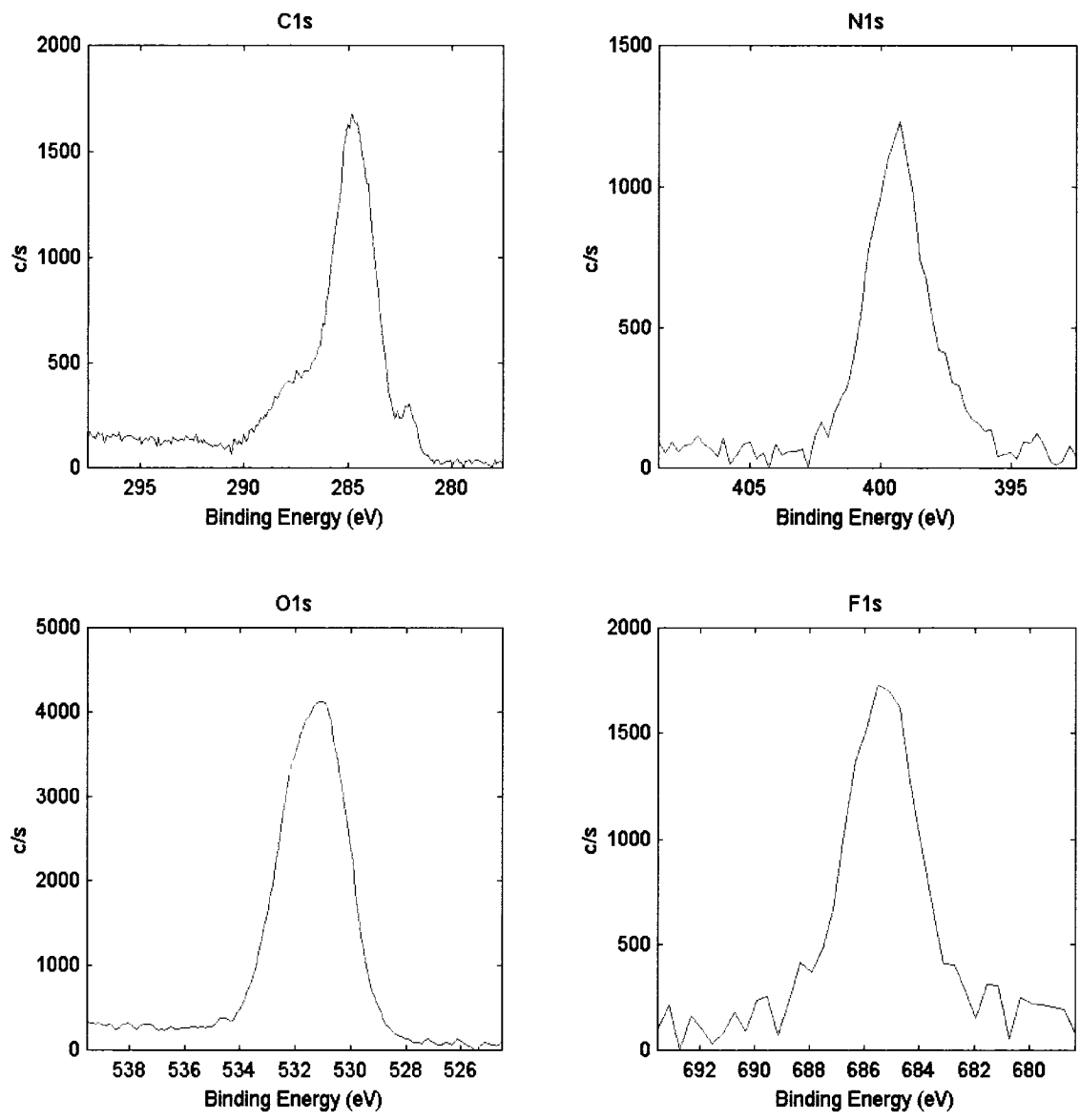


Figure 111. Bonding state spectra for carbon, nitrogen, oxygen, and fluorine for weld 2.

C07N7289_37.spe: Croom: Welds EAG
2007 May 14 Al mono 39.7 W 200.0 μ 45.0° 23.50 eV 5.7077e+003 max 3.02 min
O1s/Point3: s2/1 (Shft SG3)

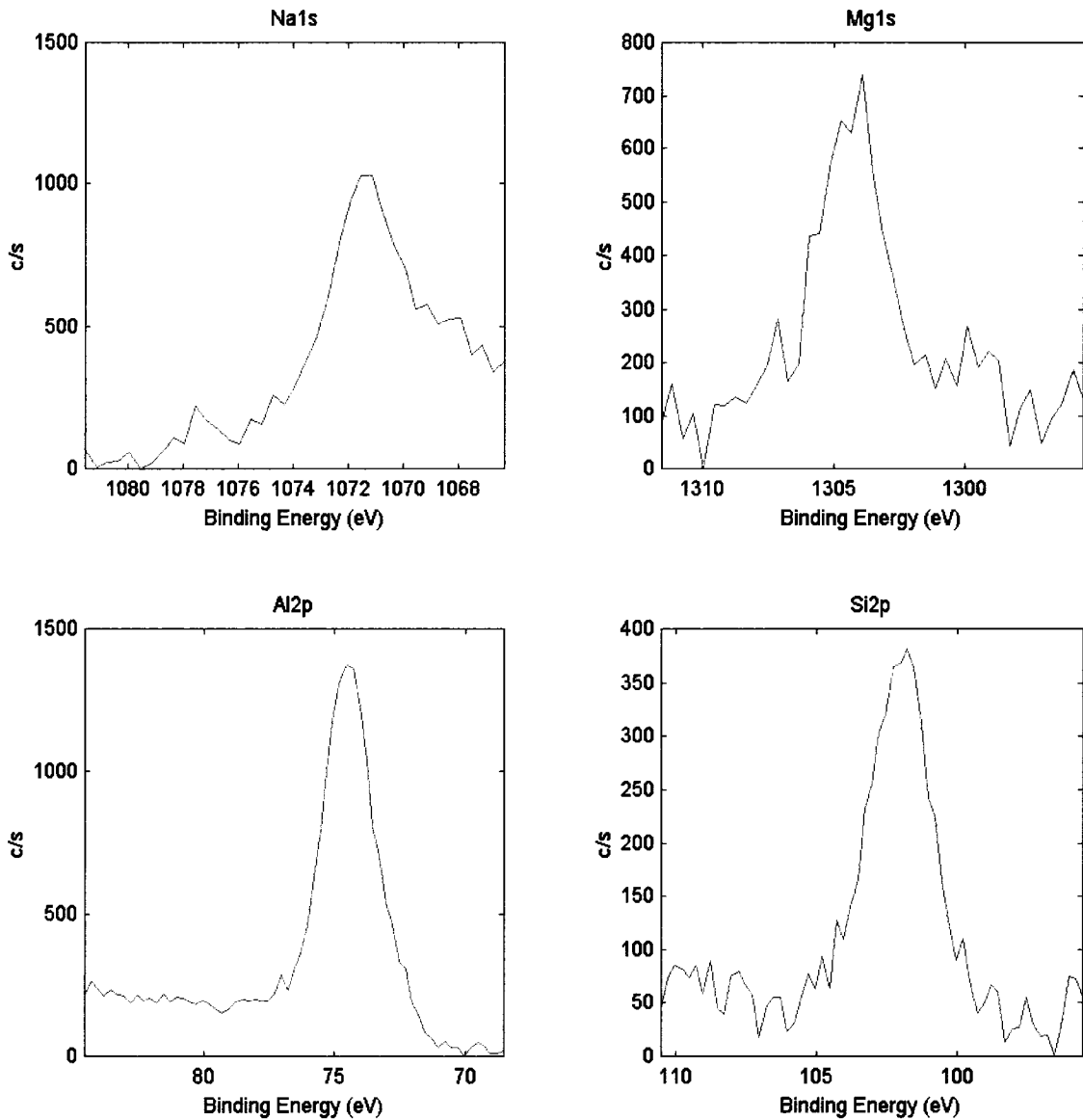


Figure 112. Bonding state spectra for sodium, magnesium, aluminum, and silicon for weld 2.

C07N7289_37.spe: Croom: Welds EAG
 2007 May 14 Al mono 39.7 W 200.0 μ 45.0° 23.50 eV 5.7077e+003 max 3.02 min
 O1s/Point3: s2/1 (Shift SG3)

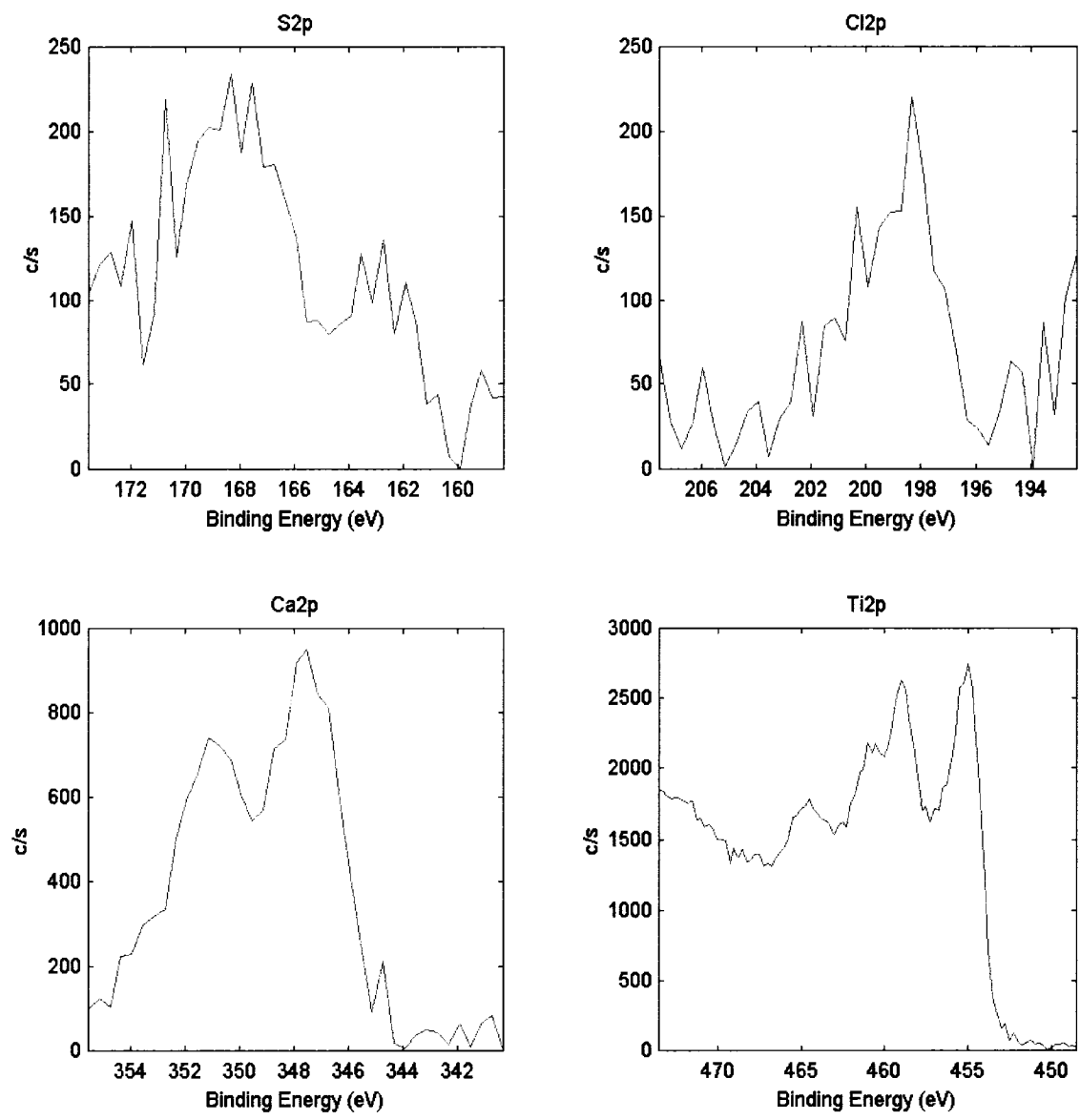


Figure 113. Bonding state spectra for sulfur, chlorine, calcium, and titanium for weld 2.

C07N7289_37.spe: Croom: Welds EAG
2007 May 14 Al mono 39.7 W 200.0 μ 45.0° 23.50 eV 5.7077e+003 max 3.02 min
O1s/Point3: s2/1 (Shift SG3)

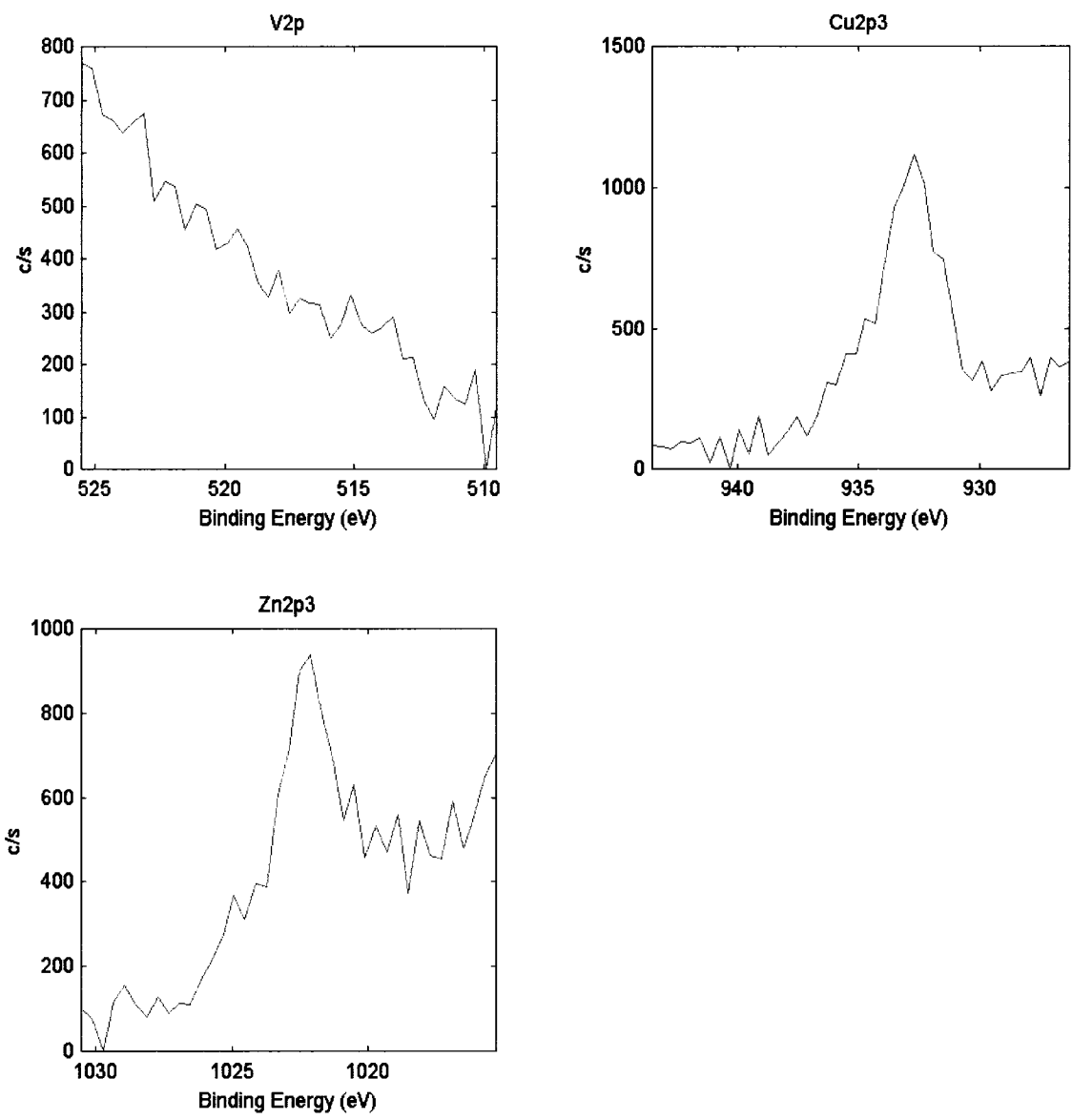


Figure 114. Bonding state spectra for vanadium, copper, and zinc for weld 2.

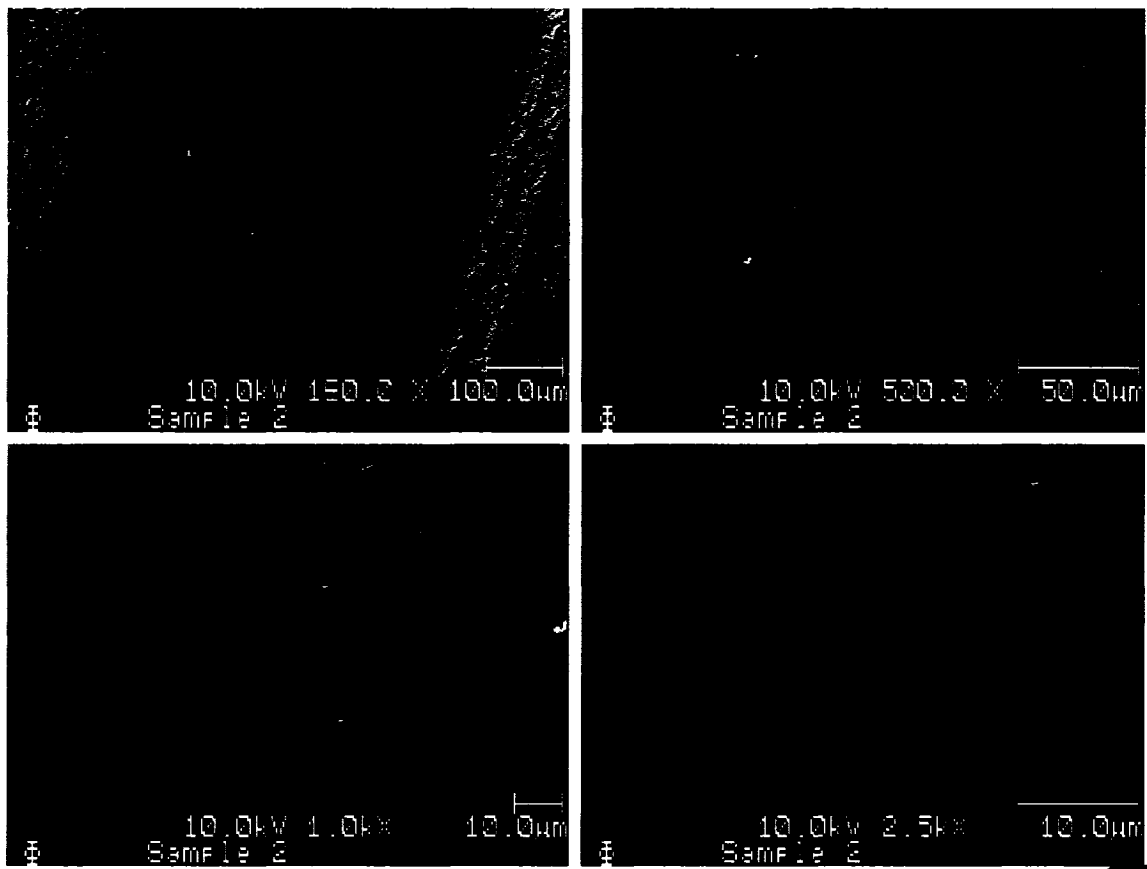


Figure 115. SEM images of the surface of weld 2.

C07N728920.spe: Sample 2
 2007 May 29 10.0 keV 0 FRR
 Sur1/Ful1 (S9D9)

EAG-CA
 3.0726e+004 max
 10.85 min

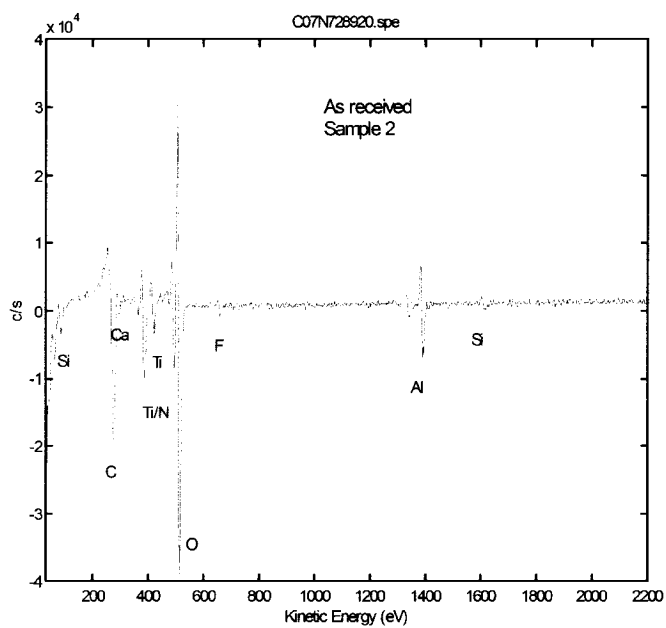


Figure 116. As received auger survey spectrum for the weld 2 specimen.

C07N728922.spe: Sample 2
 2007 May 29 10.0 keV 0 FRR
 Sur1/Ful1 (S9D9)

EAG-CA
 4.1276e+004 max
 6.51 min

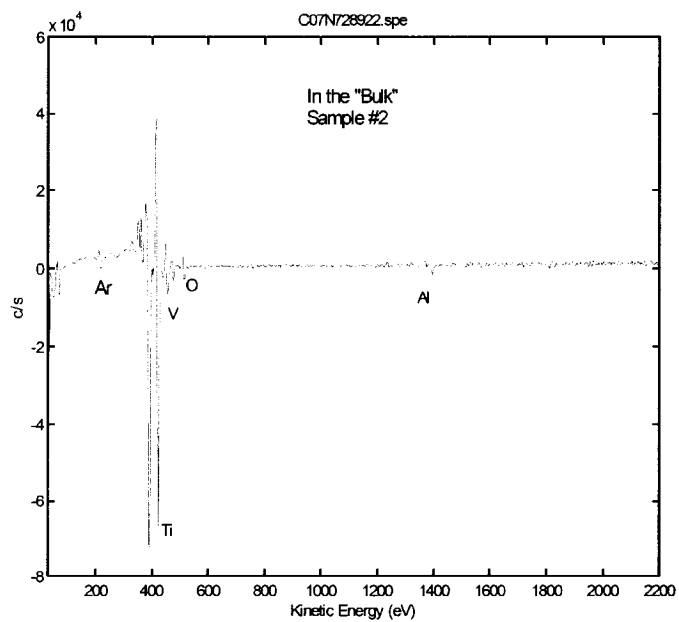


Figure 117. After sputtered auger survey spectrum for the weld 2 specimen.

APPENDIX H – SURFACE ANALYSIS RESULTS FOR WELD 4

C07N7289_38.spe: Croom: Welds						EAG
2007 May 14	Al mono	39.7 W	200.0 μ	45.0°	58.70 eV	4.0732e+003 max
Ti2p/Point6: s4/1 (Shift)						4.71 min

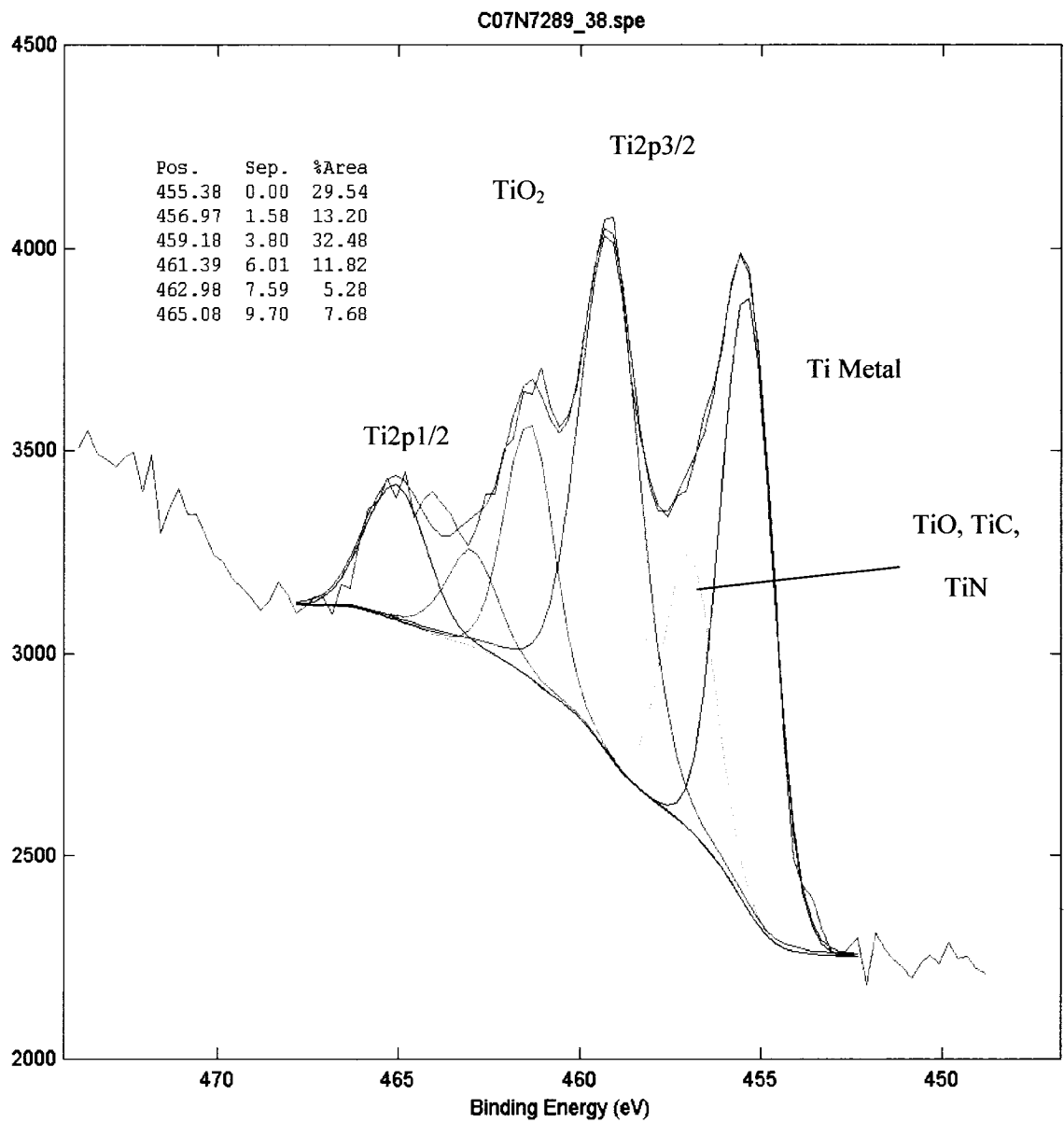


Figure 118. Titanium bonding state spectrum for weld 4.

C07N7289_38.spe: Croom: Welds EAG
 2007 May 14 Al mono 39.7 W 200.0 μ 45.0° 58.70 eV 1.3055e+003 max 3.80 min
 Al2p/Point6: s4/1 (Shft)

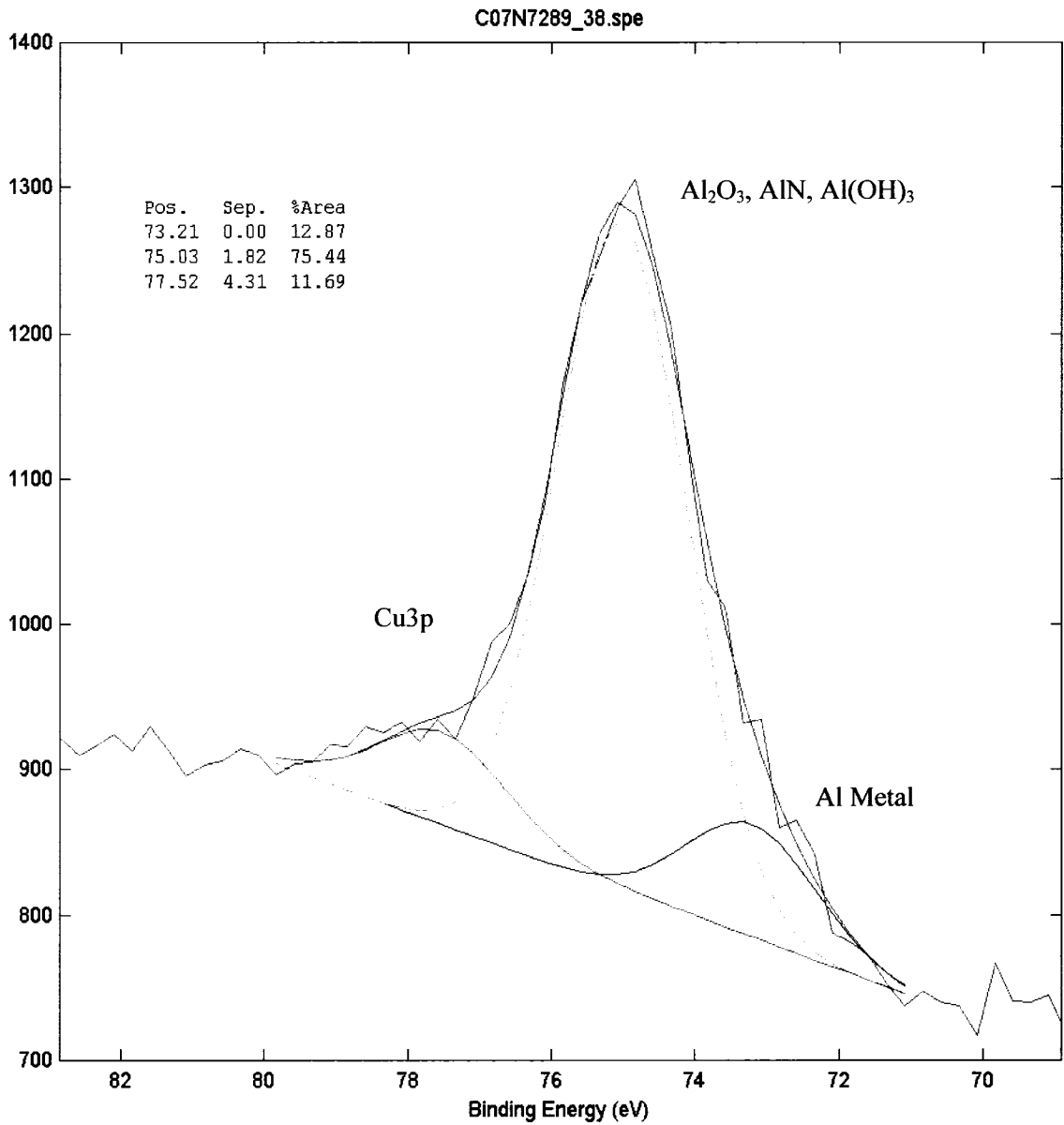


Figure 119. Aluminum bonding state spectrum for weld 4.

C07N7289_38.spe: Croom: Welds EAG
 2007 May 14 Al mono 39.7 W 200.0 μ 45.0° 23.50 eV 4.6792e+003 max 2.42 min
 O1s/Point6: s4/1 (Shft)

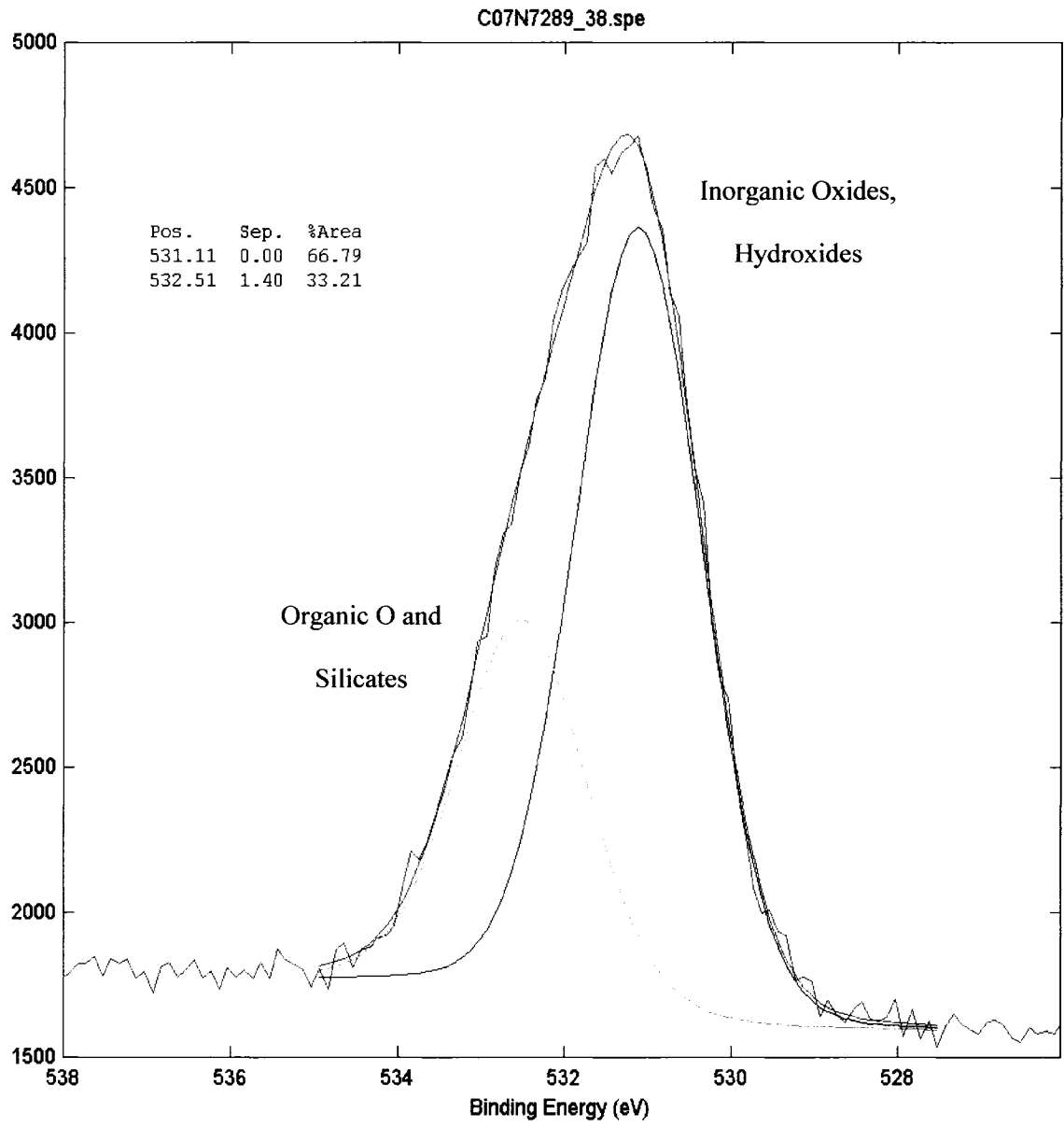


Figure 120. Oxygen bonding state spectrum for weld 4.

C07N7289_38.spe: Croom: Welds EAG
 2007 May 14 Al mono 39.7 W 200.0 μ 45.0° 23.50 eV 2.4764e+003 max 8.58 min
 C1s/Point6: s4/1 (Shft)

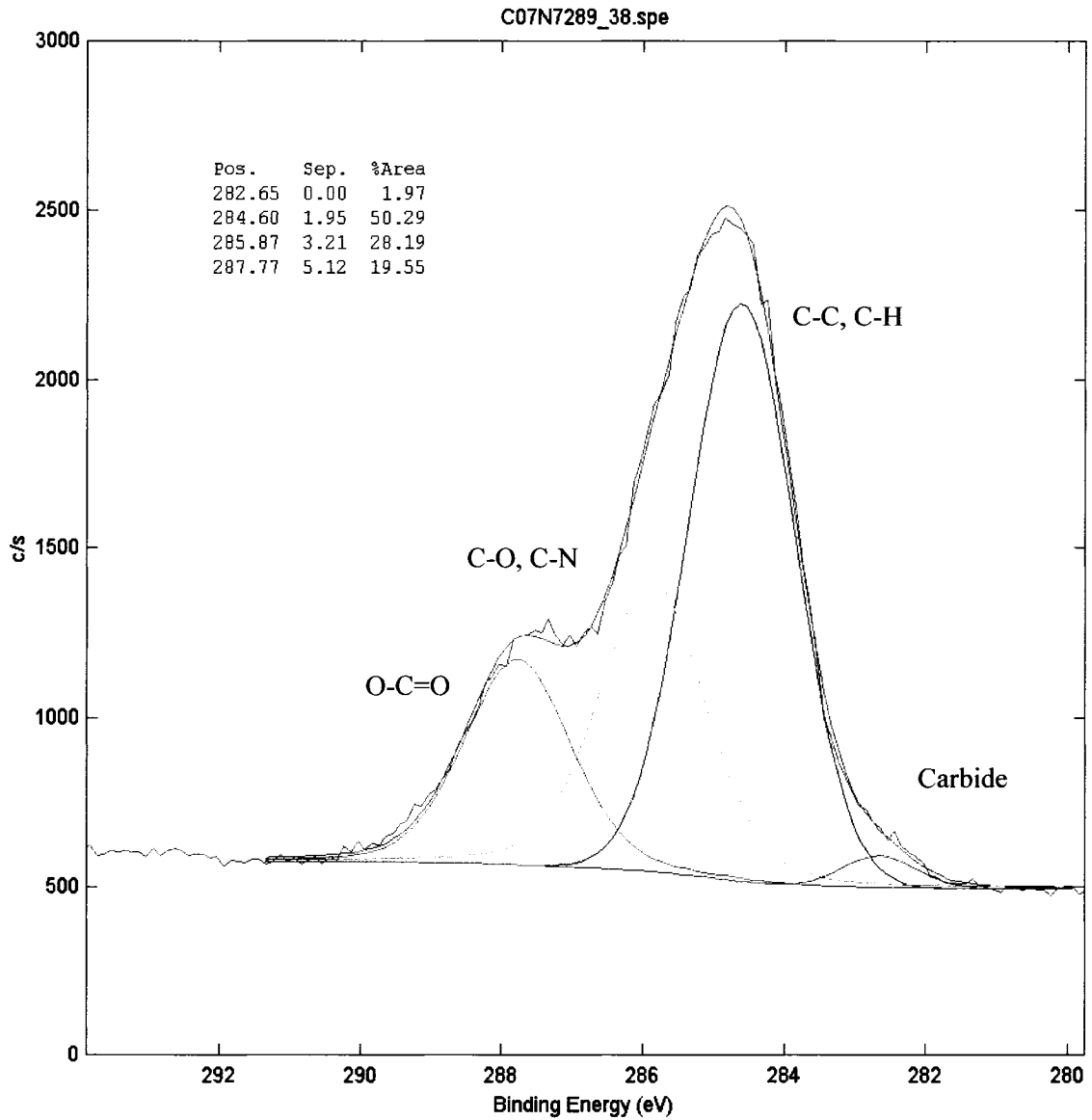


Figure 121. Carbon bonding state spectrum for weld 4.

C07N7289_38.spe: Croom: Welds EAG
 2007 May 14 Al mono 39.7 W 200.0 μ 45.0° 58.70 eV 5.0296e+003 max 2.24 min
 N1s/Point6: s4/1 (Shift)

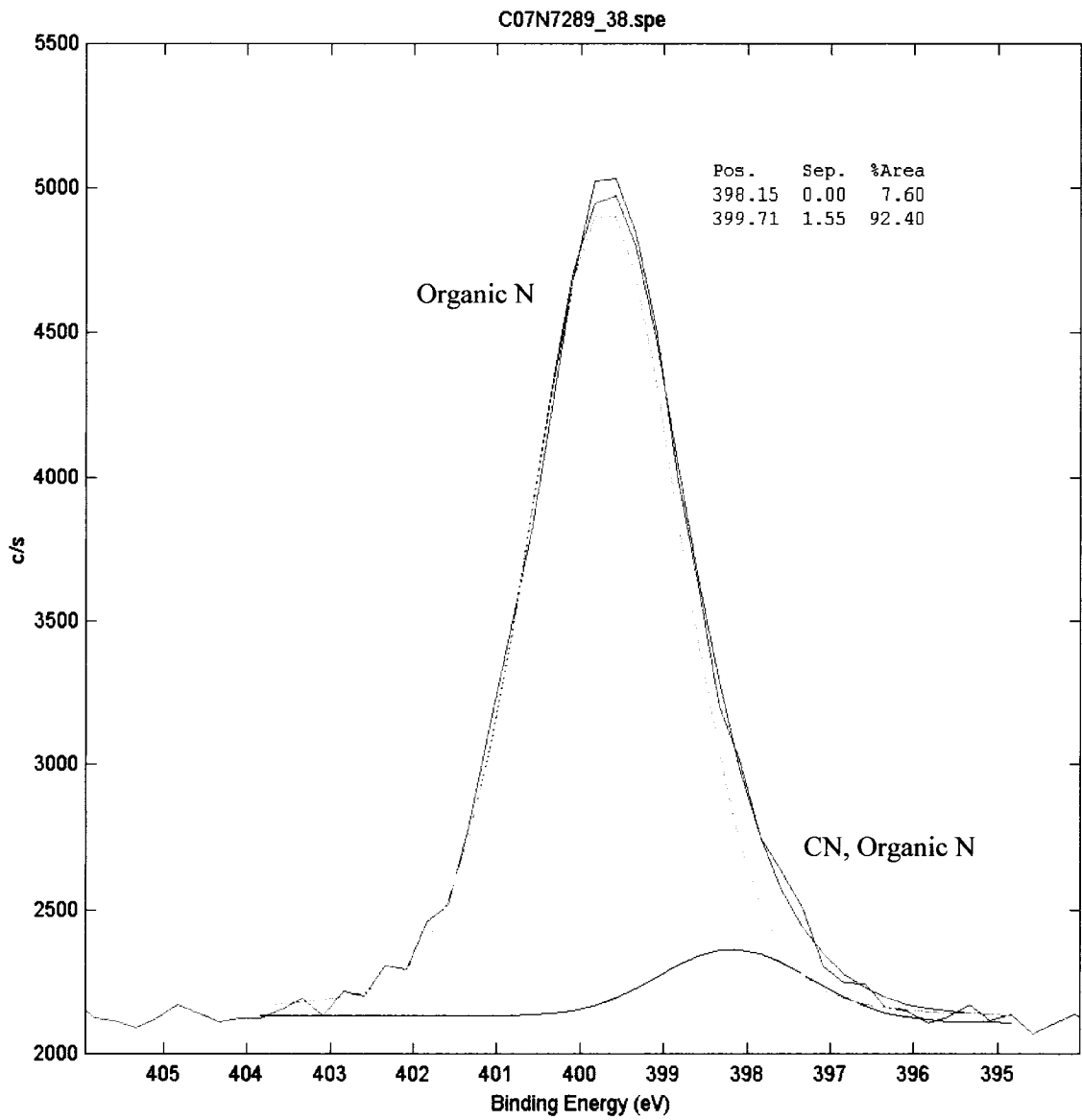


Figure 122. Nitrogen bonding state spectrum for weld 4.

C07N7289_38.spe: Croom: Welds EAG
 2007 May 14 Al mono 39.7 W 200.0 μ 45.0° 23.50 eV 4.6792e+003 max 3.02 min
 O1s/Point6: s4/1 (Shft)

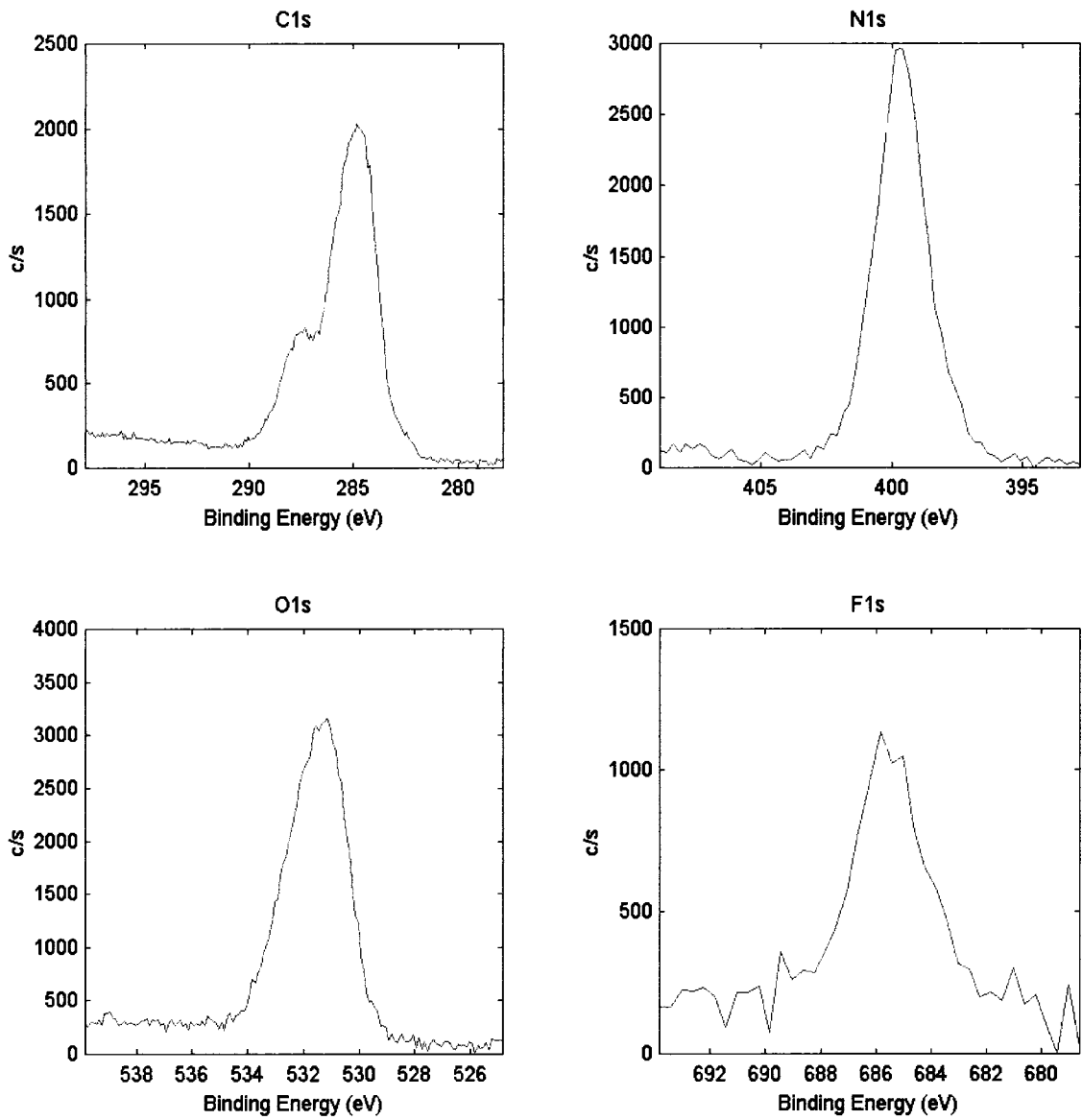


Figure 123. Bonding state spectra for carbon, nitrogen, oxygen, and fluorine for weld 4.

C07N7289_38.spe: Croom: Welds			EAG				
2007 May 14	Al mono	39.7 W	200.0 μ	45.0°	23.50 eV	2.4764e+003 max	12.06 min
C1s/Point6: s4/1 (Shft)							

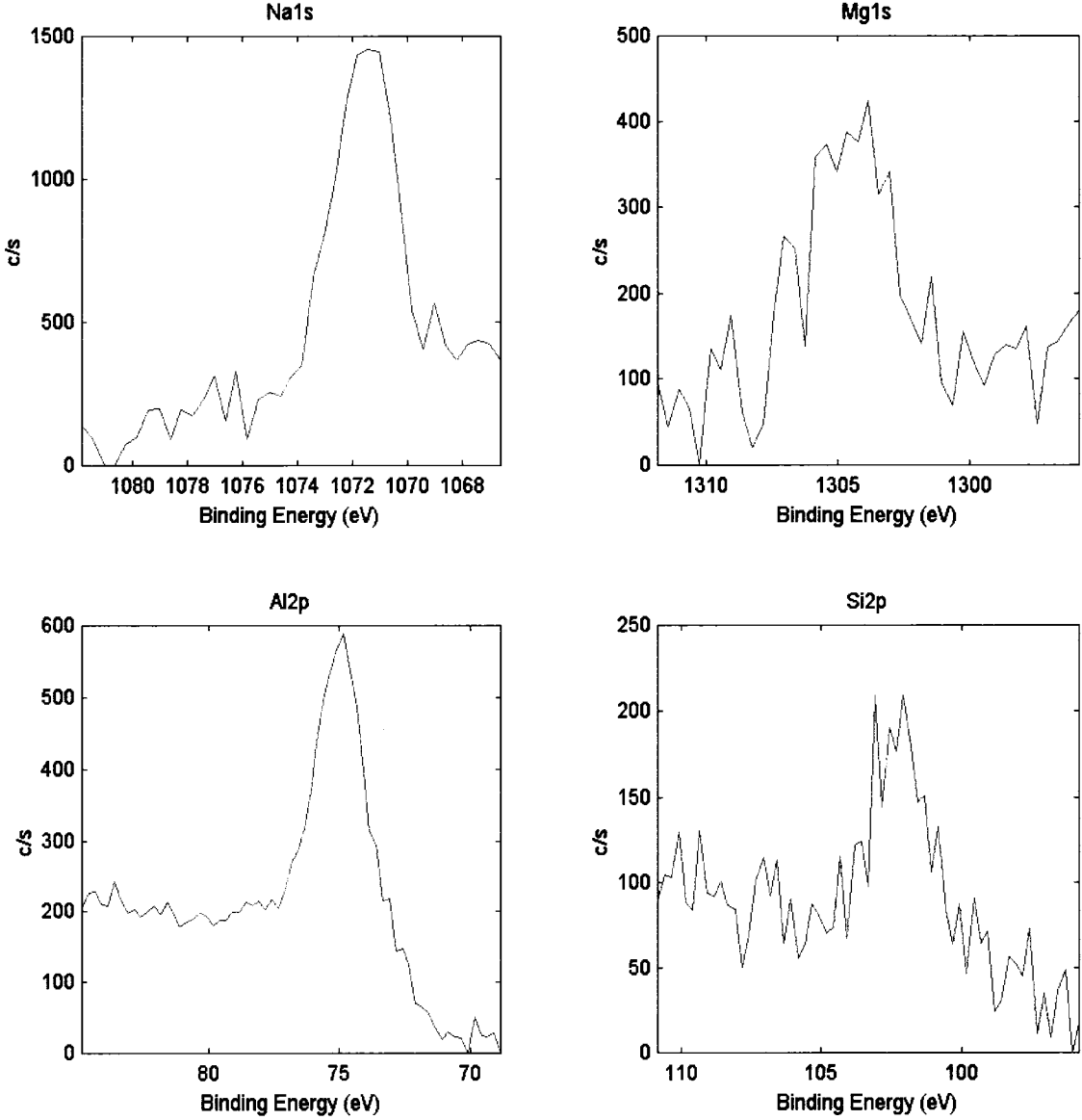


Figure 124. Bonding state spectra for sodium, magnesium, aluminum, and silicon for weld 4.

C07N7289_38.spe: Croom: Welds EAG
2007 May 14 Al mono 39.7 W 200.0 μ 45.0° 23.50 eV 4.6792e+003 max 3.02 min
O1s/Point6: s4/1 (Shft)

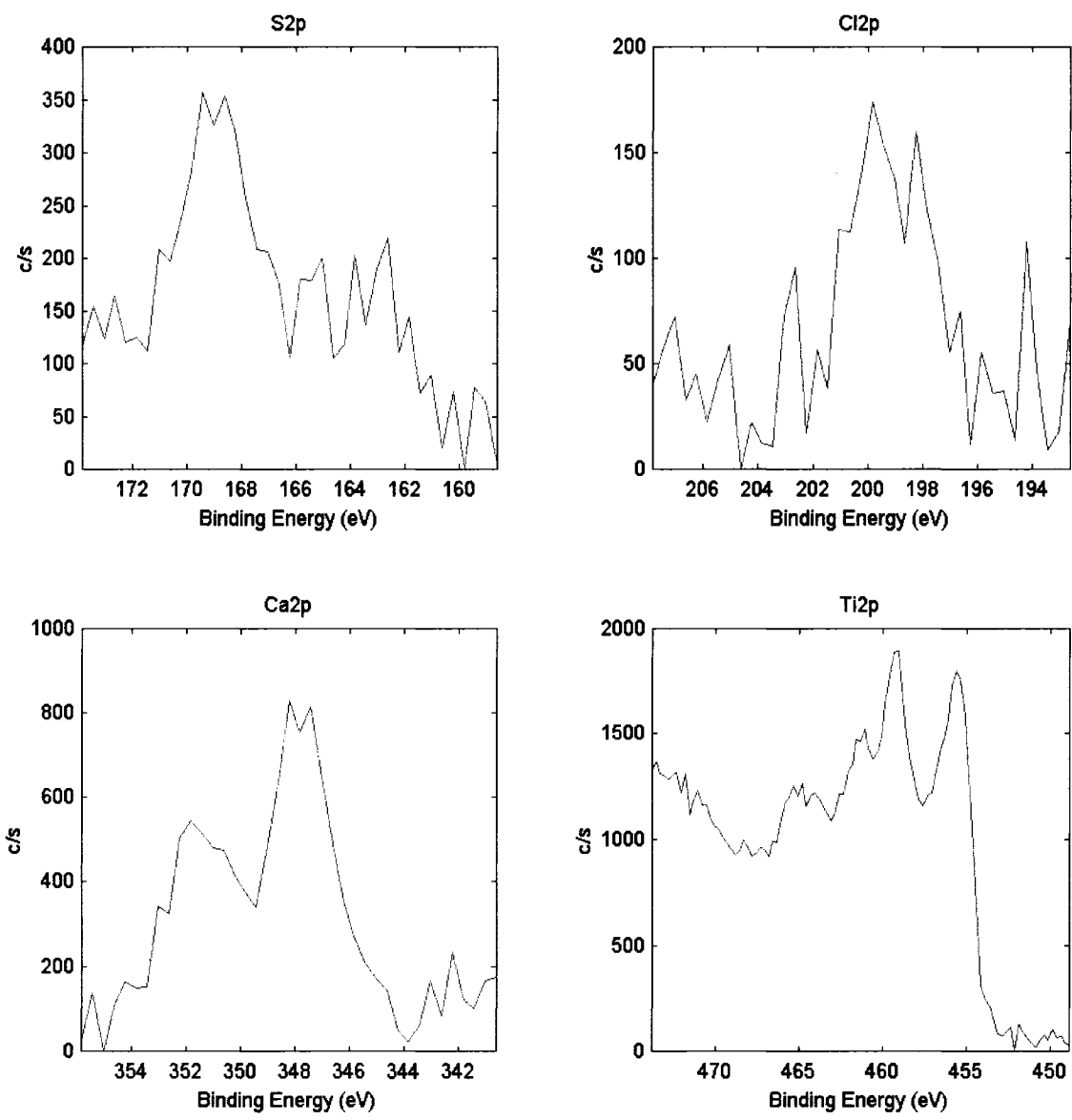


Figure 125. Bonding state spectra for sulfur, chlorine, calcium, and titanium for weld 4.

C07N7289_38.spe: Croom: Welds EAG
2007 May 14 Al mono 39.7 W 200.0 μ 45.0° 23.50 eV 4.6792e+003 max 3.02 min
O1s/Point6: s4/1 (Shift)

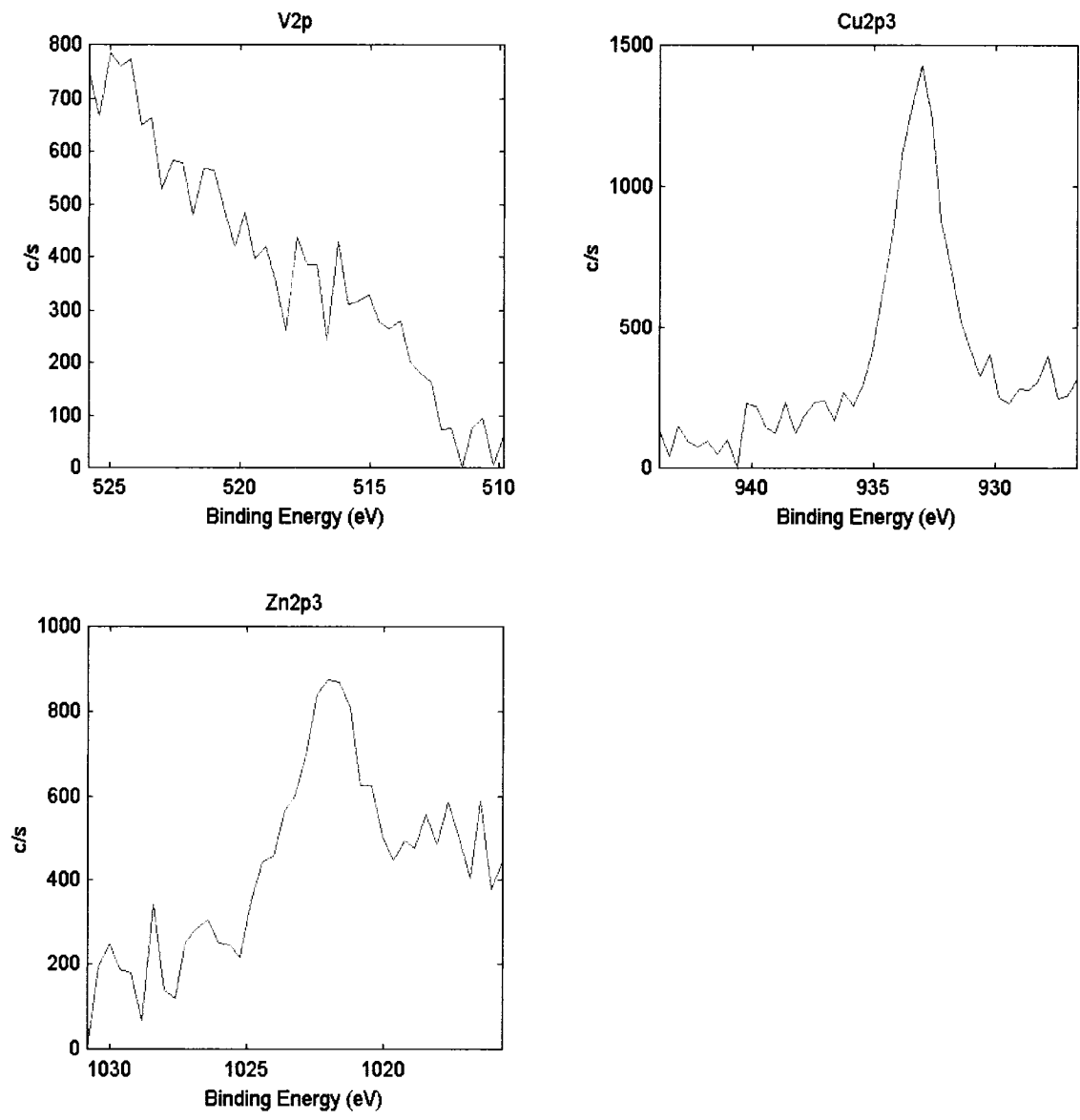


Figure 126. Bonding state spectra for vanadium, copper, and zinc for weld 4.

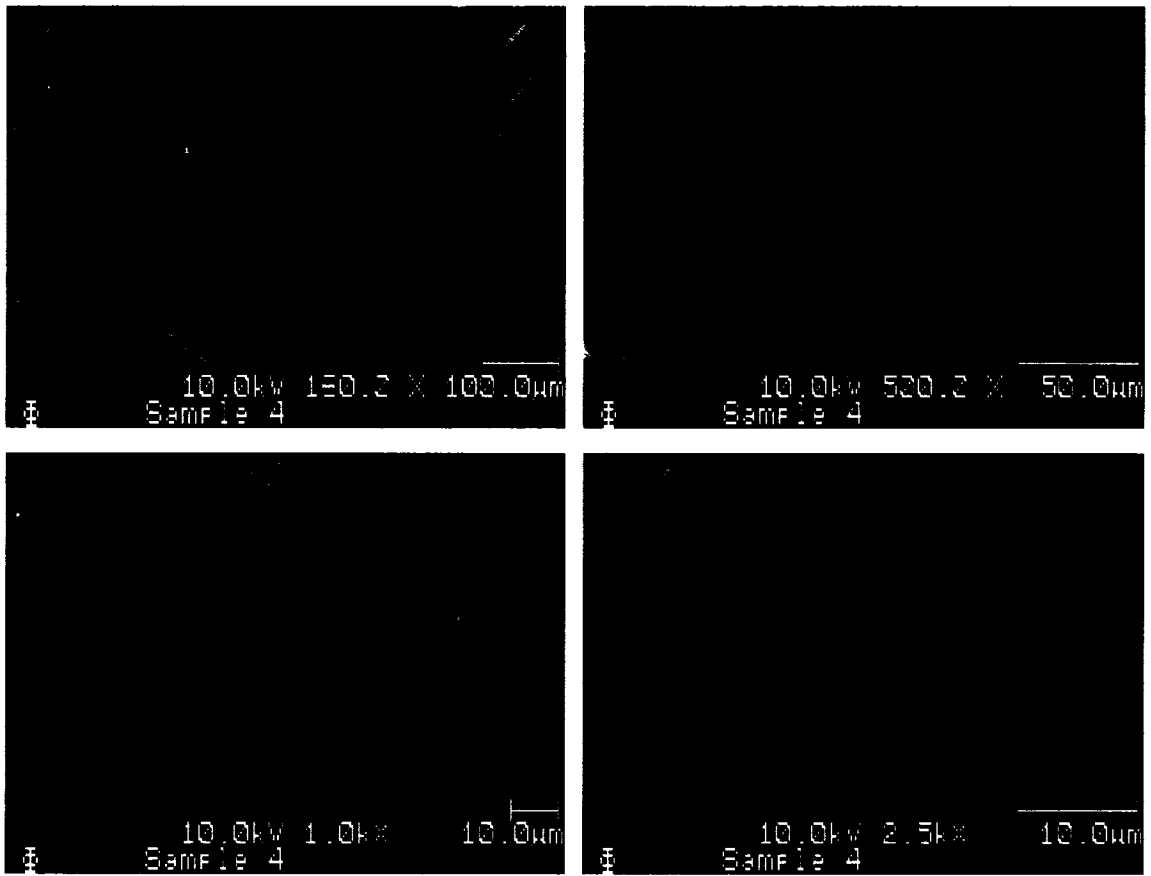


Figure 127. SEM images of the surface of weld 4.

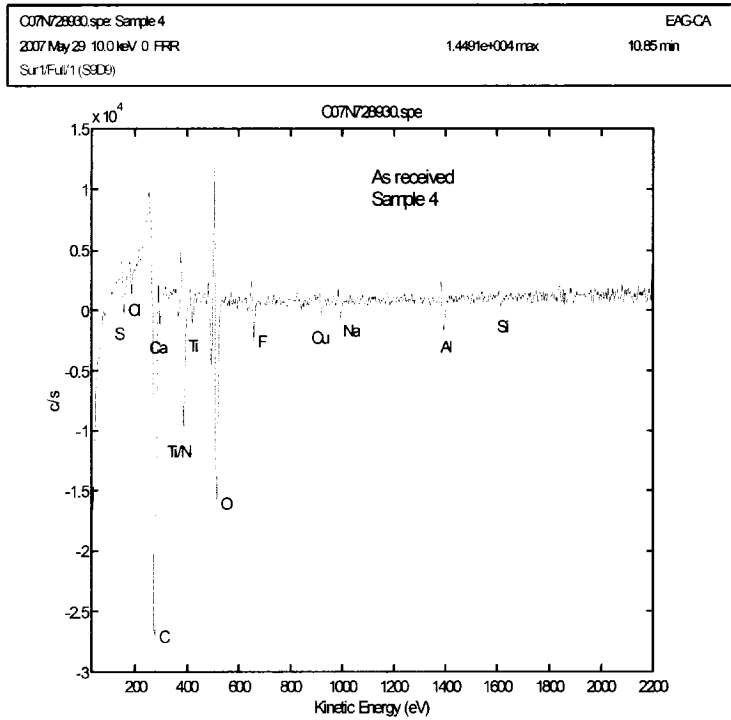


Figure 128. As received auger survey spectrum for weld 4.

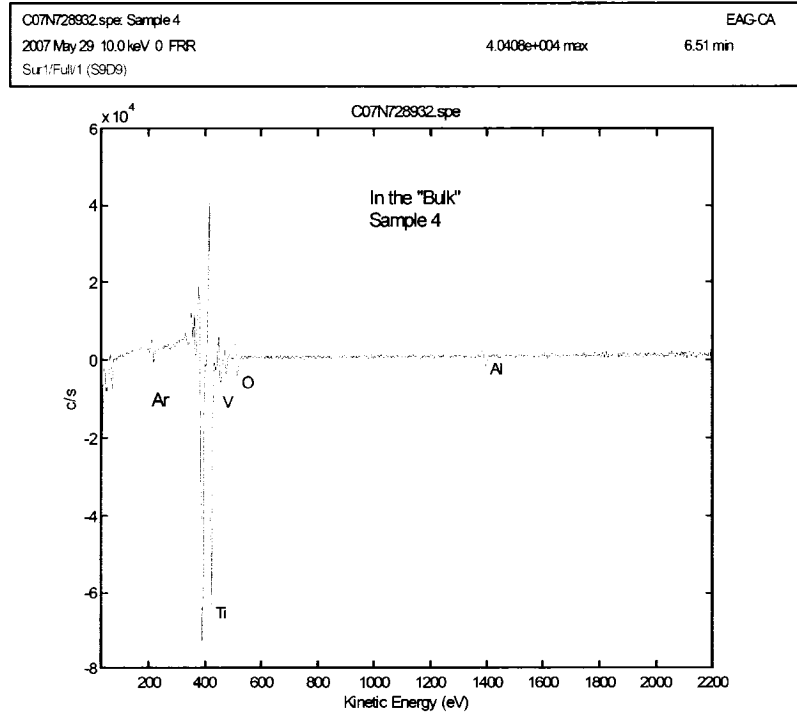


Figure 129. After sputtered auger survey spectrum for weld 4.

APPENDIX I – SURFACE ANALYSIS RESULTS FOR WELD 7

C07N7289_36.spe: Croom: Welds EAG
 2007 May 14 Al mono 39.7 W 200.0 μ 45.0° 58.70 eV 7.6168e+003 max 3.83 min
 Ti2p/Point5: s7/1 (Shift)

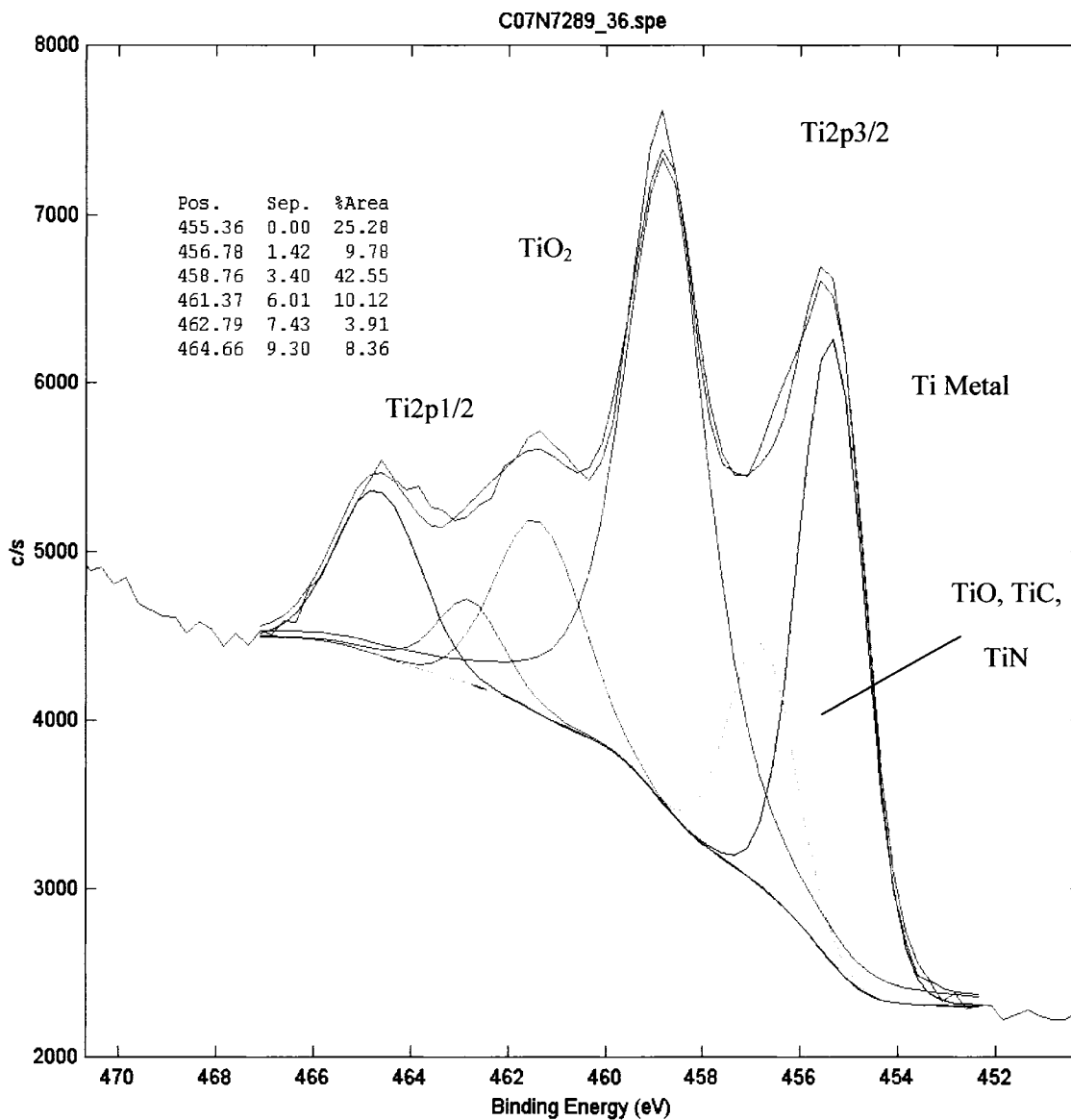


Figure 130. Titanium bonding state spectrum for weld 7.

C07N7289_36.spe: Croom: Welds EAG
 2007 May 14 Al mono 39.7 W 200.0 μ 45.0° 58.70 eV 2.7233e+003 max 2.53 min
 Al2p/Point5: s7/1 (Shft)

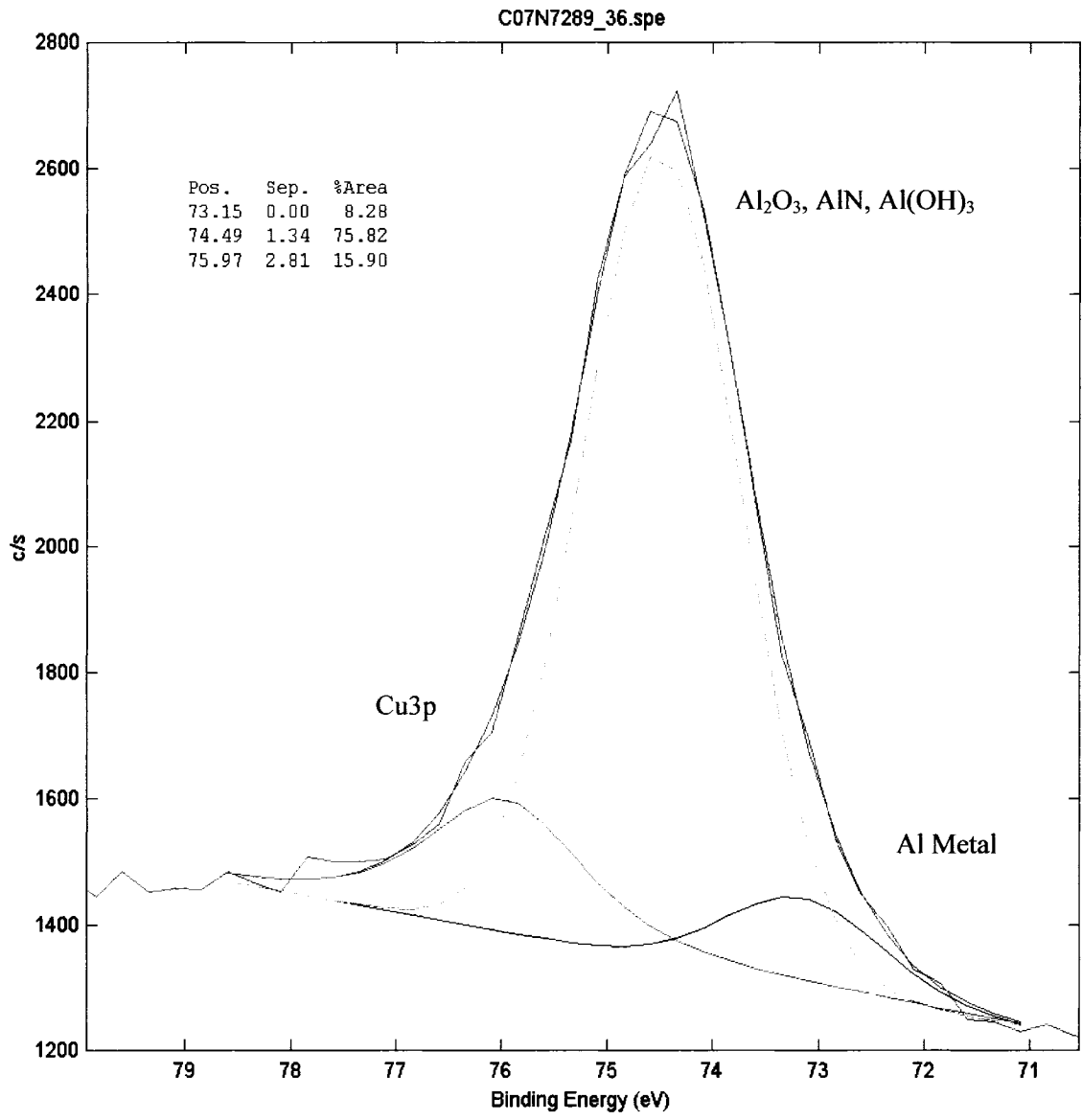


Figure 131. Aluminum bonding state spectrum for weld 7.

C07N7289_36.spe: Croom: Welds EAG
 2007 May 14 Al mono 39.7 W 200.0 μ 45.0° 23.50 eV 8.4417e+003 max 2.28 min
 O1s/Point5: s7/1 (Shft)

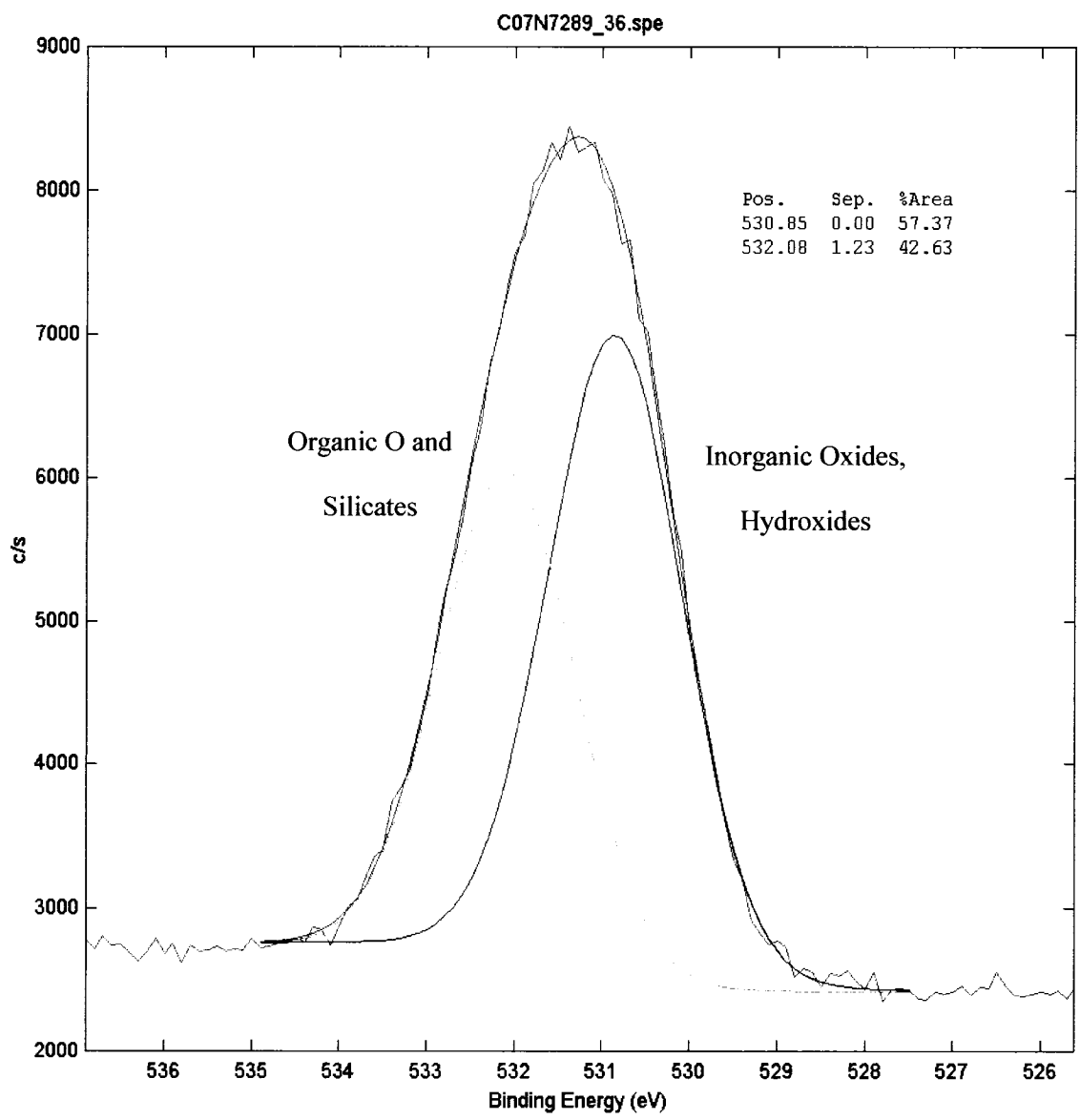


Figure 132. Oxygen bonding state spectrum for weld 7.

C07N7289_36.spe: Croom: Welds EAG
 2007 May 14 Al mono 39.7 W 200.0 μ 45.0° 23.50 eV 2.0883e+003 max 7.68 min
 C1s/Point5: s7/1 (Shft)

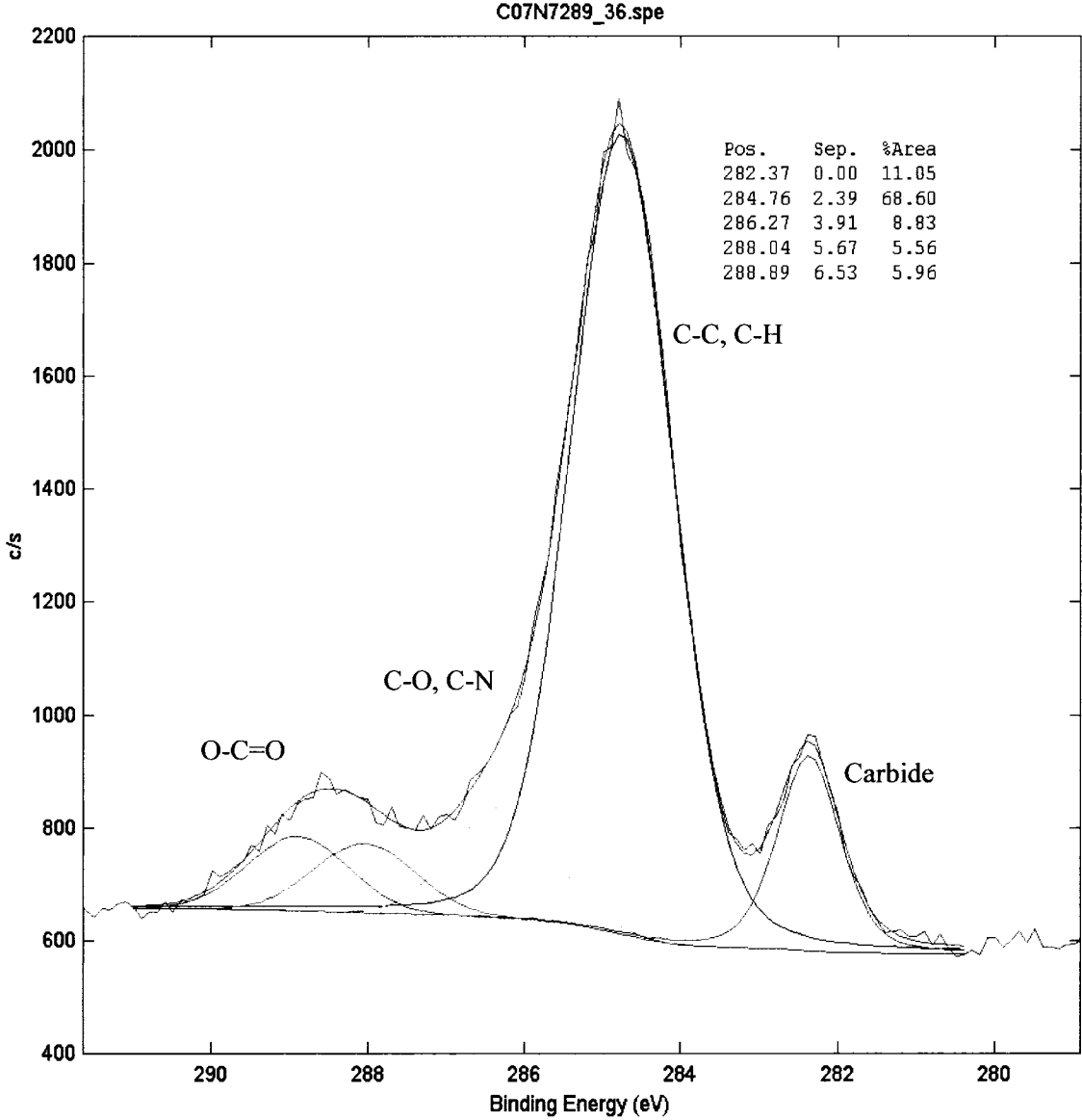


Figure 133. Carbon bonding state spectrum for weld 7.

C07N7289_36.spe: Croom: Welds EAG
 2007 May 14 Al mono 39.7 W 200.0 μ 45.0° 58.70 eV 2.9664e+003 max 2.52 min
 N1s/Point5: s7/1 (Shft)

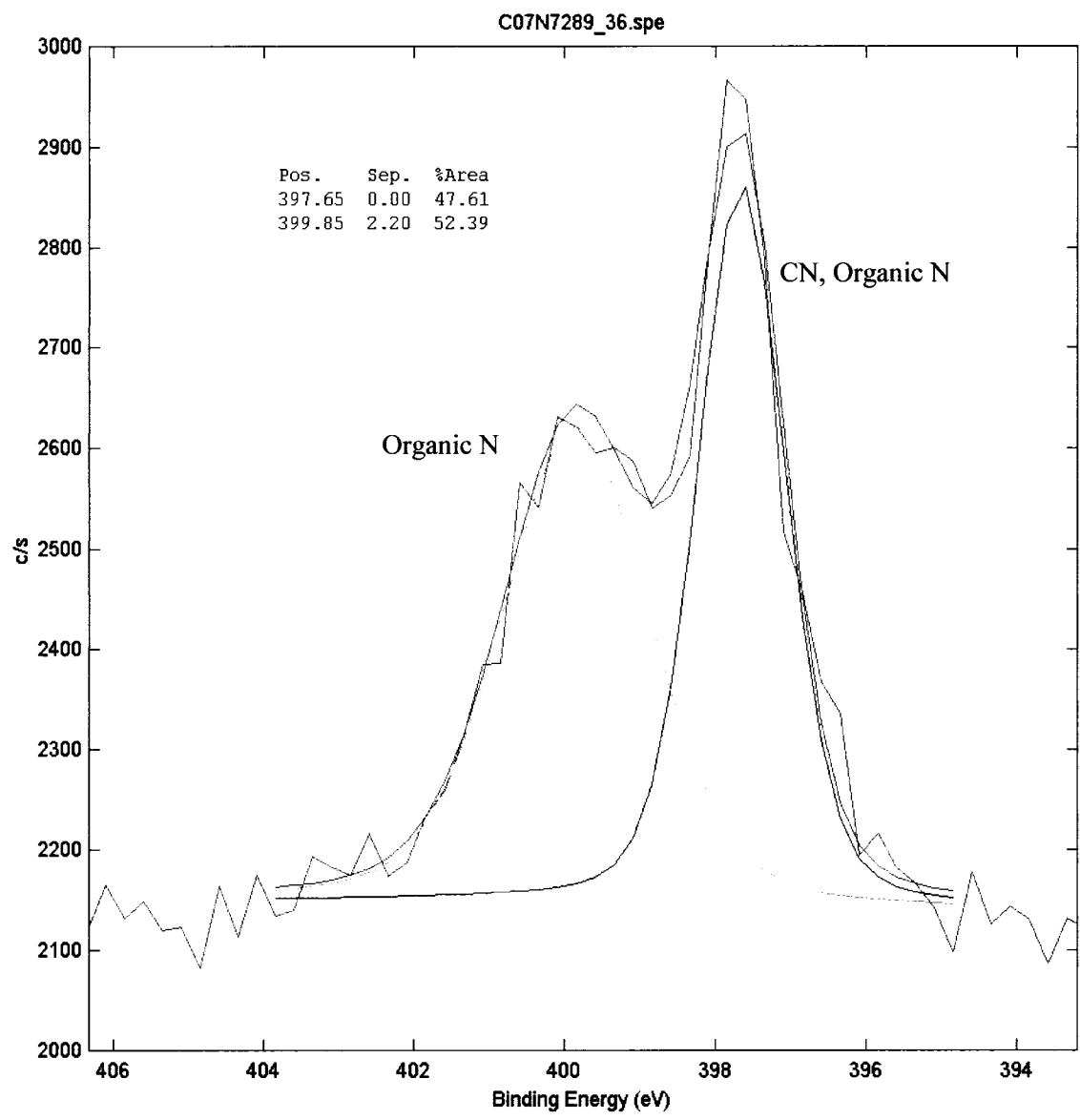


Figure 134. Nitrogen bonding state spectrum for weld 7.

C07N7289_36.spe: Croom: Welds EAG
2007 May 14 Al mono 39.7 W 200.0 μ 45.0° 23.50 eV 8.4417e+003 max 3.02 min
O1s/Point5: s7/1 (Shft)

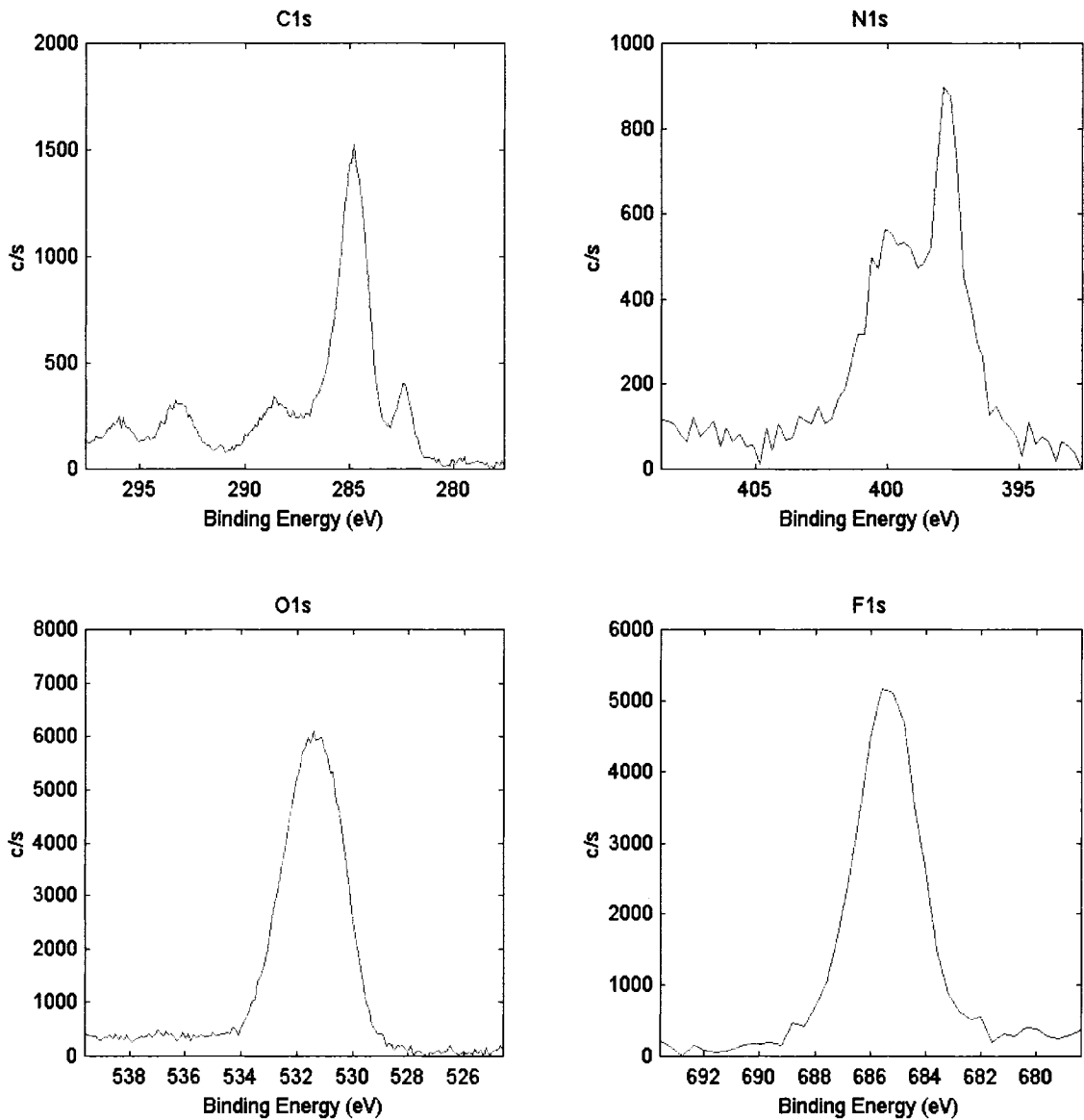


Figure 135. Bonding state spectra for carbon, nitrogen, oxygen, and fluorine for weld 7.

C07N7289_36.spe: Croom: Welds			EAG
2007 May 14	Al mono 39.7 W 200.0 μ 45.0°	23.50 eV	8.4417e+003 max 3.02 min
O1s/Point5: s7/1 (Shft)			

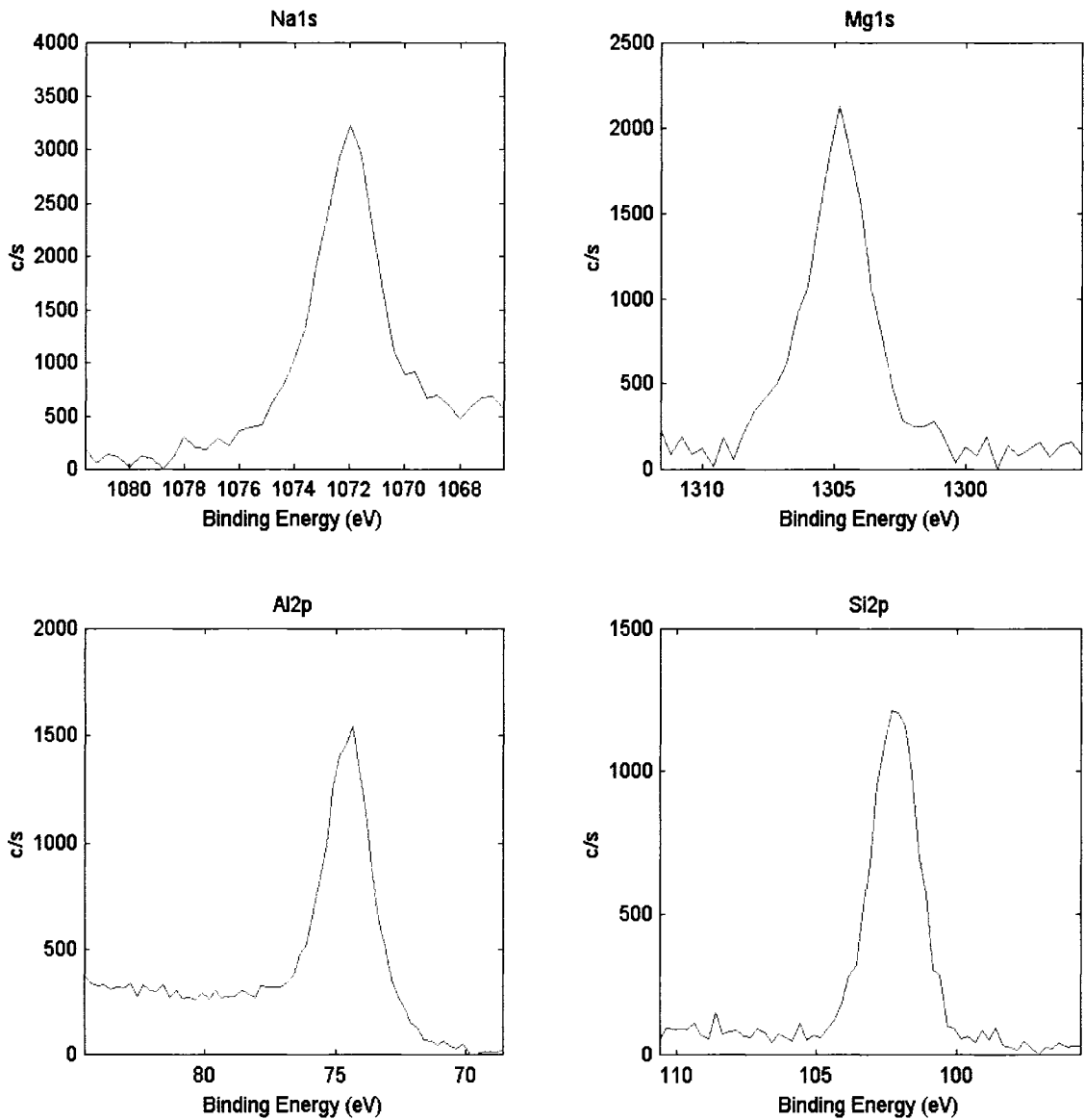


Figure 136. Bonding state spectra for sodium, magnesium, aluminum, and silicon for weld 7.

C07N7289_36.spe: Croom: Welds			EAG
2007 May 14	Al mono 39.7 W 200.0 μ 45.0°	23.50 eV	8.4417e+003 max 3.02 min
O1s/Point5: s7/1 (Shft)			

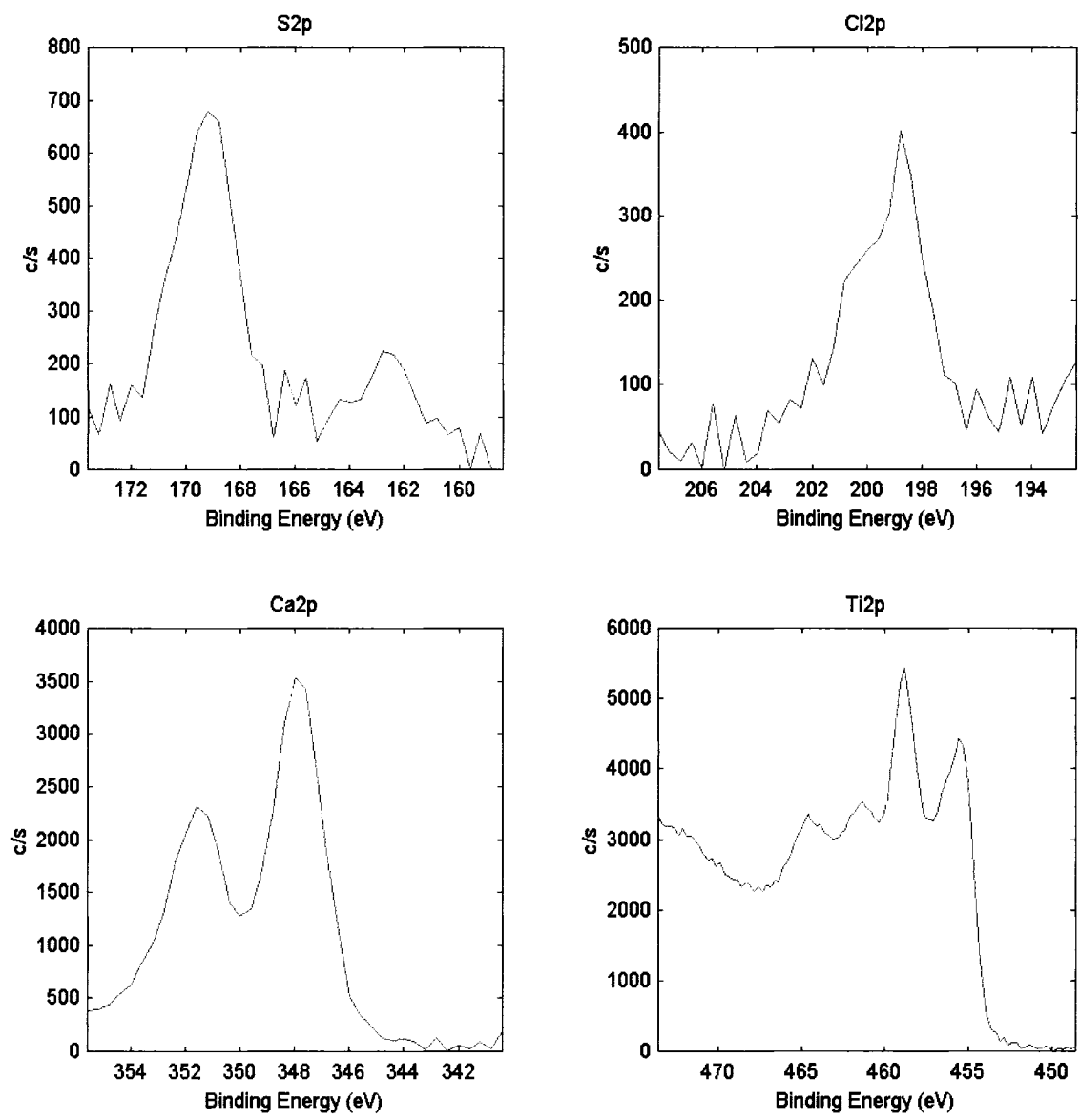


Figure 137. Bonding state spectra for sulfur, chlorine, calcium, and titanium for weld 7.

C07N7289_36.spe: Croom: Welds EAG
2007 May 14 Al mono 39.7 W 200.0 μ 45.0° 23.50 eV 8.4417e+003 max 3.02 min
O1s/Point5: s7/1 (Shift)

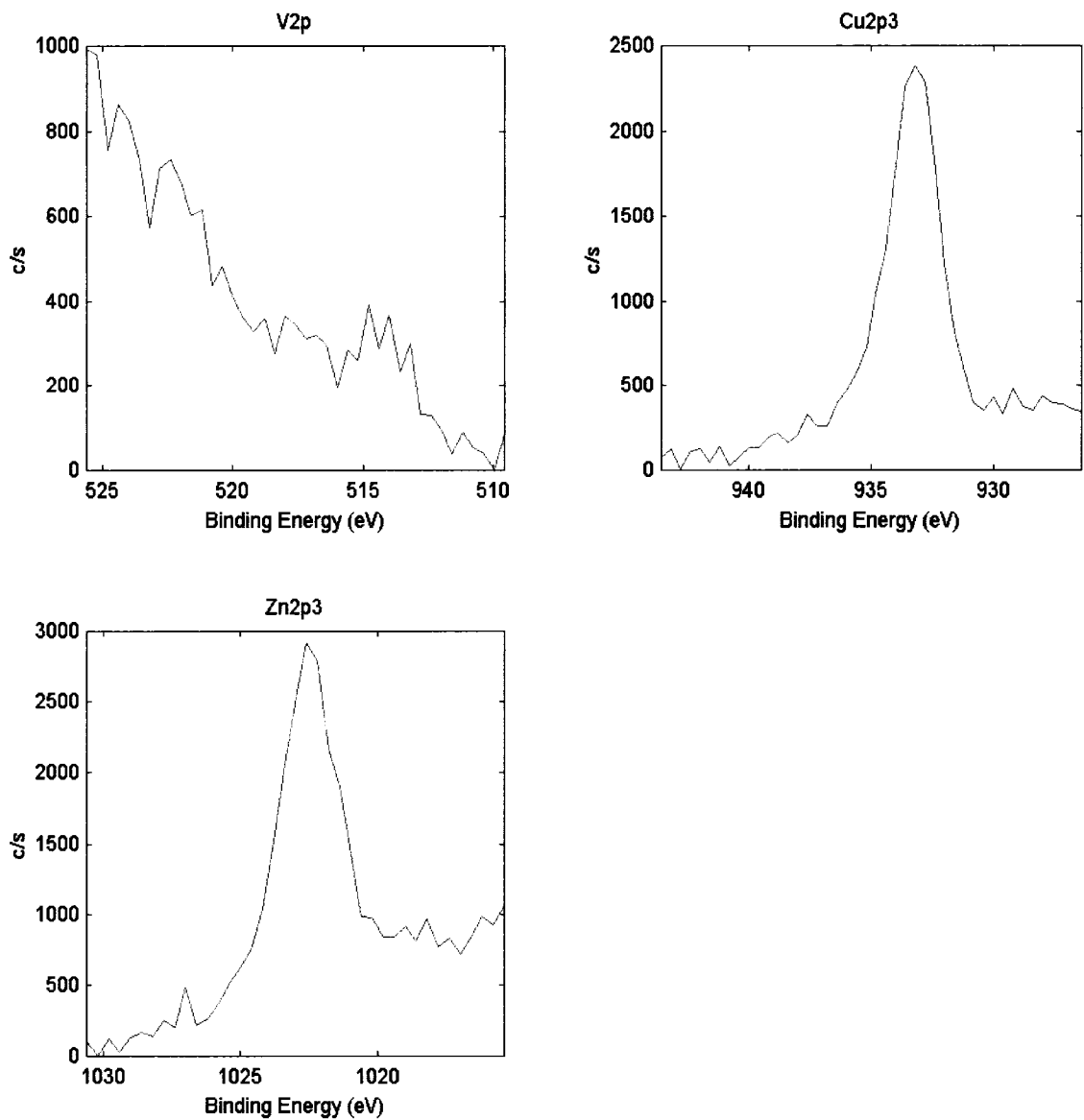


Figure 138. Bonding state spectra for vanadium, copper, and zinc for weld 7.

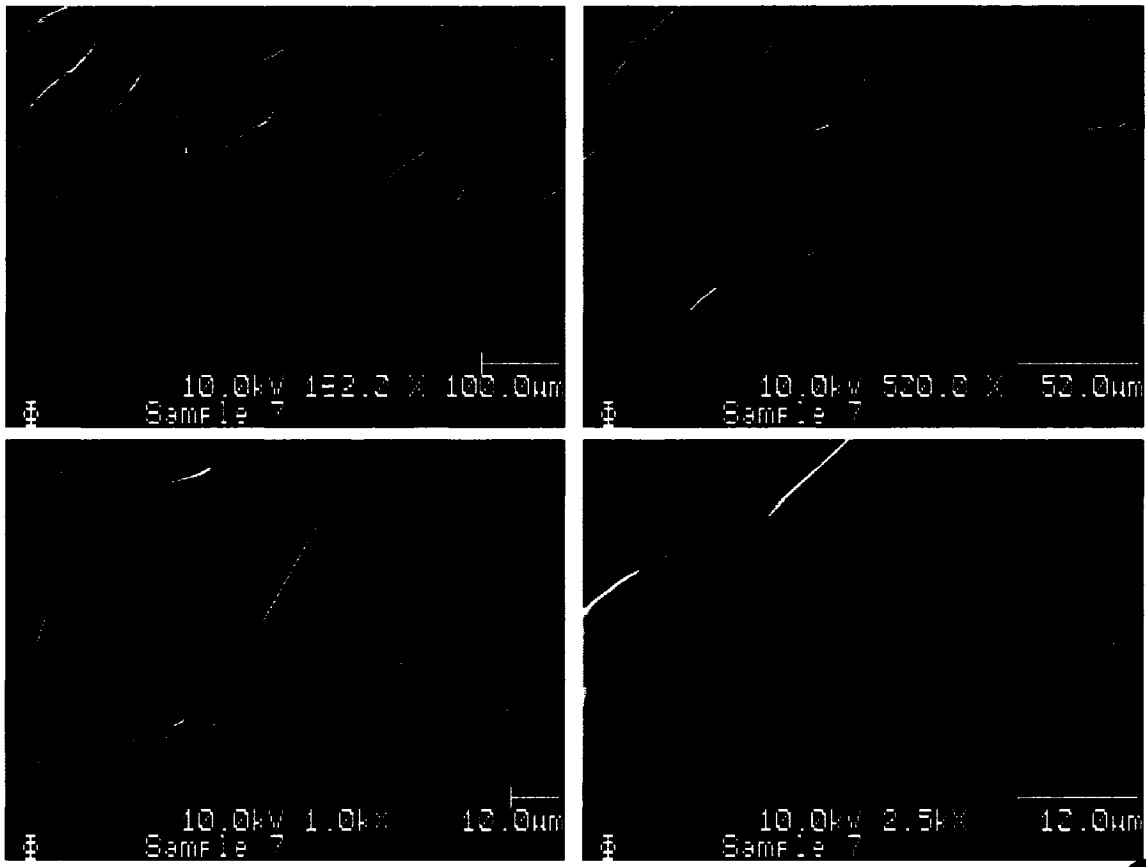


Figure 139. SEM images of the surface of weld 7.

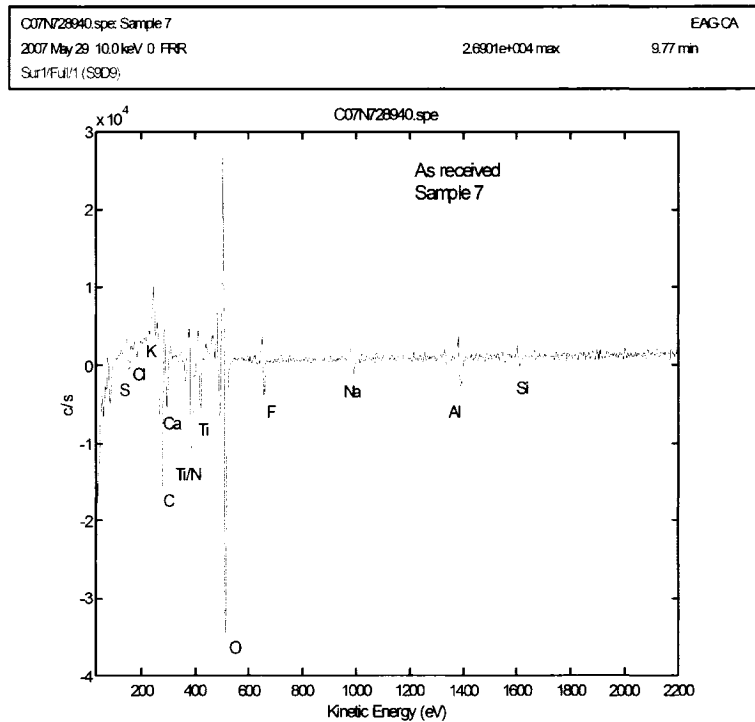


Figure 140. As received auger survey spectrum of weld 7.

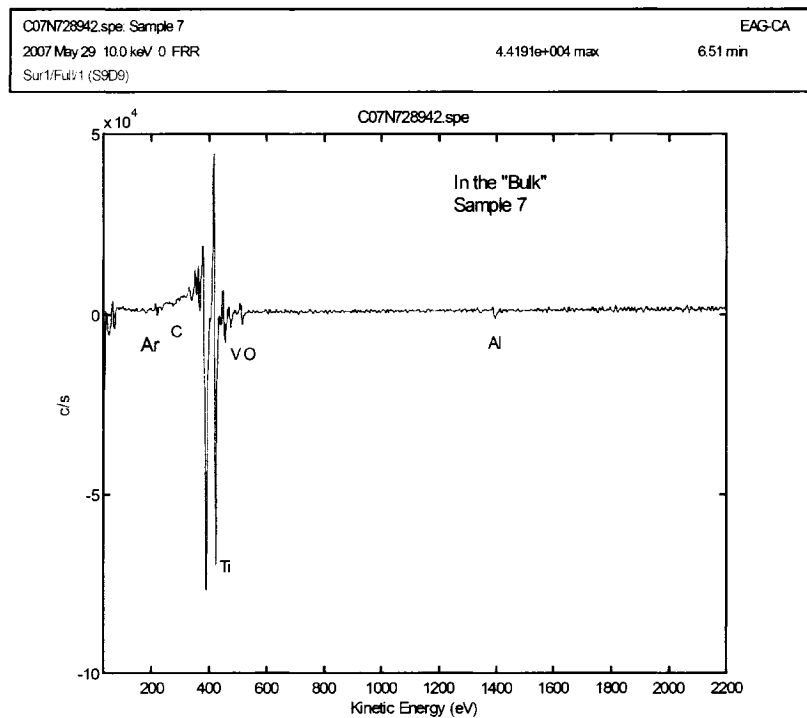


Figure 141. After sputtered auger survey spectrum of weld 7.

APPENDIX J – XPS BONDING STATE COMPARISON SPECTRA RESULTS

C07N7289_34.spe: Croom: Welds	EAG
2007 May 14 Al mono 39.7 W 200.0 μ 45.0° 58.70 eV	1.0000e+000 max 4.71 min
Ti2p/Point1: Control/1 (Shft)	

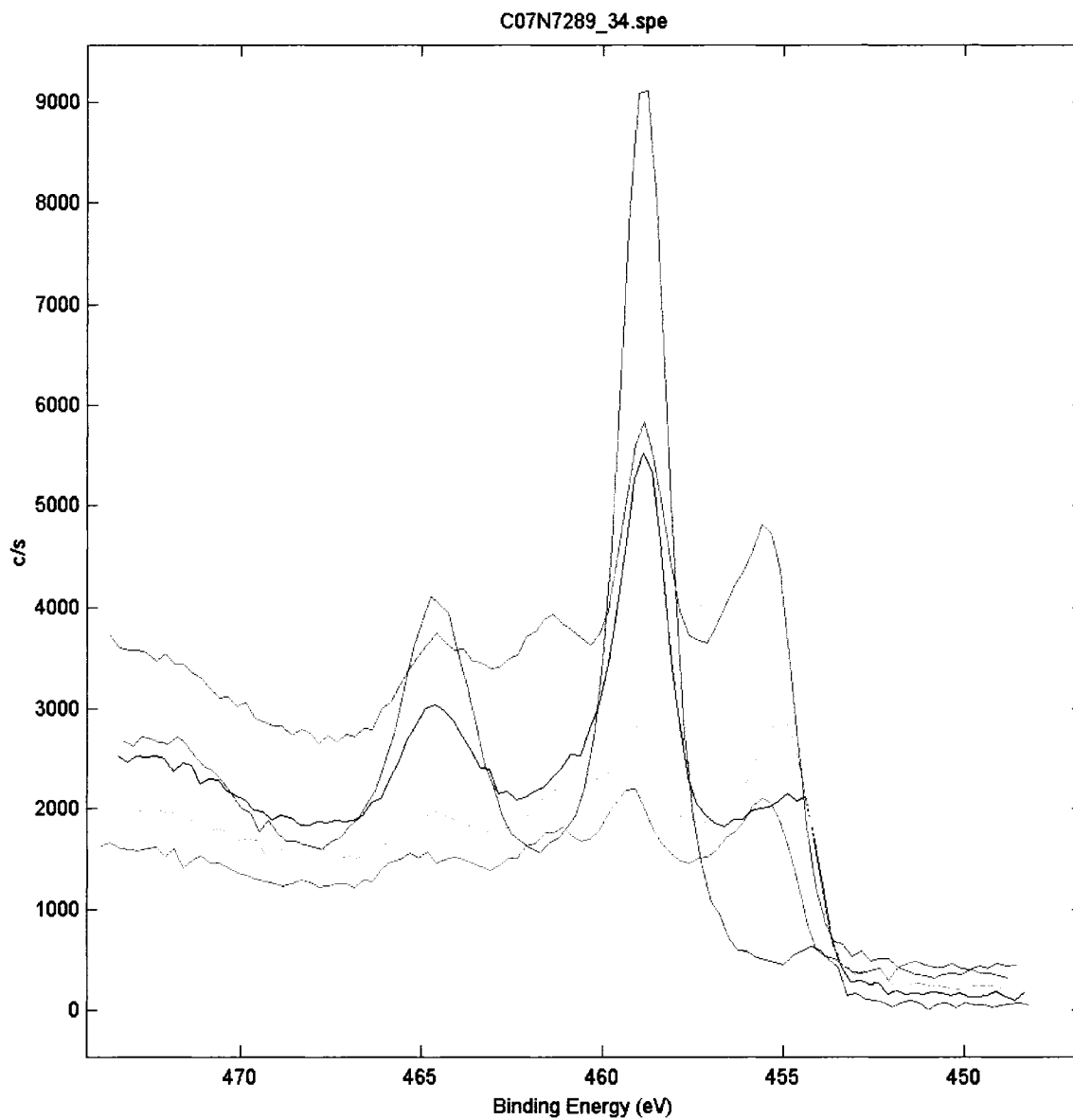


Figure 142. Overlay of the titanium bonding state spectra.

C07N7289_34.spe: Croom: Welds EAG
2007 May 14 Al mono 39.7 W 200.0 μ 45.0° 58.70 eV 1.4458e+003 max 4.33 min
Al2p/Point1: Control/1 (Shft)

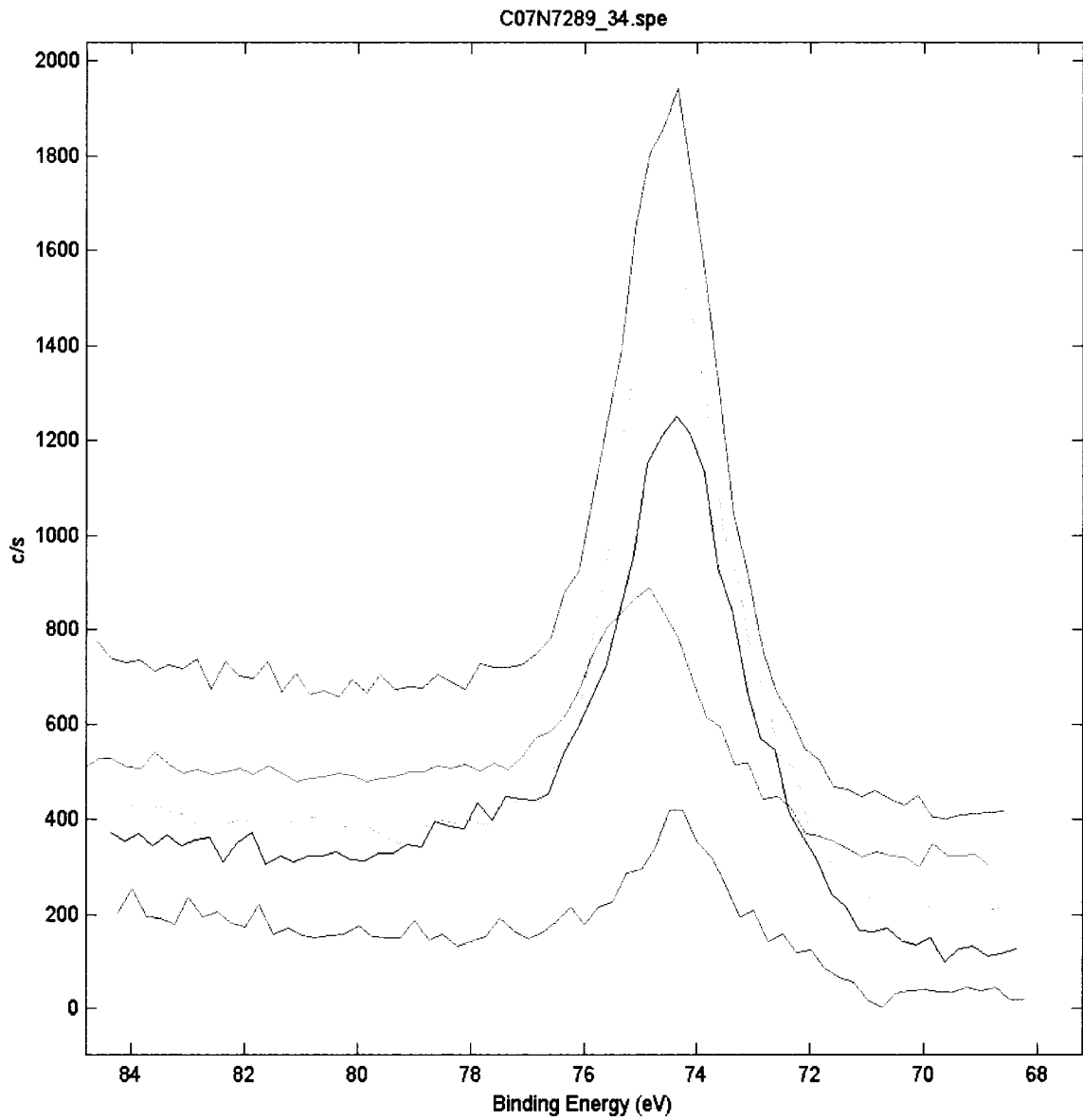


Figure 143. Overlay of the aluminum bonding state spectra.

C07N7289_34.spe: Croom: Welds EAG
2007 May 14 Al mono 39.7 W 200.0 μ 45.0° 23.50 eV 1.0000e+000 max 3.02 min
O1s/Point1: Control/1 (Shft)

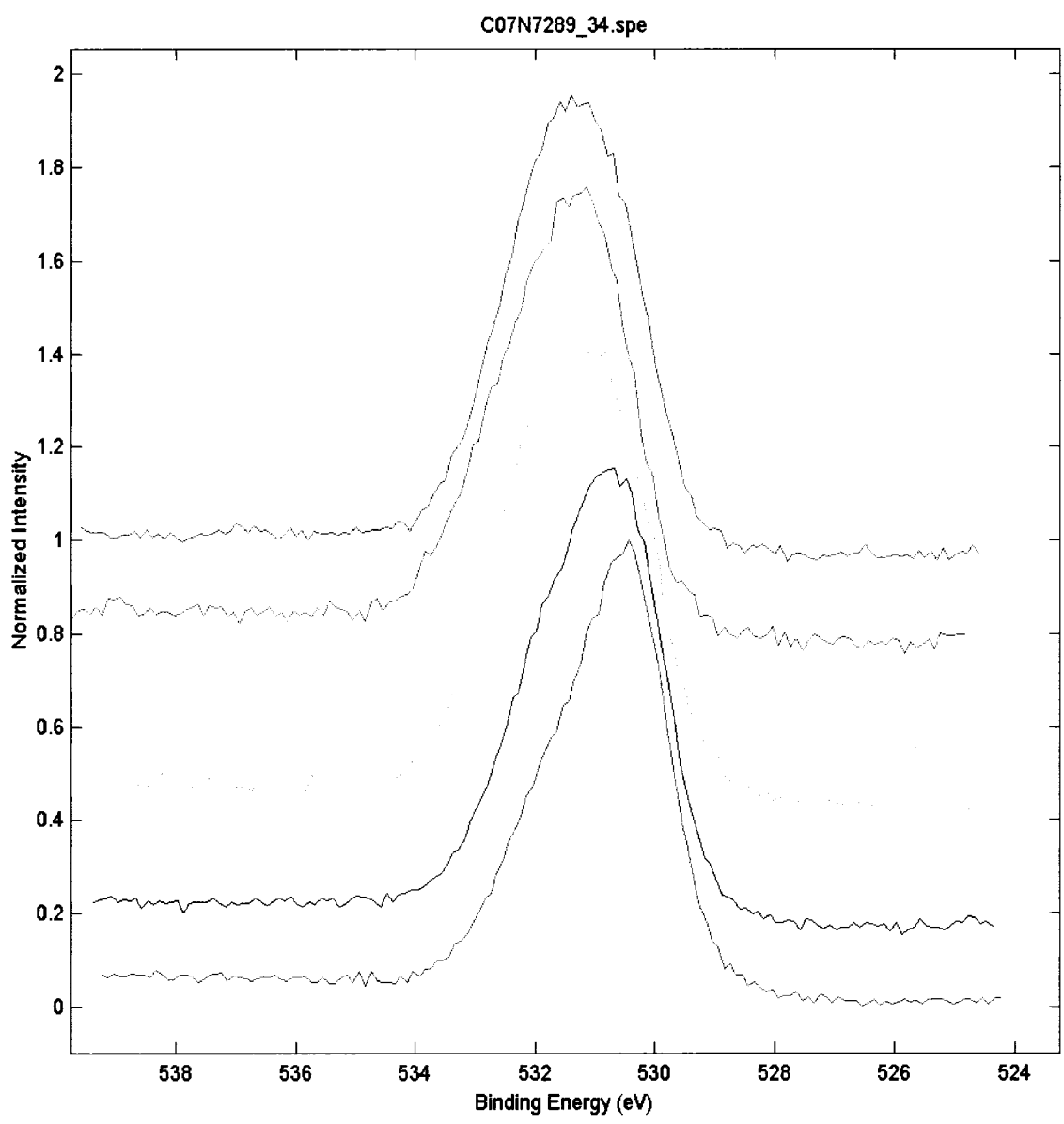


Figure 144. Overlay of the oxygen bonding state spectra.

C07N7289_34.spe: Croom: Welds EAG
2007 May 14 Al mono 39.7 W 200.0 μ 45.0° 23.50 eV 2.3452e+003 max 4.02 min
C1s/Point1: Control/1 (Shft SG3)

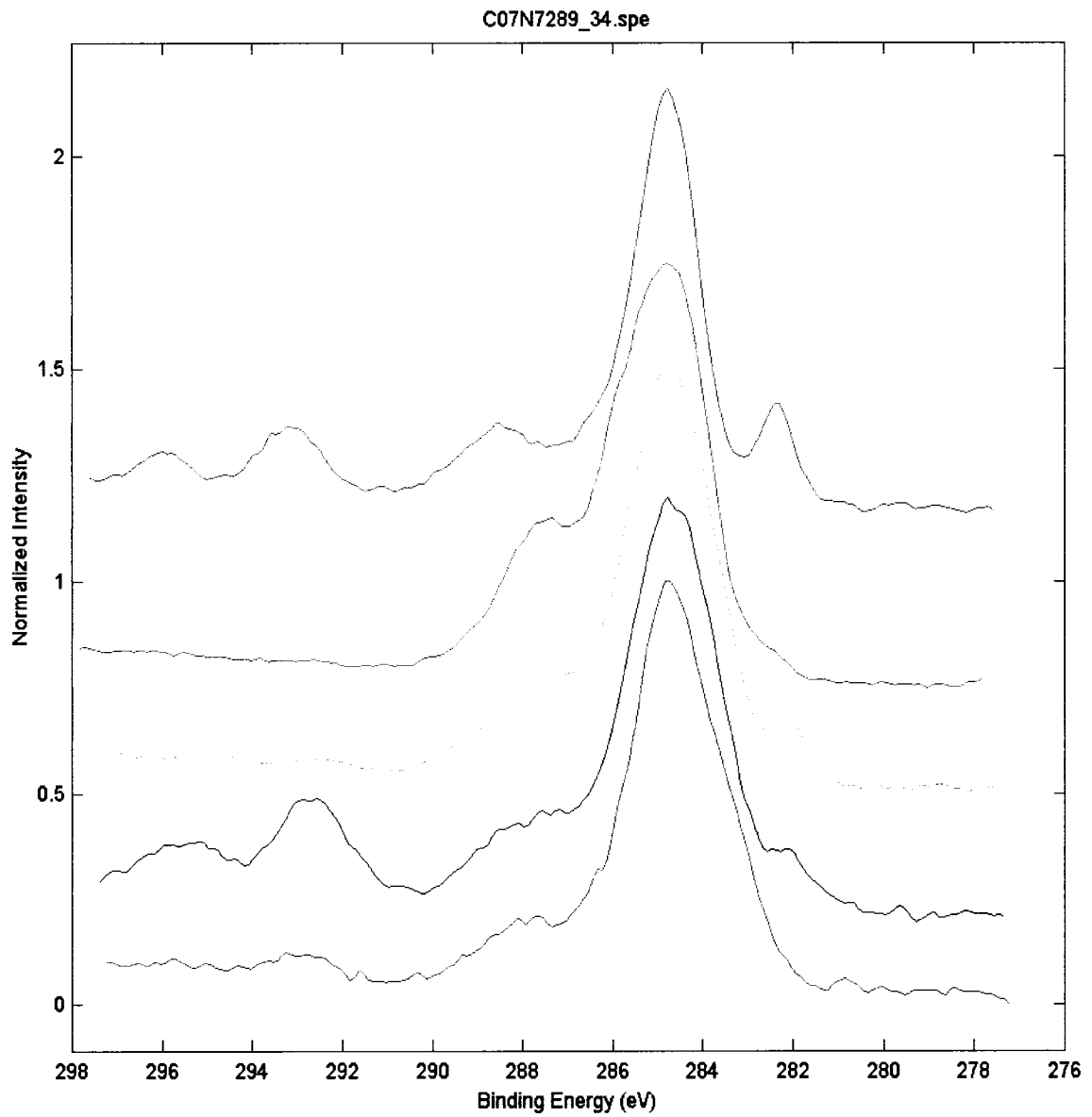


Figure 145. Overlay of the carbon bonding state spectra.

C07N7289_36.spe: Croom: Welds EAG
2007 May 14 Al mono 39.7 W 200.0 μ 45.0° 58.70 eV 4.4694e+003 max 3.03 min
N1s/Point5: s7/1 (Shft)

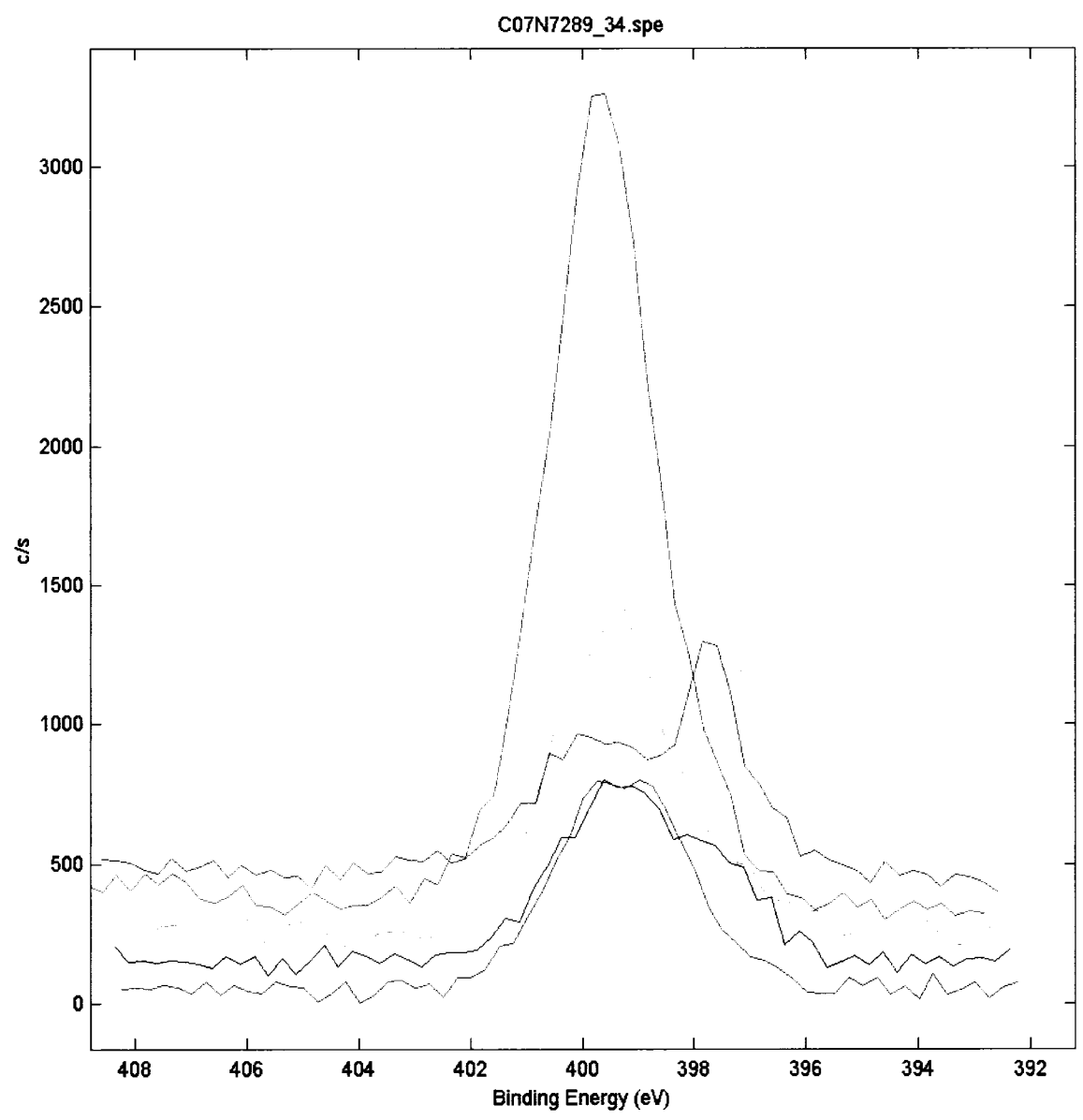


Figure 146. Overlay of the nitrogen bonding state spectra.

C07N7289_34.spe: Croom: Welds EAG
2007 May 14 Al mono 39.7 W 200.0 μ 45.0° 58.70 eV 2.0954e+003 max 2.85 min
Si2p/Point1: Control/1 (Shft)

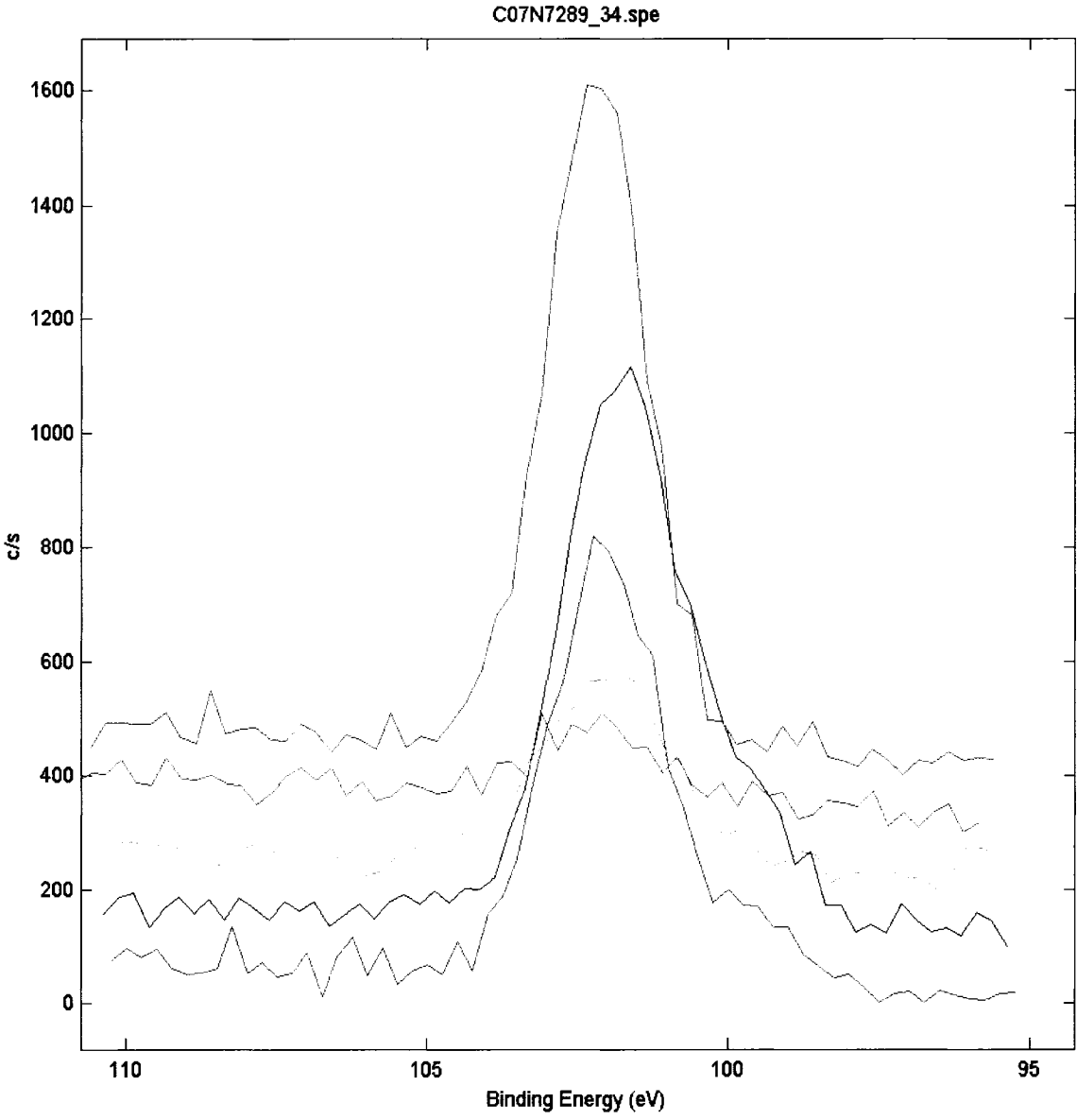


Figure 147. Overlay of the silicon bonding state spectra.